MMW/60GHz Liquid Crystal Tuneable Periodic Filters

Abdolreza DIVSALAR

A thesis submitted for the degree of

Doctor of Philosophy

School of Computer Science and Electronic Engineering

University of Essex

February 2026

Declaration

This work has not previously been accepted in substance for any degree and is not concurrently submitted in candidature for any other higher degree.

Signed: 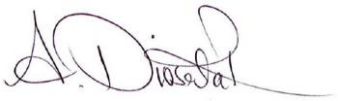 Date: 14/02/2026

Statement 1

This thesis is being submitted in partial fulfilment of the requirements for the degree of …PhD……..(insert as appropriate PhD, MPhil, EngD)

Signed: 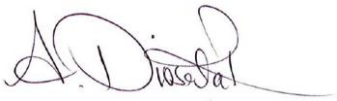 Date: 14/02/2026

Statement 2

This thesis is the result of my own independent work/investigation, except where otherwise stated. Other sources are acknowledged by explicit references.

Signed: 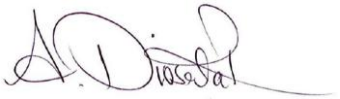 Date: 14/02/2026

Statement 3

I hereby give consent for my thesis, if accepted, to be available for photocopying, inter-library loan and for the title and summary to be made available to outside organisations.

Signed: 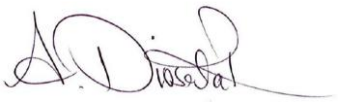 Date: 14/02/2026

Abstract

This thesis presents a design method for liquid-crystal–tuneable periodic microstrip filters at 60 GHz built around a three-stage synthesis. (1) Odd–even mode analysis provides closed-form starting dimensions for a symmetric unit cell on an anisotropic, voltage-biased LC substrate, placing the shunt/series resonances, target impedances and coupling needed for compact selectivity. (2) Reflection-coefficient (Γ) optimisation then refines the geometry using an analytical Γ expression for the unit cell, improving matching across the intended passband/stopband while preserving manufacturability; the criterion naturally incorporates the LC's bias-dependent effective permittivity. (3) Periodic cascade prediction forms the full filter by chaining optimised cells via the ABCD matrix to extract the Bloch propagation constant, locate the Bragg edges, and forecast insertion and return loss versus the high-level targets (centre frequency, selectivity and tuning range).

Validation relies on full-wave electromagnetic simulation in two independent platforms, Keysight ADS (Momentum) and CST Studio Suite, with harmonised substrate stacks, metallisation and bias conditions. The results show continuous, voltage-controlled frequency tuning around 60 GHz, low insertion loss in the passband and strong return loss, with close agreement between matrix-based predictions and EM responses. Cross-tool correlation substantiates the robustness of the synthesis and the practicality of biasing LC substrates at millimetre-wave.

The contribution is an LC-aware, synthesis workflow that unifies odd–even sizing, Γ-based optimisation and ABCD/Bloch prediction, together with a reproducible cross-platform validation protocol. The method provides a tractable path to reconfigurable 60-GHz front-end filtering and is readily extendable to other periodic topologies and frequency bands.

Acknowledgements

I would like to express my gratitude to my supervisor, Professor Dariush Mirshekar, who guided me throughout this research study.

Additionally, I would like to thank my family who supported, encouraged and motivated me throughout this journey, especially my wife Susan, my son and his wife (Saeed and Donia) and my daughter and her husband (Negar and John).

Table of Contents

List of Figures

List of Tables

Nomenclature

Abbreviations

3GPP	Third Generation Partnership Project
5G/6G	5th and 6th Generation Mobile Networks
ADS	Advanced Design System
AM	Amplitude Modulation
AR	Augmented Reality
BPF	Band Pass Filter
BSF	Band Stop Filter
BW	Bandwidth
CMOS	Complementary metal–oxide–semiconductor
DBR	Dual Behaviour Resonator
eMMB	Enhanced Mobile Broadband
EBG	Electromagnetic Band Gap
ECIT	Electronic, Communication & Information Technology
EM	Electromagnetic Simulation
ER	Equal Ripple
FBW	Fractional Bandwidth
FCC	Federal Communications Commission
FDTD	Finite Difference Time Domain

FEL	Finite Element Line Approach
FEM	Finite Element Method
GHz	Giga Hertz
HDMI	High-Definition Multimedia Interface
HPF	High Pass Filter
IEEE	Institute of Electrical and Electronics Engineers
ICs	Integrated Circuits
IET	Institute of Engineering and Technology
ITU	International Telecommunication Union
IMT	International Mobile Telecommunications
IoT	Internet of Things
LAN	Local Area Network
LC	Liquid Crystal
LTE	Long Term Evolution (4th Generation)
LPF	Low Pass Filter
MATLAB	Matrix Laboratory
MEMS	Micro electro- mechanical system
MHz	Mega Hertz
MNO	Mobile Network Operators
MMW	Millimetre Wave
NRA	National Regularity Authority

PCB	Printed Circuit Board
PTL	Planar Transmission Line
RF	Radio Frequency
RL	Return Loss
RLC	Resistor (R), Inductor (L), and capacitor (C)
RSPG	Radio Spectrum Policy Group
Tx/Rx	Transmitter / Receiver
UCL	University College London
UMTS	Universal Mobile Telecommunication System
UWB	Ultra-Wide Band
VSWR	Voltage Standing Wave Ratio
VR	Virtual Reality
WB	Wide Band
WiFi	Wireless Fidelity
WiGig	Wireless Gigabit
WLAN	Wireless Local Area Network

Notations

$\begin{bmatrix} A & B \\ C & D \end{bmatrix}$	ABCD Transmission Matrix
$\begin{bmatrix} A & B \\ C & D \end{bmatrix}^{EV}$	Diagonal Matrix made up of Eigenvalues
$\begin{bmatrix} A & B \\ C & D \end{bmatrix}^{PS}$	Transmission Matrix of Periodic Structure
$\begin{bmatrix} A & B \\ C & D \end{bmatrix}^{UC}$	Transmission Matrix of Unit Cell
A_{UC}	Element A of Unit Cell Transmission Matrix

A_{PS}	Element A of Periodic Structure Transmission Matrix
B_{UC}	Element B of Unit Cell Transmission Matrix
B_{PS}	Element B of Periodic Structure Transmission Matrix
C	Capacitance
C_0	Characteristic capacitance
C_{UC}	Element C of Unit Cell Transmission Matrix
C_{PS}	Element C of Periodic Structure Transmission Matrix
D_{UC}	Element D of Unit Cell Transmission Matrix
D_{PS}	Element D of Periodic Structure Transmission Matrix
$F_n(\omega)$	Elliptical function
$\Im$	Imaginary part
P_{in}	Power at input port
P_{out}	Power at output port
$\Re$	Real part
$S_{11}, S_{12}, S_{21}, S_{22}$	Scattering Matrix parameters
$T_n(\omega)$	Chebyshev function
Z_0	Transmission line characteristic impedance
Z_B	Bolch Impedance
Z_{UC}	Unit Cell characteristic impedance
Z_{in}	Impedance seen by a signal at the input
Z_L	Load impedance
Z_{OC}	Open circuit transmission line impedance
Γ	Reflection coefficient
Γ_{in}	Input reflection coefficient
Γ_N	Reflection coefficient or port N
α	Transmission line attenuation constant
β	Transmission line phase constant
γ	Transmission line Propagation Constant
ε	Permittivity (ε_0 : Permittivity of air =8.854 x 10-12 Farads/meter)
ε_{eff}	Effective Permittivity
ε_r	Relative Permittivity of Substrate
θ	Transmission line electrical length
θ_s	Electrical length of source transmission line
θ_r	electrical length of resonator transmission line
λ_0	Wavelength of cut-off frequency [m]

λ_{eff}	Effective wavelength
μ	Permeability (μ_0 : Permittivity of air = $4\pi \times 10^{-7}$ H/m)
μ_r	Relative permeability
v_p	Phase Velocity
π	π- number (i.e. 3.14159)
ω	Angular frequency [rad/s]
ω_c	Cut-off frequency

Chapter1 : Introduction

1.1 Context and motivation

The rapid growth of wireless connectivity and the push for multi-gigabit links have driven design activity into the millimetre-wave (mm-wave) bands. Within this space, the 60 GHz band stands out for its large contiguous spectrum, high spatial re-use, and suitability for short-range, high-data-rate links used in wireless backhaul, immersive VR/AR, and uncompressed video distribution. In all wireless communications bands, front-end filters are important: they suppress adjacent-channel interference and strong blockers, protect low-noise receiver stages, and ensure compliance with emission masks, yet they must do so in a compact, low-loss, and tuneable form to support dynamic spectrum use.

Periodic microstrip structures offer an attractive lever for achieving sharp selectivity and compact implementations through Bragg and slow-wave effects. In parallel, liquid-crystal (LC) substrates provide voltage-controlled, anisotropic permittivity with comparatively low loss at mm-wave, enabling electrically tuneable components that can shift operating frequency without altering the physical footprint. Combining periodic structures with LC substrates therefore promises frequency-agile filters that retain the simplicity and manufacturability of microstrip while unlocking genuine reconfigurability for next-generation systems.

1.2 Problem Statement

Tuneable filters are essential at 60 GHz because they allow devices to select desired bands and reject unwanted signals as channel conditions and such regulatory allocations vary. Systems operating at such high frequencies face adjacent-channel interference, strong in-band interferers, and the need for efficient spectrum utilisation across closely spaced channels. While filter banks composed of multiple fixed filters can achieve the necessary selectivity, they are bulky, add weight and complexity, and are poorly matched to agile operation. A single tuneable

filter can reduce size and mass while adapting to differing channels and waveforms; however, achieving a wide tuning range together with high selectivity, low insertion loss, low return loss, and a small footprint remains challenging at mm-wave.

Traditional tuneable approaches often exhibit a trade-off between tuning span and quality factor, with losses increasing as tuning elements are introduced. Many techniques also require complex biasing or non-standard fabrication. When periodic structures are combined with tuneable substrates such as LCs, additional difficulties in design and fabrications arise: accurate electromagnetic modelling is required to capture anisotropy and bias dependence, optimisation must be guided by meaningful figures of merit rather than trial-and-error, and layout must respect manufacturability and bias distribution to ensure reliable operation at 60 GHz. Moreover, design flows that begin and end with full-wave simulation can be slow and opaque; there is a need for a synthesis-oriented method that links unit-cell physics and cascade structure behaviour in a way that is sufficiently accurate to guide geometry before resorting to heavy EM sweeps.

Periodic structures themselves provide a promising basis for tuneable filters. Composed of repeating unit cells, they can realise bandpass, bandstop, and slow-wave behaviours, offering a flexible means of shaping frequency response while keeping layouts compact. At millimetre-wave frequencies, periodic microstrip implementations can be engineered for high selectivity and low insertion loss, and when paired with LC substrates their passbands or stopbands can be shifted by voltage-controlled changes varying effective permittivity. In this context, LC materials are particularly attractive as these anisotropic dielectrics whose properties vary with applied field enable real-time adjustment of resonant behaviour. This capability is critical for modern communication systems operating in dynamic and crowded spectral environments, where adaptive filtering and frequency agility directly translate to robustness and throughput.

1.3 Research Objectives

The overarching objectives of this research are to develop a novel class of 60 GHz tuneable microstrip filters using periodic structures on liquid-crystal substrates and to demonstrate a synthesis-driven design method that is compact, transparent, and validated. The work aims, first, to design periodic microstrip structures that exhibit high selectivity and low insertion loss while retaining a practical footprint; secondly, to analyse how LC properties—particularly anisotropy and bias-dependent permittivity—affect the performance and tuneability of these filters; thirdly, to develop theoretical models and a simulation framework that together enable effective optimisation of unit-cell geometry and periodic cascade behaviour; and finally, to verify the proposed designs through full-wave electromagnetic simulation and cross-platform comparison.

The study concentrates on the design, simulation, and validation of tuneable microstrip filters operating in the 60 GHz band. It leverages periodic structures for compact, ease of design, single bias point for application of tuneable devices and LC substrates for easy implementation for electrical tuneability. Particular attention is given to the role of unit-cell geometry and resonator configuration, to the selection and modelling of substrate properties, and to practical issues such as fabrication constraints, LC alignment layers, electrode structures, and bias distribution. The research also considers integration with other mm-wave components in order to situate the filter within a realistic front-end environment. In doing so, it seeks to bridge the gap between theoretical advances in periodic structures and the practical realisation of reconfigurable hardware, providing design guidance that can be reproduced and extended.

1.4 Structure of the Thesis

This thesis is organized as follows:

- **Chapter 1** introduces the research background, articulates the problem, objectives, and defines the objectives and scope.

- **Chapter 2** reviews the relevant literature on periodic structures, microstrip filter design, and liquid-crystal substrates, and explains why tuneable periodic filters can be significant in modern telecommunication systems.
- **Chapter 3** summarises the fundamentals of microstrip filters and conventional design methods, illustrating baseline behaviour through reference simulations that serve as points of comparison for later chapters.
- **Chapter 4** surveys LC material characteristics and behaviour under external bias at a molecular level, focusing on aspects that determine microwave and mm-wave performance and that directly influence filter tuneability
- **Chapter 5** develops a comprehensive formulation of microstrip periodic structures for tuneable filters, introduces the design methodology used to determine physical dimensions for specified frequency and bandwidth targets, and outlines the numerical techniques employed for analysis. It also foreshadows the role of unit-cell modelling, reflection-coefficient criteria, and ABCD/Bloch-based prediction as tools for guiding geometry.
- **Chapter 6** documents the proposed algorithms and programs with further calculations to design periodic filters and then provides the simulation and optimization results of different microstrip tuneable filters in MMW frequencies with different unit cell structures. It also verifies filters' responses using different software platforms.
- **Chapter 7** covers the conclusion statements summarizing the research outcomes and their contributions to the field of tuneable LC periodic filters for modern communication systems and follows with the proposed future works which can be done in future as the expansion of this research.

Chapter2 : Background Information

2.1 Why 60-GHz frequency band?

The wide frequency band of 57-66 GHz (extended to 57–71 GHz in some regions), which is a specific spectrum of V- Band and millimetre-wave (MMW), is widely licence-exempt. It offers large, contiguous bandwidth capable of multi-gigabit links while naturally favouring short range deployments (for this reason has potential applications in ad-hoc wireless communications and in robotic). From a physical-layer perspective, three properties make it especially attractive. First, the short wavelength (≈ 5 mm in free space) allows electrically large apertures and practical phased arrays on compact platforms, enabling narrow beams and high spatial re-use. Second, atmospheric absorption, dominated by oxygen near 60 GHz, introduces additional path loss over distance; although modest at room or building scales, it helps confine interference, enhances link privacy, and reduces inter-cell coupling (Fig 2.1). Third, the wide channels available in this band support very high data rates with relatively straightforward waveforms and moderate signal-processing complexity, as demonstrated by 60-GHz wireless standards (e.g., IEEE 802.11ad/ay) targeting multi-gigabit connectivity [1].

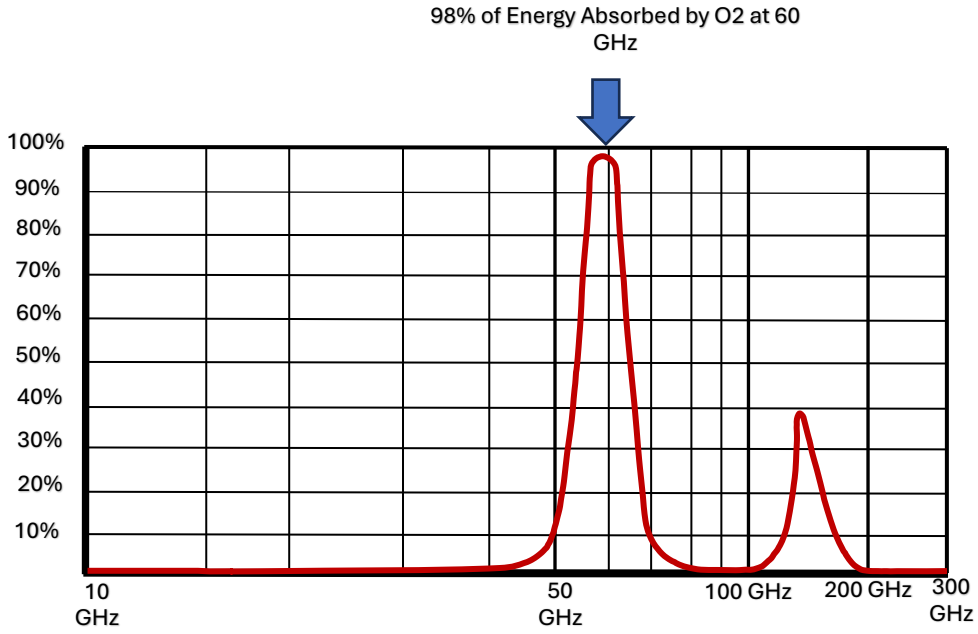

Fig 2.1 Oxygen attenuation in 60GHz frequency

These physical attributes translate into clear system-level advantages for short-haul and indoor links: high-throughput distribution of uncompressed or lightly compressed HD/4K video, device docking and cable replacement, VR/AR streaming, and compact backhaul/relay nodes. Because beams are narrow and ranges are short, multiple radios can operate concurrently in the same venue with limited mutual interference. The equipment footprint can also be small; short guided wavelengths favour compact front-end modules and small antennas, easing integration into consumer and enterprise devices. Importantly, the band's interference profile is benign relative to crowded sub-6-GHz ISM bands: oxygen absorption limits long-range interference, and non-penetrative propagation through walls can be advantageous for room-scale frequency planning [2].

The 60 GHz frequency band offers several key advantages for telecommunication systems. Its wide bandwidth and high data rate make it ideal for fast data transfer applications. The short range and wavelength, along with reduced likelihood of interference from devices operating in other frequency bands, further enhance its utility. This band supports multi-gigabit communication systems and benefits from limited signal penetration through obstacles, primarily due to atmospheric absorption. Additionally, the small wavelength allows for compact equipment sizes and the use of small antennas, making it a highly efficient choice for modern telecommunication needs.

One of the main advantages of the 60 GHz band is its ability to support the very large channel bandwidths required by emerging 5G and future 6G communication systems. The extensive spectrum available in the millimetre-wave region enables multi-gigabit data rates, which are increasingly necessary to accommodate the continued growth of internet traffic and high-capacity wireless services. In particular, operation around 60 GHz can support data rates on the order of several gigabits per second over short-range links, making this band attractive for high-throughput access, backhaul, and indoor wireless applications. The availability of more than 7 GHz of contiguous spectrum further enhances its suitability where wide bandwidth is required.

For outdoor and mobile deployments, the use of unlicensed spectrum requires appropriate spectrum-sharing and regulatory considerations; as a result, upper millimetre-wave bands such as 57–71 GHz have been identified as potential candidates for enterprise users and mobile network operators. In this context, national regulatory authorities have introduced licensing and regulatory frameworks for technologies operating in the 60 GHz band, in line with ongoing studies on 6G development and future spectrum requirements [3].

The use of 60GHz in 5G networks are already recommended and are part of ongoing research and technology standards. The use of MMW band supports Enhanced Mobile Broadband (eMBB) services with high data rate applications. For 6G which is still in early stages (expected to be launched in 2030), even terahertz frequencies which are beyond MMW are recommended. Considering the performance, cost, and volume of microwave devices, and the requirement for compact components in limited spaces application of 60GHz technologies and solutions has been already initiated [4].

Other applications of MMW range are developed for wireless communication and radars. These include the high-speed wireless communications 24.05–24.25 GHz and 57–64GHz bands for wireless communications and the 22–29 GHz and 76–77 GHz bands for automotive radar [5].

The 60GHz technology which is now developing in a wide range of solution for microwave system applications, has also a great potential to be used for military uses as well as commercials. The V-band and E-band backhaul networks for wireless systems have become increasingly common. The MMW technology is going to be even more important as many small-cell deployments are utilizing these networks. Another example of 60 GHz technology application is in automotive systems such as electronic sensors and radar detectors. Microwave devices and technologies operating in 60GHz frequencies have the potential of being even more spread in different sectors of the advance technologies in the future. The limited range of 60 GHz frequencies arises from high atmospheric absorption (particularly by oxygen) can restrict

their usability in long-range communication. However, for applications that do not require extensive coverage, this limitation can actually work in favour of 60 GHz systems.

2.2 Industry Trends

Initial applications of MMW system were in military and radio astronomy fields. The military and defence uses included missile and fire-control systems, together with research on phased-array antennas in the extremely high frequency (EHF: 30-300GHz) range, while radio astronomy also exploited these bands. In addition, applications of millimetre-wave (MMW) systems have gained significant attention from industry in various areas, including the next generation of wireless communication systems, navigation and satellite communications, intelligent transport systems, and vehicle short-range radar.

Huge commercial benefits can be achieved by developing 60GHz enabled devices. These devices can provide gigabit bandwidths for fast data/audio/video distribution indoors (e.g., inside planes, trains, cars and offices).

The importance of tunability in 60 GHz systems arises from variation in allocated unlicensed frequency bands across different regions and the need to meet diverse operational requirements and use cases. Countries and regions such as North America, Europe, Australia, Japan and Korea have different regulatory frameworks governing the allocation of unlicensed spectrum within the 60 GHz band, typically ranging from 57–66 GHz (with some extending to 57–71 GHz) and with differences in precise bandwidth and usage constraints.

The need for tunability in 60 GHz systems arises from both regulatory and practical considerations. Variations in allocated unlicensed frequency ranges across different regions necessitate frequency agility to ensure compliance with regional spectrum regulations. In addition, manufacturing tolerances, environmental effects, and changes in operating conditions can introduce frequency shifts at millimetre-wave frequencies, where small dimensional or material variations result in significant electrical changes. Tuneable filter structures therefore

provide an effective means to compensate for these variations, enabling robust operation across different regions, deployment scenarios, and use cases within the 60 GHz band.

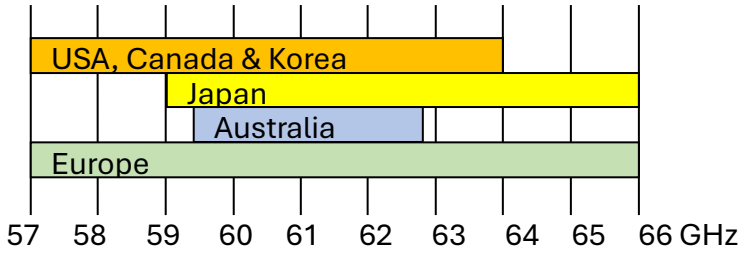

Fig 2.2 Unlicenced MMW frequency band around the world

Both cellular and Wi-Fi networks are experiencing increasing demand as they seek to deliver more data to more users. Possible responses include adding more towers/access points, freeing bandwidth by better balancing multiple user requests on a node and increasing network speed. Telecom companies are exploring so-called fifth generation (5G) wireless technologies for this purpose. The 60 GHz band spectrum is therefore relevant for wireless applications.

The first popular standards for Wireless LAN (IEEE 802.11a and 802.11b) were designed primarily to serve laptops in homes and offices and later to allow mobile connectivity in hotels, airports and shopping centers. These were followed by other standards to meet the need for higher throughput at higher frequencies [6].

- 802.11 a : 54 Mb/s Bandwidth @ 5GHz
- 802.11 b : 11 Mb/s Bandwidth @ 2.4GHz
- 802.11 g : 54 Mb/s Bandwidth @ 2.4GHz
- 802.11 n : 100-250Mb/s Bandwidth @ 2.4 & 5GHz
- 802.11 ac : 500 Mb/s Bandwidth @ 5GHz
- 802.11 ad : 7 Gb/s Bandwidth @ 60GHz (short range),
- 802.11 ay : 100Gb/s Bandwidth, Multiple modulation scheme @ 60GHz (enhanced amendment to 802.11ad, supporting up to 8.64GHz channel bonding)

WiGig specialists collaborate with leading manufacturers, such as Cisco, to integrate the technology alongside Wi-Fi into enterprise infrastructure capable of operating across three radio bands: 2.4GHz, 5GHz, and 60GHz. These tri-band networks incorporate WiGig in addition to mainstream Wi-Fi systems, enhancing connectivity across the 2.4GHz and 5GHz spectrum bands.

Fig 2.3 Wireless LAN, IEEE 802.11 standards

WiGig-enabled devices, based on IEEE 802.11ad and 802.11ay standards, have been integrated into a wide range of wireless network equipment, including docking stations, adapters, routers, access points, virtual reality (VR) and augmented reality (AR) headsets, wireless display solutions, laptops, tablets, smartphones, WiGig dongles, and network kits.

Key technology players such as Intel, Dell, Qualcomm, Asus, and Netgear have incorporated WiGig capabilities into their products, underscoring the growing adoption of this technology. With its high-speed and low-latency features, WiGig is well-suited for emerging applications in the Internet of Things (IoT), smart homes, and other cutting-edge technologies.

2.3 Technology Requirement, Tuneability

Several technology elements must come together for 60-GHz–enabled equipment to be viable in the commercial market. Advanced modulation and coding, high-gain compact antennas and front-end RF components, low-noise amplifiers, mixers and frequency synthesis, and tuneable filters all need to operate reliably at mm-wave frequencies and continue to improve in performance and integration.

Filters are key RF components used to select or reject specific frequency bands. Tuneability refers to adjusting a filter so that it provides the same functional performance at different centre

frequencies. A number of technologies have been reported to realise tuneability in microstrip filters:

1. Liquid Crystal Substrate, to control substrate electrical characteristic under external field
2. Varactor diodes, which are semiconductor devices with variable capacitance under an applied voltage.
3. Micro-electro-mechanical systems (MEMS), employing mechanical element with movable components to provide tunability
4. Ferroelectric materials, with spontaneous varying polarization under external electric field to achieve tunability
5. Geometry Adjustment Microstrip, which provides tunability using manual or automatic geometry adjustment of microstrip line

Table 2.1 summarises the main approaches and compares their typical advantages, disadvantages and applications for 60-GHz filters. This table provides a high-level overview of tuning approaches applicable to 60 GHz filters. A more detailed technical comparison of voltage-controlled tuning mechanisms is presented later in Chapter 4.

While each technology has strengths and limitations, LC-based tuning is particularly attractive in this work because it offers useful tuning range with planar integration, moderate complexity, and low cost. Varying the bias voltage across the LC layer rotates the director and changes the effective permittivity between its ordinary and extraordinary values. This alters the electrical length of the unit cell and therefore moves the filter passband/stopband within the target frequency range, without mechanically changing the geometry. The approach is compatible with compact microstrip layouts and can be implemented using standard low-temperature processes, which motivates its selection for the tuneable periodic filters studied in subsequent chapters.

Tuning Method	Description	Advantages	Disadvantages	Typical Applications
Mechanical Tuning	Physically adjustment such as tuning screws inserting or adjusting resonant cavities to change their effective dielectric volume or coupling.	- High precision - Post-fabrication correction. - Relatively simple in concept.	- Labor-intensive and time-consuming, - Requires skilled operators and specialized equipment - Permanent adjustment, Mistakes are irreversible. - Not suitable for dynamic tuning during operation. - difficult to miniaturized or integrated filters.	-Prototype development, high -Performance cavity filters, post -Fabrication calibration for fixed-frequency applications.
Electronic Tuning (Voltage-Controlled)	Voltage variable electrical properties can be by an applied. Common methods: - Varactor Diodes - Liquid Crystal (LC) Materials - Ferroelectric/ Piezoelectric Materials	- Real-time, continuous, and fast tuning capability. - Can be integrated on-chip or into compact modules. - Allows for adaptive tuning to compensate for environmental changes (temperature, load variations). - Enables reconfigurable or multi-band filter designs.	- Increased insertion loss and reduced Q-factor compared to passive fixed filters due to losses in tuning elements. - Power consumption for bias circuitry. - Limited tuning range compared to the overall 60 GHz band. - Non-linearity and intermodulation distortion at high power levels. - Complexity in integration and control.	Dynamically reconfigurable filters, adaptive filtering in transceivers, multi-standard radios, compact integrated modules for beamforming/sensing .
MEMS-based Tuning (Micro-Electro-Mechanical Systems)	Incorporates tiny mechanical structures that can be moved or actuated electrically to change filter characteristics. This can involve: - MEMS Switches: Physically connecting/disconnecting resonant elements. - MEMS Varactors/Capacitors: Changing the gap between capacitor plates to alter capacitance. - MEMS Resonators: Directly tuning the mechanical resonance of a structure that acts as an RF filter.	- Miniaturization and Compact Size - Low Cost (Mass Production) - Low Power Consumption - High Sensitivity and Accuracy - Durability and Reliability - Integration with Electronics - Fast Response Time	- High Initial Investment and Design Complexity - Fragility and Sensitivity - Manufacturing Challenges and Low Reproducibility - Environmental Sensitivity - Limited Frequency Range	- Automotive Industry -LiDAR Systems: Micromirrors for laser beam steering in autonomous vehicles. -Smartphones and Wearables - Navigation and stability control. -Medical and Biomedical Applications (BioMEMS):

Table 2.1 Comparison of tuning methods for 60 GHz filters (high-level overview)

2.4 Relevant works published in peer review journals

Research on 60-GHz millimetre-wave (MMW) systems and components has expanded rapidly in recent years. The allocation of ~7 GHz of spectrum for unlicensed use by the FCC in the early 2000s opened access to substantial bandwidth, and—together with advances in wireless technology—focused attention on this part of the spectrum for new systems and components.

Synthesis and design of a tuneable filters using Liquid Crystals with dual-behaviour resonator (DBR) technology in MMW frequencies is reported in [7]. The research confirms the observation of potential agility of the LC based devices. The agility could be obtained by varying dielectric permittivity of liquid crystal using external voltage source.

Broader concepts for LC-tuneable devices at MMW frequencies are reviewed in [8] and as a summary GT3-23001 and GT3-24002 mixtures of liquid crystals are introduced as the common materials used, due to their voltage-dependent effective permittivity.

Reported advantages of LC technology relevant to 60-GHz filters, including low operating voltage, millisecond-scale switching, simple planar structures, useful dielectric anisotropy, and low loss, are summarised in Table 2.2 with supporting references [9]–[11].

A recent article [12] reports a liquid crystal based tuneable band-stop filter using wave interface technique. Wave interface techniques refer to methodologies that directly manipulate the electromagnetic wave properties at the interface of different media or structures within a device. These techniques focus on the physical behaviour of waves, such as reflection, refraction, transmission, and scattering, rather than relying on approximate models like lumped-element equivalent circuits. Wave interface techniques enable the precise control of electromagnetic wave propagation through LC-based devices by optimizing the interaction between the wave and the LC material. By using wave interface techniques, the impedance between LC layers and surrounding structures can be carefully matched to minimize reflections and maximize tunability. LC filters rely on phase changes introduced by altering the orientation

of the LC molecules. Wave interface techniques help in designing structures where these phase changes produce desired filtering effects, such as sharp stopbands or wide passbands.

The research demonstrates an LC based tuneable band pass filter with an inverted microstrip line structure with conventional open stub structures with different stub length to achieve the desired frequency rejection behaviour. The developers could obtain a wider rejection bandwidth and higher rejection ratio by applying wave interface technique instead of lumped equivalent circuit analysis. Traditional lumped-element designs typically exhibit rejection bandwidths of 5%-10% of the centre frequency. Wave interface techniques, in contrast, can achieve rejection bandwidths of up to 20%-30%, in the millimetre-wave spectrum. Lumped equivalent circuit-based designs often deliver rejection ratios in the range of 20-30 dB.

Advantage	**Quantitative Details**	**Ref.**
Low Voltage Requirement	Tuning achieved with voltages as low as 1–10V (AC or DC). The low voltage requirement makes LC devices ideal for integration into low-power systems, enabling compatibility with modern electronics.	[9]
Fast Switching Speed	Switching times in the range of 10ms to 100ms, depending on the LC mixture and device design. Millisecond switching times are highly suitable for dynamic applications, such as beam steering and adaptive filtering.	[10]
Simple Architecture	Typical configurations involve enclosed coplanar waveguides or planar glass substrate layers with electrodes. Simplified designs reduce fabrication complexity, making LC devices cost-effective and scalable.	[9] , [11]
snipHigh Dielectric Anisotropy	Dielectric anisotropy values of $\Delta\varepsilon = 10$ to 20 for common LC mixtures (e.g., GT-series) at mmWave frequencies. High anisotropy ensures strong tunability, while low loss preserves signal integrity at mmWave frequencies.	[10], [11]
Low Loss with Frequency	Loss tangents as low as 0.003–0.005 at 60 GHz for GT-series LCs. This feature preserves the quality of transmitted signals, ensuring high data rates and minimal errors , reduces power dissipation, critical for power-sensitive and thermally constrained applications.	[10], [11]
Lightweight and Low Power	LC-based devices are 30–50% lighter compared to mechanical tuning. The lightweight nature and minimal power draw make LC devices particularly attractive for portable or space-constrained applications.	[9]

Table 2.2 Reported advantages of liquid crystals for 60 GHz filters

With wave interface optimization, rejection ratios can exceed 40–50 dB, providing a significant improvement in signal isolation and interference mitigation. Wave interface techniques, in contrast, can achieve rejection bandwidths of up to 20%–30%, particularly in the millimetre-wave spectrum.

The liquid crystals were recognised and suggested to be used for microwave dielectric substrates in early 1990 [13]. and early tuneable resonators/filters employing LC, such as half-wavelength open-circuit stub resonators and second-order filters, were demonstrated with standard mixtures (e.g., K15, BL037) [14]. The research discussed a half-wavelength open-circuit stub resonator and a 2nd order resonator filter using standard K15 and BL037 liquid crystal substrates. Several successful reports of experimental & simulation designs in 5GHz band have been published in the recent years [15], also valuable studies and approaches have been carried out in a research group formed by the university of Essex and UCL to develop the world first studies on "Voltage Tuneable Liquid Crystal Devices for 60 GHz Wireless Networks". These studies also include a basic approach to the design concepts of MMW tuneable band-pass filters on 33 GHz, as an individual component [16].

Complementary device technologies relevant to 60 GHz filters are also well represented in the literature. Silicon-based RF platforms for microwave/mm-wave applications are reviewed in [17]. Also, applications of silicon-based systems at MMW frequencies are reported in [18]. Application of RF micro-electro-mechanical system (MEMS) in tuneable bandpass filter in 60 GHz is reported in [19]. Ring resonator with open circuit stub is proposed to design a millimetre-wave band pass filter using CMOS technology in [20]. Filter-in-Package Solutions based on PCB and low temperature co-fired ceramics (LTCC) in 60GHz is reported in [21].

2.5 Summary

This chapter surveys the foundational concepts, industrial drivers, technological requirements, and prior research on tuneable periodic microstrip structures realised on liquid-crystal (LC)

substrates for operation at 60 GHz. The 60-GHz allocation offers roughly 9 GHz of contiguous spectrum for short-range, multi-Gb/s links in wireless backhaul, immersive VR/AR, and uncompressed video. Its short wavelength enables compact front-end components; however, higher propagation and material losses, blockage sensitivity, and stringent emission masks raise the bar for selectivity, insertion loss, stability, and reproducibility. These pressures make tunability a first-order requirement, allowing radios to adapt to spectral congestion and changing link budgets without proliferating hardware variants.

LC substrates are attractive because their effective permittivity is voltage-controlled, enabling continuous electrical tuning without mechanical reconfiguration. When periodic microstrip structures, whose dispersion characteristics support bandgap formation, slow-wave behaviour, and Bragg-edge shaping, are combined with LC anisotropy, designers gain additional degrees of freedom to control passband placement, bandwidth, and selectivity–loss trade-offs. This combination has motivated increasing research interest in LC-based tuneable components at microwave and millimetre-wave frequencies.

The reviewed literature demonstrates that periodic loading can realise compact and selective responses, while LC technology enables credible and repeatable frequency tuning across a range of components, including filters, phase shifters, and antennas. Reported studies commonly employ circuit-level models supported by full-wave electromagnetic solvers (e.g., ADS Momentum and CST) to validate performance trends. These works collectively establish the feasibility of LC-based tuning and periodic structures at millimetre-wave frequencies.

However, comparison across published results remains challenging. Differences in substrate stack-ups, LC materials, biasing schemes, packaging approaches, and measurement methodologies lead to heterogeneous reporting and limit reproducibility. Cross-tool validation is often qualitative, with limited disclosure of calibration procedures, de-embedding strategies, or uncertainty budgets. As a result, it is difficult to extract generalisable design rules or to translate reported concepts into a consistent synthesis methodology.

Collectively, these observations highlight the absence of a unified, LC-aware synthesis framework that systematically links analytical unit-cell design, dispersion-based performance prediction, and geometry refinement within a coherent workflow. This gap motivates the structured methodology proposed in this thesis.

Chapter3 : Microstrip Filter Theories and Realisation

3.1 Microstrip Filter Design

This chapter reviews classical filter synthesis and its realisation in microstrip as a basis for the periodic, LC-tuneable designs used later. Filters control the frequency response at a given point in a system, suppressing unwanted frequencies and allowing desired frequencies to pass. Traditional designs of microwave filters use the microstrip line which provides a better compromise in terms of size and performance compared to other possible physical structures. Microstrip planar filters consist of a conducting strip separated from a ground plane by a dielectric layer known as substrate. Shape and dimensions (i.e. length, width & thickness) of conducting strip and the thickness of substrate are the design parameters to form the capacitive and inductive elements needed to obtain the desired filter transfer function. The operating frequency of a filter is a function of both the physical characteristics (dimensions and thicknesses of the strip and substrate) and the electrical characteristics of the microstrip line. For a tuneable filter, altering the physical characteristics of a fabricated component is difficult; therefore, it is preferable to adjust the electrical characteristics. This can be achieved by changing the effective permittivity (ε_{eff}) of the dielectric layer(s).

Design procedure of a filter can be categorised in two mail processes: mathematical and implementation. These processes can be also referred to as scientific and artistic processes.

3.1.1 Mathematical (Scientific) Process

The mathematical or scientific part of design process is based on the required parameters of filter such as cut-off frequencies, slope of filter response (i.e. order of filter), filter passband and stopbands, allowed level of passband ripples, return loss and forward transmission and VSWR. In general, a microstrip filter might be shown as a 2 port network as shown in Fig 3.1, that the input, output and signal response, can characterise the filter behaviour. The scattering

parameters S_{11}, S_{12}, S_{21} and S_{22} describe the relationship between the incident and reflected signals at filter input and output ports. The first number in the subscript refers to the responding port, while the second number refers to the incident port, thus S_{21} means the response at port 2 due to a signal at port 1.

Fig 3.1 Filter two-port description and S-parameter matrix

For a reciprocal, symmetrical circuit terminated in matched load, $S_{11} = S_{22}$ and $S_{12} = S_{21}$. In this case:

- S_{11}: input-port reflection coefficient,
- S_{12}: reverse transmission (isolation),
- S_{21}: forward transmission (insertion),
- S_{22}: output-port reflection coefficient.

For passive microwave devices $P_{out} \leq P_{in}$, also for ideal lossless lines the absorbed power (i.e. converted to heat) is zero and therefore: $P_{in} = P_{out} + P_{ref}$

where P_{in} is the input power, P_{out} is output power and P_{ref} is the reflected power.

In a filter for a given signal frequency of ω_s we are in Pass band or Stop band when:

- Pass Band ➔ $P_{ref} \rightarrow 0$, $P_{in} \approx P_{out}$ → $|S_{21}| \approx 1$ (0 dB) and $|S_{11}|$ is small
- Stop Band ➔ $P_{out} \rightarrow 0$, $P_{in} \approx P_{ref}$ → $|S_{11}| \approx 1$ (0 dB) and $|S_{21}|$ is small

However, the scattering elements (S-parameters) of the filter transfer function are functions of signal frequency. S_{21} of a filter is also called as filter transfer function and in complex presentation is equal to:

$$S_{21}(\omega) = \Re\{S_{21}(\omega)\} + j\,\Im\{S_{21}(\omega)\} = |S_{21}(\omega)|\; e^{j\angle S_{21}(\omega)} \quad , \qquad (3.1)$$

where:

$$\angle S_{21}\,(\omega) = \tan^{-1}\left\{\frac{\Im\, S_{21}\,(\omega)}{\Re\, S_{21}\,(\omega)}\right\}\,. \tag{3.2}$$

This can be also shown as a complex polynomial $S_{21}(\omega) = N(\omega) / D(\omega)$ where N and D are the numerator and denominator functions of the transfer function. The values of ω at which the N(ω) becomes zero are the zeros and the values of ω at which the D(ω) function becomes zero are the poles of $S_{21}(\omega)$ [22].

In a stable filter the poles should lie on the left-hand side of imaginary axis otherwise, if we have poles on the right-hand side then exponentially increasing oscillations happens. However, the zeros may lie anywhere on complex plane. The most famous functions to represent the filter transfer function $S_{21}(\omega)$, are listed as follows:

1. Butterworth (Maximally flat) function
2. Chebyshev (equal ripple) Function
3. Elliptical Function

3.1.1.1 Butterworth (maximally flat) function

For a Butterworth prototype, the (normalised) magnitude response is

$$|S_{21}(\Omega)|^2 = \frac{1}{(1+\Omega^{2n})} \tag{3.3}$$

Where $\Omega=\omega/\omega_c$ is the normalised frequency with cut-off at Ω=1 Ω=1 (–3 dB point), and n is the order (a positive integer). The order n corresponds to the number of reactive elements in the low-pass prototype required to realise the response. Butterworth filters are also known as maximally flat because the passband magnitude is monotonic and as flat as possible at Ω=0 (no ripple). They provide a gradual roll-off and are therefore used where maximum passband flatness is required [23]. Figure 3.2 illustrates a typical Butterworth passband with the cut-off frequencies indicated.

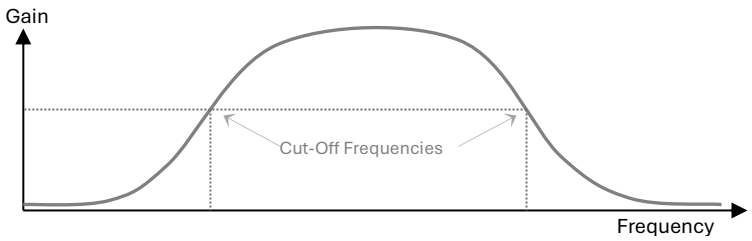

Fig 3.2 Butterworth (maximally flat) filter frequency response

3.1.1.2 Chebyshev (Equal Ripple) function

In a Chebyshev filter, the transfer function can be expressed as:

$$|S_{21}(\Omega)|^2 = \frac{1}{\{1 + \varepsilon^2 T_n^2(\Omega)\}} \tag{3.4}$$

where $\Omega=\omega/\omega_c$ is the normalised frequency, ε is the ripple factor and related to a given parameter of passband ripple L_{Ar} by:

$$\varepsilon^2 = 10^{(L_{Ar}/10]} - 1 \tag{3.5}$$

and $T_n(\omega)$ is Chebyshev function of order "n" and defined as:

$$T_n(\Omega) = cos(n\, cos^{-1}(\Omega)) \qquad |\Omega| \leq 1, \tag{3.6}$$

$$T_n(\Omega) = cos\, h\, (n\, cosh^{-1}(\Omega)) \qquad |\Omega| \geq 1. \tag{3.7}$$

Unlike Butterworth filters, the bandpass ripple can be controlled via ε in Chebyshev filters. The zeros of filter transfer function are located at infinity therefore Chebyshev is also an all-pole filter. Chebyshev filters are defined for integer orders n (odd or even) and provide a steeper roll-off than Butterworth filters at the expense of equal ripple in the passband. They are therefore chosen when a sharper skirt is required.

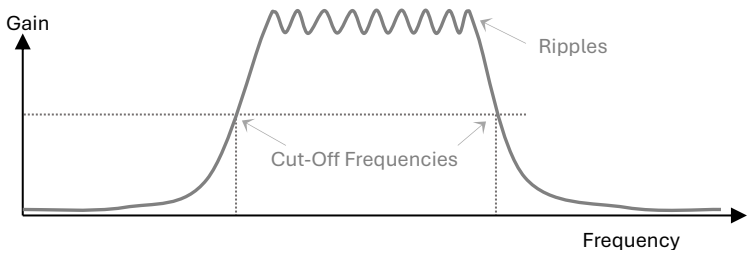

Fig 3.3 Chebyshev (equal ripple) magnitude response and cut-off frequencies.

3.1.1.3 Elliptical function

For an elliptic prototype the (normalised) magnitude response may be written as:

$$|S_{21}(\Omega)|^2 = 1/\{1 + \varepsilon^2 F_n^2(\Omega)\}, \tag{3.8}$$

where:

$$f_n(\Omega) = \begin{cases} M\dfrac{\prod_{i=1}(\Omega_i^2 - \Omega^2)}{\prod_{i=1}^{n/2}(\Omega_s^2 \,/\, \Omega_i^2 - \Omega^2)} & for\ n\ even \\ N\dfrac{\Omega\prod_{i-1}^{(\Pi-1)}(\Omega_i^2 - \Omega^z)}{\prod_{i=1}^{(n-1)/2}(\Omega_s^2/\Omega_i^2 - \Omega^2)} & for\ \ n \geq 3, odd \end{cases} \tag{3.9}$$

where $0<\Omega i<1$ and $\Omega s>1$ denote critical (normalised) frequencies that set the passband extrema and the finite-frequency transmission zeros; M and N are constants to be defined. $F_n(\omega)$ will oscillate between ±1 for $|\Omega| \leq 1$, and $|F_n(\Omega = \pm 1)| = 1$ [24] [25]. Elliptic filters provide the steepest transition from passband to stopband for a given order, with equal ripple in the passband and equal ripple in the stopbands due to the finite transmission zeros. The price paid is a more non-linear phase response than Butterworth or Chebyshev.

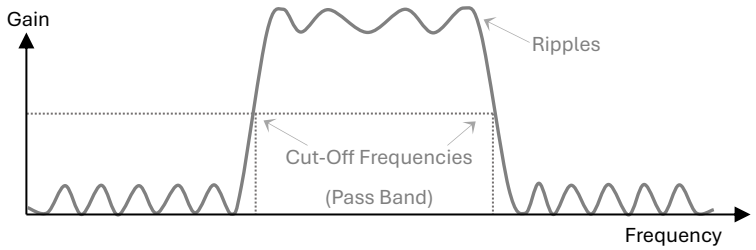

Fig 3.4 Elliptical filter frequency response

In all analogue filters a steeper roll-off can be obtained by increasing the order n. However, higher order also increases insertion loss, worsens phase linearity, enlarges size and cost, and raises sensitivity to tolerances and environment [26]. In practice, passive microstrip filters usually keep the order modest (e.g., $n \lesssim 10$). Once the type and order are chosen, the lumped LC prototype may be designed using standard coefficient tables in classical references such as [27]-[28]. Fig 3.5 illustrates some examples of prototype LC filters.

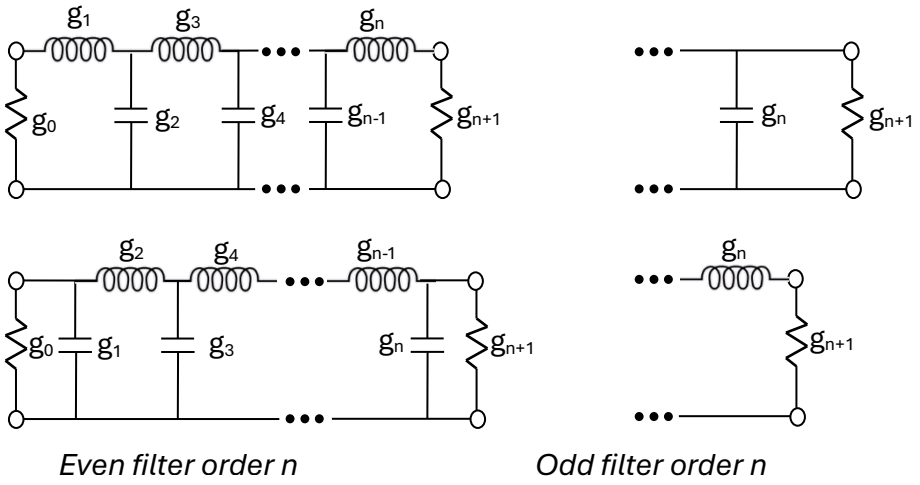

Fig 3.5 Examples of prototype topologies illustrating type and order.

3.1.2 Implementation (artistic) Process

The first phase of filter design (i.e. mathematical or scientific) process would be completed by determining the values of the lumped inductive and capacitive components of the filter. For microwave filters, the next step is filter implementation in desired frequencies.

At microwave frequencies the filters are realised using distributed microstrip or stripline transmission lines. Distributed transmission lines can emulate the behaviour of a lumped-element network with series inductors and shunt capacitors.

Assuming the thickness and the dielectric constant of the substrate are intact, the characteristic impedance of a microstrip line is adjusted by changing the strip width. An impedance step behaves, to first order, like an equivalent T-network of a low-pass filter with effective lumped *L* and C. Short and open circuited stubs act as resonant elements: for small electrical length an open stub is capacitive, a short-circuited stub is inductive, and at $\lambda/4$ each forms a resonator (open-circuited $\lambda/4 \rightarrow$ near-short; short-circuited $\lambda/4 \rightarrow$ near-open).

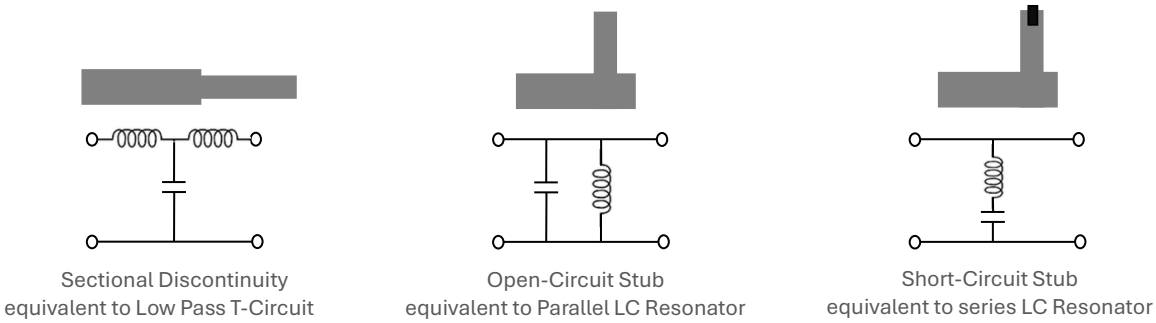

Fig 3.6 Microstrip discontinuity and stub sections

For microwave realisation using microstrip elements, commensurate lines of electrical length $\lambda/8$ at the cut-off frequency are commonly employed to implement a low-pass prototype via Richards' transformation (introduced in §3.1.2.2) and Kuroda's identities (§3.1.2.1). In this mapping, each lumped inductance or capacitance is replaced by a short- or open-circuited transmission-line stub of electrical length $\theta_0=\pi/4$ at ω_c; the characteristic impedances/admittances are chosen according to the prototype element values (after normalisation to ω_c and the reference impedance/admittance). In practice the system reference is usually Z0=50Ω. Sections of λ/8 transmission lines have the same lengths in filter designs

N	g_1	g_2	g_3	g_4	g_5	g_6	g_7	g_8	g_9	g_{10}	g_{11}
1	0.6986	1.0000									
2	1.4029	0.7071	1.9841								
3	1.5963	1.0967	1.5963	1.0000							
4	1.6703	1.1926	2.3661	08419	1.9841						
5	1.7058	1.2296	2.5408	1.2296	1.7058	1.0000					
6	1.7254	1.2479	2.6064	1.3137	2.4758	0.8696	1.9841				
7	1.7372	1.2583	2.6381	1.3444	2.6381	1.2583	1.7372	1.000			
8	1.7451	1.2647	2.6564	1.3590	2.6964	1.3389	2.5093	0.8796	1.9841		
9	1.7504	1.2690	2.6678	1.3673	2.7939	1.3673	2.6678	1.2690	1.7504	1.0000	
10	1.7543	1.2721	2.6754	1.3725	2.7392	1.3806	2.7231	1.3485	2.5239	0.8842	1.9841

a. Example table of Cerbyshev LPF coefficients for filter with 0.5dB Ripples

N	g_1	g_2	g_3	g_4	g_5	g_6	g_7	g_8	g_9	g_{10}	g_{11}
1	2.0000	1.0000									
2	1.4142	1.4142	1.0000								
3	1.0000	2.0000	1.0000	1.0000							
4	0.7654	1.8478	1.8478	0.7654	1.0000						
5	0.6180	1.6180	2.0000	1.6180	0.6180	1.0000					
6	0.5176	1.4142	1.9318	1.9318	1.4142	0.5176	1.0000				
7	0.4450	1.2470	1.8019	2.0000	1.8019	1.2470	0.4450	1.0000			
8	0.3902	1.1111	1.6629	1.9615	1.9615	1.6629	1.1111	0.3902	1.0000		
9	0.3473	1.0000	1.5321	1.8794	2.000	1.8794	1.5321	1.0000	0.3473	1.0000	
10	0.3129	0.9080	1.4142	1.7820	1.9754	1.9754	1.7820	1.4142	0.9080	0.3129	1.0000

b. Example table of Butterworth LPF coefficients

Table 3.1 Low pass filter coefficients

and are called commensurate lines. Commensurate lines are particularly useful for microstrip filter distributed element design.

Commensurate-line designs use sections of the same electrical length at ω_c, which simplifies synthesis and is particularly useful for distributed-element microstrip filters.

3.1.2.1 Kuroda Identities

Kuroda's identities were developed for the synthesis of distributed-element networks. They are network transformations that use unit elements (λ/8 lines at the prototype cut-off) together with impedance/admittance inverters to (i) convert series stubs to shunt stubs (and vice versa) and (ii) transform impractical characteristic impedances into practical values for microstrip implementation.

In essence, a λ/8 transmission-line element that is difficult to realise can be converted into an equivalent but more feasible element by inserting unit elements and an inverter. For example, short-circuited series stubs can be transformed into open-circuited shunt stubs adjacent to a unit element. The normalised inverter relation (see Fig 3.7) is:

$$n = 1 + \frac{Z_2}{Z_1} \tag{3.10}$$

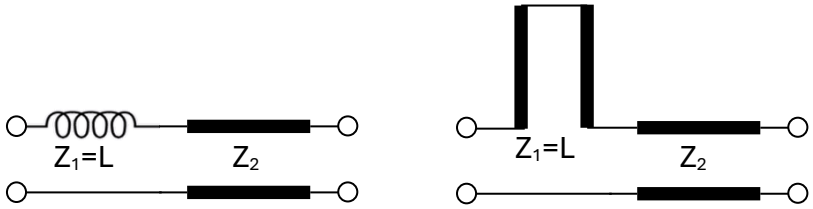

Fig 3.7 Microstrip inductive sections

where Z_1 and Z_2 are the characteristic impedances of the adjacent unit elements. In the usual normalised low-pass prototype (with Z_0=1, Ωc=1) , the element mappings shown in the figure apply (e.g., $L \leftrightarrow Z_1$, $C \leftrightarrow 1/Z_2$).

Fig 3.7 shows a circuit of inductive element which is equivalent to a short circuit stub of a microstrip line.

The broader conversions and the impedance-/admittance-inverter forms used in this chapter are summarised in Fig 3.8 and Fig 3.9, respectively.

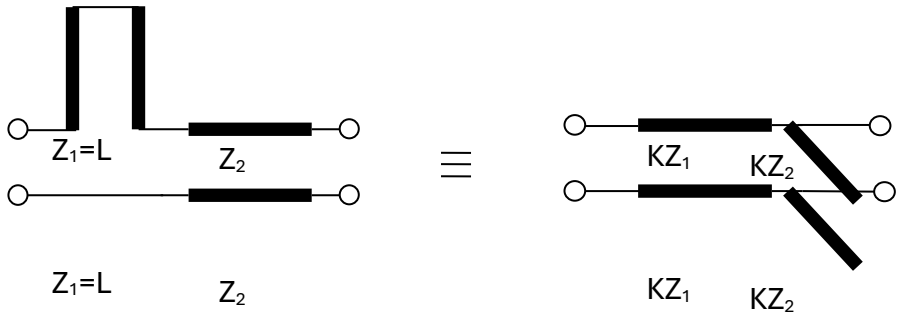

Fig 3.8 Microstrip stub series to shunt conversion

These transformations are applied in Section 3.1.3, where simple stub-based filters are analysed and validated with ADS EM and CST simulations.

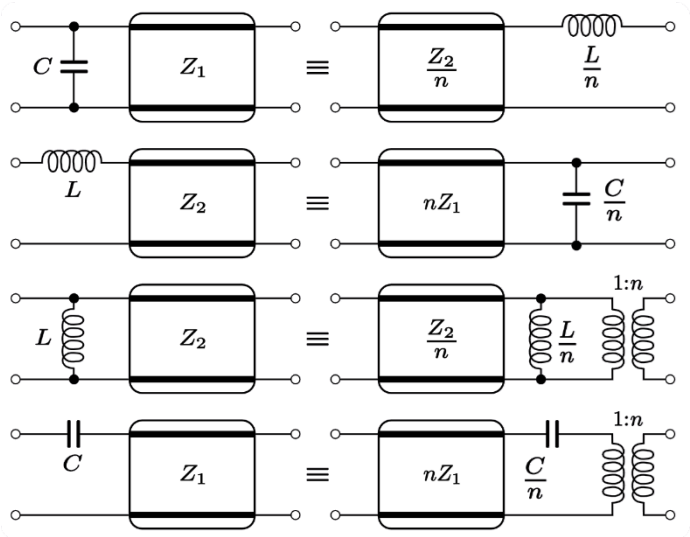

$L = Z_1, \quad C = 1/Z_2, \quad n = 1 + Z_2/Z_1$

Fig 3.9 Kuroda's identities

3.1.2.2 Richard Transformation

Richards' transformation is widely used as the basis of distributed filter design. It converts open- and short-circuited transmission-line sections into equivalents that realise the behaviour of lumped inductive and capacitive elements. In practice, lumped inductors are replaced by short-circuited stubs and lumped capacitors by open-circuited stubs, with characteristic impedances chosen from the normalised prototype values. Each unit element has an electrical

length of $\pi/4$ radians (45°) at a specific frequency, referred to as the design frequency f_0 . The electrical length of the unit element at any other frequency f is given by:

$$\theta = \frac{\pi}{4}\left(\frac{f}{f_0}\right) \tag{3.11}$$

For layout practicality, series/short stubs are usually converted to shunt/open stubs using Kuroda's identities so that the final structure is easier to implement in microstrip [29].

The overall flow starts with the lumped low-pass prototype; next, form distributed open- and short-circuited stubs using Richards' transformation; then insert unit elements and apply Kuroda's identities to convert series stubs to shunt stubs and obtain practical impedances. This process is illustrated in Fig 3.10. The resulting network is ready for circuit-level and EM simulation (ADS/Momentum and CST) in the next section.

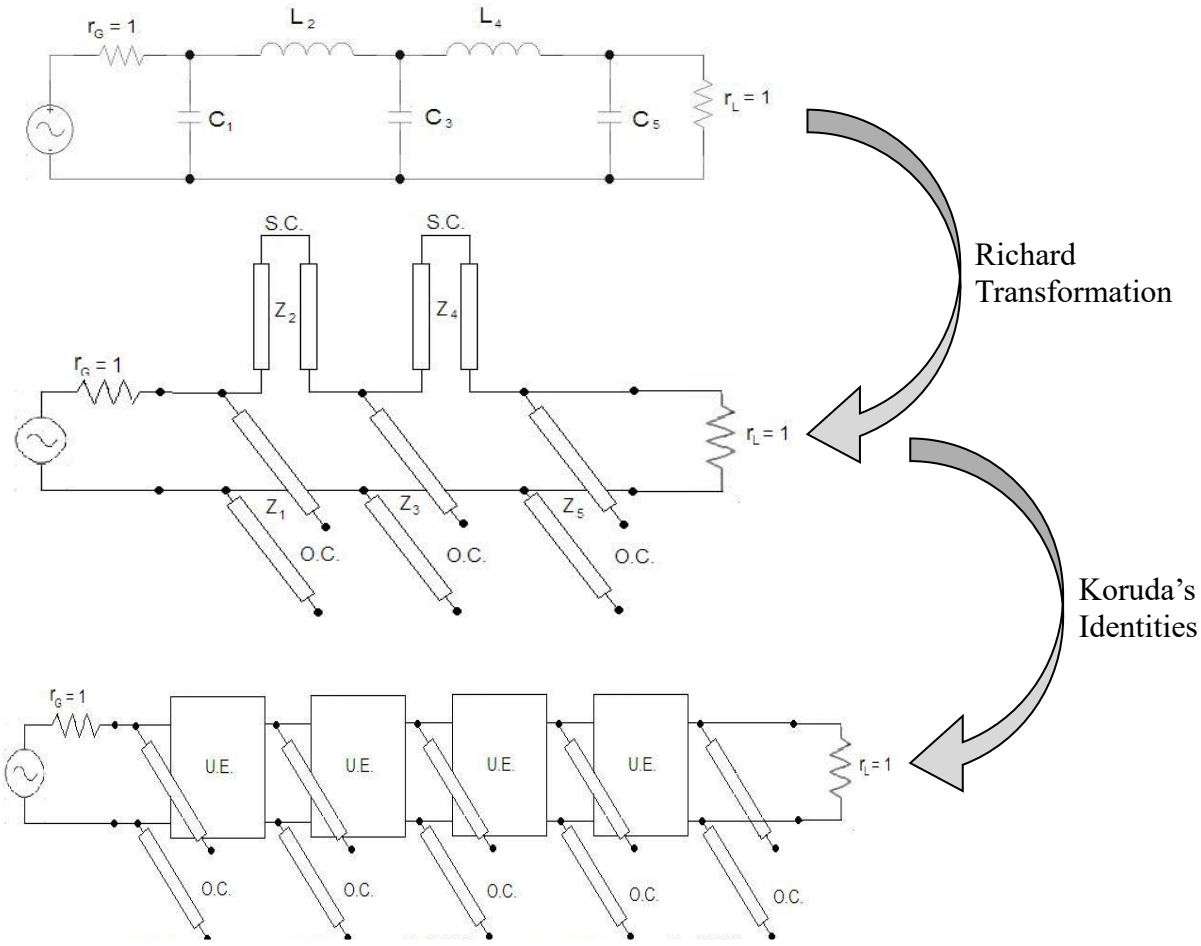

Fig 3.10 Richard transformation and Koruda's identities

3.1.3 Dielectric-Tuning Sensitivity: Non-Periodic vs. Periodic

We employ periodic microstrip lattices of unit cells (with and without SIR-based stubs) to realize strong, bias-controlled tuning via the effective permittivity ε_{eff}. One of the main advantages of periodic structure vs. unit structure for tuning filter application using LC substrate is its better frequency sensitivity to ε_{eff} changes.

In a non-periodic (standalone) quasi-TEM microstrip resonator (e.g., a $\lambda/4$ open/short stub or an SIR in isolation), the fundamental resonance scales primarily with electrical length, hence with ε_{eff} via

$$f_0 \approx \frac{c}{4\, l_{eff}\, \sqrt{\varepsilon_{eff}}} \rightarrow \frac{\Delta f_0}{f_0} \approx -\frac{1}{2}\, \frac{\Delta\, \varepsilon_{eff}}{\varepsilon_{eff}} \,. \tag{3.12}$$

Thus, the normalized dielectric-tuning sensitivity is $|\partial \ln f_0 / |\partial \ln \varepsilon_{\text{eff}}| = 1/2$, i.e., a relatively gentle dependence [16] , [28]. In practice, fringing fields, discontinuity capacitances and SIR impedance ratios Z_1/Z_2 slightly perturb the coefficient but do not change the basic $\sim \varepsilon_{\text{eff}}^{-1/2}$ trend [30].

By contrast, a periodic microstrip structure is a spatially repeated network of line sections and reactive loads. Its passbands and stopbands arise from wave interference across many unit cells. Even a small change in ε_r slightly perturbs the phase advance and reactive loading in each cell; accumulated over the cascade, that tiny per-cell change becomes a large, coherent shift of the band edges and passband centre. In other words, periodic filters provide a longer “lever arm” for dielectric tuning because the effect compounds across the array of cells, yielding a much higher apparent sensitivity than a lone SIR can offer [31]. This increased dielectric-tuning sensitivity arises from the cumulative nature of phase and impedance perturbations in a periodic structure. In a non-periodic resonator, a change in effective permittivity primarily alters the electrical length of a single resonant element, resulting in a proportional and relatively weak shift in resonance frequency. In contrast, a periodic structure consists of many cascaded unit cells, each experiencing a small ε-dependent change in phase advance and reactive loading.

When repeated over the lattice, these small per-cell perturbations accumulate coherently through the Bloch propagation constant, leading to a significantly larger shift in the passband centre and band edges. As a result, the apparent frequency sensitivity to ε in a periodic filter scale with the number of unit cells and the dispersion characteristics of the lattice, rather than being limited to the response of an isolated resonator.

This distinction also clarifies why SIRs still appear in the periodic designs later in the thesis. The SIR is used there as a building block inside the unit cell (to set local resonance, Q, and coupling), while the periodicity is what delivers strong tunability with ε_r. The role of the SIR is local shaping; the role of the lattice is global, interference-based control of the transmission spectrum. Together they provide compactness, selectivity, and enhanced dielectric-tuning efficacy that a standalone SIR cannot achieve.

Fig 3.11 provides a conceptual graph of normalised centre-frequency sensitivity of non-periodic and periodic filters versus dielectric constant. Although the true behaviours are mildly nonlinear, over a modest range (e.g., ε_r = 2.2 → 3.0) the curves are close to linear, which is sufficient for the present conceptual comparison. The non-periodic trend is obtained from the quasi-TEM resonance behaviour of an isolated microstrip resonator, where the centre frequency scales approximately as $f_0 \propto 1/\sqrt{\varepsilon_{eff}}$ [16], [27]. The periodic trend is derived from the Bloch-

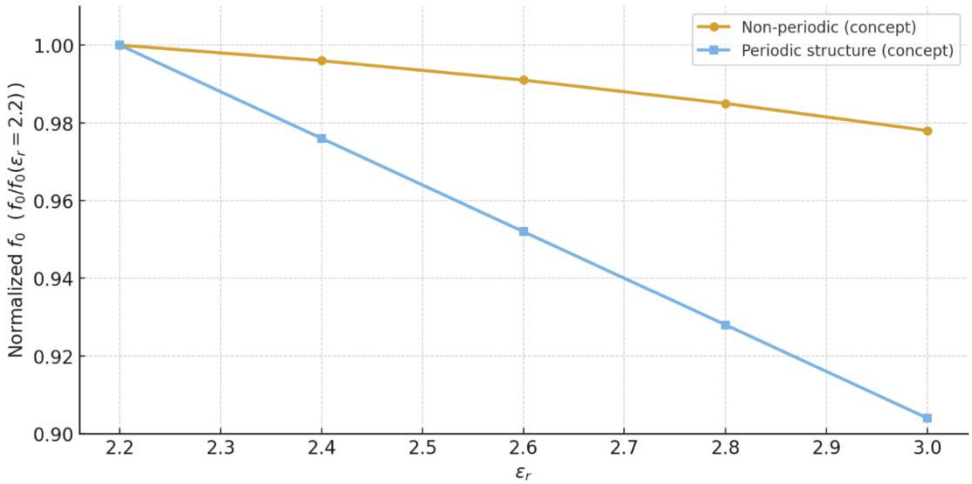

Fig 3.11 Conceptual normalized f_0 vs. ε_r sensitivity (non-periodic and periodic structures)

wave dispersion relation of a cascaded periodic transmission-line lattice, in which variations in

ε_{eff} perturb the Bloch propagation constant [31], [111]. Quantitative ADS simulation is provided in section §6.1 of in Chapter 6, which validates these trends. The non-periodic curve in Fig 3.11 is derived from the quasi-TEM resonance behaviour of an isolated microstrip resonator, where the centre frequency scales primarily with the inverse square root of the effective permittivity [16], [27]. In contrast, the periodic curve represents the behaviour of a cascaded periodic lattice, in which changes in effective permittivity perturb the Bloch propagation constant and the dispersion relation of the structure [31], [111]. The comparison therefore contrasts a single-resonator electrical-length model with a qualitative Bloch-wave-based periodic model, highlighting the cumulative effect of permittivity changes across multiple unit cells rather than serving as a quantitative design prediction.

3.2 Periodic Structure for LC tuneable filter

Although LC tunability can be realised in multiple microstrip filter topologies, the periodic structure approach leverages dispersion engineering to multiply the tuning effect, yielding larger frequency agility, higher selectivity, and lower loss in a compact form.

Liquid crystal (LC) controllable permittivity enable continuous frequency tuning in a variety of conventional planar filter topologies such as single or coupled microstrip resonators [32], [33], [34] and other structures such as hairpin filters [35]. In such designs, the tuning mechanism is relatively a proportion to one-half of LC's change of effective permittivity (i.e. $\Delta\varepsilon_{\text{eff}}$) which impacts the electrical length of resonator, therefore shifting its resonate frequency. This rather linear relation is moderate in magnitude, means even large $\Delta\varepsilon_{\text{eff}}$ of 10% produces about 5% frequency tuning. For example, as reported in [35] increasing LC permittivity from 2.4 to 2.8 at 60 GHz shift the centre frequency of LC hairpin filters by only 2–3 GHz. Consistently, the ADS/Momentum and CST sweeps in §3.1.3 show that varying ε_r across practical LC ranges produces only modest movement of the S_{11} minima and the cut-off

frequency. This confirms that single-resonator/stub realisations offer limited tuning leverage compared with the periodic structures used later.

In contrast, a periodic structure introduces a fundamentally different physical mechanism. Periodic structures operate near Bragg resonances, where the dispersion curve is very flat. A Bragg resonance is a strong reflection that occurs when a wave traveling through a periodic structure meets a repeating impedance pattern whose period p (physical repeat distance of the pattern) is related to the wavelength λg in a specific way. Under such conditions the reflected waves from each cell add in phase and produces constructive interference in the backward direction and destructive interference in the forward direction and result is a stopband or a range of frequencies where transmission drops sharply. In other words, in microwaves and RF circuits, periodic structures act like a "crystal" for guided waves, and Bragg resonance in happens in optics and acoustics. [36], [31]. More details of this periodic structure properties and its passband and stopband characteristics are provided in chapter 5.

Near the Bragg resonance frequency, a small change in effective permittivity can produce a disproportionately large shift in the passband or stopband edges due to the steep dispersion characteristics of periodic structures. This behaviour effectively amplifies the tuning action of the LC substrate through the cumulative phase and impedance perturbations across the lattice, a mechanism that is well recognised in periodic and metasurface systems operating near band-edge conditions [37]. In contrast, conventional single-resonator or stub-based implementations exhibit frequency shifts that scale approximately with the fractional permittivity change and therefore provide only limited tuning leverage.

This distinction is confirmed by the comparative electromagnetic simulation results presented later in the thesis. For non-periodic resonator-based structures, the ADS and CST results in Fig 6.1 and Fig 6.2 show only modest shifts in centre frequency and cut-off characteristics over practical LC permittivity ranges. By comparison, the periodic structures examined in Fig 6.7 – Fig 6.9 exhibit substantially larger and more coherent shifts of the passband and stopband edges

under comparable permittivity variation, demonstrating the enhanced dielectric-tuning sensitivity enabled by periodicity. Table 3.2 summarises this comparative behaviour across different tuneable filter structures.

Criteria	Periodic Structures	Single-Resonator Structures	Metamaterial Structures	Planar Transmission Lines (e.g., CPW, Microstrip)
Tuning Mechanism	Tunable through bandgap shifts by LC dielectric modulation.	Resonant frequency shifts via LC permittivity change.	Tunable through LC-based effective medium properties.	Impedance matching or phase delay tuning via LC.
Frequency Selectivity	High selectivity with well-defined passbands/stopbands.	Moderate selectivity with sharp resonance peaks.	High selectivity, often focused on narrow bandwidth.	Moderate selectivity, dependent on line length and geometry.
Adaptability	Supports wideband or narrowband tuning with flexible design.	Limited to narrow tuning range, dependent on resonator size.	Highly adaptable for specific resonant modes.	Moderate, tuning is geometric or dielectric-based.
Compactness	Very compact due to periodicity at millimeter-wave scales.	Compact but scales with resonator size at higher frequencies.	Typically compact but complexity increases with design.	Compact, but less efficient at very high frequencies.
Ease of Fabrication	Moderate, requires precision for periodicity.	Easy to fabricate, minimal complexity.	Challenging due to complex material and geometry.	Simple, well-suited for planar fabrication techniques.
Performance at 60 GHz	Excellent; supports low loss and sharp filtering.	Good; depends on resonator quality factor (Q).	Excellent; tailored performance with negative index.	Moderate; loss increases significantly at higher frequencies.
Bandwidth Control	Tunable, supports multi-band or wideband operation.	Limited, typically narrowband only.	Tunable with controlled bandwidth but narrow by design.	Limited, depends on line configuration and dielectric.
Power Consumption	Low, tuning requires small electric field for LC.	Very low; LC tuning via small electric fields.	Low, LC tuning requires electric field application.	Very low; depends on LC tuning voltage.
Design Flexibility	High; unit cells can be customized for diverse applications.	Moderate; dependent on resonator geometry and placement.	High, but requires expertise in metamaterial design.	Moderate; dependent on transmission line parameters.
Scalability	Scalable for multi-cell configurations.	Less scalable for large arrays.	Scalable but fabrication becomes challenging.	Scalable for longer lines but limited by performance.
Suitability for Dynamic Environments	Excellent; allows real-time adaptive filtering.	Moderate; fixed tuning may lag in dynamic changes.	Excellent; supports adaptive behavior in high-Q designs.	Moderate; relies on LC tuning for adaptation.
Complexity of Integration	Moderate; requires alignment of unit cells with LC layer.	Low; simple structure easy to integrate.	High; metamaterial designs are intricate.	Low; planar structures are inherently easy to integrate.

Table 3.2 Periodic structures vs. other possible structures for tuneable LC filters

Table 3.3 compares some of the key parameters of LC based tuneable filters for conventional topologies with periodic structure.

Feature	Stepped Impedance	Single Stub	Periodic Structure
Tuning Range per $\Delta\varepsilon r$	Low (~3–4%)	Low–Medium (~4–5%)	**High (~8–10%)**
Selectivity	Medium	Medium	**High (steep band edges)**
Stopband Width	Narrow	Narrow–Medium	**Wide, multiple Bragg bands**
Loss at 60 GHz	Moderate–High	Moderate	**Low (distributed)**
Size for same selectivity	Larger	Larger	**Compact**

Table 3.3 Key parameters of periodic Structure LC filters vs other topologies

3.3 Filter types and structures

This section reviews common microstrip filter structures from the viewpoint of their suitability for LC-tuneable periodic implementations at mm-wave.

3.3.1 Stub Filters

This filter structure can be formed using Richards' transformation and Kuroda's identities and as noted earlier by eliminating short series circuit stubs to open circuit shunt stubs. Unit elements of λ/8 may be added at the ends so the network is referenced to Z_0 at the cut-off frequency. Typical layouts are shown in below Fig 3.12:

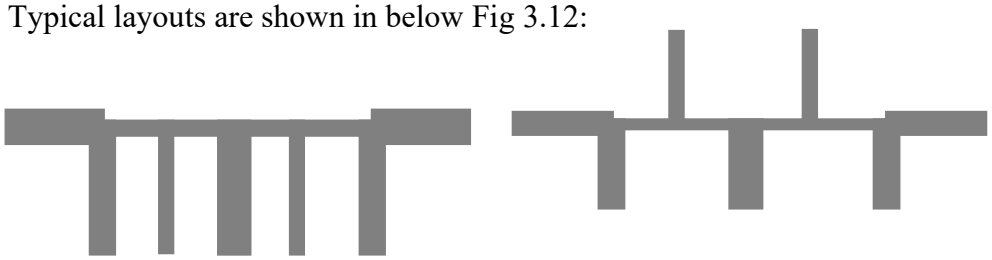

Fig 3.12 Stub filter

As usually implemented, these are not intrinsically periodic, so they are not preferred for the periodic approach adopted here.

3.3.2 Stepped Impedance Filters

Another approach models short sections of transmission line as equivalent impedances: a high-impedance section behaves inductively, while a low-impedance section behaves capacitively at the design frequency (illustrated in Fig 3.13). Alternating high/low sections form stepped-impedance low-pass filters (example in Fig 3.14).

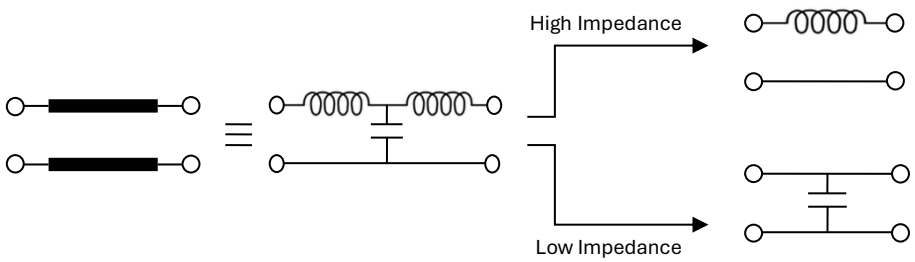

Fig 3.13 Microstrip line equivalent impedance

These structures are generally non-periodic and therefore less suitable for the present periodic LC design. However, they can be rendered periodic if successive high-impedance sections share the same value and successive low-impedance sections share the same value [38]. At 60 GHz on LC, tuning sensitivity is modest and discontinuity parasitics become significant.

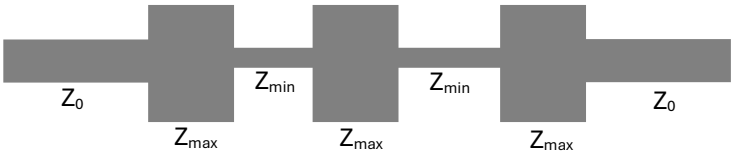

Fig 3.14 Stepped impedance low-pass filter

3.3.3 Coupled Line Filters

Coupled line microstrip filters are formed by open circuit coupled microstrip lines. In these structures when the length of microstrip lines are λ/4, the filter provides a shunt resonant circuit. The gap between the microstrip lines correspond to the admittance inverters. In filter design, the even and odd mode characteristic impedances of parallel-coupled resonators will be determined using admittance inverters [16]. Fig 3.15 sketches the equivalent circuit for two coupled $\lambda/4$ lines; a typical layout is shown in Fig 3.16.

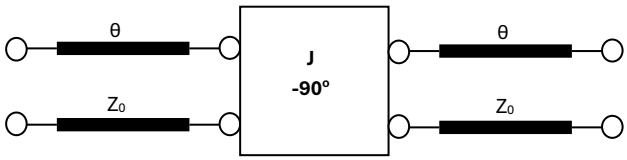

Fig 3.15 Equivalent circuit of two λ/4 coupled microstrip lines

For LC substrates at mm-wave, very small gaps are needed for tight coupling, which is difficult to realise and bias reliably. The structures are therefore not favoured for periodic LC-tuneable filters.

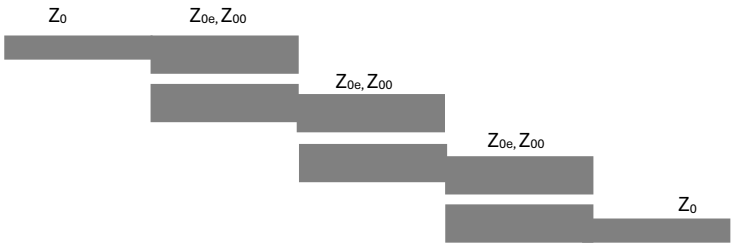

Fig 3.16 Coupled microstrip lines filter

3.3.4 Interdigital Filters

Interdigital filters use short-circuited $\lambda/4$ fingers in a compact rectangular footprint; the hairpin is a folded variant. A special form of interdigital filter is called Hairpin filter and has a structure like Fig 3.17. The resonant frequency is controlled by finger length and spacing. Interdigitated and hairpin filters are extensively utilized in the industry for their ability to selectively pass or reject signals within specific frequency ranges. Their popularity stems from their customizable performance, compact form factor, and ease of integration and fabrication [16].

Fig 3.17 Interdigital (left) and Hairpin filters (right)

They are potential candidates for LC tuning thanks to their quasi-periodic geometry, but effective controlled coupling on LC and bias integration are challenging; so they are less attractive for the periodic scheme pursued here.

3.3.5 Capacitive Coupled Resonator Filters

Another type of microstrip filters can be structured by coupling resonator elements through capacitive interactions. With a series of N resonant sections of microstrip or stripline transmission line (N+1 capacitive gaps in between) for a filter of N^{th} order. The gaps act as series capacitors [16].

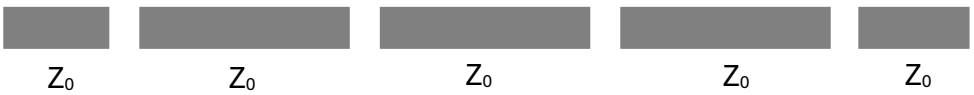

Fig 3.18 Capacitive coupled resonator filter

For LC-periodic realisations they are not ideal: the many gaps complicate LC alignment and require multipoint multi voltage biasing, and the geometry is not inherently periodic in the sense required here.

3.3.6 Comb-Line Filters

Another useful structure for microstrip filers using capacitive gaps between λ/4 resonators which can be also designed with tuning screws for final adjustment, is called Comb-Line filter. In this structure all λ/4 sections of transmission lines are grounded at one end. The major benefit of these filters is that it would be possible to eliminate the higher order passbands by interchange of lumped and distributed elements.

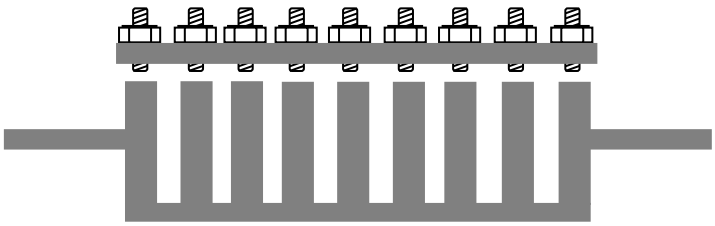

Fig 3.19 Comb line filter

However, they are not suitable for LC-based periodic filters: the screw-tuned hardware is not planar-LC friendly, and coupling control at 60 GHz is demanding.

None of the above families, as commonly realised, are as suitable for a periodic LC-tuneable microstrip filter. In particular at mm-wave, coupling tolerances and LC bias integration become limiting. The most appropriate structure for a periodic design is a stub-resonator chain, in which multiple open-circuit stubs are connected to a feed line at regular intervals. (On LC substrates the short-circuit version is impractical, hence the choice of open stubs.) The electrical length of each open stub sets the resonance, allowing flexible shaping of the response (including stepped-impedance resonator variants) with low passband loss. This is the structure adopted for the tuneable periodic filters developed and analysed in Chapter 5.

3.4 Summary

This chapter explores the design of microstrip filters, providing a dual perspective: the mathematical (scientific) process that establishes the theoretical foundation, and the implementation (artistic) process that turns the theory into a realisable circuit. Together,

mathematical rigour and careful engineering enable efficient, high-performance filters for RF and microwave applications.

Butterworth filters were outlined, emphasising their maximally flat passband. Their suitability where a smooth, ripple-free response is required was noted, alongside the transfer functions and prototype coefficients. Chebyshev filters were introduced for their equal-ripple passband and sharper roll-off than Butterworth, with the trade-off between ripple magnitude and stopband attenuation made explicit. Elliptic filters were described as offering the steepest transition by introducing ripples in both passband and stopbands via elliptic rational functions, at the cost of greater complexity and phase non-linearity.

On the realisation side, Kuroda's identities were used to transform impractical series stubs and impedances into feasible shunt-stub forms and practical line impedances. Richards' transformation mapped lumped L–C prototypes to distributed commensurate line sections suitable for microstrip implementation.

Several common microstrip filter structures are described, with an emphasis on their unique features and applications. The design of open and short-circuited stub filters is discussed, highlighting their compactness and suitability for narrowband filtering. The stepped Impedance filters characterized by alternating high- and low-impedance sections, are explored for their simplicity and ability to achieve miniaturization in certain designs. Coupled line filters, which use the electromagnetic coupling between adjacent transmission lines, are analysed for their effectiveness in achieving wideband filtering. The chapter then details the structure and design of interdigital filters, which employ alternating open-ended lines to achieve compact and highly selective designs. The capacitive coupled resonator filters are discussed for their ability to achieve high Q-factors and strong frequency selectivity through capacitive coupling between resonators. The design and operation of comb-line filters, which use short transmission line resonators and capacitive coupling, are explained for applications requiring compact high-

frequency filters. Finally, the limiting factors as to the use of the above class of filters in LC based tuneable filters are noted.

This chapter bridges the mathematical and implementation aspects of microstrip filter design. The mathematical framework covering Butterworth, Chebyshev, and elliptical functions lays the foundation for filter performance optimization, while the artistic implementation process applies practical techniques like Kuroda identities and Richard transformation. The discussion of various filter types and structures provides readers with a toolkit to design filters tailored to specific applications, balancing theoretical precision with practical constraints.

Chapter4 : Liquid Crystal Substrates and Devices

4.1 Background and motivation

In 1888, an Austrian scientist called Friedrich Reinitzer noticed the two distinct melting points of cholesteryl benzoate of carrots. At 145 ^{o}C the material melted into a cloudy fluid and again in 179 ^{o}C into a clear liquid. He also observed that the material reflects and rotates the polarisation of polarised light. He then studied the cloudy fluid under microscope with the assistance of a German physicist Otto Lehmann and they observed the crystallites.

They discovered that the cloudy phase has rod-like molecular structure, and the molecules are almost ordered in one direction and he concluded that this is a new phase of material and called it liquid crystal. The liquid crystals exhibit both physical characteristics of crystals but flow like liquids. Materials with this property of unusual phase intermediations are “mesogenic” and the different phases for these materials are called “mesophases” [39]. The molecular reorientation of these materials in response to electric field is the key property and basis of their wide range of technology applications.

Liquid crystals can be found in plants as well as most substances containing carbon components. Beetles’ shells and slug slime as well as human bone and DNA molecules also contain liquid crystals.

A crystal is an ordered system in that molecules are arranged in phase at specific positions and with even spacing, liquids have disorder structure with random molecule positions, the liquids with rod-shape molecules at random position and orientation are called isotropic liquids. By decreasing temperatures, the isotropic liquids turn to liquid crystal phase in that the position of molecules are still random but not the orientations. By further lowering the temperature the liquid crystal turns to a solid crystal with both position and direction are stable and nor random.

Industrial use of LC began in 1960s by Richard Williams at RCA Laboratories. Williams noted that the crystals of LCs enter into a nematic state with stripe pattern under the effect of an

electric field, which is called “William’s domain” and was the beginning of liquid crystal application in screens and displays. The function of liquid crystals was to modulate the polarization of transmitted light waves in response to the applied electric field intensity. However, for this functionality, liquid crystal had to be in “nematic state” under a high temperature which was not easily achievable for normal display or screen uses. Finally, a research team in RCA, discovered that by changing the number of carbons, atoms, room temperature will be adequate for this functionality. That was the beginning of industrial use of liquid crystals for displays. In 1969 RCA announced the first liquid crystal commercial displays [40].

Fig 4.1 Liquid crystal molecules

4.2 Phases of Liquid Crystal

Liquid crystals (LCs) are materials with distinct phase between solid (crystalline) and liquid (isotropic). Depending on types of states, the behaviour (or phase) of liquid crystals states varies between various phases:

- Nematic Phase
- Smectic Phase
- Cholesteric Phase
- Columnar Phase

In the nematic phase of LCs, which is the simplest phase, the positions of the rod-like or disc-like molecules are not ordered but they tend to point in the same direction; therefore, the nematic phase is one in which the orientation of the molecules is in one direction. Nematic

liquid crystals are uniaxial, which means the average direction of the long axis of molecules is in a well-defined direction $\vec{n}$(the director), and the short axes of the rod-shaped molecules are

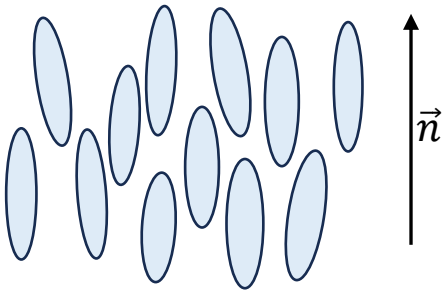

Fig 4.2 Nematic phase of liquid crystal

not ordered in a defined orientation because the molecules can still diffuse [41]

In the isotropic materials the properties of materials are identical for all directions of their molecules, but LCs are not isotropic materials which means that the property of the material depends on the directions of its molecules. Liquid crystals are anisotropic, and the material properties changes depend on the direction. The optical, electrical, and magnetic properties of LCs changes with the alignment and direction.

The Smectic Phase refers to the soap and slippery feature of Liquid crystals. In this phase molecules are in a translational situation which is not available in nematic phase. Molecules in this phase tend to be aligned in different layers like lines of soldiers. There is limited movement between the layers and in this phase the liquid crystal is closer to a solid substance compared to nematic phase. Several types of smectic phase liquid crystals are identified. Smectic-A and

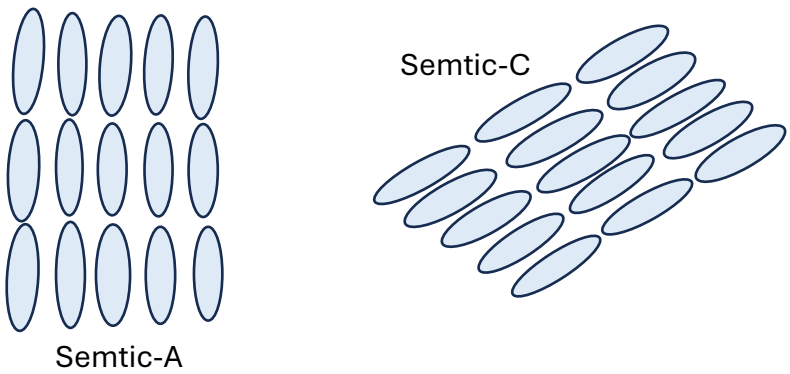

Fig 4.3 Smectic phase of liquid crystal A and C

smectic-C are discussed here (Fig 4.3). In smectic-A the direction of rod-shape molecules is perpendicular to the plane of molecules but in smectic-C the direction of molecules is in a tilt angle compared to smectic-A.

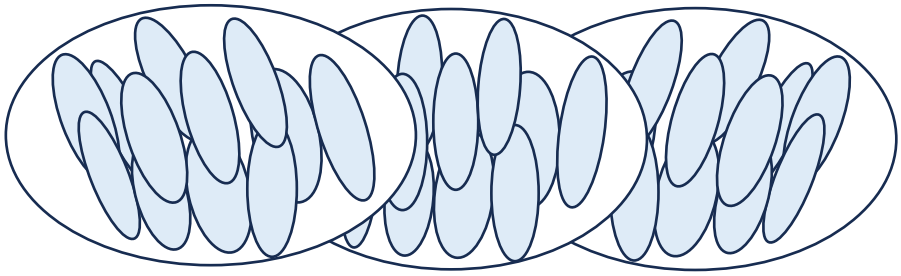

Fig 4.4 Cholesteric phase of liquid crystals

Certain types of nematic type of LCs in that the molecules are optically active are cholesteric phase [42]. The structure of this phase contains a helical axis perpendicular to the molecule's direction. The molecules in cholesteric liquid crystals are in a twisted and chiral arrangement. This structure can be visualized as group of two-dimensional nematic form of layers. Cholesteric liquid crystals are also known as chiral nematic LCs.

The Columnar LCs have disk shape of long rods. In this phase the stack columns of molecules are the characteristic of mesophase, as shown in Fig 4.5 . The structure is a system of columns which are packed together and form two-dimensional lattice. The actual position of molecules in each column well as the arrangement of the columns form new mesophases.

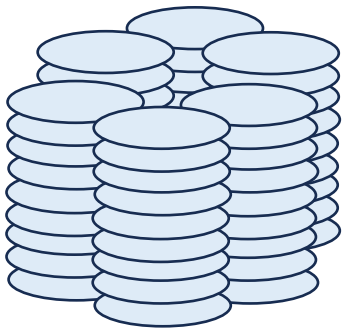

Fig 4.5 Columnar phase of liquid crystals

4.3 Liquid Crystal characteristics at microwave/mm-wave

Liquid Crystals (LC) are materials having a phase somewhere between liquid and solid. Therefore, LC materials can flow like liquids, but still its molecules are oriented in a crystal-like way. Frome the viewpoint of phase behaviour (i.e. crystalline for solid and isotropic for liquid), the liquid crystals can be categorised to three phases of Nematic, Smectic and Cholesteric. Nematic LCs are anisotropic materials, and their physical properties change with the alignment and direction of rod-shaped molecules. The relative permittivity of a nematic LC varies between two values of $\varepsilon_{r\parallel}$ and $\varepsilon_{r\perp}$ for when the molecular orientations are aligned with the surface of LC and $\varepsilon_{r\parallel}$ varies between 2.6 to 3.5, or perpendicular with the surface of LC and $\varepsilon_{r\perp}$ varies between 2.2 to 2.8 [71], [72], [73] & [74]. An external voltage that changes the LC director field can control the molecular orientation of LC. The difference between $\varepsilon_{r\parallel}$ and $\varepsilon_{r\perp}$ is known as liquid crystal anisotropy. The tune-ability of liquid crystal dielectric would be defined as LC anisotropy divided by its parallel permittivity. This is a useful parameter to measure tuning capability of a mixture substrate of liquid crystal.

Nematic phase of liquid crystals is the most common phase used in microwave and MMW frequencies. The basis of the nematic LCs tunability is in orientation of its rod-shape molecules align with tensor $\vec{n}$ which is average direction of long axis of molecules and is also called as liquid crystal director. When the rod-shape molecules are aligned with tensor $\vec{n}$, the relative permittivity of the LC is denoted by $\varepsilon_{r\parallel}$, and for when the molecules long axis are in a direction orthogonal to tensor $\vec{n}$, the relative permittivity is denoted by $\varepsilon_{r\perp}$ for a LC substrate sandwiched between two metals electrodes and at no voltage (i.e. V=0) tensor $\vec{n}$ will be aligned in a parallel with the metal plates. For a three dimensional of molecular orientation of liquid crystal between two metal plate (electrodes) as shown in Fig 4.9, the permittivity vector can be derived from below formula:

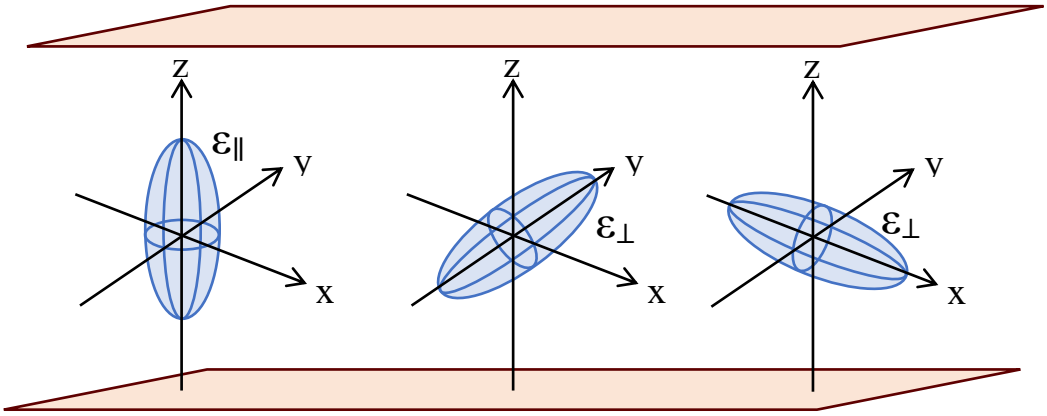

Fig 4.6 Orientation of liquid crystal molecules

$$\overrightarrow{\varepsilon_{\perp}} = \begin{bmatrix} \varepsilon_{\parallel} & 0 & 0 \\ 0 & \varepsilon_{\perp} & 0 \\ 0 & 0 & \varepsilon_{\perp} \end{bmatrix} \tag{4.1}$$

The molecules oriented along z-direction, $\varepsilon_{\parallel}$ characterise liquid crystal permittivity and for the molecules in x or y directions, liquid crystal permittivity will be $\varepsilon_{\perp}$. A bias voltage V_b when increases from zero to a maxim voltage V_{max}, can re orient the molecules directions.

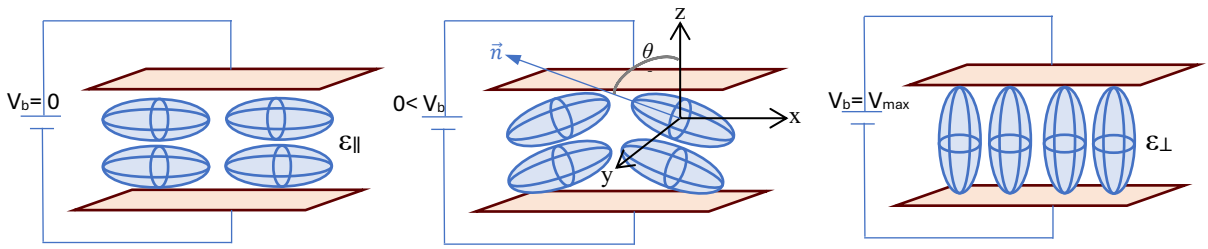

Fig 4.7 Liquid crystal molecules in different states

For the voltages between 0 and Vmax molecular orientation of the tensor $\vec{n}$ changes continuously. In this case the liquid crystal distribution is random and can be expressed by [75], [76] :

$$S = \langle \frac{3}{2} \cos^2 \theta - \frac{1}{2} \rangle \tag{4.2}$$

In that θ is the average angle between the molecular tensor $\vec{n}$ and z-direction and ⟨ ⟩ represent the expected molecular orientation.

For the liquid crystal anisotropy $\Delta\varepsilon = \varepsilon_{\parallel} - \varepsilon_{\perp}$, permittivity vector will be a function of tensor $\vec{n}$ and can be expressed by below formula [49]:

$$\begin{aligned}\vec{\varepsilon} &= \varepsilon_{\perp}\begin{pmatrix}1 & 0 & 0\\ 0 & 1 & 0\\ 0 & 0 & 1\end{pmatrix} + \Delta\varepsilon\,.\,(\vec{n}\otimes\vec{n})\\ &= \varepsilon_{\perp}\begin{pmatrix}1 & 0 & 0\\ 0 & 1 & 0\\ 0 & 0 & 1\end{pmatrix} + \Delta\varepsilon\begin{pmatrix}n_x^2 & n_xn_y & n_xn_z\\ n_xn_y & n_y^2 & n_yn_z\\ n_xn_z & n_yn_z & n_z^2\end{pmatrix}\end{aligned} \tag{4.3}$$

In the above formula $\otimes$ is vectors outer product where $\vec{n}\otimes\vec{n} = \vec{n}\,.\,\vec{n}^{T}$

The permittivity vector of equation 4.3 can be also expressed as:

$$\vec{\varepsilon} = \begin{pmatrix}\varepsilon_{\perp} + \Delta\varepsilon\,\sin^2\theta & 0 & \Delta\varepsilon\,\sin\theta\cos\theta\\ 0 & \varepsilon_{\perp} & 0\\ \Delta\varepsilon\,\sin\theta\cos\theta & 0 & \varepsilon_{\perp} + \Delta\varepsilon\,\cos^2\theta\end{pmatrix} \tag{4.4}$$

By increasing the bias voltage and at a certain voltage V_{max}, the rod-shape molecules of liquid crystals will be in vertical orientation (compared to the metal plates) and therefore $\theta = 0$ and for the vertical permittivity, we have:

$$\overrightarrow{\varepsilon_{\parallel}} = \begin{bmatrix}\varepsilon_{\perp} & 0 & 0\\ 0 & \varepsilon_{\perp} & 0\\ 0 & 0 & \varepsilon_{\parallel}\end{bmatrix} \tag{4.5}$$

In this situation when tensor $\vec{n}$ is in the same orientation of the electric field lines generated because of bias voltage, the effective permittivity will be $\varepsilon_{eff} = \varepsilon_{\parallel}$.

The liquid crystal relative permittivity is measured in [77] as a function of temperature change between two melting and clearing points which is shown in Fig 4.8. In nematic phase permittivity is also a function of temperature and $\Delta\varepsilon$ is not constant in different temperature.

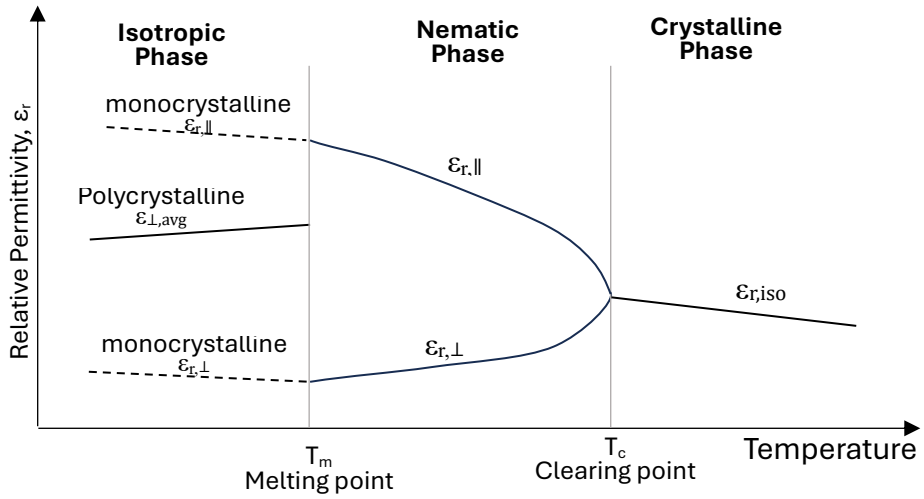

Fig 4.8 Relative permittivity vs temperature changes

LC-based substrate in microstrip planar filters provide controllable effective permittivity (i.e. ε_{eff}), this property can be used to tune the rejection frequencies of periodic filters.

The permittivity of liquid crystals is complex value including real and imaginary parts:

$$\varepsilon = \Re\,\varepsilon - j\,\Im\,\varepsilon \;=\; \Re\,\varepsilon\,(1 - j\,\frac{\Im\,\varepsilon}{\Re\,\varepsilon}\,) \tag{4.6}$$

The relative permittivity of a liquid crystal is related to the real part i.e. $\Re\,\varepsilon = \varepsilon_r\varepsilon_0$ and the ratio of "$\Im\,\varepsilon\,/\,\Re\,\varepsilon$" represents the loss tangent of the dielectric. The power dissipation in the material or heat due to vibration of dipole moments is due to $\Im\,\varepsilon$. The electrical tunability of the liquid crystal substrate is a function of its permittivity which can be controlled by applying an external voltage. Assuming the permittivity of tuned and untuned situations as $\varepsilon_r(E)$ and $\varepsilon_r(0)$, the tunability of the liquid crystal can be defined as:

$$Tunability\;(E) = \frac{\varepsilon_r(E) - \varepsilon_r(0)}{\varepsilon_r(0)} \tag{4.7}$$

The other parameters important to be considered in liquid crystal - based circuits design are loss angles for two molecules orientations.

From (4.7) we have:

$$\varepsilon\mathrm{r},\parallel = \Re\,\varepsilon_{r,\parallel} - j\Im\,\varepsilon_{r,\parallel} \;=\; \Re\,\varepsilon_{r,\parallel}\,(1 - j\,\frac{\Im\,\varepsilon_{r,\parallel}}{\Re\,\varepsilon_{r,\parallel}}\,) \tag{4.8}$$

$$\varepsilon r, \| = \Re\, \varepsilon_{r,\perp} - j\Im\, \varepsilon_{r,\perp} \;=\; \Re\, \varepsilon_{r,\perp}\,(1 - j\,\frac{\Im\, \varepsilon_{r,\perp}}{\Re\, \varepsilon_{r,\perp}}\,) \tag{4.9}$$

The loss tangents for two orientations will be defined as follows:

$$tan\ \delta_{\|} = \; -\,\frac{\Im\, \varepsilon_{r,\|}}{\Re\, \varepsilon_{r,\|}} \qquad and \qquad tan\ \delta_{\perp} = \; -\,\frac{\Im\, \varepsilon_{r,\perp}}{\Re\, \varepsilon_{r,\perp}} \tag{4.10}$$

Changing of permittivity provides tuning of the filter in different frequencies. It is expected that a tuneable filter provides a frequency tunability ($\Delta f_c/f_c$) of 10% or more, depending on the tuning mechanism and filter topology. This allows the tuneable filters to be used in multiband systems with the advantage of low power consumption and reduced size and easier tuning facility compared to is we have fixed filters for each centre frequency [78] .

Tunability of the liquid crystal can be defined as difference between relative permittivity of the substance in vertical and horizontal orientation of rod-shape molecules divided by the maximum value of the relative permittivity which is normally vertical one:

$$\tau = \;\frac{\left|\,\varepsilon_{r,\|} - \,\varepsilon_{r,\perp}\,\right|}{max\,(\varepsilon_{r,\|}\,,\varepsilon_{r,\perp})} \;=\frac{\varepsilon_{r,\|} - \,\varepsilon_{r,\perp}}{\varepsilon_{r,\|}} \tag{4.11}$$

For different liquid crystal substrate, this is normally given in %. And finally, the other parameter defined for the tuning efficiency of liquid crystal is LC merit which is the above – mentioned tunability divided by the maximum tangent loss in vertical and horizontal conditions:

$$\eta = \;\frac{\tau}{\max\,(tan\ \delta_{\|}\,,tan\ \delta_{\perp})} \tag{4.12}$$

Merit η has no unit and will be given as a decimal number.

Table 4.1 lists some of the most common nematic liquid crystals which are already used at microwave and millimetre- wave frequencies, the value are for room temperature of 20∘C and might change slightly at different frequencies and room temperature [50] :

Samples	Permittivity		Dielectric anisotropy	Loss tangent		Operating frequency
	$\varepsilon \perp$	$\varepsilon \parallel$	$\Delta\varepsilon$	tan $\delta\perp$	tan $\delta\parallel$	F (GHz)
K15(5CB)	2.72	2.90	0.18	0.03	0.03	1–10
BL037	2.35	2.61	0.26	0.06	0.06	1–10
BL006	2.62–2.69	3.11–3.12	0.49–0.43	0.015–0.007	0.035-0.036	4.8–8.7
E7	2.72	3.17	0.45	0.12	0.02	5-6
GT3-23001	2.46–2.50	3.28–3.30	0.82–0.80	0.0143	0.0038–0.004	13.5–19
GT3-24002	2.50	3.30	0.80	0.0123	0.0032	6–10

Table 4.1 Liquid crystals specification

4.4 Microwave devices tuning techniques

Initial research efforts to implement tuneable periodic filters focused on varactor and PIN diodes, ferroelectric materials and MEMS technology; however, for mm-wave operation each presents significant limitations in cost, reliability, linearity or size/complexity (see Table 4.2) [43].

PIN-diode components are semiconductor devices which, at microwave frequencies, can act as a variable resistor. The resistance changes with bias voltage (i.e. positive voltage) causes lower resistance and negative voltage increases resistance. Therefore, switching between forward and reverse bias provides a switching function. Tuneable filters using PIN-diode technology are often based on substrate-integrated waveguide (SIW) circuits. SIW combines the advantages of waveguide cavities and planar structures on a single high-frequency substrate. SIW circuits are formed from top and bottom metal layers and rows of vias along the substrate edges forming the waveguide walls, while the planar microstrip acts as the transmission line for RF input/output.

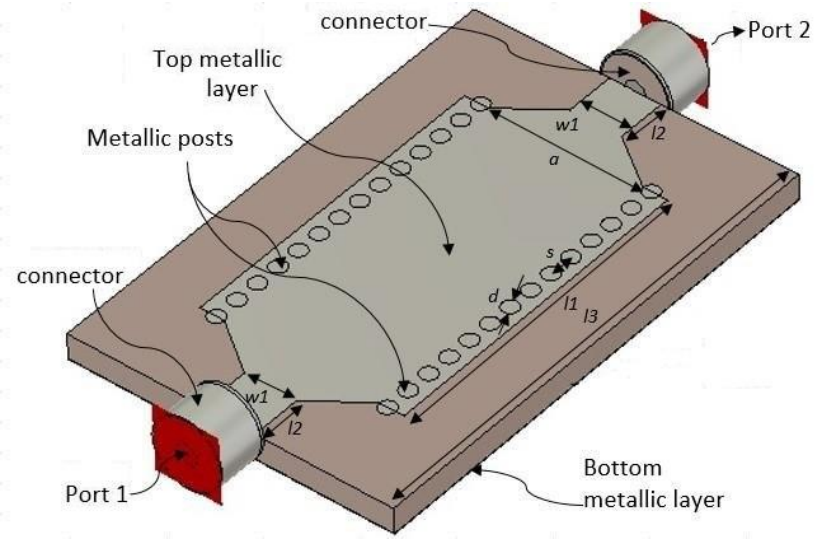

Fig 4.9 Substrate integrated waveguide (SIW) based device

In the PIN-diode method, the electromagnetic field distribution inside the waveguide changes by switching between operation states when the metal via posts are connected or disconnected. The filter bandwidth can then be tuned through the PIN-diode switching functionality. Tuning is achieved by connecting/disconnecting the tops of the perturbing via posts to/from the top metal layer of the SIW cavities. The PIN-diode switch technique enables digital frequency tuning with reasonably good isolation and linearity. However, the bandwidth is not stable when tuning around a desired centre frequency, and fabrication complexity increases because the structure can require multiple transmission-line levels.

A major limitation of the PIN-diode method for mm-wave tuneable devices is the low phase-shift resolution, owing to the limited number of control bits or lines that can be switched. Also, due to the high dissipation factor of materials and device parasitics, solid-state PIN-based components exhibit unacceptably high losses at mm-wave frequencies [44] .

Micro-electromechanical Systems (MEMS) is the technology that uses microscopic components with both electrical and moving parts. Use of MEMS in tuneable filters provides microsecond switching speed together with a much higher linearity and lower insertion loss over a large bandwidth and with less power consumptions compared to other solid-state technologies. The tuning function of filters using MEMS is achieved using capacitive shunt switches. MEMS technique for tuneable devices are excellent for the applications requiring compact components are needed, such as mobile phones and wide band WiFi and tracking systems. In MEMS technique, movements in the scale of micrometre provides the required switching. This tuning method provides low distortion loss and high linearity. Two types of tuning approaches are generally reported: MEMS-based and varactor-diode-based. MEMS devices achieve high linearity and reliability, while varactor diodes, commonly used for analogue tuning, offer fast tuning speed, compact size and low cost but at the expense of limited tuning range, poor linearity, low quality factor and the need for high voltage. Capacitance

changes in diodes due to the applied voltage to diode p-n junctions are reversely a function of square root of the applied voltage [44] .

In digital type it is possible to tune filters on discrete frequencies with a wide tuning range. The MEMS filters are less sensitive to temperature and bias voltage. However, the limitation is that MEMS switches are not commercially available for frequencies higher that 40GHz.

Ferroelectric materials provide tunability via an applied electric field that changes their dielectric permittivity. In contrast, magnetically tuneable filters employ ferrite materials whose permeability is varied by a static magnetic field, shifting the resonant frequency.

In ferroelectric tuneable materials, for the temperatures below a certain temperature (called Curie temperature) the polarisation can be changed and reversed with the effect of an electric field. Polarisation switching function is a key property for the ferroelectric materials to have a wide range of application in microwave and optics [45]. In ferroelectric materials (and has HfO_2) the permittivity increases by phase transformation but needs a very high temperature to be stabilised. However, by doping of HfO_2 with ZrO_2 and atomic layer deposition, it has been possible to achieve a tetragonal phase of HfO2 at room temperature. The result ferroelectric material which comes from HfO_2 doped with Zirconium (Zr) called HfZrO can be used for voltage dependent permittivity applications in room temperature. Microwave tuneable filter designs using HfZrO with thickness of 5-10 nm are reported in 1-8GHz, when a Bias voltage changes between 0-5Volt DC [46].

Ferroelectric-based tuneable filters offer fast, electric-field control (ns–µs) and moderate-to-large fractional tuning (typically 10–40%). However, mm-wave loss can be a concern for some films, and while legacy perovskites are not CMOS-friendly, $HfZrO_x$ thin films provide a more CMOS-compatible path at the cost of somewhat lower tunability.

Other techniques used to provide tunability in filters are mechanical tuning which are considered as the earliest techniques. In these techniques physical movement or rotation tunes the filter. This technique has capability to handle high power with high quality factor but has

Feature / Method	Varactor Diodes	Liquid Crystals (LCs)	Ferroelectric Materials (e.g., BST)	Piezoelectric Materials (e.g., PZT, AlScN)
Tuning Mechanism	Voltage-controlled capacitance of a p-n junction.	Voltage-induced reorientation of anisotropic molecules, changing dielectric constant.	Voltage-induced change in dielectric constant (permittivity).	Voltage-induced mechanical deformation, leading to physical changes or stress in a resonant structure.
Response Speed	Fast (ns to µs)	Slow (ms to s)	Fast (ns to µs)	Medium (µs to ms)
Tuning Range	Good to excellent (dependent on varactor quality)	Moderate to good (dependent on LC material)	Moderate to good (dependent on material tunability)	Moderate to good (dependent on actuator displacement)
Power Consumption	Low (bias voltage, minimal current)	Low (static voltage once tuned)	Moderate (requires bias voltage and can have leakage currents)	Low (primarily for voltage control of actuators)
Insertion Loss	Moderate to high (due to series resistance at high frequencies)	Moderate to high (inherently lossy at mm-wave frequencies)	Moderate to high (due to dielectric losses)	Low to moderate (can be very low if mechanical tuning avoids direct RF path)
Q-Factor	Moderate (limited by varactor losses)	Moderate to low	Moderate (limited by material losses)	High (if mechanical tuning affects high-Q resonant structures)
Linearity	Can be an issue, especially at high power	Generally good for small signals	Can be non-linear (hysteresis effects)	Generally good (if displacement is linear with voltage)
Temperature Stability	Generally good, but characteristics can drift with temperature.	Sensitive to temperature (LC properties change significantly).	Sensitive to temperature (dielectric constant changes).	Good, but material properties can have some temperature dependence.
Integration	Relatively easy to integrate with planar circuits.	Requires specialized integration for LC cell formation.	Can be integrated as thin films, but requires specific material processing.	Can be integrated as thin films (e.g., AlScN on silicon) or separate actuators.
Complexity	Moderate	Moderate to high (packaging, alignment)	Moderate to high (material deposition, annealing)	Moderate (actuator design, mechanical coupling)
Applicability at 60 GHz	Widely used, but losses increase at higher frequencies.	Emerging, showing promise but with challenges for low loss.	Promising, but high losses are a major challenge.	Promising for high-Q applications, often involves mechanical tuning of resonators.

Table 4.2 Technical comparison of voltage-controlled tuning methods at 60 GHz

the disadvantages of low tuning speed and bulky sizes. Building on the overview of tuning

methods introduced in Chapter 2, Table 4.2 focuses specifically on voltage-controlled tuning mechanisms and compares their performance characteristics at millimetre-wave frequencies.

4.5 LC-based tuning methods and applications

Among all the other methods reported here for tuneable devices in MMW frequency bands, liquid crystals have the following advantages:

- Low-to-moderate bias voltage and straightforward digital control.
- Straightforward fabrication leveraging processes similar to LCD stacks
- Decreased loss and increased anisotropy with frequency change
- Low power consumption and mass
- Competitive cost

LC substrates are therefore strong candidates for developing tuning devices at mm-wave, because of the above advantages. Table 4.3 summarises key LC properties and their implications for filter design.

Property / Advantage	**Typical Value for Nematic LC (≈60 GHz)**	**Effect on Filter**	**References**
Low-to-moderate bias; simple control	5–20 V DC; essentially zero static current once biased	Voltage-only tuning with simple bias network; negligible DC power	[47] , [48]
Fast electrical tuning	~1–100 ms (cell-gap/viscosity dependent)	Adequate for channel switching / beam steering at mmWave	[47], [49], [50]
LCD-like fabrication maturity	Polyimide alignment 50–200 nm; LC gap 20–500 μm; UV/thermal sealing; process temps ≤ ~250 °C	Repeatable RF cells; straightforward scaling to arrays	[47], [51], [52],
Low dielectric loss; useful anisotropy	tan δ ≈ 0.005–0.02; dielectric anisotropy Δε ≈ 0.2–0.8 (material-dependent)	Keeps insertion loss reasonable; Δε enables wide ε_{eff} tuning	[48], [49]
Low power and mass	Static power ≈ 0 mW (capacitive drive); LC density ~1–1.1 g cm^{-3}	Very low energy per tune; lightweight RF stacks	[47], [50]
Competitive cost	Commodity LC materials; no exotic epi/ferro films; standard PI/UV processes	Lower material/process cost vs many ferroelectric/MEMS options	[47], [50]

Table 4.3 Properties of LC substrate

Electrically tuneable material (i.e. LC) enables continuous frequency shifting in resonator-based filters without any mechanical motion. Recent research has therefore focused on varying

LC electrical properties with an applied bias voltage to tune RF components. LCs combine low cost, low operating voltage, negligible static power, and stable, continuous electrical tuning.

LC-Based phase shifters

Tuneable phase shifters using liquid crystals were first developed in 1990s using microstrip line at 10.5GHz [53]. Later in 2004 design of phase shifters on inverted microstrip lines on operating 1GHz and 20GHz were proposed with insertion loss better that -5dB and return loss lower than -10dB [54]. For higher frequencies of 20-30 GHz a ring resonator used for a tuneable phase shifter in 2010 on that shift of centre frequency reported from 33.1 to 35.4GHz with the advantage of small size which enable connection of two-phase shifters in series for a reflect-array antenna [55]- [56]. At higher frequencies LC-based phase shifters are developed which can achieve 92^{o} shift at 76GHz and with 2.4dB insertion loss [57]. In 2019 a tuneable nonradiative dielectric waveguide (NDR) phase shifter using liquid crystal is reported in [58], in that the LC is inserted in the core of waveguide dielectric , considering the no-radiation property of NDR, a differential phase of 280^{o} could be achieved with a bias voltage of 150V and insertion loss between 2.9 dB to 4.9dB. Another phase shifter of dielectric waveguide structure is reported in 2017 in [59] which part of the core material in the waveguide is replaced with liquid crystal to provide the required continuous tuneability, with an electric bias of 550V a maximum phase shift of 430^{o} could be achieved with insertion loss between 2.8 to 5.5 dB with standard WR10 connections.

LC-Based Resonators

The first method suggested for liquid crystal for tuneable resonator in 40GHz frequencies are reported 2010 using a planar patch resonator which was used to measure dielectric constant of LC E7 [60]. Another method of designing tuneable resonators at 3.5GHz frequency band was reported in 2012 using two K15 and GT3-23001 layers of liquid crystal samples with tuning

ranges of 4% and 8% in a resonator [61]. This has been followed using a five-layer 3 GHz tuneable filter with the possibility to be used for WiFi applications.

LC-Based Filters

One of the earliest reports for LC-based tuneable filters in 2006 uses a λ/2 open-circuit stub resonator on a second order filter to provide limited tunability the liquid crystal was drilled into a cavity in substrate to prevent leakage [62], [18] , [63]. Although LC cavity is a reasonable measure to stop liquid leak but controlling of drilling thickness which affects design parameters is still a challenge. In 2010 a three-pole bandpass LC-based 20GHz tuneable filter has been proposed with 2GHz tuning range and 10% tunability. Another report of coupled microstrip line structure tuneable filter in 2012 has been developed at 33GHz and 2GHz tuning range on that the insertion loss needs to be improved [60]. An inverted microstrip line band stop tuneable filter with 1825 liquid crystal substrate has been proposed in 2013 with 275MHz tuning range for 0-6V bias voltage, it is suggested that narrower stop bands could be achievable using low loss liquid crystals [64]. In 2017 design of a tuneable inverted microstrip LC1917-based bandpass filter were reported using three λ/2 open stubs and λ/4 connecting lines, operating on 30, 50 and 85 GHz with 10% tuning around central frequencies with 14V AC bias providing 3.76 dB insertion loss and -9 to -25dB return loss and reasonable impedance match and Q-factor of 6 [65]. A wideband miniaturized tuneable LC-based band-pass filter using periodic loading square spiral resonators on microstrip structure has been developed in 2020 reported for operating on frequency range between 39.08 to 40.67 GHz and 1.59GHz tuning band due to external bias voltage change between 1V to 30V, insertion loss 3.9dB [66].

A proposal for biasing of liquid crystal 30 GHz tuneable filter using simultaneous magnetic and electric fields is proposed in 2022 to simplify the design and reduce the number of electrodes and bias voltage and increasing tunning efficiency by full exploitation of the LC's anisotropy because of homogeneous filed [67].

Application of liquid crystals on tuneable filters are also reported for other microwave waveguide devices and technologies.

Liquid crystal filled waveguide resonator and bandpass filter are reported in [68] with a higher q-factor compared to planar structures offering two possible approaches for liquid crystal positioning. The filter operates at centre frequency of 20GHz with 1% relative bandwidth and a tunability of 450MHz with magnetic biasing. Orientation of the rod-shape molecules of LC in this design will be influenced by an external magnetic field.

A reconfigurable waveguide bandwidth and frequency tuneable filter based on liquid crystal, in Ka-band at 30 GHz with ability to tune both centre frequency and bandwidth independently is reported in [69]. Liquid crystal is used in the structures of resonator and coupling structures and a two-layer electrode structure is proposed for the waveguide structure. In 2016 design of another tuneable structure of substrate integrated waveguide (SIW) with nematic liquid crystal and combined with split-ring resonators is reported for frequencies between 3.79 to 6.78 GHz when the permittivity of the liquid crystal changes from 2.79 to 3.56 and can provide a passband of 490MHz [70].

4.6 Fabrication of LC microstrip filter

Because of the fluid nature of liquid crystal material, the LC substrate should be confined in a cavity inside the device and then sealed. For this reason, the topology of inverted-microstrip in that the line substrate covers liquid crystal cavity, would be the most adequate design [79]. An inverted microstrip topology for a tuneable LC filter is shown in below Fig 4.10 [80].

The bias voltage in the figure can change the electric field and therefore the effective permittivity of the microstrip line in the structure which changes filter transfer function. Liquid Crystals typically require a very low bias voltage for tuning and are commercially available and can be integrated with flexible printing technologies [81]

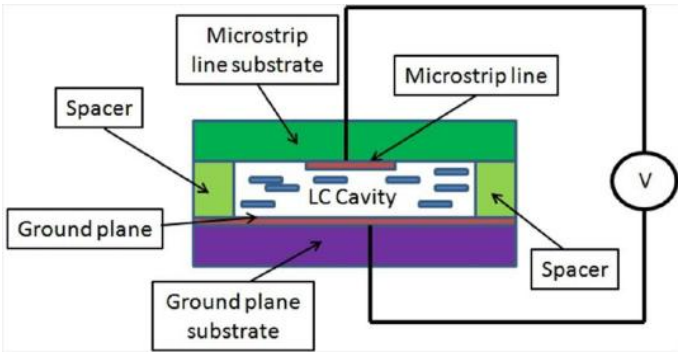

Fig 4.10 Cross-section of a tuneable microstrip component using liquid crystal

.

4.6.1 Design considerations of LC microstrip devices

Integrating LCs within microstrip structures introduces significant fabrication challenges, particularly regarding cavity formation, LC containment, sealing, and long-term stability [47]. Fig 4.11 illustrates a layer-by-layer structure and technical aspects of LC device fabrication. The structure in the figure consists of multiple stacked layers: a copper microstrip conductor, dielectric and polyimide films, an LC cavity, and a copper ground plane. Fabrication involves micron-precision assembly, material compatibility management, and hermetic sealing of the LC cavity.

- **Microstrip Conductor (Copper, typical 17 µm thickness):** acts as RF signal path, and also as the top electrode for LC tuning. Fabrication considerations include uniform thickness is critical for impedance control. Copper oxidation risk, which may require protective plating (e.g., gold flash). Patterning must maintain edge definition to reduce conductor losses
- **Inverted Substrate (typical h = 0.5 mm, ε_r = 2.2, tanδ = 0.0001):** provides mechanical support and electrical isolation between conductor and LC. Consideration for fabrications are tight tolerance in ε_r to maintain predictable filter characteristics, impact of thickness uniformity on impedance and bonding reliably to polyimide layer.

- **Upper Polyimide Film (typical T = 2.5 µm, ε_r = 3.3):** provides alignment and compatible surface for LC. Polyimide should have uniform thickness for cavity control and adhesion to both dielectric and LC-facing surfaces must be strong, also rubbing or photoalignment process must not wrinkle or deform the film.
- **Liquid Crystal Layer (typical h = 0.2 mm, ε_r = 2.2–2.7** (voltage-controlled)**, tanδ = 0.005–0.02):** is the main tuneable medium which should be bubble free and in that contamination from adhesive, solvents or dust should be prevented. Also, sealing of LC with no leakage or moisture ingress is a key fabrication point.
- **Frame Dielectric Substrate (typical h = 0.2 mm, ε_r = 2.2):** is the base structure holding LC cavity and providing support. It is important to machine, use 3D printing or etching cavity without damaging substrate and achieving precise cavity wall geometry for LC containment. Cavity should not be too thin or thick or non-uniform. In very thin cavity LC molecules may not reorient fully and thick cavity higher driving voltage needed and response is slower. Non uniform cavity cause Phase errors, increased insertion loss, degraded filter shape
- **Lower Polyimide Film (typical T = 2.5 µm, ε_r = 3.3):** Must bond reliably to copper ground plane without voids plus the same consideration of the upper Polyimide layer.
- **Ground Plane (Copper, typical 17 µm):** is the RF return path and acts as bottom electrode for LC tuning. Must have good electrical contact to DC bias feed without introducing RF loss. Ground plane surface flatness also impacts LC cavity sealing.

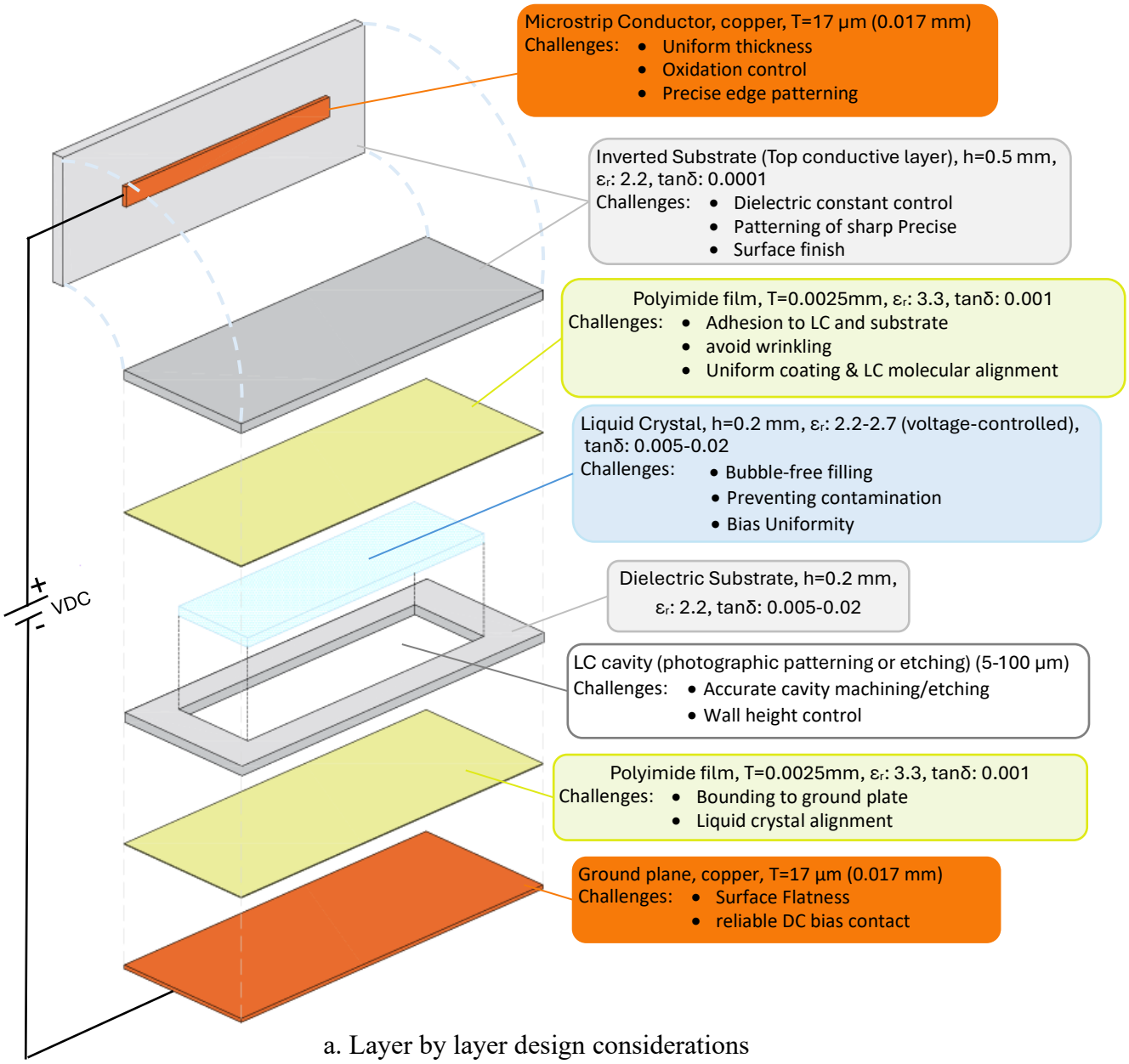

a. Layer by layer design considerations

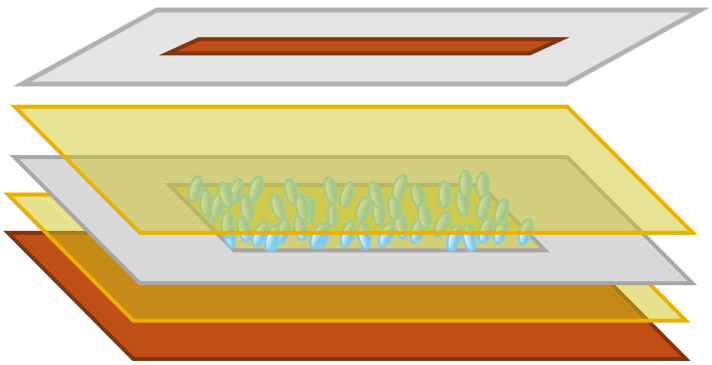

b. LC microstrip sandwich configuration

Fig 4.11 LC based microstrip device configuration

4.6.2 Fabrication process flow

Cavity formation and spacer definition, is one of the most critical parts of the filter structure, because it impacts thickness of LC layer and uniformity of the electric field. Spacer materials are typically selected from a range of established technologies, including glass microspheres, photolithographically defined polymer spacers, and adhesive or patterned spacer films. The choice depends on the required LC layer thickness, uniformity tolerance, process compatibility, and RF performance. [51]. Size will be selected to match the target LC layer thickness (e.g., 20–500 μm). High-precision grades (±1–2 μm) are preferred to ensure uniform gap height. Table 4.4 is a list of common spacer technologies and considerations [82].

Spacer Material	Process Method	Pros	Cons
SU-8 photoresist	Photolithography	Precise thickness, planar	Requires cleanroom, brittle
Polyimide	Spin-coating + etch	Flexible, LC compatible	Thickness control more difficult
Glass fiber spheres	Dispersed in adhesive	Easy to control height	May cause scattering in RF path
Adhesive films	Laser-cut cavity pattern	Simple lamination	Adhesive outgassing possible

Table 4.4 Sealant types and properties

Bonding method, typical bounding methods are adhesive bonding, thermal bonding and anisotropic conductive film (ACF) [83]. Adhesives are low viscosity epoxy or UV-curable which will be applied along the perimeter and for that creeping into LC cavity must be avoided. Thermal bolding used for thermoplastic substrates by applying heat and pressure to fuse layers around the cavity. In cases where electrical contact is also needed along the cavity edges, ACF can be used. During bonding deformation (especially for thin copper/dielectric layers) must be avoided. A precision jig can be used to control pressure, so spacers maintain their nominal height. Also, particle contamination should be avoided as any dust can locally change the gap and cause LC defects [84].

Liquid Crystal filling, must ensure complete cavity coverage without bubbles to avoid air bubble formation due to surface tension effects, LC contamination by residual solvents or dust and provide long filling times for narrow cavities, best practice for this issue is vacuum-filling through a small fill port, followed by curing/sealing [48]. Once filled, the LC cavity must be hermetically sealed to prevent evaporation and moisture ingress. Sealant should chemically

react with LC, minimize curing temperature and prevent mechanical stress that can distort cavity height. Table 4.5 lists some sealant type and properties [52].

Sealant Type	Curing Method	Pros	Cons
UV-curable epoxy	UV exposure	Low-temp process, fast	Needs UV access, possible shrinkage
Thermal epoxy	Heat curing (60–150 °C)	Strong mechanical bond	May damage LC if overheated
Silicone adhesive	Ambient curing	Flexible, stress relief	Lower mechanical strength

Table 4.5 Sealant types and properties

Anchoring the LC molecules in the initial state is crucial for predictable RF performance before bias is applied. This is usually called surface alignment or pre-tilt setting. Table 4.6 lists typical implementation process of LC anchoring [85]:

Process	Descriptions
Alignment Layers	**Material:** Polyimide films are the most common (however certain PVA or SiO_2 coatings are also used). **Deposition:** A thin LC alignment coating is formed at the surface of the polyimide layer. The active molecular alignment region is typically on the order of ~50–200 nm. The underlying polyimide film, which primarily provides mechanical support and contributes to the electromagnetic model, is in the micrometre range (e.g., ~2.5 μm). **Function:** This layer interacts chemically and physically with LC molecules to define their preferred orientation (planar, vertical, or tilted).
Surface Treatment for Planar Alignment	**Rubbing Method:** After polyimide curing, the surface is gently rubbed with a velvet cloth or roller in one direction. This creates microscopic grooves that give the LC molecules a uniform azimuthal direction. This is a common method for achieving planar alignment in nematic liquid crystal (LC) devices. **Photoalignment:** Uses polarized UV light to induce anisotropy in a photosensitive layer (like azo-dye polyimides). This is a Non-contact method which avoids particles from rubbing. This method is better for high-frequency LC devices where surface contamination is a concern.
Vertical Alignment (VA)	Achieved by using special homeotropic alignment polyimides or surfactant coatings. In that LC molecules stand perpendicular to the substrate at zero bias, this method is useful for certain tunable RF designs.
Pre-Tilt Angle Control	By adjusting surface chemistry or curing temperature, you can set a small tilt (1–3°) so LC molecules respond more uniformly when an electric field is applied
Anchoring Strength Considerations	• **Strong anchoring** → More stable alignment but requires higher voltage to reorient. • **Weak anchoring** → Easier reorientation, but risk of slow relaxation or drift. • For microwave LC filters, moderate anchoring is often chosen to balance stability and tunability.

Table 4.6 Typical implementation process of LC anchoring

For tuneable LC microstrip periodic structure filter the following process can be followed [86]:

1) Clean substrates (top and bottom surfaces of LC cavity) thoroughly.
2) Spin-coat polyimide alignment layer on both surfaces.
3) Cure at the manufacturer's recommended temperature (often 200–250 °C).
4) Rubbing or photoalignment to define molecular orientation.
5) Assemble cavity with spacers, then fill with LC.
6) Seal cavity without disturbing alignment.

Reliability concerns, thermal cycling, moisture ingress and electrode corrosion can impact the reliability of the structure due to mismatch, degrade LC dielectric properties and not isolation from air, the mitigation of the impact includes hermetic sealing of full package encapsulation, UV- blocking coating and testing before assembly.

The successful fabrication of this LC-based microstrip filter requires precision in layer stacking, compatibility between all materials, and stringent sealing of the LC cavity. Each layer, from copper conductor to ground plane, has specific manufacturing tolerances and bonding requirements, and the LC handling process is the most delicate stage.

From the viewpoint of the final structure, in a typical structure of capacitive elements, where a liquid crystal substrate can be sandwiched between two metal electrodes, thin layers of polyimide film of approximately 0.4 micro-meter with fine grooves placed on top and bottom metal layers to align the liquid crystal molecules when unbiased as shown in Fig 4.11-b [62].

4.6.3 Optimisation of LC microstrip devices

For the optimisation of tuneable devices based on liquid crystals, some parameters should be considered in fabrication [62].

A. Signal transmission line which is typically copper should have a thickness of at least 3 times of the skin depth. In MMW frequencies the skin depth is around 0.5 μm or less.

A very thin layer of gold cover on copper line can help to prevent liquid crystal chemical reaction with copper.

B. Low loss substate materials should be used to support the copper line. Taconic TLX or Rogers Duroid materials are recommended materials to be used. Also, a new generation of borosilicate glasses are recently developed to be used in high frequencies.

C. Different type of losses should be considered. One of the losses which should be controlled is caused by eddy current, which is a rotating electrical current in moving copper in a magnetic field, or variable magnetic field over the copper. This current such as any currents flow in copper and generate losses. This loss will be a function of magnetic field strength and dimension of the metal.

D. Liquid crystals are low loss materials but not zero loss. Depending on the type of liquid crystal the tangent loss can be between 0.002 to 0.02.

E. Tuning of liquid crystal can be obtained by the applied voltage that reorients the molecules of liquid crystals. Configuration and location of voltage electrodes have an essential effect. Normally the signal line and ground plates are the electrodes, too. Optimisation of electrodes can improve the device function.

F. Viscosity coefficient, elastic constants and anisotropy liquid crystal type chosen for a device has effect of speed of device tuning. Thicker liquid crystals have more tuning response time.

For the best performance of a liquid crystal based tunable devices in MMW frequencies all above-mentioned parameters should be considered. However, the main parameter for a tunable microwave device is the response time which should be around microseconds. Another important parameter is that liquid crystal is the molecular homogeneity in all directions or anisotropy factor. This allows designing compact devices at lower losses. This opens the challenges to develop new types of liquid crystals materials for microwave tunable devices.

4.7 Integration of LC-Based Devices on silicon platform

MMW filters are part of a wireless radio system and should be integrated with the other components on the same platform (circuits/chip). A common platform (medium) for RF systems is Silicon. Therefore, a silicon-based design approach is appropriate to assist MMW system development. Silicon based integrated technology are successfully used for implementing of Microwave filters for a variety of different communication systems. This technology has illustrated adequate performance due to the properties of silicon semiconductors at microwave frequencies. Also, the silicon-based semiconductors provide low power consumption and cost.

Silicon has become a viable technology platform for realizing compact, power-efficient, CMOS-compatible microwave integrated circuits. Silicon wafers are used as foundation upon which devices such as electronic and microwave integrated circuits (ICs) are deposited. Silicon technology has been used in the area of MMW component designs because of the possibility in transistor scale designs, level of integration and lower cost of implementation and high yield [87]. Silicon is a low-cost platform and foundation for microstrip passive circuits such as antennas and filters.

The LC microstrip filter can be implemented as an interposer-level or package-level module that interfaces with silicon RF integrated circuits through controlled impedance transitions. Integration strategies include Flip-Chip Bonding [88] [89], Silicon Interposer with LC Module [90] , [91] and Co-Packaged Module [92], [93]. Table 4.7 provide a summary of descriptions, advantages and challenges of these strategies.

However, one of the primary challenges in integrating Lc-based MMW tuneable filter on a silicon platform is signal attenuation due to surface wave excitation in the substrate [94]. When an RF or MMW signal propagates along a planar transmission line (e.g., microstrip, coplanar waveguide) on a high-permittivity substrate such as silicon ($\varepsilon_r \approx 11.9$), part of the electromagnetic energy can couple into surface waves that travel laterally through the

substrate–air interface rather than staying fully confined to the intended transmission line mode. Surface wave loss happens due to the different permittivity and thickness of substrate and super-state layers (i.e. LC and Silicon) [95] . The power transfer into the surface wave modes does not contribute to the main signal flow but scatters from the edges as loss. At lower microwave frequencies, this coupling is small, but at MMW frequencies, the wavelength becomes comparable to substrate dimensions, and surface wave modes are more easily excited and therefore the surface wave losses lead to increased insertion loss, unwanted coupling and distorted frequency response.

Integration Strategy	Description	Advantages	Challenges	Typical Use Cases
Flip-Chip Bonding	LC filter fabricated on its own substrate and bonded directly to silicon die using solder bumps or copper pillars.	- Minimal interconnect length - Low parasitic inductance - Independent LC substrate optimization	- CTE mismatch between LC substrate and Si - LC alignment layer may degrade during bonding heat cycle	Compact frontends, low-loss interconnects at mm-wave
Silicon Interposer	LC module mounted on a silicon interposer that routes RF and DC signals between RFIC and package.	- High-density interconnects - Additional passives on interposer	- Added fabrication complexity - Hermetic sealing during assembly	Multi-chip moules, phased array beamformers
Co-Packaged Module (SiP)	LC filter and RFIC placed side-by-side in one package, interconnected via wire bonds or short transmission lines.	- Simplified thermal management - Easier yield optimization for each device	- Slightly longer interconnects - Potential higher parasitics vs flip-chip	System-in-Package designs, wideband tunable modules

Table 4.7 Integration Strategies for LC Microstrip Filters on Silicon Platforms

The following can be considered as migration methods to reduce the impacts of surface wave losses [96], [97]:

1) Use of a low-permittivity dielectric layer (e.g., BCB, polyimide) between the transmission line and silicon to reduce coupling to substrate modes.
2) Micromachining / substrate removal, locally thin or remove silicon underneath the RF lines to suppress surface wave propagation.
3) Ground Vias / Electromagnetic Bandgap (EBG) structures, periodic via fences or EBG patterns confine the electromagnetic fields and suppress lateral modes.

4) Hybrid integration, place MMW passive components (e.g., LC filter) on a low-loss interposer or organic substrate and connect to silicon active circuits via flip-chip or wire bonding.

Although Silicon remains attractive for compactness and CMOS compatibility, however, there are also other alternative approaches for integrating an LC-based tuneable microstrip filter with other components. Each alternative comes with different trade-offs in terms of loss, complexity, cost, and integration density. Table 4.8 list some of these alternatives.

Platform	Description	Advantages	Challenges	Typical Applications	Ref
Glass Substrate (e.g., Fused Silica, Borosilicate)	LC filter fabricated on or integrated with a low-loss glass substrate, either as the main carrier or as an interposer between active devices.	- Very low dielectric loss at MMW - Dimensional stability - Optical transparency for LC alignment control	- Lower mechanical robustness than Si - Higher cost for precision micromachining	High-Q filters, optical–RF hybrid devices	[98] , [99]
High-Resistivity Silicon (HR-Si)	Uses Si with resistivity > 2 kΩ·cm to reduce substrate losses.	- CMOS-compatible - Lower loss than standard doped Si	- Still relatively high ε_r (≈11.9) → surface wave risk remains	5G mm-wave phased arrays, compact RFICs	[97] , [96]
Low-Temperature Co-Fired Ceramics (LTCC)	LC cavity embedded in a multilayer LTCC stack along with other passives.	- Multi-layer routing capability - Excellent thermal stability - Good hermeticity	- Not CMOS-compatible - More difficult LC alignment process	Rugged RF modules, aerospace systems	[100], [101]
Polymer-Based (e.g., BCB, Polyimide)	LC cavity integrated on flexible or semi-flexible organic substrates.	- Very low dielectric constant and loss tangent - Conformal form factors - Easy to machine cavities	- Thermal stability limits - Long-term hermetic sealing of LC can be challenging	Wearable RF devices, conformal antennas	[102]
3D Printed RF Structures	Additively manufactured substrate and cavity with LC filling.	- Rapid prototyping - Complex geometries possible	- Limited RF performance (surface roughness) - Reliability concerns	Experimental tunable RF devices	[103], [104]
Hybrid Integration on Organic Interposers	LC filter fabricated separately and mounted on an organic interposer that connects to active components via flip-chip or wirebond.	- Low-cost packaging - Good RF performance if low-loss laminate is used	- Moisture ingress risk - Lower thermal conductivity		[105], [106]

Table 4.8 Alternatives to silicon-based integration for LC microstrip devices

4.8 Summary

This chapter examines the liquid crystal (LC) substrate for tuneable devices including periodic structures, emphasizing the unique properties and advantages of LCs and its application as a tuneable 60GHz filters. It highlights the integration of LC technology with periodic structures for achieving dynamic reconfigurability and enhanced performance in high-frequency applications. An introduction to liquid crystals is provided, covering their dual nature as anisotropic fluids that combine properties of both liquids and crystalline solids. The chapter emphasizes their dielectric tunability under an external electric field, making them highly suitable for microwave and RF applications. The different phases of liquid crystal, nematic, smectic, and cholesteric, are explained, with a focus on the nematic phase due to its easy voltage-controlled tunability and widespread use in RF and microwave devices. An overview of various tuning techniques used in microwave devices is provided, including mechanical adjustments, semiconductor-based tuning, and LC-based methods. The advantages of LC-based approaches, such as low power consumption and seamless reconfigurability, are highlighted.

The chapter then explores the fundamental mechanisms of LC-based tuning, focusing on how variations in the dielectric constant are utilized for real-time frequency adjustment. The design and operation of LC-based phase shifters and resonators are discussed, illustrating how the anisotropic properties of LC enable precise control of phase shifts and tuneable resonant in signal propagation, critical for beamforming and phased array systems. The integration of periodic structures with LC resonators is highlighted for advanced filter designs. The chapter delves into LC-based filters. The use of LC substrates in periodic filter designs enables wideband tuning and compact implementations suitable for 60GHz applications. The key properties of liquid crystals relevant to periodic structures are discussed, including their anisotropic permittivity, response time, thermal stability, and loss characteristics. The impact of these properties on device performance is analysed.

The chapter concludes with an overview of the fabrication processes for LC-based devices, including substrate preparation, alignment layer deposition, LC cell assembly, and encapsulation. Challenges such as achieving uniform alignment and minimizing insertion loss are addressed.

Overall,, this chapter provides a comprehensive understanding of liquid crystal substrates and their integration with periodic structures for tuneable millimetre-wave devices. By covering the fundamental properties of liquid crystals, tuning mechanisms, and practical applications, it establishes the importance of LC technology in advancing reconfigurable RF components. The insights gained from this chapter pave the way for developing high-performance, tuneable devices for modern communication and sensing systems.

Chapter5 : Periodic Filter Design

A periodic filter exhibits passbands, where signal propagation is allowed, and stopbands, where propagation is suppressed. Several cascade microstrip elements are referred to as a periodic structure. Filter designs at microwave frequencies are not feasible using discrete components because the wavelengths of the operating frequencies would be comparable with the dimensions of filter elements. Therefore, the filter components must be in the form of distributed microstrip elements. Microstrip technology is the most popular method for microwave filter designs because of its compact size and easiness of implementation.

Periodic filters are normally designed to provide passband and stopband characteristics in different frequency bands depending on the design criteria. To design a specific filter, we should consider and convert the frequency characteristics to the filter parameters.

Periodic-structure filters at microwave frequencies exhibit strong dispersion that sets the locations of passbands and stopbands. The band edges are dictated by the unit-cell geometry through the Bloch phase βd (where β is the phase constant of the host line and d is the unit cell period), with the first Bragg edge near $\beta d \approx \pi$; consequently, the response is highly sensitive to structural tolerances and to variations in effective permittivity. Microstrip planar circuits are attractive for such realisations because of their low weight, compact size, reduced cost, and reliability; however, they trade lower power-handling capability and a lower unloaded quality factor than waveguide owing to conductor and dielectric losses. In this work the quality factor is taken in the loaded sense, Q_L; for a narrowband passband $Q_L \approx f_0/\mathrm{BW_{3dB}}$, (with f_0 the passband centre frequency and $\mathrm{BW_{3dB}}$ the 3-dB bandwidth). The rigorous definition is $Q \equiv \omega_0 W/P_{\mathrm{diss}}$, where $\omega_0=2\pi f_0$, W is the time-average stored electromagnetic energy, and Pdiss is the time-average power dissipated in conductors and dielectrics; moreover $1/Q_L=1/Q_u+1/Q_e$, with Q_u the intrinsic (unloaded) Q and Q_e the external Q set by terminations/coupling. Limited

Q_u in microstrip manifests as higher passband loss and gentler skirts, constraining the ultimate selectivity achievable with a given periodic topology [16], [27], [28].

5.1 Theory of Microstrip Periodic Structures

Microstrip periodic structures are composed of repeated intervals of identical transmission line sections and reactive elements, which together form the unit cells of the structure. The output of each unit cell serves as the input to the next, enabling signal propagation through the cascade. A unit cell in a periodic structure may consist of a simple T-section or a more complex circuit topology.

Compared with conventional microstrip filters, periodic structures exhibit distinctive characteristics that are particularly valuable at microwave and millimetre-wave frequencies:

- Dispersion-driven sensitivity: The passband and stopband edges of a periodic filter are determined by the Bloch phase constant (βd) and the unit-cell susceptance. This results in strong sensitivity of the transmission response to substrate permittivity and geometrical variations, a principle first established in the classical theory of wave propagation in periodic media [109], and widely applied in microwave engineering [27], [31], [36].
- Enhanced tunability with dielectric control: Because of their dispersive behaviour, periodic filters can achieve disproportionately large frequency shifts from relatively small changes in effective permittivity. This makes them especially effective when combined with tuneable dielectrics such as liquid crystals, yielding greater tuning ranges than conventional stub or stepped-impedance designs [34], [60], [71].
- Compact realisation of higher-order responses: By cascading relatively simple unit cells, sharp band-edge transitions and higher-order bandpass responses can be implemented without requiring large or complex resonator geometries, making periodic structures attractive for integrated microwave and mm-wave circuits [16], [36], [107].

The unit cells are typically formed from low-loss transmission line sections loaded with reactive elements. Resonators, in particular, are well-suited as building blocks for periodic filters, enabling bandpass responses with sharp rejection outside the passband. Short and open circuited λ/4 microstrip transmission lines are one type of simple resonators to be used in periodical structures (Fig 5.1).

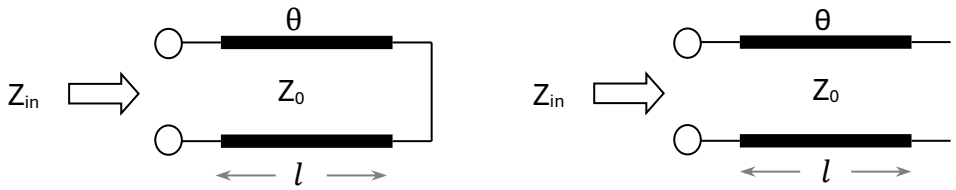

Fig 5.1 Short-circuit and Open-circuit λ/4 transmission lines

The input impedance can be expressed as follows (for a transmission line with characteristic impedance Z_0 and propagation constant $\gamma = \alpha + j\beta$):

$$Z_{in,SC} = Z_0 \tanh(\gamma l) \approx jZ_0 \tan(\beta l) \quad (\alpha l \ll 1), \tag{5.1}$$

$$Z_{in,OC} = Z_0 \coth(\gamma l) \approx -jZ_0 \cot(\beta l) \quad (\alpha l \ll 1), \tag{5.2}$$

$$\tan(\gamma l) = \frac{\tan(\alpha l) + j \tan h(\beta l)}{1 + j \tan(\alpha l) \tan h(\beta l)} . \tag{5.3}$$

Where α is the attenuation constant and β is the propagation constant of the transmission line with characteristic impedance Z_0, for a lossless line $\alpha = 0$.

The propagation constant β is directly proportional to angular frequency ω and reverse proportional to transmission line phase velocity v_p. Also, the wavelength λ is given by the ratio of phase velocity to frequency:

$$\lambda = v_P / f , \tag{5.4}$$

$$\beta = \omega / v_p = 2\pi f / v_P = 2\pi / \lambda . \tag{5.5}$$

At the frequency when the length of the transmission line l is equal to λ/4 we have $\beta l = \frac{\pi}{2}$ and therefore $tan(\beta l) \to \infty$ and cot(βl)→0: a short-circuited $\lambda/4$ stub behaves as an open (parallel resonance), and an open-circuited $\lambda/4$ stub behaves as a short (series resonance). Therefore both

open- or short-circuited transmission lines of length $\lambda/4$ (or an odd multiple of it) exhibit resonant behaviour and can be modelled by equivalent series or parallel RLC circuits as shown in Fig 5.2.

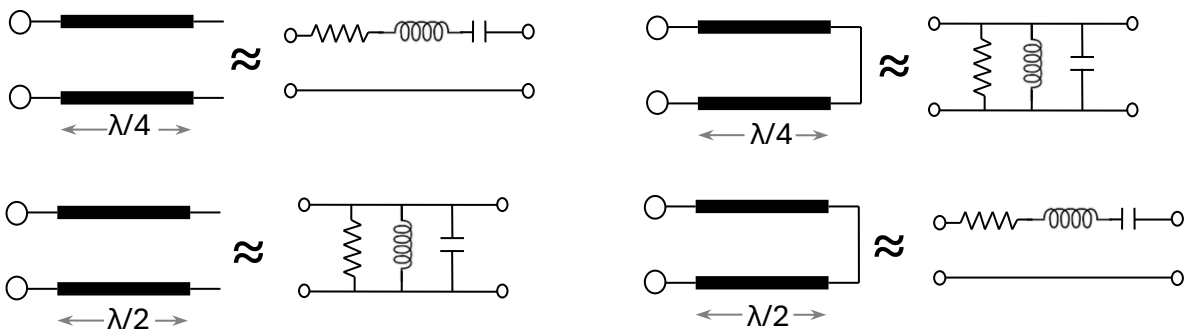

Fig 5.2 RLC equivalent of short and open circuit λ/4 transmission lines

5.2 Quarter-Wave Microstrip Resonator Design

Quarter-wavelength resonators are commonly used elements in periodic microstrip filter structures due to their simplicity and well-defined resonant behaviour. The design of such resonators requires determining the width and length of both the resonator and feed lines based on a given operating frequency and substrate properties. The formulas for the design of a quarter wave microstrip resonator are as follows [108]. Using these formulas, the width of the resonator and feed line will be calculated for a given frequency and feed line and quarter wave resonator. Also, by calculation of the effective permittivity of the substrate the effective wavelength of the propagation wave and therefore the length of resonator (i.e. quarter wavelength) can be calculated. Fig 5.3 illustrate the structure of a single stub λ/4 resonator.

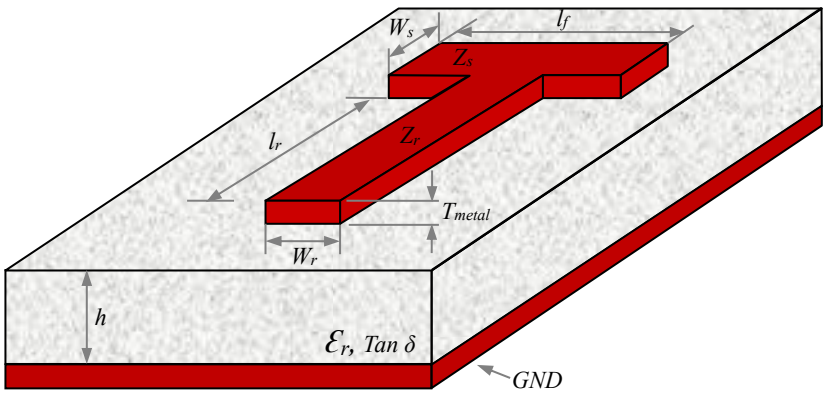

Fig 5.3 Single stub λ/4 resonator

$$\lambda_{eff} = \frac{\lambda_0}{\sqrt{\varepsilon_{eff}}} \ , \tag{5.6}$$

$$W < h \ \rightarrow \begin{cases} Z_0 = \dfrac{60}{\sqrt{\varepsilon_{eff}}} \, Ln\left(\dfrac{8h}{W} + \dfrac{W}{4h}\right) \\ \varepsilon_{e_{ff}} = \dfrac{\varepsilon_r + 1}{2} + \dfrac{\varepsilon_r - 1}{2}\left[\left(1 + \dfrac{12h}{W}\right)^{-1/2} + 0.041\left(1 - \dfrac{W}{Wh}\right)^2\right] \end{cases} , \tag{5.7}$$

$$W > h \rightarrow \begin{cases} Z_0 = \dfrac{120\pi}{\sqrt{\varepsilon_{eff}}} \left[\dfrac{W}{h} + 1.39 + 0.667 \, Ln\left(\dfrac{W}{h} + 1.44\right)\right]^{-1} \\ \varepsilon_{eff} = \dfrac{\varepsilon_r + 1}{2} + \dfrac{\varepsilon_r - 1}{2}\left(1 + \dfrac{12h}{W}\right)^{-1/2} \end{cases} , \tag{5.8}$$

where W is line width and h is substrate thickness. An equivalent and convenient set used to find W/h for a target impedance Z_0 is:

$$A = \frac{Z_m}{60}\left(\frac{\varepsilon_r + 1}{2}\right)^{\frac{1}{2}} + \frac{\varepsilon_r - 1}{\varepsilon_r + 1}\left(0.23 + \frac{0.11}{\varepsilon_r}\right) , \qquad B = \frac{377\pi}{2Z_m\sqrt{\varepsilon_r}} , \tag{5.9}$$

$$A < 1.52 \rightarrow \quad \frac{W}{h} = \frac{8e^{(A)}}{e^{(2A)} - 2} \ , \tag{5.10}$$

$$A > 1.52 \rightarrow \frac{W}{h} = \frac{2}{\pi}\left\{B - 1 - Ln(2B - 1) + \frac{\varepsilon_r - 1}{2\varepsilon_r}\left[Ln(B - 1) + 0.39 - \frac{0.61}{\varepsilon_r}\right]\right\}, \tag{5.11}$$

The quarter-wave resonator length is then:

$$L \approx \frac{\lambda_{eff}}{4} . \tag{5.12}$$

Fig 5.4 shows the actual cross-section employed in this work (polyimide–LC–polyimide under the strip with a protective lid/superstrate above), which is the same structure introduced in Chapter 4 (cf. Fig 4.11). The presence of multiple dielectrics and the lid change the phase velocity and characteristic impedance of the line. For quasi-TEM microstrip, these effects can be absorbed into an effective stack permittivity and an equivalent height. Consequently, the

design relations in formulas (5.6) - (5.12) remain valid provided that we replace the single layer quantities ε_r by $\varepsilon_{r,stack}$ and height h by h_{eq} [27], [109] when:

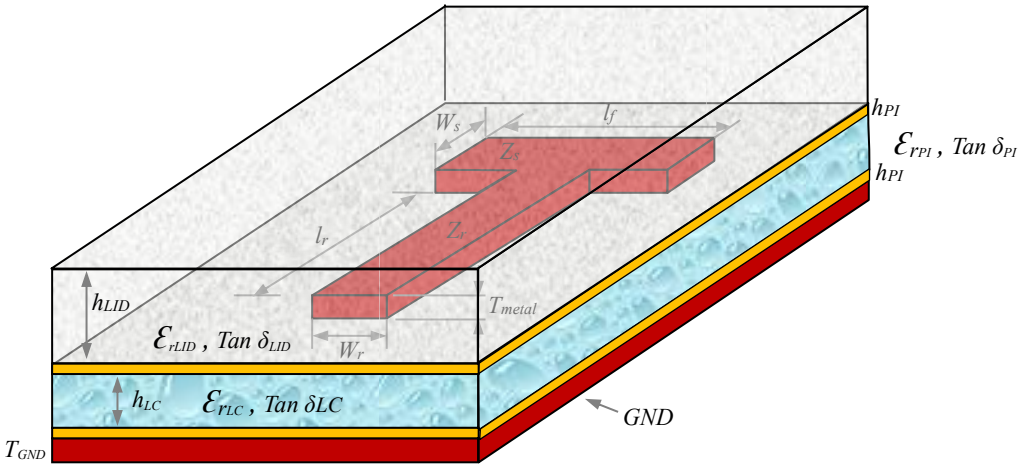

Fig 5.4 Inverted microstrip Structure

$$h_{eq} = h_{LC} + 2\,h_{PI}\ , \tag{5.13}$$

$$\varepsilon_{r,stack} \approx 1 + \frac{\varepsilon_b - 1}{2}\left(1 + \frac{12\,h_{eq}}{W}\right)^{-1/2} + [1 - \left(1 + \frac{12\,h_{eq}}{W}\right)]^{-1/2} F_{LID}\,(\varepsilon_{LID} - 1)\,, \tag{5.14}$$

where ε_b is the composite permittivity of the layer of substrates below microstrip and,

$$\varepsilon_b = \frac{2h_{PI} + h_{LC}}{\frac{2h_{PI}}{\varepsilon_{rPI}} + \frac{h_{LC}}{\varepsilon_{rLC}}}\ , \tag{5.15}$$

and F_{LID} is fringe field fraction that resides inside the lid of thickness h_{LID} and,

$$F_{LID} = 1 - \exp\,(-\pi\,\frac{h_{LID}}{W})\ . \tag{5.16}$$

The propagation of electromagnetic waves in a microstrip resonator is influenced not only by its electrical length and material parameters, but also significantly by its geometrical shape and termination. This is due to the fact that standing wave patterns, which determine the resonance behaviour, are formed as a result of wave reflection and interference, both of which are geometry-dependent. In a quarter-wavelength (λ/4) microstrip resonator, resonance occurs when the physical length of the resonator corresponds to one-quarter of the effective wavelength in the substrate medium. At this length, the structure supports a standing wave with

specific voltage and current distributions depending on whether it is short- or open-circuited at the end.

This can be intuitively understood by considering wave reflection. When an electromagnetic wave propagates along a microstrip line and encounters a discontinuity (e.g., an open or a short), part or all the wave is reflected. At resonance, the forward and reflected waves constructively interfere to form standing waves with fixed nodes and antinodes.

These standing wave patterns vary based on the termination:

- For a short-circuited stub, the voltage is zero at the short end (a node), and maximum at the open end (an antinode).
- For an open-circuited stub, the current is zero at the open end (a node), and maximum at the junction with the main line (an antinode).

These behaviours are shown in Fig 5.6, which illustrates the voltage and current waveforms along both short- and open-circuited λ/4 stubs. These stubs can be modelled as series or parallel RLC resonators depending on the boundary conditions, allowing them to provide band-stop or band-pass responses in periodic filters.

The periodic repetition of such resonators leads to a spatially periodic structure that supports wave interference effects, including Bragg reflection, thereby forming multiple frequency stopbands or passbands depending on the configuration. Understanding this fundamental wave behaviour is crucial for designing high-performance periodic microstrip filters. Any other lengths of microstrip transmission line are equivalent to a combination of inductive and/or capacitive elements (parallel or series), which can be added to the periodic stubs to achieve the required performance.

Example (60 GHz): using (5.6) - (5.12) for LC BL037 with $\varepsilon r \approx 2.3$ and a 50-Ω microstrip:

$$A = \frac{Z_r}{60}\left(\frac{\varepsilon_r + 1}{2}\right)^{\frac{1}{2}} + \frac{\varepsilon_r - 1}{\varepsilon_r + 1}\left(0.23 + \frac{0.11}{\varepsilon_r}\right) = 1.159092$$

$$A < 1.52 \rightarrow \frac{W}{h} = \frac{8e^{(A)}}{e^{(2A)} - 2} \quad ; \quad h = 0.2 \ \rightarrow W = 0.6251$$

$$W > h \rightarrow \varepsilon_{eff} = \frac{\varepsilon_r + 1}{2} + \frac{\varepsilon_r - 1}{2}\left(1 + \frac{12h}{W}\right)^{-1/2} = 1.8727$$

$$\lambda_{eff} = \frac{\lambda_0}{\sqrt{\varepsilon_{eff}}} = 3.653678 \rightarrow \frac{\lambda_{eff}}{2} = 1.825 \quad ; \frac{\lambda_{eff}}{4} = 0.912 \quad ; \frac{\lambda_{eff}}{8} = 0.456$$

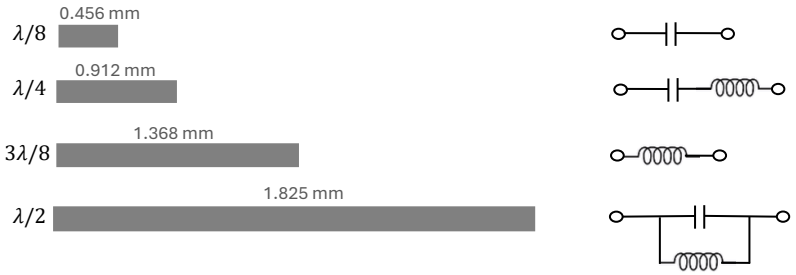

Fig 5.5 Equivalent circuits of multiple of λ/4 in 60GHz

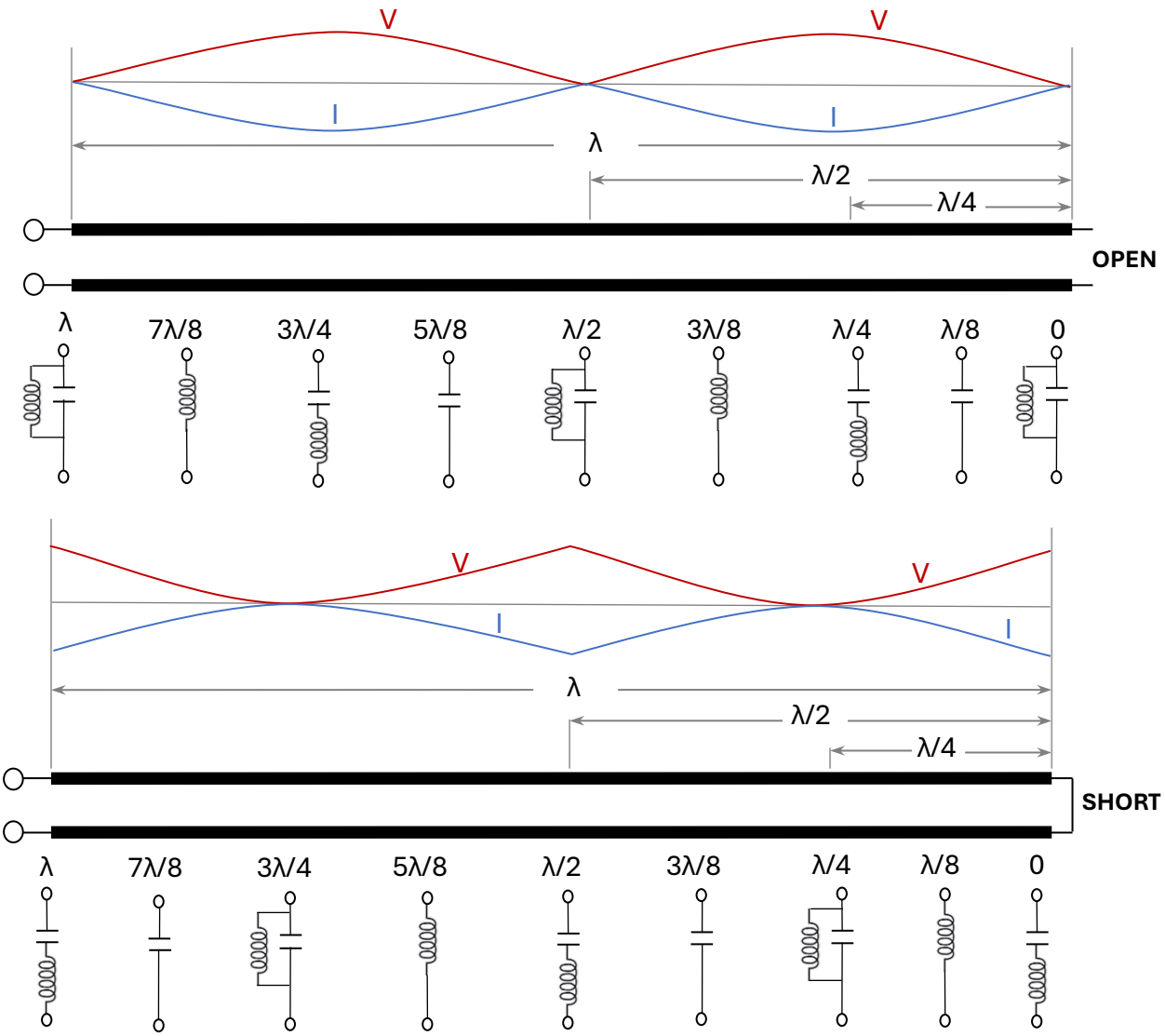

Fig 5.6 Voltage and current wave forms in λ/4 stubs

5.3 Cascade Structure of Multiple Resonators

Cascade structures formed by connecting several quarter-wave (λ/4) resonators or capacitive/inductive stubs in a transmission line create a periodic filter. The number of stubs determines the filter order and therefore the selectivity and stopband rejection of the response, while their spacing defines the width and position of the passband. The location of the feed line is especially important for symmetric structures, as it directly affects impedance matching and hence influences both the return loss and the achievable transmission gain [110]. A transmission line periodically loaded with λ/2 or λ/4 resonators or capacitive elements exhibits passband-stopband characteristics, acting as a bandpass filter. This behaviour is due to the propagation and reflection of electromagnetic waves, which vary with frequency [25] [111]. Fig 5.7 illustrates this periodic structure. Each unit cell consists of a transmission line segment of length $d/2$, a shunt susceptance element jb, and another $d/2$ segment. Cascading such unit cells builds the full structure [112].

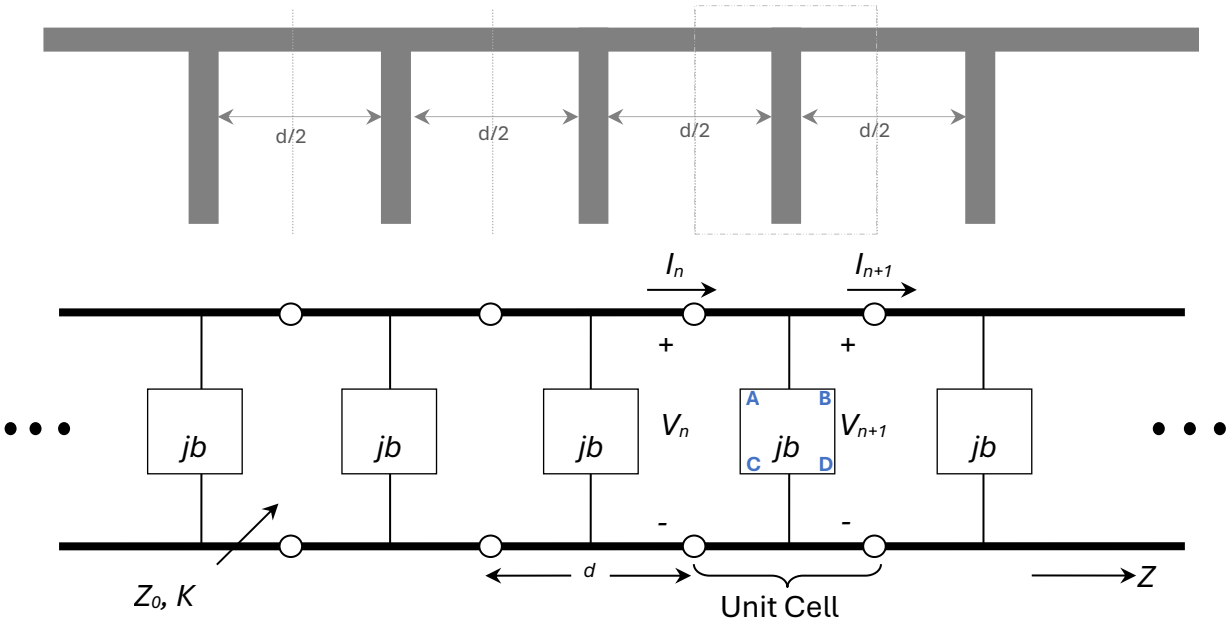

Fig 5.7 Periodic structure

According to the cascading rule, the signal propagation along a periodic structure, composed of a transmission line with susceptance b followed by another section of transmission line, can

be analysed by forming the ABCD matrix of a single unit cell and then applying it repeatedly to model the entire structure [27].

The ABCD matrix is an analysing tool for periodic transmission line in that the matrix elements are related to transmission line characteristics and defined as:

- A: Voltage scaling factor for the forward-traveling wave.
- B: Voltage scaling factor for the reverse-traveling wave.
- C: Current scaling factor for the forward-traveling wave.
- D: Current scaling factor for the reverse-traveling wave.

For uniform periodic structures, the ABCD matric of the entire structure can be calculated by cascading the ABCD matrixes of the unit cells.

The ABCD matrix for the voltage and current for node n to node n+1would be as follows:

$$\begin{bmatrix} V_n \\ I_n \end{bmatrix} = \begin{bmatrix} A & B \\ C & D \end{bmatrix} \begin{bmatrix} V_{n+1} \\ I_{n+1} \end{bmatrix}, \tag{5.17}$$

For the symmetric unit cell in Fig. 5.6 (line of length $d/2$, shunt susceptance jb, line of length $d/2$, with characteristic impedance Z_0 and phase delay $\theta=\beta d/2$ =kd/2, the ABCD matrix becomes [113]:

$$\begin{bmatrix} A & B \\ C & D \end{bmatrix} = \begin{bmatrix} \cos(2\theta) - \frac{b}{2}\sin(2\theta) & j\,Z_0[\sin(2\theta) - \frac{b}{2}(1-\cos(2\theta))] \\ j\,[\sin(2\theta) + \frac{b}{2}(1+\cos(2\theta))]/Z_0 & \cos(2\theta) - \frac{b}{2}\sin(2\theta) \end{bmatrix}. \tag{5.18}$$

Also, for a periodic structure which supports wave propagation, it is necessary for the voltage and current at each terminal to be same as the current and voltage of the adjacent terminal apart from a phase delay which happens because of propagation time over the length of transmission line section. Therefore, the voltage and currents at terminals n+1 and n are related as follows:

$$V_{n+1} = e^{-\gamma d} V_n \;\; ; \;\; I_{n+1} = e^{-\gamma d} I_n \,. \tag{5.19}$$

where $\gamma = \alpha + j\beta$ is the complex propagation constant and α is the attenuation constant and β is the propagation constant of the periodic structure. Matching ABCD matrix formulation with the phase shift expression yields:

$$\cos \mathrm{h}\, \gamma \mathrm{d} = \frac{(A+D)}{2} = \cos\theta - \frac{b}{2} sin\ \theta, \tag{5.20}$$

$$\cos \mathrm{h}\, \gamma d = \cos \mathrm{h}\, (\alpha + j\beta)d\,, \tag{5.21}$$

$$\cos \mathrm{h}\, \gamma d = \cos \mathrm{h}\, \alpha d\,.\cos\ \beta d + j\ \sin \mathrm{h}\, \alpha d\,.\sin\ \beta d = \cos\theta - \frac{b}{2} sin\ \theta. \tag{5.22}$$

This relationship determines whether a wave propagates (passband) or attenuates (stopband) based on the value of the right-hand side of the above equation is real, therefore the left-hand side should be also real. This is happening when:

1. **Pass band:** if $\alpha = 0$, and $\beta \neq 0$: the attenuation constant is zero and the wave propagates without attenuation and the periodic structure represents the bandpass feature of the structure, therefore:

$$\cos \beta d = \cos\theta - \frac{b}{2}\ sin\ \theta \leq 1 \tag{5.23}$$

The left-hand side of the above equation should be less than one, If the right-hand side becomes greater than one in magnitude, β cannot be real and propagation does not occur.

2. **Stopband:** if $\alpha \neq 0$, and $\beta = 0, \pi$: the propagation constant is not zero, the wave attenuates along the periodic structure. This property represents the stopband feature of the structure.

$$\cos h\, \alpha d = \left| \cos\theta - \frac{b}{2} \sin\theta \right| \geq 1 \tag{5.24}$$

These alternating propagation conditions across frequency result in the filter behaviour of periodic structures. These opposite behaviours happen in separate parts of frequency band therefore the periodic structure performs as a filter. That means that the frequency bands for which un-attenuated propagation takes place are separated by the frequency bands in which the wave is attenuated and therefore propagation is stopped.

The information of the periodic structure propagation can be plotted on a kd - βd plane. The formula is calculated for typical “b” values (unit structure susceptance) and plotted in Fig 5.8.

The band-pass region is for the frequency band where $cos\,(kd) - \frac{b}{2}\,sin\,(kd)$ is less than one and therefore there is a value for $cos\,\beta d$ and βd. These areas are shown in green bands in Fig 5.8. For the frequencies that cos kd – b/2 sin kd is larger than 1, there is no value for βd. These regions are shown in red. The kd - βd diagram also shows that the passbands and stopbands will be repeated in a periodic structure as frequency increases. The largest passband is the first one and as frequency increases, we have smaller passbands.

As shown in Fig 5.8 βd only has value for certain kd values. Quantity k is also known as wavenumber and is a function of frequency and β is the imaginary part of γ, the complex propagation constant. "k" represents the propagation characteristics of the line, regardless of its structure, but γ (and therefore β) represents actual behaviour of wave propagation alongside

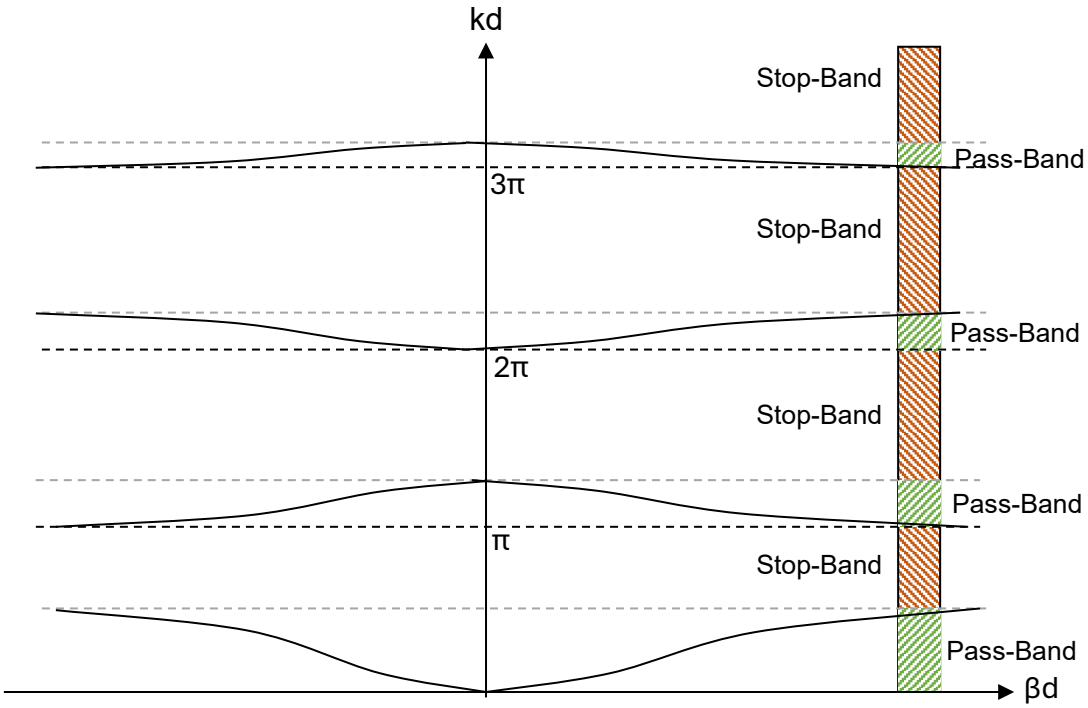

Fig 5.8 kd - βd diagram for a typical unit susceptance

the circuit or structure. When there is no value for β, it means that there is no propagation, or we are in the stop-band region.

To analyse the effect of the value of susceptance "b" in periodic structure as shown in Fig 5.7, a formula of propagations in periodic structures has been developed. By expressing the normalized susceptance as:

$$b = Bk \quad ; \quad B = cC_0Z_0 \quad ; \quad C_0 = \frac{0.67\,(\varepsilon_r + 1.41)}{Ln\,[\frac{5.98H}{0.8W + T}]}. \tag{5.25}$$

where c is speed of light (i.e. $3x10^8$ m/s)

By this replacement now B is independent from the frequency and only represents the impedance characteristics of the unit cell shunt susceptance. Z_0 is the characteristic impedance of periodic structure and C_0 is the unit capacitance of the shunt susceptance, where:

The propagation condition becomes:

$$\cos \beta d = \cos(kd) - B\,k\,\mathrm{Sin}\,(kd). \tag{5.26}$$

Fig 5.9 illustrates the βd-kd drawing is plotted based on the above assumptions and equations.

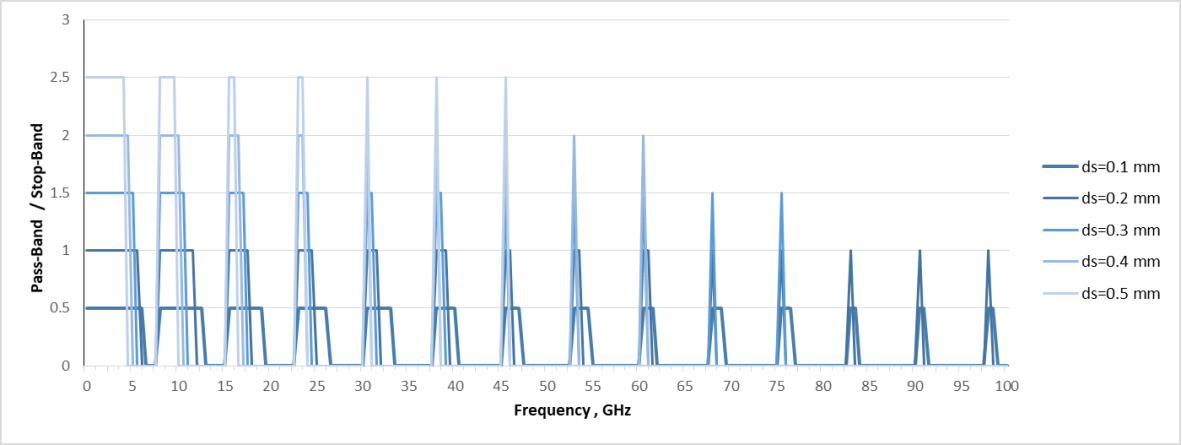

Fig 5.9 Passband and stop-band of periodic structure, for different susceptance values

As initial estimation of the value of "ds", length of microstrip stub (i.e. susceptance) is considered to be 0.1, 0.2, 0.3, 0.4 and 0.5 mm. This is based on the experiment results for the suitable stub length of resonators and circuits in 60 GHz.

The horizontal axes of the diagram represent the frequency of the transmitted signal. The plot is drawn using different values for ds which is the length of microstrip stub, the vertical axes show the band pass frequency area for different values of B. This drawing shows that the bandwidth of the filter in a periodic structure can be controlled by the value of capacitance of the shunt susceptance. Also as shown, the width of the passband reduces in higher frequencies.

The other approach to the theory of periodical structures is wave approach in that forward and backward propagating waves exist in each unit are analysed. This would be based on Bloch wave requirements concludes the same findings as above. The Bloch wave which can propagate in the periodic structure is made up from forward and backward propagating normal transmission-line or waveguide waves that exist between discontinuities.

The other characteristic of the periodic structures is the advantage of slow wave propagation. In a normal transmission line such as a coaxial cable the phase velocity is:

$$v_p = (LC)^{-1/2} = (\mu_0 \varepsilon_r \varepsilon_0)^{-1/2} \tag{5.27}$$

In a uniform line, reducing v_p requires increasing both L and C per unit length [107]. Since $LC=\mu_0\varepsilon$, increasing C automatically decreases the series inductance L. However, in a periodic structure an increase of shunt capacitance per unit length can be achieved without affecting the unit-line inductance L [114].

5.4 Terminated Periodic Structures

The periodic structure of Fig 5.7 and the above analysis of its behaviour is for an unloaded line with unlimited number of repeated cells. However, in practice such a structure would be terminated in a circuit. Fig 5.10 shows a terminated periodic structure.

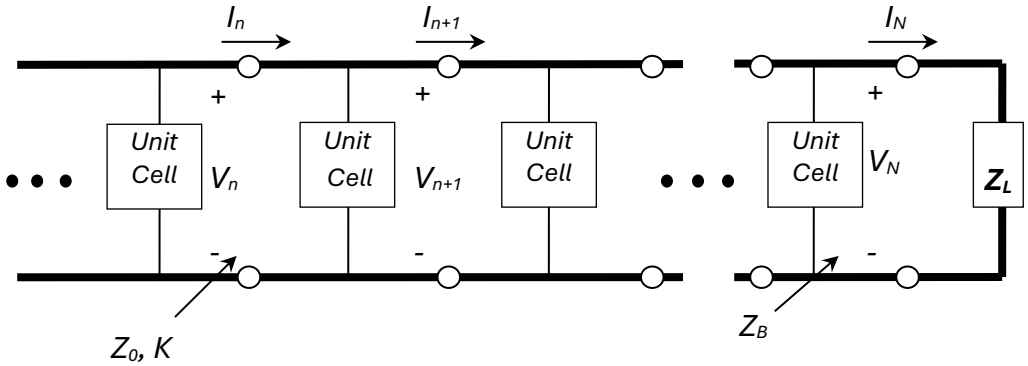

Fig 5.10 Periodic structure terminated by Z_L

The characteristic (Bloch) impedance of the periodic line can be defined from the voltage and current of the Bloch wave. Bloch impedances are used to study periodic-structure impedances

and characterize the interaction of waves with a periodic medium:

$$Z_B = \frac{V_n}{I_n} = \frac{V_{n+1}}{I_{n+1}} \ . \tag{5.28}$$

where Z_B is the Bloch impedance and a type of wave function for a particle in periodically repeating environment. Using the unit-cell ABCD matrix $[ABCD]$ (for the symmetric cell of Sec. 5.3, A=D) and replacing the values of V_{n+1} and I_{n+1} and solve the equation for $e^{\gamma d}$, we will have the following:

$$Z_B^{\pm} = \frac{\pm B}{\sqrt{A^2 - 1}} \ . \tag{5.29}$$

The positive or negative solutions (i.e. ±) relates to traveling wave sign of I_n. The value of $B = [sin(2\theta) - \frac{b}{2}(1 - \cos(2\theta)]$ is always imaginary.

- In the Passband region, ($\alpha = 0$ and $\beta \neq 0$): $Cosh\ \gamma d = A \leq 1$ → Z_B is real.
- In the Stopband region ($\alpha \neq 0$ and $\beta = 0$): $Cosh\ \gamma d = A \geq 1$ → Z_B is imaginary.

In the terminated periodic structure of Fig 5.10, the reflection coefficient at load can be defined as the ratio of forward (i.e. positive) and reverse (i.e. negative) voltage signal and for symmetrical structure would be as follows:

$$\Gamma = \frac{z_L - z_B}{z_L + z_B}. \tag{5.30}$$

The reflection coefficient is zero when $Z_L = Z_B$, therefore in a lossless periodic structure the load impedance should be equal to Bloch Impedance (which is real value) to avoid reflection in passband region. With the load matched to the Bloch impedance, the terminated periodic structure exhibits the same passband/stopband behaviour as the ideal infinite case. A quarter-wavelength transformer may also be used to realize the match where appropriate [31], [115]. The passband and stopband characteristic of a periodic structure will be maintained as long as it is terminated to match impedances equal to the line Bloch impedance. Even though the number of unit cells affects the overall structure (e.g., cut-off frequencies, insertion loss,

bandwidth), the periodic nature ensures filtering properties are preserved if symmetry and impedance matching are maintained [25] [36].

5.5 Theoretical Analysis of Periodic Structures

The behaviour of a periodic microstrip filter can be analytically predicted by studying its fundamental unit cell. Since the overall characteristics of the periodic structure stem from the repeated elements, the dispersion relation and filter performance are tightly coupled with the design of the unit element. As the number of repeated cells increases, the sharpness of the passbands and stopbands becomes more prominent, highlighting the importance of unit cell optimization. The practical experiments prove that the passband characteristics of the filter happens on the frequency range where the impedance of the filter is matched with the line impedance which is typically 50 Ohm. As the repeated stubs are formed from the combination of microstrip discontinuities, therefore, to analyse the behaviour of the stubs which act as the periodic structure unit cells, the impedance of the stubs should be determined based on the dimensions of microstrip parts forming the stubs. Another approach will be also to model the structure using the circuit equivalent of the discontinuities.

In periodic microstrip filters, repeated open-circuited stubs are often formed by combinations of microstrip discontinuities such as T-junctions, steps, and crossovers. These discontinuities behave as reactive components and can be modelled using lumped-element equivalent circuits, as shown in Fig 5.11. This is a typical equivalent circuit models for an open stub, a step discontinuity, and a crossover junction using series inductors and shunt capacitors or vice versa.

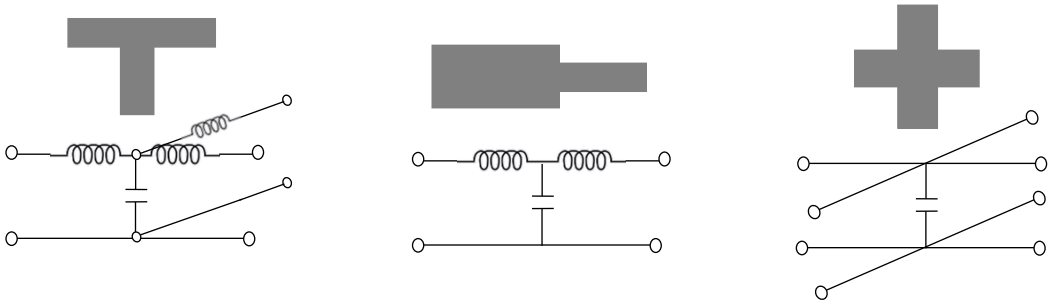

Fig 5.11 Equivalent circuits of open stub, step and crossover microstrip discontinuities

The above shown microstrip discontinuities are the fundamental elements of complex such as periodic filters therefore it is important to understand frequency dependant properties of the reflection and transmission of each element.

These basic discontinuities serve as building blocks for complex periodic structures. Understanding the frequency-dependent reflection and transmission behaviour of these elements is crucial in predicting the response of the entire filter.

Several methods are used to model the equivalent circuit of the discontinuities to calculate the properties, such as Babinet's principle, calculations using capacitance of the microstrip discontinuities [116] [117] [118] [119], or inductive elements of the circuits [120] [121] [122]. The properties of the complex microstrip circuits which are formed from discontinuities, can be determined using the energy stored in higher order cut off modes of microstrip lines [123] and [124]. For the purpose of our calculation, we only study less complex structures with symmetrical dimensions.

In a microstrip circuit, the effective width of the microstrip and the effective permittivity ε_{eff} of the substrate are frequency dependent. Using the characteristic impedance, the effective width can be calculated knowing the ε_{eff} of the dielectric substrate. It is assumed that the height of the substrate is so small that the electrical fields is independent of the y coordinate.

In a method suggested in [125], a microstrip discontinuity is divided to different regions for each an effective substrate permittivity can be defined. An example is shown in Fig 5.12 for a non-symmetrical microstrip T junction which is divided to regions I, II, III and IV. The regions I, II, and III are microstrips with effective substrate permittivity ε_{eff1}, ε_{eff2} and ε_{eff3} or the three microstrip lines. For the calculation of the effective dielectric constant of region IV it would be considered that the electric standing field is only available at edges with no connection [126]. The electric fields of regions I, II and II need to be matched to the field of region IV, which is then the component of all regions can be calculated.

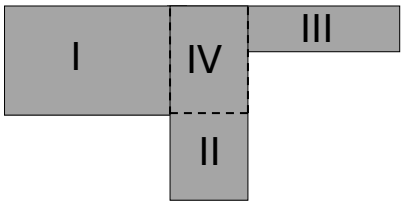

Fig 5.12 Non-symmetrical microstrip T-junction

The stubs used for the design of periodic filters are periodic and less complex than the non-symmetrical microstrip discontinuity of Fig 5.12. The free end of the stub in periodic structures are left open-circuit. Neglecting microstrip line losses, the input impedance of microstrip open-ended stub depends on its electrical length is purely reactive; either capacitive or inductive. That is the reason of stubs function as resonators. The input impedance of a lossless open circuit and short-circuit stub is given by [16]:

$$Z_{OC} = -jZ_0 \cot(\beta\, l)\ ,\ Z_{SC} = jZ_0 \tan(\beta\, l) \tag{5.31}$$

Depending on whether the tangent/cotangent is positive or negative, the stub behaves as an inductor or capacitor, respectively. Thus, stubs can be tuned to resonate at a desired frequency. To synthesize a required inductance L or capacitance C, the length of the stub is calculated as:

- If an inductive stub of inductor L is needed, then the length of the stub should be:

$$\omega l = Z_0 \tan(\beta\, l) \ \rightarrow l = \frac{1}{\beta}\left[arc\ tan\ \frac{\omega L}{Z_0}\right], \tag{5.32}$$

- If a capacitive stub of capacitor C is needed, then the length of the stub should be:

$$\frac{1}{\omega C} = -Z_0 \cot(\beta\, l) \rightarrow\ l = \frac{1}{\beta}\left[arc\ tan\ \omega C Z_0\right]. \tag{5.33}$$

These relations allow a desired capacitance or inductance to be obtained for a microstrip stub used in a periodic structure.

5.6 Control of Periodic-Structure Parameters

For the practical design and implementation of periodic structures with desired filtering characteristics, it is essential to understand how various parameters influence the structure's electromagnetic behaviour. These parameters directly affect key filter properties such as centre

frequency, bandwidth, insertion loss, ripple, and stopband attenuation. By analysing the transmission coefficients and wave interaction mechanisms within periodic structures, designers can designers can precisely tailor filters for specific performance goals.

As shown in the previous sections, a periodic structure made of repeated unit cells functions as a bandpass filter, exhibiting passband-stopband behaviour due to the alternating propagation and attenuation of Bloch waves. The spatial modulation of microstrip characteristics results in a frequency-selective response [115].

However, the ideal periodicity of unit cells can introduce significant ripple within the passband, caused by reflections at the boundaries and discontinuities between cells. To mitigate these ripples, tapering techniques are sometimes applied, where the physical or electrical properties of unit cells (such as impedance or width) are gradually varied. As reported in experimental studies, tapering can reduce passband ripple and improve impedance matching at the input/output ports [25], [127], [128]. “Tapering” refers to gradually changing the dimensions or properties of a transmission line, and it is often used as a technique to minimize or eliminate ripples. In the present design, tapering was not implemented because the primary aim was to study the intrinsic dispersion and tunability of strictly periodic unit cells on a liquid-crystal substrate. Introducing tapering would change the periodicity, complicate the Bloch-wave analysis, and mask the sensitivity enhancement effects that are central to this research. Instead, impedance matching (S_{11}) was addressed through careful design of the unit-cell geometry and choice of feed structure, ensuring that the evaluation of periodic tuning effects remained isolated from additional tapering optimisation.

To model and optimize periodic structures, each unit cell can be decomposed into simpler lumped or distributed elements, such as series inductances and shunt capacitances, to derive an equivalent circuit. This modelling helps determine transmission coefficients (S-parameters) and calculate propagation constants ($\gamma = \alpha + j\beta$) across the structure.

A key point in tuning the filter characteristics is understanding how the impedance profile of the unit cell affects the dispersion relation and consequently the position and width of passbands and stopbands. The periodic structure supports wave propagation (passband) when the Bloch impedance is real and becomes reflective (stopband) when it is imaginary [111], [107]. This is expressed in formulas (5.19) and (5.20).

The following subsections will elaborate on how the four major parameters, (1) feed line impedance, (2) unit cell impedance, (3) spacing between unit cells, and (4) number of repeated unit cells, affect the filter performance. These design parameters provide a multi-dimensional control space for tailoring periodic filters to meet specific frequency-domain requirements in microwave and millimetre-wave systems.

Passband ripple in periodic microstrip filters arises primarily from multiple internal reflections between repeated unit cells and from impedance mismatch between the external feed line and the Bloch impedance of the periodic structure. Because the structure is finite, truncation of an otherwise infinite periodic lattice introduces standing-wave effects that manifest as amplitude ripple within the passband. The magnitude of this ripple is therefore governed by the strength of inter-cell reflections, the quality of feed-to-structure matching, and the number of unit cells. Ripple reduction can be achieved through several complementary design strategies. First, matching the feeder transmission line impedance to the Bloch impedance at the passband centre minimises input reflections and suppresses standing-wave formation. Second, appropriate choice of unit-cell impedance ratios and inter-cell spacing controls the dispersion slope and reduces reflection strength within the passband. Third, increasing the number of unit cells averages out residual reflections, leading to improved passband flatness at the expense of increased size and group delay. Tapering or apodisation of unit-cell parameters is also a well-known ripple-suppression technique; however, it intentionally breaks strict periodicity and complicates Bloch-wave analysis. For this reason, tapering was not adopted in this work, as

the objective was to isolate and study the intrinsic dispersion and tunability properties of strictly periodic LC-loaded unit cells.

5.6.1 Impedance of Feeder Transmission Line

The performance of a periodic microstrip structure is highly sensitive to the characteristic impedance of the feed line, particularly at the input and output ports. The feed line impedance (typically denoted Z_0) plays a crucial role in determining the matching condition, reflection, and transmission efficiency of the filter. In periodic structures, wave propagation is governed by Bloch theory, and the impedance seen at the boundary of the structure is the Bloch impedance Z_B. maximum power transfer (i.e., zero reflection) is achieved only when Z_B=Z_0. Any mismatch between the feed line impedance and the Bloch impedance leads to in-band reflection, degraded return loss, and ripples in the passband. If $Z_0 \neq Z_B$, even within the passband of the periodic filter where Z_B is real, a non-zero reflection coefficient introduces standing waves and undesired ripple in the transmission response S_{21}. This is particularly important in narrowband filters, where even slight mismatches can distort the filter response.

In practice, the choice of feed line impedance not only affects impedance matching but also controls the effective length and coupling of the stubs. For example, a lower feed line impedance increases capacitive loading [129], potentially narrowing the passband If the Bloch impedance is inherently different due to substrate choice, periodic spacing, or stub geometry, a matching section (e.g., a quarter-wave transformer or tapered transition) must be designed to ensure that:

$$Z_{match}^2 = Z_0 Z_B \ . \tag{5.34}$$

This ensures broadband impedance matching at the interface between the feed and the periodic structure.

5.6.2 Impedance of Unit Cells

The unit cell impedance of a periodic structure plays a critical role in defining the dispersion properties, passband/stopband behaviour, and overall filter performance. Each unit cell typically consists of a combination of microstrip transmission lines and discontinuities (e.g., stubs, steps, junctions), which together determine its impedance profile. A unit cell with a lower impedance (e.g., due to larger shunt capacitance or narrower transmission lines) will shift the bandgap lower and narrow the passband, whereas a higher impedance cell (e.g., with wider lines or lower shunt capacitance) will broaden the passband and raise the cut-off frequency.

To avoid reflection at the feed interface and within the cascade, the impedance of the unit cell must be matched to the feed line impedance which (i.e., Z_B). The impedance ratio between the stub and the main line defines the selectivity and slope of the band edges [130]. Lower impedance stubs support slow-wave propagation, allowing for filter miniaturization at the cost of narrower bandwidth [28].

5.6.3 Spacing Between Unit Cells

In periodic microstrip filters, the spacing between unit cells, typically referring to the length of the transmission line segment between discontinuities or stubs, directly affects the electrical length, phase shift, and dispersion behaviour of the overall structure. It controls both he passband-stopband transition and the frequency positioning of Bragg resonances, thereby influencing the filter's bandwidth, cutoff characteristics, and rejection levels. In a periodic structure the phase delay between adjacent cells is denoted by:

$$\theta = \beta d = \frac{2\pi f d}{v_p} \equiv kd\,, \tag{5.35}$$

where:

- θ is the phase shift across the inter-cell spacing,
- d is the physical spacing (length) between adjacent cells,

- $k = \beta = \omega\sqrt{\mu\varepsilon_{eff}}$ is the wave number,
- v_p is the phase velocity on the microstrip line.

The dispersion relation of the periodic structure will follow formula (5.22). The inter-cell spacing d appears as a periodic argument in both trigonometric functions, showing its strong influence on bandwidth, centre frequency, and location of stopbands.

The Bragg condition, where reflection causes a stopband, occurs approximately when the phase shift between cells equals π, therefore, for Bragg frequency f_B:

$$kd = \pi \Longrightarrow f_B = \frac{v_p}{2d}. \tag{5.36}$$

Thus, increasing d shifts the Bragg (cutoff) frequency lower, while decreasing d shifts it higher. Larger spacing leads to sharper band edges and potentially narrower passbands, while smaller spacing can result in wider passbands but with reduced selectivity [115]. Reducing inter-cell spacing is a common strategy to miniaturize filters, but this can cause weaker stopband suppression and increased coupling between neighbouring stubs if spacing becomes too tight. Proper spacing helps suppress spurious bands. Very small spacing increases coupling between neighbouring stubs and may introduce parasitic resonances [25], [30].

5.6.4 Number of Unit Cells

The performance of a periodic microstrip filter is strongly influenced by the number of repeated unit cells. While the unit cell defines the local response (i.e., dispersion and impedance characteristics), the number of repetitions determines the global filter characteristics such as stopband attenuation, passband ripple, transition sharpness, and filter selectivity.

Let the total number of unit cells in the periodic structure be denoted by N. For a symmetric and lossless periodic filter, increasing N leads to the following effects:

Sharpening of Passband–Stopband Transitions: The attenuation constant α in the stopband governs the exponential decay of the wave along the periodic structure. The transmission coefficient T is given by:

$$| T | \approx e^{-\alpha N d} \tag{5.37}$$

where d is the unit cell length, and Nd is the total filter length. As N increases, the suppression in the stopband becomes exponentially stronger. This results in steeper roll-off at the band edges and higher out-of-band rejection [36].

Increase in Stopband Attenuation: The stopband rejection improves approximately by 20x log of ratio in dB per doubling of N in ideal cases. For example, comparing 5- and 10-unit cells the rejection improvement is 6 dB in stopband attenuation at a given frequency point within the stopband.

Widening of Effective Passband Flatness: While the centre frequency and band edges are defined by the unit cell's dispersion relation, increasing the number of cells reduces passband ripple and allows a flatter transmission within the passband, since multiple reflections between unit cells average out [128].

Beside the above mentioned which can be considered as positive impact, more N also have negative effects, one of them increase in group delay and selectivity. More cells contribute to phase accumulation, impacting group delay. With higher N, the group delay increases, enhancing selectivity but also increasing signal latency. Therefore, while increasing N improves selectivity and stopband rejection, it also increases the circuit size, group delay, and fabrication sensitivity. Therefore, in practical design, the number of unit cells is optimized based on system-level constraints such as bandwidth, insertion loss, and physical area.

5.7 Stepped-Impedance Resonator (SIR) Analysis

One of the recently developed approaches to design and characterise of unit cells for periodic filters is to use stepped impedance resonators (SIR) stubs on a microstrip line [131]. Sharp

rejection and spurious suppression are reported in band pass filters with high performance in [132] and [133]. Wideband bandpass and band stop filters using SIR are reported in [134]. Filters with SIR stubs are designed and reported widely in [135], [136], [137], [138], [139], [140], [141], [142], [143]. The main design concept used is to determine and control the input admittance of a unit cell and control microstrip dimensions of SIR stubs (i.e. length and widths of SIR sections) to obtain the required characteristics for the desired stub resonate frequencies. The input admittance of the structure is zero on the resonate frequencies. The philosophy behind this analyse is to calculate the electrical length and therefore physical lengths of the microstrip conductors for different parts of SIR, for the given desired frequencies and impedances.

The admittance values are reciprocal of impedances and can be calculated by $Y_0 = 1/ Z_0$ and Z_0 can be calculated from the following formulas:

$$Z_0 = \begin{cases} \dfrac{60}{\sqrt{\varepsilon_{eff}}} \ln\left(8\dfrac{H}{W} + 0.25\,\dfrac{W}{H}\right)(\Omega) & when \quad W \le H \\ \dfrac{120\,\pi}{\sqrt{\varepsilon_{eff}}\,x\,\left[\dfrac{W}{H} + 1.393 + \dfrac{2}{3}\ln\left(\dfrac{W}{H} + 1.444\right)\right]}\ (\Omega) & when \quad W \ge H \end{cases} \tag{5.38}$$

Assuming the fixed value for substrate height (i.e. H) in microstrip circuits the design parameter for specific impedance (and admittance) will be microstrip conductor width (i.e. W). The graphs of Fig 5.13 show the changes of characteristic impedance and admittance of a microstrip transmission lines for different substrate permittivity and for a fixed substrate height which is assumed to be 0.2 mm.

$$Y_{open} = -j\,Y_0\,\tan\theta \tag{5.39}$$

$$Y_{close} = -j\,Y_0\,\cot\theta \tag{5.40}$$

where Y_0 is the characteristic admittance and θ is the electrical length of the microstrip conductor. When a transmission line with characteristic admittance Y_0 is terminated with a load admittance Y_L then the input admittance of the circuit can be calculated as:)

$$= Y_0 \frac{Y_L + \mathrm{j}\, Y_0 \tan\theta}{Y_0 + j\, Y_L \tan\theta} \tag{5.41}$$

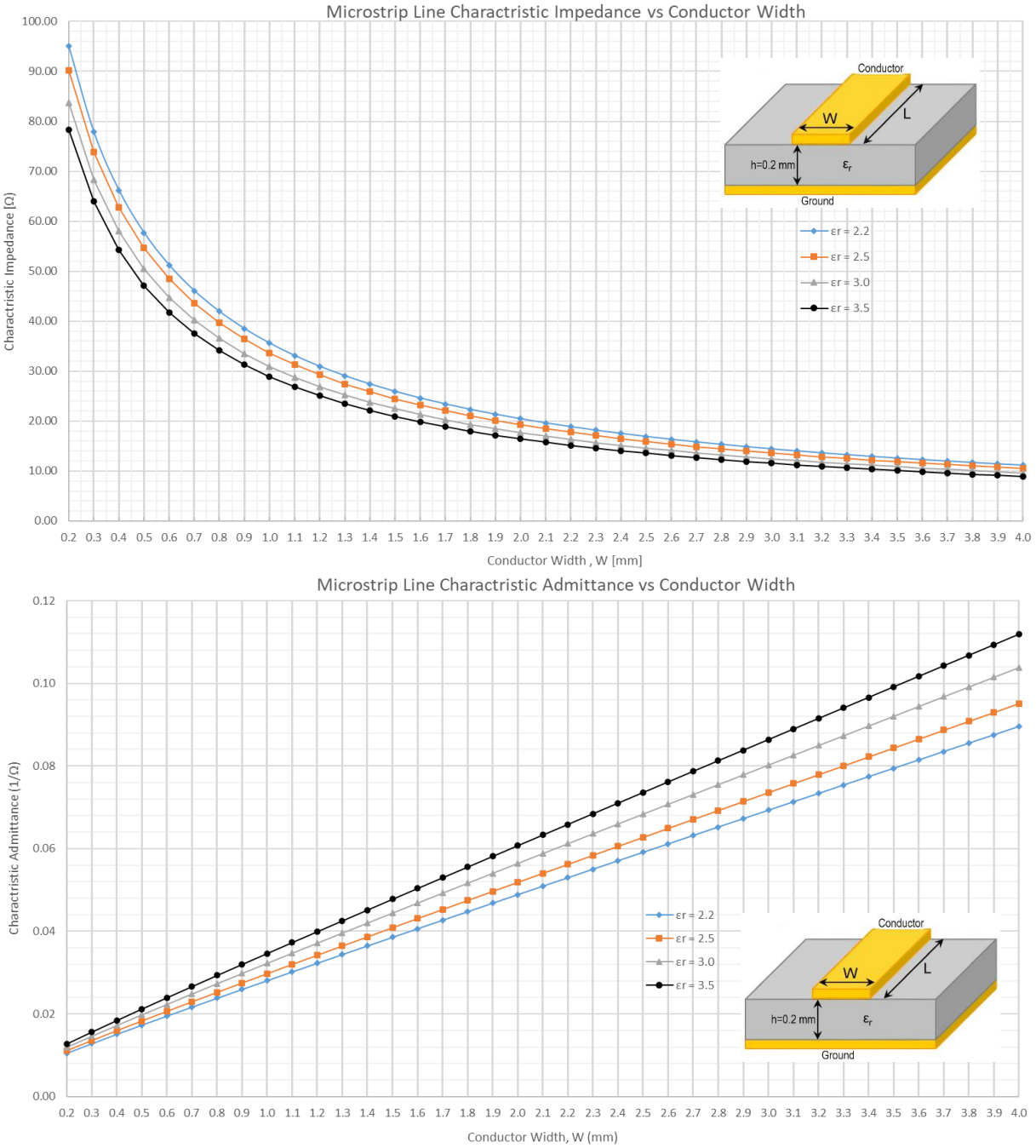

Fig 5.13 Microstrip stub impedance and admittance with different permittivity's

5.7.1 Odd-Even Analysis of Symmetric Structures

The unit cells of periodic structures can be symmetrical. In symmetrical transmission lines the mode of propagation can be modelled as a combination of two fundamental even and odd modes in the microstrip line [144]. The even and odd mode technique can be used to study and analyse of the structure characteristics. In odd mode which is an electric current distribution analysis the direction of current will be studied based on a hypothetical electrical wall on structure symmetry line while in Even mode which is a magnetic current distribution analysis the current flow direction will be characterised based on a magnetic wall in structure symmetry line (Fig 5.14).

These analyses help to find the characteristic impedance (and therefore admittance) of the structure. This will be a key important parameter for microstrip circuit designs. Odd and even mode characteristic impedances are normally different.

The odd and even mode analysis are widely used for SIR structures to determine the resonant frequencies of the filter. Basically, the even mode (i.e. magnetic current) is the symmetric mode, and the odd mode (i.e. electric current) is the anti-symmetric mode therefore the even mode impedance is the impedance seen by a wave propagating due to a symmetric excitation is, while the odd mode impedance is the impedance seen by a wave propagating of an anti-symmetric excitation.

Different unit cells using SIR stubs are analysed in the following sections and experimental simulations for the relevant designed periodic filters are provided in chapter 6.

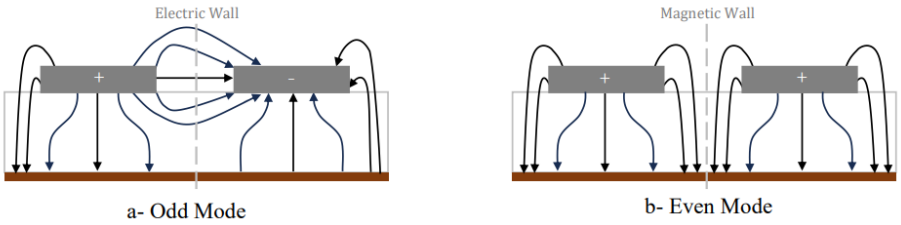

Fig 5.14 Odd-Even mode current distributions

Sections 5.7.2-5.7.6 present odd–even (OE) mode analysis for a set of symmetric periodic unit-cell topologies with increasing structural complexity, including single-stub, multi-SIR, balanced, and unbalanced configurations. The purpose of this section is not to introduce independent filter designs for each topology, but to demonstrate the generality and scalability of the OE analytical framework when applied to periodic microstrip unit cells. Several of these analyzed structures are subsequently instantiated in the designed periodic filters presented later in this thesis (Topologies 1–3), while others are included to establish analytical completeness, design intuition, and extensibility of the proposed synthesis workflow to future unit-cell variants.

5.7.2 Single Stub Odd-Even Mode Analysis

In the symmetrical unit cell of Fig 5.15, the even / odd mode analysis can be followed. The unit cell includes the source line and a resonator stub. The odd mode and even mode circuits of the symmetric structure are depicted in Fig 5.15-b and c. The characteristic admittance of different sections can be calculated from the widths of microstrip conductor and the electrical length θ of each section can be calculated from the physical length of conductor line.

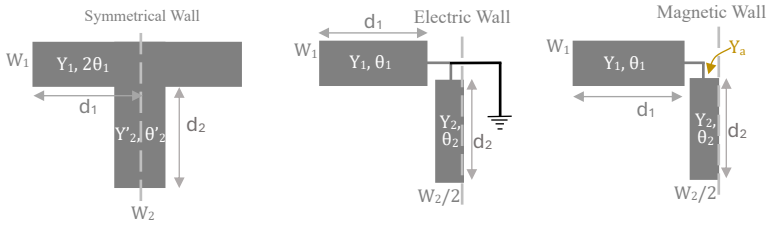

a- Unit Cell b- Odd Mode c- Even mode

Fig 5.15 Single Stub Odd-Even Analysis

Note: Y'_2 and θ'_2 are admittance and electrical length for full conductor width W_2 and Y_2 and θ_2 are for half conductor width $W_2/2$

For odd mode excitation when the equivalent circuit is terminated to a short circuit at the symmetrical line, the input admittance of the circuit is:

$$Y_{in,odd} = -\,j\,Y_1\,\cot\theta_1\,, \tag{5.42}$$

For even mode, the input admittance of the open symmetrical line is:

$$\begin{cases} Y_{in,even} = Y_1 \dfrac{Y_a + \mathrm{j}\,\mathrm{Y}_1 \tan\theta_1}{\mathrm{Y}_1 + j\,Y_a \tan\theta_1} \\ Y_a = j\,Y_2\,\tan\theta_2 \end{cases}. \tag{5.43}$$

At resonating frequencies $Y_{in,even}$ and $Y_{in,odd}$ are zero therefore:

$$Y_{in,odd} = 0 \;\rightarrow \cot\theta_1 = 0 \rightarrow\; \theta_1 = \beta d_1 = \frac{2n+1}{2}\,\pi \;\; (n = 0, 1, 2\,\ldots)\,, \tag{5.44}$$

by replacing the formula of propagation constant β:

$$\beta = \frac{2\pi}{\lambda_g} \;\Rightarrow\; d_1 = \frac{2n+1}{4}\,\lambda_g = (2n+1)\frac{\lambda_g}{4} \quad (n = 0, 1, 2, \ldots)\,. \tag{5.45}$$

Which is an expected result as resonation happens on each odd multiply of the quarter of effective wavelength.

The resonate frequency of odd mode excitation can be calculated as follows:

$$\lambda_g = \frac{4}{2n+1}\,d_1\,;\; f_{o1} = \frac{c}{\lambda_g} = \frac{2n+1}{4d_1}\,c\,;\; d_1 = \frac{2n+1}{4f_{o1}}\,c \quad (n = 0, 1, 2, \ldots)\,. \tag{5.46}$$

By choosing a value for d_1 the resonate frequencies for the odd mode can be determined. For example, when d_1=1.25 mm, the odd resonate frequency will be 60GHz.

From equation (5.43) for resonation in even mode:

$$\begin{cases} Y_{in,even} = 0 \rightarrow\; Y_2 + Y_1 \tan\theta_1 \cot\theta_2 = 0 \\ K_1 = \dfrac{Y_1}{Y_2} = -\,\cot\theta_1 \tan\theta_2 \;\rightarrow\; \tan\theta_2 = -\,\mathrm{K}_1 \tan\theta_1 \\ \cot\theta_2 = 0 \;\Rightarrow\; \theta_2 = \beta d_2 = \dfrac{2\mathrm{n}+1}{2}\,\pi \quad (\mathrm{n} = 0, 1, 2, \ldots.) \end{cases}. \tag{5.47}$$

Therefore, the length of the stub should be also an odd multiple of effective wavelength for the structure to resonate on given frequency in even mode. The stub length d_2 determines the even resonate frequency, for example for an even resonate frequency of 65GHz, d_2 will be 1.153mm.

5.7.3 Single and Multi-SIR, Single-Stub Odd-Even Mode Analysis

The unit cell of Fig 5.16 and Fig 5.17 are symmetrical and therefore odd-even mode analysis can be followed. The unit cell includes the source line and a stub of stepped impedance resonator (SIR). The odd mode and even mode circuits of the symmetric structure are depicted in Fig 5.16-b/c and Fig 5.17. The characteristic admittance of different sections can be calculated from the widths of microstrip conductor and the electrical length θ of each section can be calculated from the physical length of conductor line.

For odd mode resonation the same formula of (5.42) applies to both these unit cell structures. For even mode analysis, calculations and analysis of the conditions for the resonation are provided in Appendix B

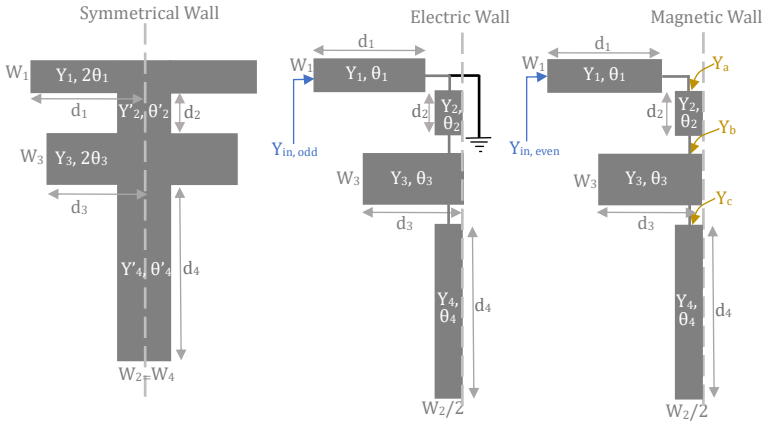

Fig 5.16 Single SIR Stub Odd-Even Analysis

Note: Y'_n and θ'_n are admittance and electrical length for full conductor width and Y_n and θ_n are for half conductor width

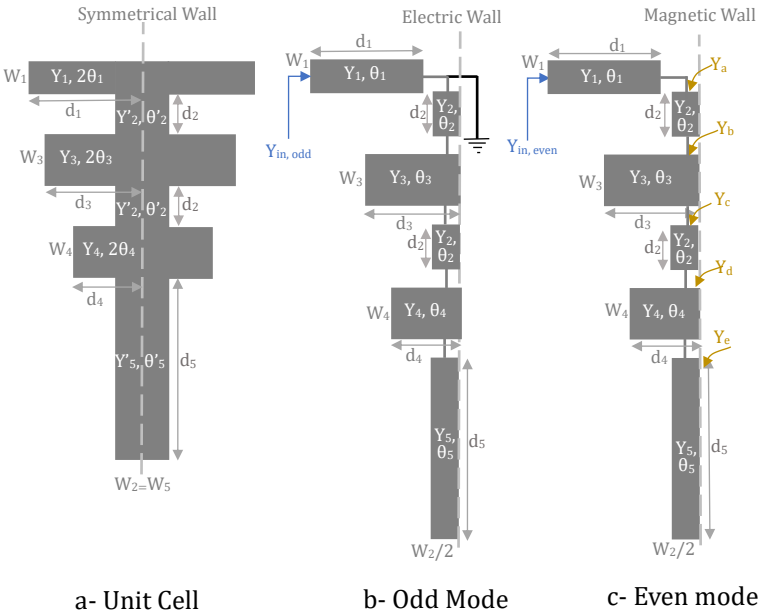

a- Unit Cell b- Odd Mode c- Even mode

Fig 5.17 Multiple SIR Single Stub Odd-Even Analysis

Note: Y'_n and θ'_n are admittance and electrical length for full conductor width and Y_n and θ_n are for half conductor width

5.7.4 Double-Balanced Stub Odd-Even Mode Analysis

With a similar concept as analysed for even/odd modes for previous unit cell structures, Fig 5.18 shows the odd mode and even mode of the unit cell structure, for odd mode resonation the formula (5.42) applies to this unit cell structure:

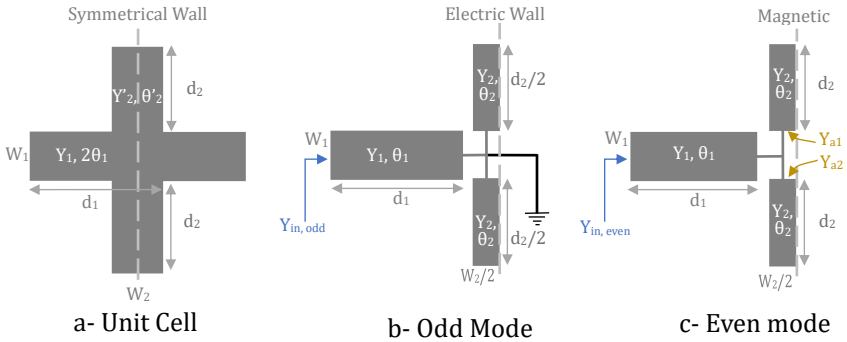

a- Unit Cell b- Odd Mode c- Even mode

Fig 5.18 Double Balance Stub Odd-Even Mode

Note: Y'_n and θ'_n are admittance and electrical length for full conductor width and Y_n and θ_n are for half conductor width

$$Y_{in,even} = Y_1 \frac{Y_a + \mathrm{j}\, Y_1 \tan\theta_1}{Y_1 + j\, Y_a \tan\theta_1}, \tag{5.48}$$

$$Y_a = Y_{a1} + Y_{a2} = j\, Y_2 \tan\theta_2 + j\, Y_2 \tan\theta_2 = j\, 2\, Y_2 \tan\theta_2 . \tag{5.49}$$

5.7.5 Double-Balanced, Multi-SIR Stub Odd-Even Mode Analysis

Similar structures of unit cells with balanced stepped impedance resonators on both sides of transmission line are illustrated in Fig 5.19 and Fig 5.20. The odd modes analysis of both these structures will be similar as discussed before in formula (5.42). The even mode analysis are provided in Appendix B.

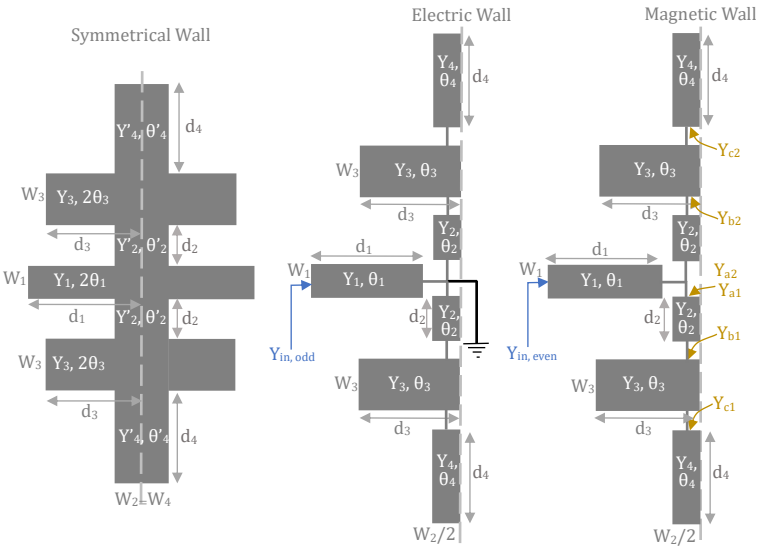

a- Unit Cell b- Odd Mode c- Even mode

Fig 5.19 Double balance multiple SIR stub odd-even mode analysis

Note: Y'_n and θ'_n are admittance and electrical length for full conductor width and Y_n and θ_n are for half conductor width

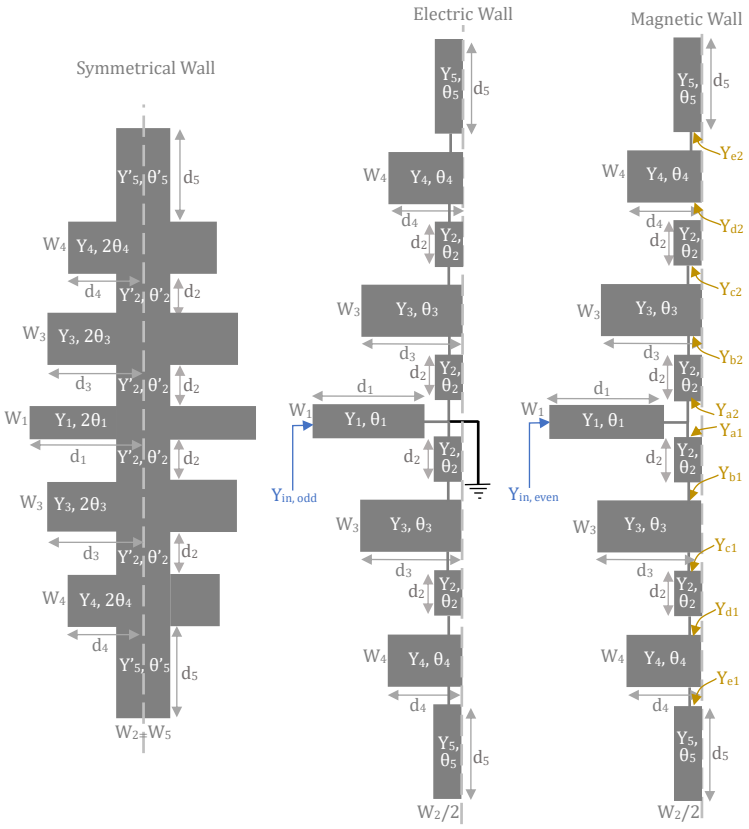

a- Unit Cell b- Odd Mode c- Even mode

Fig 5.20 Multiple balance SIR stub odd-even mode analysis

Note: Y'_n and θ'_n are admittance and electrical length for full conductor width and Y_n and θ_n are for half conductor width

5.7.6 Double-Unbalanced Stub Odd-Even Mode Analysis

This unit cell has two non-identical stubs in two top and bottom sides, but still the structure is symmetrical and odd-even mode analysis can be used. For odd mode resonation the formula (5.42) applies to this unit cell structure for even mode:

$$Y_{in,even} = Y_1 \frac{Y_a + \mathrm{j}\, Y_1 \tan\theta_1}{Y_1 + j\, Y_a \tan\theta_1} \tag{5.50}$$

$$\begin{cases} Y_a = Y_{a1} + Y_{a2} \\ Y_{a1} = jY_2 \tan\theta_2 \\ Y_{a2} = jY_3 \tan\theta_3 \end{cases} \tag{5.51}$$

Another symmetrical unit cell structure with different stubs in top and bottom sides is shown in Fig 5.22 .

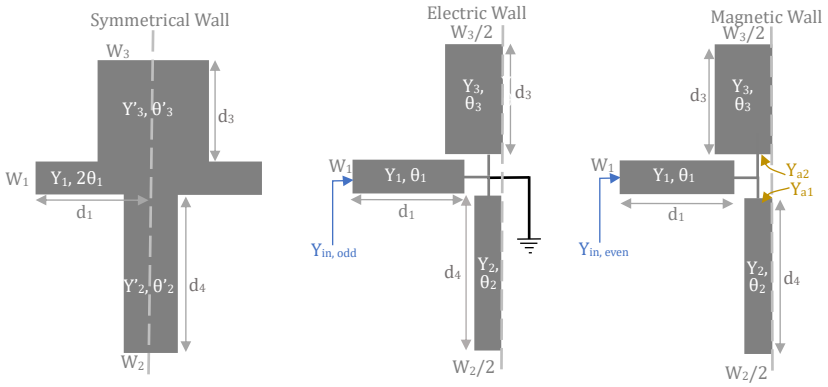

a- Unit Cell b- Odd Mode c- Even mode

Fig 5.21 Double un-balanced stub odd-even mode analysis

Note: Y'_n and θ'_n are admittance and electrical length for full conductor width and Y_n and θ_n are for half conductor width

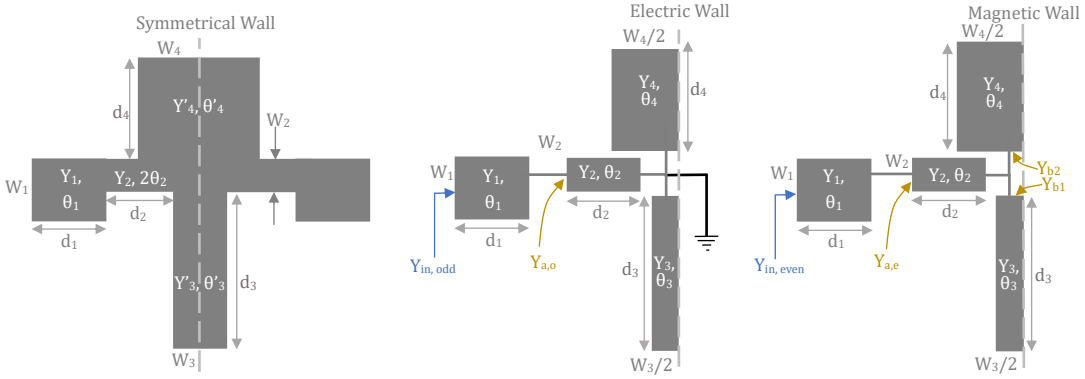

a- Unit Cell b- Odd Mode c- Even mode

Fig 5.22 Double un-balanced SIR stub odd-even mode analysis

Note: Y'_n and θ'_n are admittance and electrical length for full conductor width and Y_n and θ_n are for half conductor width

The structure odd mode admittance can be expressed as follows:

$$Y_{in,odd} = Y_1 \frac{Y_{a,o} + \mathrm{j}\, Y_1 \tan\theta_1}{Y_1 + j\, Y_{a,o} \tan\theta_1} \,, \tag{5.52}$$

$$Y_{a,o} = -\,j\, Y_2 \cot\theta_2 \quad . \tag{5.53}$$

The Formula of the even mode admittance will be as follows:

$$Y_{in,even} = Y_1 \frac{Y_{a,e} + \mathrm{j}\, Y_1 \tan\theta_1}{Y_1 + j\, Y_{a,e} \tan\theta_1} \,, \tag{5.54}$$

$$\begin{cases} Y_{a,e} = Y_2 \dfrac{Y_b + \mathrm{j}\, \mathrm{Y}_2 \tan\theta_2}{\mathrm{Y}_2 + j\, Y_b \tan\theta_2} \\ Y_b = Y_{b1} + Y_{b2} \\ Y_{b1} = j\, Y_3 \tan\theta_3 \\ Y_{b2} = j\, Y_4 \tan\theta_4 \end{cases} \tag{5.55}$$

5.7.7 Odd-Even Mode Analysis Targeting Desired Bandwidth

At this stage in the design flow, having analysed several unit cell topologies in Sections 5.7.2 to 5.7.7 using odd-even mode decomposition, it becomes important to connect that analysis to one of the most critical design parameters: the filter bandwidth. Rather than using odd-even mode analysis to retrospectively estimate bandwidth from circuit behaviour, this section presents a design-oriented approach in which bandwidth is specified at the beginning, and the odd/even mode resonant frequencies are set accordingly.

In symmetric microstrip filters, odd and even modes result in distinct equivalent circuits. Each mode leads to a unique resonance frequency:

- The odd-mode assumes a virtual ground at the plane of symmetry.
- The even-mode assumes an open circuit at the same plane.

To incorporate the desired bandwidth directly into the synthesis process, we define the target modal frequencies around a user-specified centre frequency f_0 and desired bandwidth BW as follows:

$$f_{odd} = f_0 - \frac{BW}{2} \quad , \quad f_{even} = f_0 + \frac{BW}{2} \tag{5.56}$$

Although, this is a heuristic and not an exact method to simply consider BW as the frequency spacing between f_{odd} and f_{even}, however this approach applied well for the symmetrical unit cells discussed in this section.

Using this method the bandwidth control will be embedded into the design procedure in early stage of design workflow, improving accuracy and convergence in later optimization steps. [145] [146].

5.8 Reflection-Coefficient Analysis of Periodic Structures

With the rapid advancement of wireless communication systems, it has become essential for RF engineers to explore new approaches for designing microstrip filters [147].

A general filter design methodology is proposed in [148], where a low-pass prototype filter with a specified cut-off frequency, bandwidth, and ripple is transformed into the desired multiband filter. The coupling coefficient k between coupled resonators is determined as part of this process. In [149] a design method for folded open-ring resonator filters is presented, where adjusting the dimensions of the open-loop ring allows fine-tuning of the dual-band response.

The reflection coefficient of the designed periodic structure microstrip stubs filters are calculated to evaluate filters performances. The calculation is based on electromagnetic reflection formulas.

5.8.1 Theory of Electromagnetic Reflection

In this method the reflection coefficient of the filter input will be calculated as a function of reflection coefficients of unit cell microstrip stubs of periodic structure [128] and [150]. This will be a similar approach as impedance matching between a source of electromagnetic signal and a load. A successful matching can be verified when return loss in operation frequency is less than -20dB.

The total reflection coefficient of a periodic structure (i.e. Γ_{in}) shown in Fig 5.23 can be calculated as follows [151]:

$$|\Gamma_{in}(f)| = \Sigma|\Gamma_n(f)|e^{\left(-j\frac{4\pi nl}{C}f\right)} \tag{5.57}$$

Where f is the frequency.

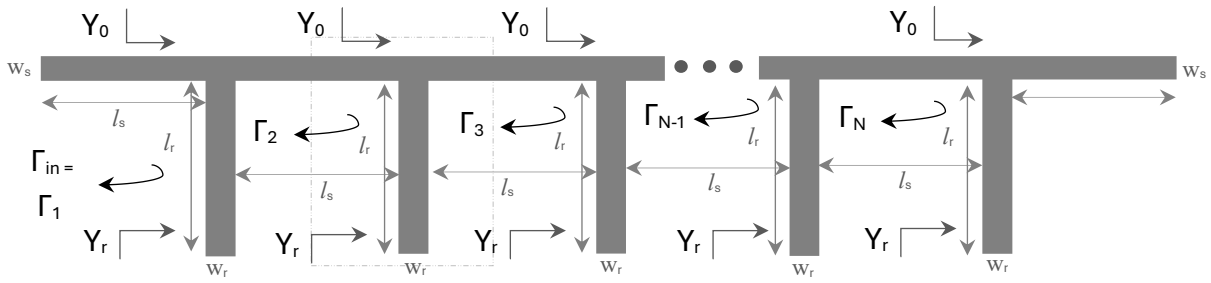

Fig 5.23 Reflection coefficient of periodic structure

This formula is used in [152] for design and calculate the frequency response of filters, with reasonable measure results, however for periodic structures of multiple stubs this method has limitation when the characteristic impedances between the neighbouring stubs has sharp changes. This approach is used to calculate periodic filters reflection coefficient, using numerical analysis method.

To develop the calculation process of Γ_{in}, we start with a single stub structure which is a very simple symmetric structure as shown in Fig 5.24.

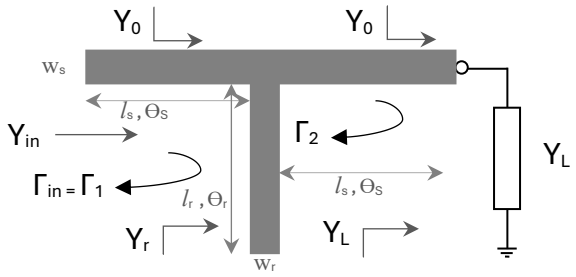

Fig 5.24 Reflection coefficient of single stub structure

In this figure equivalent admittance of the connected load is Y_L, where θ_s and θ_r, are equivalent to electrical lengths of the source line (i.e. transmission line) and resonator (i.e. microstrip stub) and input reflection coefficient is Γ_{in}. For two conditions of short stub and open stub, we have:

- Short Stub: $Y_r = \infty \rightarrow Y_{in} = Y_0 - jY_0 \cot \theta_r$
- Open Stub: $Y_r = 0 \rightarrow Y_{in} = Y_0 - jY_0 \tan \theta_r$

We would be only interested to open stub as for final design of tuneable periodic filter, short stubs will not be practical to be built, due to the liquid nature of substrate (i.e. liquid crystal).

Assuming that the characteristic impedances of the periodic structure sections are equal, then for input reflection coefficient Γ_{in} , we have [125]:

$$\Gamma_{in} = \frac{-j}{j + 2\,cot\,\theta_r} \quad (for\ open\ stub) \tag{5.58}$$

For cascade transmission line circuits, reflection coefficient can be calculated using following formula:

$$\Gamma = \frac{|\Gamma_1| + |\Gamma_2|e^{(-2j\theta)}}{1 + |\Gamma_1||\Gamma_2|e^{(-2j\theta)}} \tag{5.59}$$

The value of $|\Gamma_1|\,|\Gamma_2|$ is much smaller than 1, therefore denominator will be 1 and ignored. Now the periodic structure of Fig 5.23 is basically a repeat of the structure of Fig 5.24. For N repeats, we assume that the N stubs are loaded to the main source line in N ports 1, 2, 3… N, and $\Gamma_{r,N}$ is the reflection coefficient of the loaded stub at port N. Considering that the connected load to the periodic structure is a match impedance, then for the Nth stub we can write:

$$\Gamma_N = \Gamma_{r,N} \qquad (\Gamma_L = 0)\,, \tag{5.60}$$

$$\Gamma_{N-1} = \frac{|\Gamma_{r,N-1}| + |\Gamma_N|e^{(-2j\theta_s)}}{1 + |\Gamma_{r,N-1}||\Gamma_N|e^{(-2j\theta_s)}} \quad , \tag{5.61}$$

$$\begin{cases} \Gamma_3 = \dfrac{|\Gamma_{r,3}| + |\Gamma_4|e^{(-2j\theta_s)}}{1 + |\Gamma_{r,3}||\Gamma_4|e^{(-2j\theta_s)}} \\ \Gamma_2 = \dfrac{|\Gamma_{r,2}| + |\Gamma_3|e^{(-2j\theta_s)}}{1 + |\Gamma_{r,2}||\Gamma_3|e^{(-2j\theta_s)}} \\ \Gamma_1 = \dfrac{|\Gamma_{r,1}| + |\Gamma_2|e^{(-2j\theta_s)}}{1 + |\Gamma_{r,1}||\Gamma_2|e^{(-2j\theta_s)}} \end{cases} . \tag{5.62}$$

For the periodic structure the electrical lengths of the loaded resonator stubs will be same (i.e. θ_r), expanding the values of the stub reflection coefficients into the above formulas, then:

$$\Gamma_N = \Gamma_{r,N} = \frac{-j}{1 + 2\cot\theta_r} \qquad (\Gamma_L = 0)\ , \tag{5.63}$$

$$\begin{cases} \Gamma_{N-1} = \dfrac{\left|\dfrac{-j}{1+2\cot\theta_r}\right| + |\Gamma_N| e^{(-2j\theta_s)}}{1 + \left|\dfrac{-j}{1+2\cot\theta_r}\right| |\Gamma_N| e^{(-2j\theta_s)}} \\ \Gamma_3 = \dfrac{\left|\dfrac{-j}{1+2\cot\theta_r}\right| + |\Gamma_4| e^{(-2j\theta_s)}}{1 + \left|\dfrac{-j}{1+2\cot\theta_r}\right| |\Gamma_4| e^{(-2j\theta_s)}} \\ \Gamma_2 = \dfrac{\left|\dfrac{-j}{1+2\cot\theta_r}\right| + |\Gamma_3| e^{(-2j\theta_s)}}{1 + \left|\dfrac{-j}{1+2\cot\theta_r}\right| |\Gamma_3| e^{(-2j\theta_s)}} \\ \Gamma_1 = \dfrac{\left|\dfrac{-j}{1+2\cot\theta_r}\right| + |\Gamma_2| e^{(-2j\theta_s)}}{1 + \left|\dfrac{-j}{1+2\cot\theta_r}\right| |\Gamma_2| e^{(-2j\theta_s)}} \end{cases} . \quad (5.64)$$

From the above formulas, the reflection coefficient of the periodic structure can be calculated using numerical analytic methods to evaluate filter performance based on the value of Γ_{in} to be close to -20dB on centre frequency of the bandpass frequencies of periodic structure.

To calculate the value of Γ_{in} of microstrip stubs for periodic structure a numerical approximation method is used.

The first step is formulation to calculate the reflection coefficient of the unit cell. This can be obtained by developing an algorithm to numerically calculate the value of Γ_{in} using formula (5.59), considering that the numerical solving method should be reliable. The concept of the proposed algorithm is to calculate reflection coefficient or S_{11} (for passband). Considering the calculated values will be a validation tool for filter function and performance in bandpass when it is less than -20dB. Fig 5.25 of the next page illustrates the proposed algorithm.

5.8.2 Reflection-Coefficient guided design refinement

Calculation of the reflection coefficient can be used to refine a designed periodic filter by systematically adjusting physical dimensions of the microstrip source line and stubs to improve matching performance (i.e., reduced $|S_{11}|$ within the passband). A structured refinement procedure is illustrated in Fig 5.25 for representative periodic structures comprising 5 and 10 stubs.

Initial dimensions of the microstrip source line and unit-cell stubs are first estimated based on the target operating frequency and the selected number of stubs. Subsequently, small, controlled variations of selected geometric parameters are applied in both directions, and the corresponding reflection and transmission coefficients are recalculated using closed-form

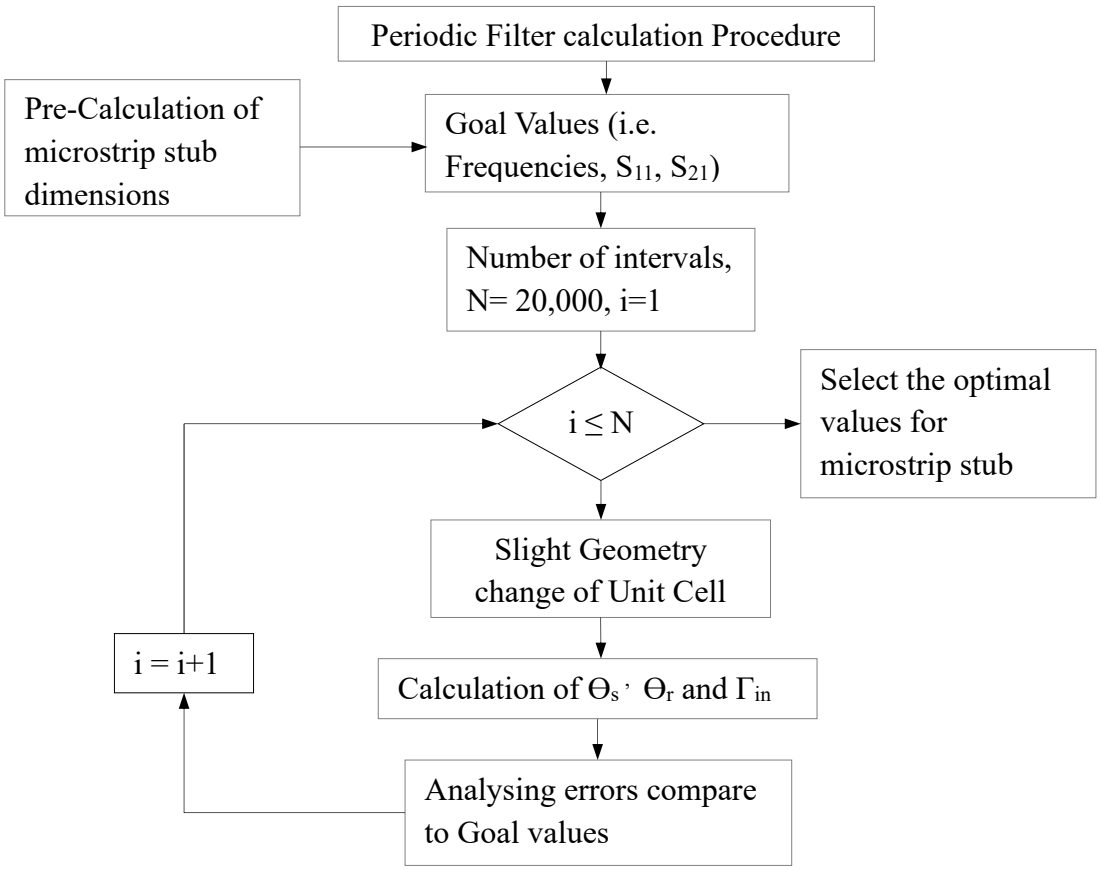

Fig 5.25 Algorithm for reflection-coefficient–guided parametric refinement

expressions. The resulting responses are compared against predefined performance targets, and the geometry that best satisfies these targets is selected. This process constitutes an analytical,

reflection-coefficient–guided design refinement rather than a numerical optimisation procedure.

5.9 ABCD Matrix - Unit Cell vs. Periodic Structure

This section formulates the ABCD (transmission) matrix of a single periodic unit cell directly from its geometry (stub lengths/widths, cell spacing d, feeder impedance) and material parameters (through the effective permittivity ε_{eff}). By cascading N identical cells, we obtain the overall network matrix and extract the Bloch phase and Bloch impedance, which determine the pass-/stop-band behaviour of the periodic line [16], [27], [31], [111]. The explicit goal is to convert these geometry-derived ABCD entries into S-parameters, so the resulting S_{11} and S_{21} curves can be used for design verification and validation of the periodic structures.

The transmission-matrix (ABCD) representation is used because it scales cleanly for cascaded periodic structures: one compact unit-cell description can be combined to model any number of cells without re-deriving the network. Compared with impedance/admittance or S-parameter forms, it avoids renormalisation issues under cascade and remains numerically stable in the presence of loss and asymmetry. It keeps reciprocity and symmetry explicit, carries geometry and material changes through a single framework, and is compact enough for symbolic work yet accurate for numerical sweeps. Most importantly, it converts unambiguously to 50-Ω S parameters, allowing direct comparison with our EM results and supporting design validation and tuning.

Insertion loss is a key figure of merit for any filter, representing the difference in signal power between the input and output of the device. Ideally, a high-quality filter should have the smallest possible insertion loss within its passband. In a real-world periodic filter, insertion loss arises from three main sources: [153].

1. Input impedance mismatch – reflections occurring because the input impedance does not perfectly match the source impedance.

2. Output impedance mismatch – reflections at the output stage due to imperfect load matching.
3. Intrinsic element losses – power dissipated within the reactive components of the filter, including conductor losses, dielectric losses, and radiation effects, as well as non-ideal reactive element behaviour.

By carefully designing the geometry and material properties of each unit cell to satisfy impedance matching and reciprocity conditions, engineers can minimize these losses and achieve a periodic filter with high selectivity, low distortion, and stable performance across its intended operating band.

Reflection loss or Return loss is because of reflections at discontinuities in transmission line. Therefore, with reference to Fig 5.7 for the nth unit cell:

$$S_{11} = Return\ Loss = \frac{Port\ \text{"n"}\ Reflected\ Voltage}{Port\ \text{"n"}\ Incident\ Voltage} = \frac{A - \frac{B}{Z_0} + CZ_0 - D}{A + \frac{B}{Z_0} + CZ_0 + D}, \quad (5.65)$$

$$S_{21} = Insertion\ Loss = \frac{Port\ \text{"n+1"}\ Incident\ Voltage}{Port\ \text{"n"}\ Incident\ Voltage} = \frac{2}{A + \frac{B}{Z_0} + CZ_0 + D}. \quad (5.66)$$

With the above definition, we develop the mathematical formulas of periodic structure based on the transmission matrix of its unit cell's transmission matrix.

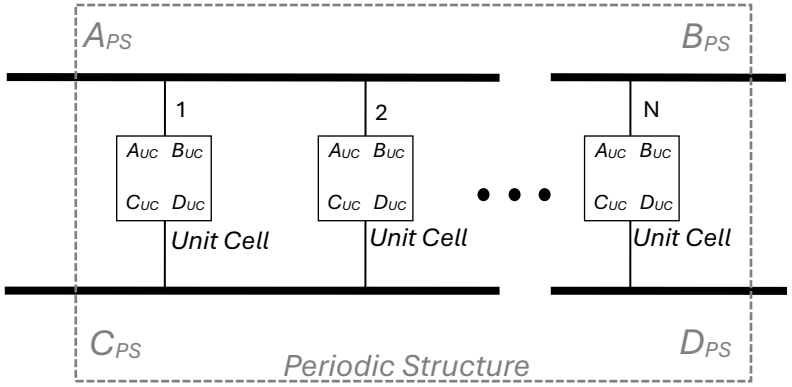

Fig 5.26 Transmission matrix of periodic structure

The transmission (ABCD) matrix of a unit cell is a 2×2 matrix that describes how voltages and currents transform as signals pass through the element. For a reciprocal network, this matrix has a unit determinant ($AD - BC = 1$) and, in many practical cases, satisfies A=. With these constraints, the matrix contains only three independent parameters, simplifying its mathematical handling.

$$\begin{bmatrix} A & B \\ C & D \end{bmatrix}^{UC} = \begin{bmatrix} A_{UC} & B_{UC} \\ C_{UC} & D_{UC} \end{bmatrix} \tag{5.67}$$

In linear algebra, the set of 2×2 matrices with unit determinant forms a group known as the special linear group in two dimensions, denoted $SL(2)$ [154]. When additional symmetry conditions such as A=D are met, the matrix can be related to a special case within simplistic or orthogonal transformation frameworks. In certain filter synthesis approaches, the 2×2 transmission matrix can be rotated, through a similarity transformation, into a form with equal diagonal elements.

A powerful way to achieve this is by applying eigen decomposition (or spectral decomposition). This method expresses the transmission matrix as the product of three matrices: one containing the eigenvectors, a diagonal matrix containing the eigenvalues, and the inverse of the eigenvector matrix. The diagonal form is particularly useful in analysing periodic structures, as it allows the propagation characteristics of the unit cell to be studied directly in terms of its eigenmodes. These eigenmodes correspond to independent wave solutions through the periodic network, enabling straightforward determination of passbands, stopbands, and dispersion relations.

To obtain a diagonal representation in the mode domain, a phase-mode transformation is applied to the transmission line matrices [155]. This transformation effectively decouples the system into independent modal channels, each represented by a scalar transfer function, rather than by a set of coupled equations. The primary motivation for this approach is computational efficiency: mathematical operations, such as multiplication, inversion, and power calculation,

are significantly simpler and faster for diagonal matrices compared to their non-diagonal counterparts [156], [157], [158]. After transformation, the resulting matrices are expressed in terms of eigenvectors and are generally composed of frequency-dependent complex elements. These complex entries account for both magnitude and phase variations of the modes across frequency. Under idealized conditions, for example, in a lossless and perfectly symmetrical transmission line, the eigenvector elements can be purely real, simplifying analysis even further. In practical scenarios, however, physical imperfections, dielectric losses, and conductor losses introduce complex-valued terms into the eigenvectors, reflecting both attenuation and dispersion effects. By working in this diagonalized mode domain, designers and analysts gain direct insight into the propagation constants and modal behaviour of the structure, enabling more intuitive filter optimization, improved numerical stability in simulations, and faster evaluation of frequency responses.

Matrix decomposition is a mathematical technique that reduces a matrix into a set of constituent matrices whose product equals the original. This process simplifies complex matrix operations, as calculations can often be performed more efficiently on the decomposed form than on the original matrix itself. In the context of periodic structures with N unit cells, decomposition provides a pathway to represent the system in its most canonical form, reducing the parameter space from $n \times n$ for a general matrix to only n parameters for a diagonal matrix. This reduction not only minimizes computational complexity but also reveals the intrinsic structural properties of the system [159].

The transformation of a given matrix into the product of canonical matrices is referred to as matrix factorization. This is a fundamental tool in linear algebra with broad applications across science and engineering, including statistical modelling, computational physics, and network analysis [160]. Different decomposition techniques, such as LU decomposition (lower and upper triangular matrices), QR decomposition, Cholesky factorization, and eigenvalue–

eigenvector decomposition, are commonly used to evaluate determinants, perform matrix inversion, and solve systems of linear equations [161].

One of the main motivations for matrix decomposition is numerical efficiency [162]. Direct computation of determinants, inverses, or solutions to matrix equations can be computationally expensive and numerically unstable for large or ill-conditioned systems. By decomposing a complex matrix into simpler factors, operations such as solving diagonal systems, evaluating modal behaviour, or performing iterative updates become significantly more stable and faster. Furthermore, decomposition preserves the essential characteristics of the original matrix, such as its symmetry, rank, and spectral properties, while making these features more accessible for analysis and interpretation. This capability is particularly valuable in filter design and periodic structure analysis, where canonical matrix forms allow for optimized algorithms and clearer physical insight into wave propagation, impedance matching, and mode coupling.

In Eigenvalue decomposition, the objective is to transform a given square matrix A into a form that reveals its fundamental spectral properties. This transformation can be expressed as:

$$\boldsymbol{A} = \boldsymbol{Q}\boldsymbol{B}\boldsymbol{Q}^{-1}\,, \tag{5.68}$$

where $\boldsymbol{B}$ is a diagonal matrix containing the eigenvalues of $\boldsymbol{A}$, and $\boldsymbol{Q}$ is a matrix whose columns are the eigenvectors of $\boldsymbol{A}$. The matrix $\boldsymbol{B}$ encapsulates the characteristic information of $\boldsymbol{A}$, such as its scaling factors along principal directions, while $\boldsymbol{Q}$ defines the transformation to the eigenvector basis. When $\boldsymbol{A}$ is symmetric (or Hermitian in the complex domain), the eigenvector matrix $\boldsymbol{Q}$ can be chosen to be orthogonal (or unitary), which means that its inverse is equal to its transpose:

$$\boldsymbol{Q}^{-1} = \boldsymbol{Q}^{T}, \tag{5.69}$$

From this property, it follows that:

$$\boldsymbol{Q}\,\boldsymbol{Q}^{T} = \boldsymbol{Q}^{T}\,\boldsymbol{Q} = I\,, \tag{5.70}$$

where I is the identity matrix. This orthogonality condition is of great computational value, as it avoids the need for explicit matrix inversion, an operation that can be costly and numerically unstable in large scale problems.

For eigenvalue-based transformations, we establish that for any $n \times n$ matrix $\boldsymbol{A}$, there exists at least one non-zero n-dimensional vector v satisfying:

$$\boldsymbol{A}v = \lambda\, v\,. \tag{5.71}$$

where λ is an eigenvalue of $\boldsymbol{A}$ and v is the corresponding eigenvector. The trace of A, defined as the sum of its diagonal elements, is given by:

$$trace\ (\boldsymbol{A}) = \sum_{i=1}^{n} a_{ii} \ = \sum_{i=1}^{n} \lambda \quad , \tag{5.72}$$

showing that the trace is equal to the sum of the eigenvalues

Using eigenvalue decomposition, the matrix $\boldsymbol{A}$ can be expressed as:

$$\boldsymbol{A} = \boldsymbol{V}\ \mathrm{diag}(\lambda)\ \boldsymbol{V}^{-1}\,. \tag{5.73}$$

where:

- $\boldsymbol{V} = \left[\boldsymbol{v}^{(1)}, \boldsymbol{v}^{(2)}, \ldots\ldots, \boldsymbol{v}^{(n)}\right]$, matrix whose columns are the eigenvectors of $\boldsymbol{A}$
- $\lambda = [\lambda_1\ ,\ \lambda_2, \ldots.\ \ \lambda_n]$ is the vector of eigenvalues, and
- $\mathrm{diag}(\lambda)$ denotes a diagonal matrix whose entries are the eigenvalues.

The characteristic equation $|\boldsymbol{A}-\lambda \boldsymbol{I}|=0$ is a polynomial in λ of degree n, known as the characteristic polynomial. While general matrix decomposition techniques can be applied to both square and non-square matrices (e.g., SVD), eigenvalue decomposition is defined only for square matrices.

A related approach is Schur decomposition, which represents a matrix in an upper-triangular form that retains the same eigenvalues. This method can be particularly useful in numerical computations where stability is a concern. For certain classes of problems, such as periodic

structure analysis, a canonical form is obtained by factorizing the matrix into its eigenvector basis and eigenvalue representation.

$$\begin{bmatrix} A & B \\ C & D \end{bmatrix}^{UC} = \begin{bmatrix} A & B \\ C & D \end{bmatrix}^{UC,canonical} \begin{bmatrix} A & B \\ C & D \end{bmatrix}^{EV} \left(\begin{bmatrix} A & B \\ C & D \end{bmatrix}^{UC,canonical}\right)^{-1}. \tag{5.74}$$

where:

$$\begin{bmatrix} A & B \\ C & D \end{bmatrix}^{UC,canonical} = Marix\ with\ corresponding\ eigenvectors\ of\ UC\ ,$$

$$\begin{bmatrix} A & B \\ C & D \end{bmatrix}^{EV} = Diagonal\ Matrix\ eigenvalues\ .$$

This canonical form preserves the key spectral characteristics of the system, making it possible to directly derive the overall ABCD matrix of a periodic structure from its constituent unit cells as follows. Details of formula derivation is in Appendix B.

$$A_{PS} = D_{PS} = \frac{\left[\left(A_{UC} + \sqrt{A_{UC}^2 - 1}\right)^N + \left(A_{UC} - \sqrt{A_{UC}^2 - 1}\right)^N\right]}{2}, \tag{5.75}$$

$$B_{PS} = \frac{B_{UC}\left[\left(A_{UC} + \sqrt{A_{UC}^2 - 1}\right)^N - \left(A_{UC} - \sqrt{A_{UC}^2 - 1}\right)^N\right]}{\left(2\sqrt{A_{UC}^2 - 1}\right)}, \tag{5.76}$$

$$C_{PS} = \frac{C_{UC}\left[\left(A_{UC} + \sqrt{A_{UC}^2 - 1}\right)^N - \left(A_{UC} - \sqrt{A_{UC}^2 - 1}\right)^N\right]}{\left(2\sqrt{A_{UC}^2 - 1}\right)}. \tag{5.77}$$

5.9.1 Analysis of the Unit-Cell ABCD Matrix

Below figure is one cell of the periodic structure shown in Fig 5.7 divided to smaller sections:

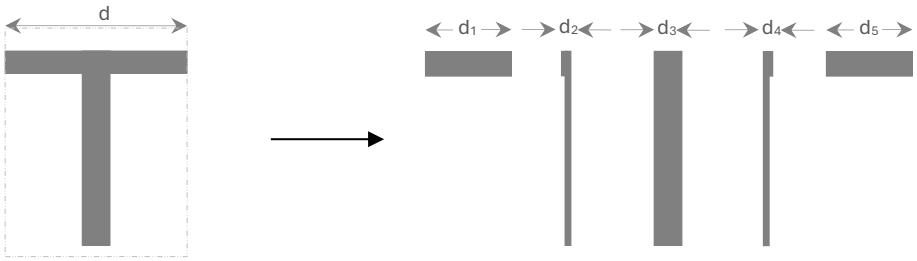

Fig 5.27 Analysis of single unit cell

The first section is a narrow part of microstrip with length d_1, the second part is the narrow to wide discontinuity with a length close to zero ($d_2 \approx 0$), the third part is the wide part of microstrip with length d_3, the fourth section is wide to narrow discontinuity with a length d_4 which is close to zero and the fifth part is another narrow part of microstrip with length d_5. As the unit cell is symmetrical the first section and fifth section have same length and also second and third section lengths are equal. The ABCD matrix of the unit cell can be now expressed as follows:

$$\begin{bmatrix} A & B \\ C & D \end{bmatrix} = \begin{bmatrix} A & B \\ C & D \end{bmatrix}^{d_1} \cdot \begin{bmatrix} A & B \\ C & D \end{bmatrix}^{d_2} \cdot \begin{bmatrix} A & B \\ C & D \end{bmatrix}^{d_3} \cdot \begin{bmatrix} A & B \\ C & D \end{bmatrix}^{d_4} \cdot \begin{bmatrix} A & B \\ C & D \end{bmatrix}^{d_5}, \tag{5.78}$$

For a narrow or wide section of microstrip the ABCD matrix can be obtained:

$$\begin{bmatrix} A & B \\ C & D \end{bmatrix} = \begin{bmatrix} \cos\frac{\theta}{2} & j\sin\frac{\theta}{2} \\ j\sin\frac{\theta}{2} & \cos\frac{\theta}{2} \end{bmatrix}, \tag{5.79}$$

For the step-up (narrow to wide) and step-down (wide to narrow) discontinuities the two sections of narrow and wide width correspond inductances of microstrip line, and the step discontinuity represent a capacitance and these sections can be modelled using the T-network as shown in below figures:

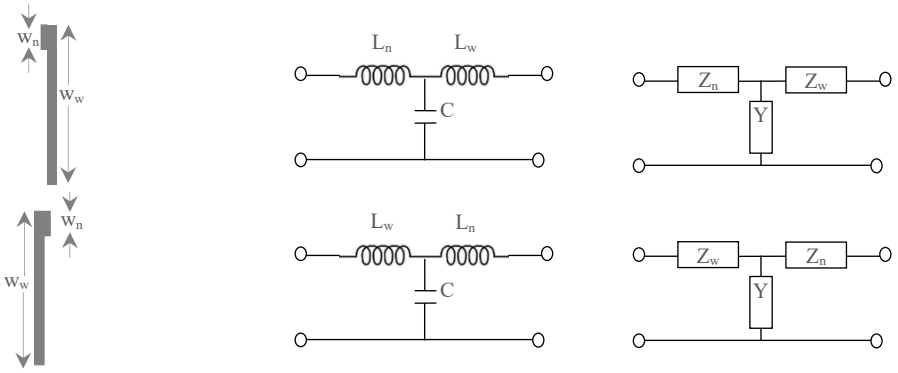

Fig 5.28 Equivalent circuit of step-up/down discontinuity

The ABCD matrix of step-up discontinuity can be then calculated as:

$$\begin{bmatrix} A & B \\ C & D \end{bmatrix}^{d_2} = \begin{bmatrix} 1 & Z_n \\ 0 & 1 \end{bmatrix} \begin{bmatrix} 1 & 0 \\ Y & 1 \end{bmatrix} \begin{bmatrix} 1 & Z_w \\ 0 & 1 \end{bmatrix}, \tag{5.80}$$

$$\begin{bmatrix} A & B \\ C & D \end{bmatrix}^{d_2} = \begin{bmatrix} 1 + Z_n Y & Z_w + Z_w Z_n Y + Z_n \\ Y & Z_w Y + 1 \end{bmatrix}. \tag{5.81}$$

and for the ABCD matrix of step-down discontinuity, we have:

$$\begin{bmatrix} A & B \\ C & D \end{bmatrix}^{d_4} = \begin{bmatrix} 1 & Z_w \\ 0 & 1 \end{bmatrix} \begin{bmatrix} 1 & 0 \\ Y & 1 \end{bmatrix} \begin{bmatrix} 1 & Z_n \\ 0 & 1 \end{bmatrix}, \tag{5.82}$$

$$\begin{bmatrix} A & B \\ C & D \end{bmatrix}^{d_4} = \begin{bmatrix} 1 + Z_w Y & Z_n + Z_n Z_w Y + Z_w \\ Y & Z_n Y + 1 \end{bmatrix}. \tag{5.83}$$

Therefore, the ABCD matrix of the unit cell can be calculated as follows:

$$\begin{bmatrix} A & B \\ C & D \end{bmatrix} = \begin{bmatrix} 1 & Z_1 \\ 0 & 1 \end{bmatrix} \cdot \begin{bmatrix} 1 + Z_n Y & Z_w + Z_w Z_n Y + Z_n \\ Y & Z_w Y + 1 \end{bmatrix} \cdot \begin{bmatrix} 1 & 0 \\ Y & 1 \end{bmatrix} \cdot \begin{bmatrix} 1 + Z_w Y & Z_n + Z_n Z_w Y + Z_w \\ Y & Z_n Y + 1 \end{bmatrix} \cdot \begin{bmatrix} 1 & Z_1 \\ 0 & 1 \end{bmatrix} \tag{5.84}$$

With a reasonable approximation the length of inductive part of the d_2 and d_4 in both narrow and wide side can be considered are closed to zero which then L_n and Lw in Fig 5.28 will be negligible and therefore for each junction in form d_2 and d_4 we have:

$$\begin{bmatrix} A & B \\ C & D \end{bmatrix}^{d_2} = \begin{bmatrix} A & B \\ C & D \end{bmatrix}^{d_4} \approx \begin{bmatrix} 1 & 0 \\ Y & 1 \end{bmatrix} = \begin{bmatrix} 1 & 0 \\ \frac{1}{Z} & 1 \end{bmatrix}. \tag{5.85}$$

The above equation for a single cell can be also expressed in the form of [Z] and [Y] matrix for the two-port network parameters as shown in Fig 5.29.

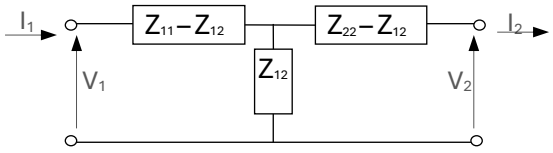

Fig 5.29 Two-port network equivalent of unit cell

To predict the periodic structure filter performance the characteristic impedance of the structure or ZUC should be obtained for the analysis of S-parameters and structural parameters' effects on wave propagation. The characteristic impedance of the unit cell would be as follows [163].

$$Z_{UC} = \frac{Z_{11} - Z_{22}}{2} + Z_{12} \sinh \gamma_c \alpha \,, \tag{5.86}$$

where:

$$sinh^2 \gamma_c \alpha = cosh^2 \gamma_c \alpha - 1 \quad and \quad cosh \gamma_c \alpha = \frac{Z_{11} - Z_{22}}{2Z_{12}} . \qquad 5(5.87)$$

For a specific periodic structure for the frequency range that Z_c has a real value the microstrip structure acts as passband filter and for the frequencies that Z_c is purely imaginary the filter is in stopband mode. In the above equation we have:

$$cosh \gamma_c \alpha = cosh[(\alpha_c + j\beta_c)\alpha] = cosh \alpha_c \alpha . cos \beta_c \alpha + j \ sinh \alpha_c \alpha . sin \beta_c \alpha. \qquad (5.88)$$

where α_c is the attenuation constant and β_c is the propagation constant of the cell, then there are two possible cases (i.e. $\alpha_c \neq 0 / \beta_c = 0$ for stopband and $\alpha_c = 0 / \beta_c \neq 0$ for passband) which are already discussed in 5.3

The stopband and pass-band characteristic of a periodic structure is however a function of the equivalent impedance of the unit cell which forms the structure. To control the filter parameters the focus would be of the dimension and configuration of unit cells, once is designed to provide the filter parameters such and cut of frequencies and bandwidth then the complete periodic structure also supports the same performance in the pass band of the structure.

A simple cell of a periodic structure is a capacitive stub in the effective wavelength of the desired frequency, which as describe before provides filter behaviour based on the frequencies where the equivalent impedance of the structure can be real, imaginary or complex for both passband and stopband.

For more complex structures when a desired characteristic is expected, the simple capacitive stubs would be replaced by more complex microstrip circuits and sections of design impedances to give control and improve of filter parameters such as centre frequency, wider or narrower band width or attenuation level of stop-band region and the ripple of the filter response curve. The concept of replacing periodic stubs configuration from capacitive to a non-resonating impedance is based on the wave-length characteristic of microstrip lines as described in 5.2 and shown in Fig 5.6.

5.9.2 Periodic Stepped Impedance Structures

The above-mentioned condition can be further verified in simple periodic stepped Impedance filters with identical cell units. A three-cell low insertion loss periodic structure filter is

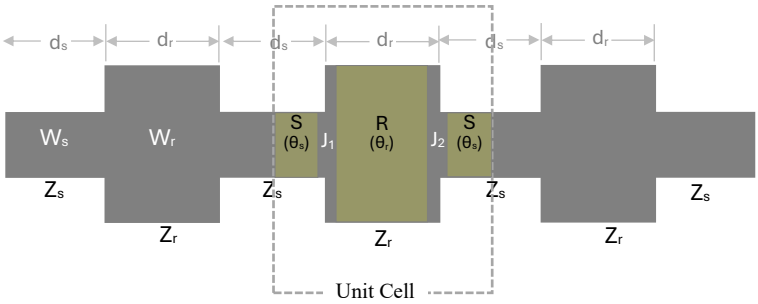

Fig 5.30 Periodic stepped impedance structure

developed for 10GHz frequency spectrum in [164]. The periodic structure is used to achieve a high-performance filter, to perform harmonic tunning in power amplifier [165], [166], [167], [168]. The nonperiodic format already reviewed in 3.2.2.

The unit cell ABCD matrix can be calculated by multiplying of three sections of transmission line highlighted S-J_1-R-J_2-S (source-resonator-source) in Fig 5.30 which formed the unit cell. Reference to section 4.6 the step-up/down discontinuity of J1 and J2 can be modelled as two inductances a lumped capacitance, for that the transmission matrix is calculated in [109] as shown below.

$$\begin{bmatrix} A & B \\ C & D \end{bmatrix}^{J1} = \begin{bmatrix} A & B \\ C & D \end{bmatrix}^{J2} = \begin{bmatrix} 1 & 0 \\ jY & 1 \end{bmatrix} \tag{5.89}$$

Y of the shunt capacitance can be expressed as Y=ωC_0 where C_0 is the capacitance and ω is angular frequency of passband. The value of this capacitance as calculated for $\varepsilon_r \leq 10$ and $1.5 \leq W_r/W_s \leq 3.5$ (with a good approximation) in [169] will be:

$$C_0 = \sqrt{W_s W_r}\{[10.1Ln(\varepsilon_r) + 2.33]W_r/W_s - 12.6Ln\,(\varepsilon_r) - 3.17\} \tag{5.90}$$

Therefore, for the unit cell, we have (UC=Unit Cell):

$$\begin{bmatrix} A & B \\ C & D \end{bmatrix}^{UC} = \begin{bmatrix} A & B \\ C & D \end{bmatrix}^{S} \begin{bmatrix} A & B \\ C & D \end{bmatrix}^{J1} \begin{bmatrix} A & B \\ C & D \end{bmatrix}^{R} \begin{bmatrix} A & B \\ C & D \end{bmatrix}^{J2} \begin{bmatrix} A & B \\ C & D \end{bmatrix}^{S}. \tag{5.91}$$

Details of formula derivation of stepped impedance unit cell ABCD matrix are provided in Appendix B.

5.9.3 Planar Periodic Structure with Balanced Open Stub

As an alternative periodic structure, we derive the formulas and equations of transmission matrix ABCD for the following planar structure in Fig 5.31

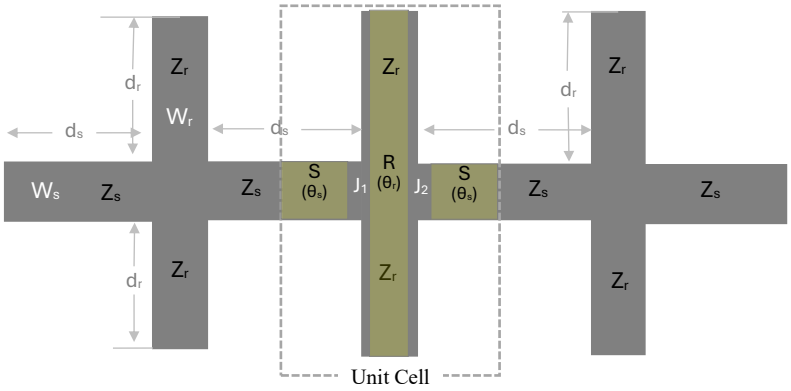

Fig 5.31 Planar Periodic structure with balanced open stub

This structured formed with a microstrip line with periodically open-ended stubs. The impedance of the stub changes with its length. For the electrical length $\theta=kd_r$, the input impedance of the stub based on its characteristic impedance will be $Z_{in} = j\frac{Z_r}{tan\,\theta}$. When $\theta=n\pi$, n=1,2, … the stub line resonates, and its impedance will be equal to characteristic impedance. The resonator stub shown in Fig 5.31 can be considered as two parallel transmission line for that the ABCD matrix of the unit cell is provided in Appendix B.

The overall periodic structure transmission matrix ABCD can be calculated using the same formulas (5.86) to (5.89) for this structure.

5.9.4 Planar Periodic Structure with T-shaped Open Stub

Different structures might be used to form a periodic structure, the next layout for unit cell to be evaluate is a T-shape open stub microstrip transmission line. Same as previous section, we derive the formulas and equations of transmission matrix ABCD for the following planar structure in Fig 5.32

This structure is formed with a microstrip line with periodically open ended microstrip stubs. The impedance of the stub changes with its length. For the electrical length $\theta=kd_r$, the input

impedance of the stub based on its characteristic impedance will be $Z_{in} = j\frac{Z_r}{tan\,\theta}$. When θ=nπ, n=1,2, … the stub line resonates, and its impedance will be equal to characteristic impedance. The resonator stub shown in Fig 5.31 can be considered as two parallel transmission line for that the ABCD matrix are provided in Appendix B.

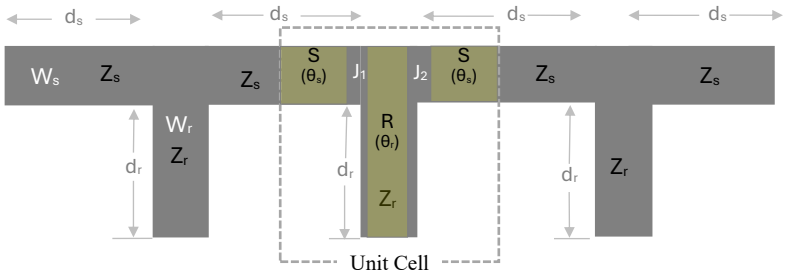

Fig 5.32 Planar Periodic structure with T-shaped open stub

5.9.5 Planar Periodic Structure with Unbalanced Open Stub

Another alternative periodic structure, which is studied is an un-balanced open stub as shown in figure we derive the formulas and equations of transmission matrix ABCD for the following planar structure in Fig 5.33. For this unit cell structure the ABCD matrix formula derivation is provided in Appendix B.

Other periodic structures with different symmetrical unit cell structures are also analysed and the ABCD matrixes are developed and formulised using the same concept of this section and some of them are included in the calculation program. Chapter 6 provide some examples of design and simulations of different structures based on these analytical studies and numerical program.

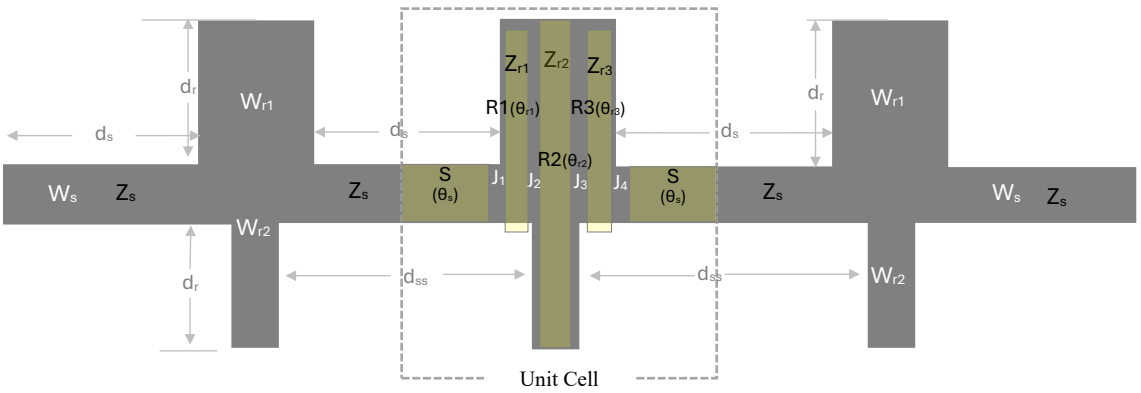

Fig 5.33 Planar Periodic structure with un-balance open stub

5.10 Design Methodology for Periodic Microstrip Filters

This section presents a unified methodology for designing microstrip filters based on periodic structures. It integrates three key theoretical tools:

1. Odd-Even Mode Analysis – for fast estimation of resonant unit cell structures
2. Reflection Coefficient Minimization – for fine-tuning unit cell parameters to reduce in-band reflections
3. ABCD Matrix Analysis – for accurate modelling of cascaded periodic structures and overall filter response

Odd-even mode analysis provides an intuitive starting point for dimension estimation. By analysing symmetrical and anti-symmetrical excitations, the effective input admittance is calculated:

- Even-mode: stub open → affects symmetry
- Odd mode: stub grounded → affects anti-symmetry

Using these, unit cell parameters such as W_1, W_2, d_1, d_2, … are derived for target resonant frequency f_0.

Initial dimensions are refined using a dedicated optimization algorithm that minimizes the input reflection coefficient $|\Gamma_{in}|$. This method assumes a periodic filter of N identical unit cells. This is based on formulas (5.59) to (5.63) and use of MATLAB fminsearch (MATLAB's derivative free Nelder–Mead simplex optimiser) to minimize |Γin| at design frequency. Yields optimized parameters (typically stub lengths). This step improves in-band matching without yet analysing full filter transmission. The third step is ABCD Matrix modelling of full N-cell periodic structure using ABCD matrix representation which acts both as a design driver and validation tool.

The total ABCD matrix of periodic structure is computed from ABCD of unit cell and formulas (5.71 to (5.73), to study passband/stopband behaviour analytically and fine adjustments of cell spacing/lengths to place the passband and stopband edges and to control in-band ripple before

any full-wave layout activity. This enables early pruning of impractical configurations and narrows the optimisation space.

The scattering parameters can be then calculated using following formulas (for equal reference impedances $Z0 = 50\Omega$) for further validation of the structure design [27]- [28].

$$S_{11} = \frac{A + \frac{B}{Z_0} - CZ_0 - D}{A + \frac{B}{Z_0} + CZ_0 + D} \qquad S_{21} = \frac{2}{A + \frac{B}{Z_0} + CZ_0 + D} \quad . \tag{5.92}$$

Table 5.1 summarised the design steps from conceptual structure to fully validated filter design with simulation-quality results.

Step	Tool	Purpose	Output
1	Odd-Even Mode	Quick dimension estimation	W and d values
2	Reflection Coefficient Minimization	Design Refinement	Refined stub/feed lengths
3	ABCD Matrix	Passband/Stopband prediction (N & Ls) System-level validation	N, Ls & 3-dB bandwidth & stopband edges S_{11} , S_{21} over frequency

Table 5.1 Periodic Structure Design steps

Fig 5.34 illustrates an algorithm for design, simulation, and test of periodic structure filter.

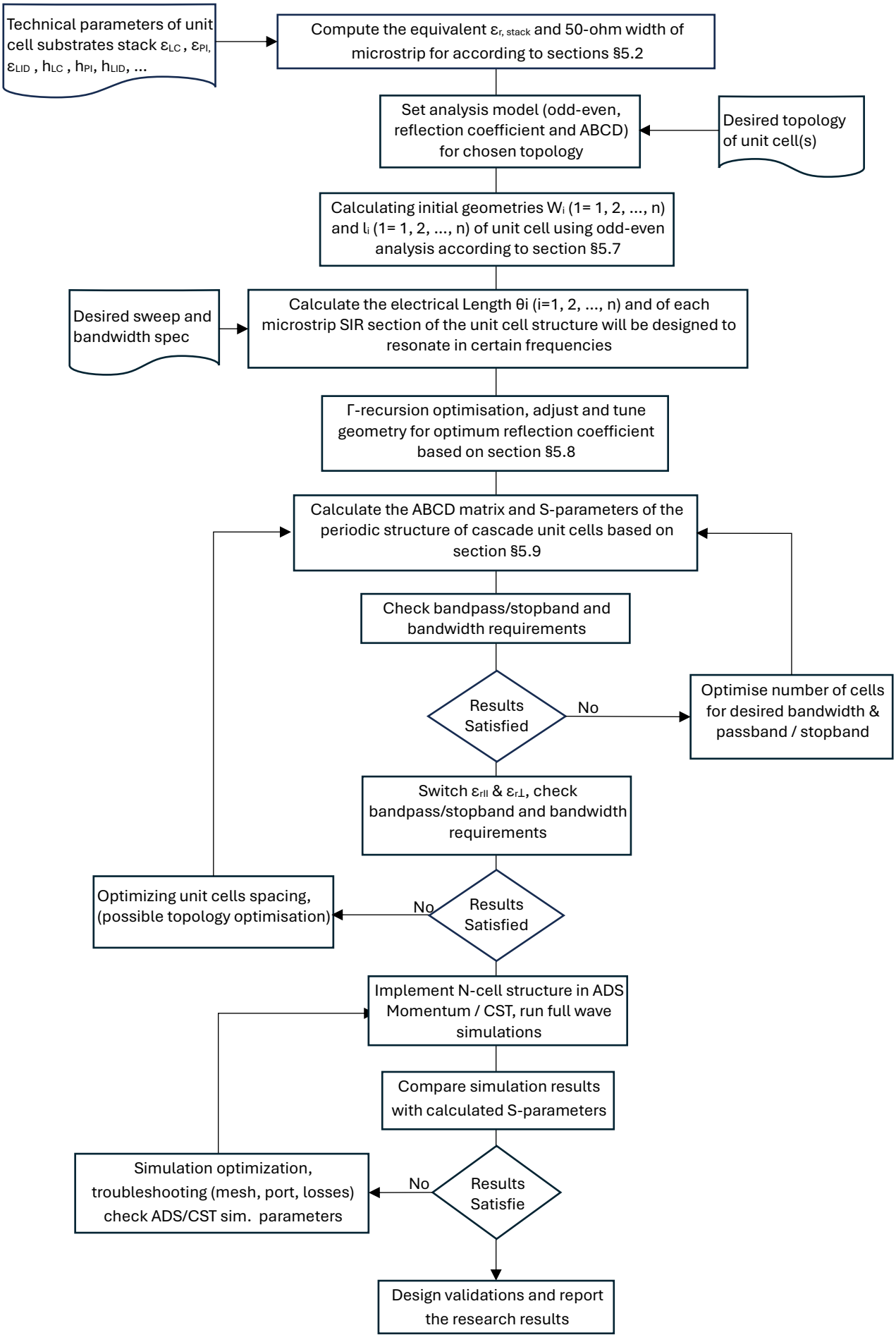

Fig 5.34 Algorithm of design, simulation and validation of Periodic Structure

5.11 Summary

This chapter provides a comprehensive exploration of periodic filter design, focusing on the implementation of microstrip periodic structures. It offers theoretical foundations, practical design methodologies, and advanced analysis techniques to create high-performance filters for RF and millimetre-wave applications. The key topics covered in this chapter is the design of microstrip quarter-wavelength ($\lambda/4$) resonators is detailed, emphasizing their fundamental role in achieving high-frequency selectivity. The analysis includes resonator geometry, impedance characteristics, and optimization for specific frequency bands.

The cascading of multiple resonators is discussed as a method to enhance filter performance, such as achieving sharper roll-off, wider stopbands, and improved passband flatness. The chapter then examines terminated periodic structures, focusing on their behaviour when terminated by specific loads. Termination impacts on passband and stopband properties are analysed to optimize filter performance.

A theoretical framework for periodic structures is developed, including the derivation of their dispersion characteristics and bandgap properties. This section introduces Bloch wave theory and its relevance to filter design. Techniques for controlling periodic structure parameters, such as unit cell dimensions, impedance, and substrate properties, are discussed to fine-tune the filter's operational characteristics.

The transmission matrix (ABCD) method is introduced for analysing the electromagnetic behaviour of periodic structures. This approach provides a systematic way to evaluate cascading effects and overall filter performance.

Design principles for periodic stepped impedance structures are covered, highlighting their versatility in creating compact and highly selective filters. Two specific configurations planar periodic structures with balanced open studs and T-shaped open stubs are explored. Their unique properties for achieving customized passband and stopband features are discussed. The

Stepped Impedance Resonator (SIR) is analysed in depth, focusing on its ability to miniaturize filters and enable multi-band operation.

The chapter then details the even-odd mode analysis method for symmetric structures, providing insights into mode splitting and its impact on filter response. A systematic algorithm for periodic filter design is presented, outlining the key steps from unit cell modelling to full filter synthesis and performance evaluation. Optimization techniques for the reflection coefficient are discussed, incorporating numerical methods to minimize losses and maximize signal integrity.

The chapter concludes with practical numerical estimation methods to validate the theoretical models and optimize the periodic filter design. Simulation results and case studies are provided to illustrate the effectiveness of the proposed techniques.

This chapter equips the reader with the theoretical knowledge and practical tools needed to design and analyse periodic filters using microstrip structures. By covering a wide range of design methodologies and optimization strategies, it provides a solid foundation for developing advanced filters tailored to the demands of modern communication and sensing systems.

Chapter6 : Simulation results

This chapter validates the design methods of Chapter 5 using full-wave electromagnetic simulation. Section 6.1 establishes a non-periodic SIR baseline, showing that while SIR filters do tune with changes in εr, the resulting cut-off shifts are modest and insufficient for practical tuneable operation around 60 GHz. Section 6.2 investigates periodic lattices, quantifying how unit-cell impedance and the number of cells N control the passband ($|Z|$, $\Re\{Z\}$, $\Im\{Z\}$ overlaid with S-parameters). Section 6.3 presents three designed periodic topologies (T1–T3) and compares ADS Momentum and CST Studio results against the MATLAB periodic-ABCD predictions, including a quantitative centre-frequency table. A common stack (Substrate_LC60GHz) and 50-Ω renormalisation are used throughout; the dielectric state ($\varepsilon_{r\perp}\approx2.2 \rightarrow \varepsilon_{r\parallel}\approx2.7$) emulates LC bias.

6.1 ADS/Momentum and CST simulations of SIR Filters

Fig 6.1 is a 3rd-order Chebyshev low-pass stub filter (substrate thickness 0.78 mm). The ADS schematic implements a 3rd-order Chebyshev low-pass using short/open stubs mapped from the lumped prototype. A parameter sweep on the substrate permittivity (ε_r = 2.2, 2.4, 2.6, 2.8, 3.0) shows the expected trend: as ε_r increases, the effective permittivity rises, electrical lengths grow, and the cut-off (and stop-band features) shift to lower frequency. Momentum and CST results agree qualitatively—the CST model includes 3-D fringing and discontinuity effects, so minor frequency offsets relative to the circuit-level mask are expected. Overall rejection improves with frequency as designed, and the passband remains monotonic for the selected ripple.

Fig 6.2 is the simulation results of a 5th-order Chebyshev stub filter ($\varepsilon_r \approx 3.55$, thickness 0.017 mm, $f_c \approx 8$ GHz). A similar study was carried out for a 5th-order realisation. Sweeping ε_r (e.g., 3.0 to 4.0) again produces a leftward shift of the cut-off with increasing ε_r, with CST confirming

the ADS/Momentum trend. The higher order sharpens the transition band and deepens the stopband, while the tuning behaviour remains monotonic.

These sweeps quantitatively support the conceptual comparison made in §3.1.3 (Fig 3.11). These results confirm that SIR non-periodic microstrip filters do tune with ε_r (and therefore with LC bias). However, the fractional frequency shift per unit change in ε_r is modest (typically only a few–ten per cent over the sweeps shown). Physically, the cut-off is set by the electrical lengths of a small number of sections whose fields are only partially confined in the tuneable dielectric; some energy resides in air/superstrate, so changes in ε_r are diluted at the mode level. By contrast, the periodic structures used later place the operating band near Bragg edges, where small changes in effective permittivity produce larger shifts in the Bloch condition; as a result, they exhibit higher tuning sensitivity to LC bias.

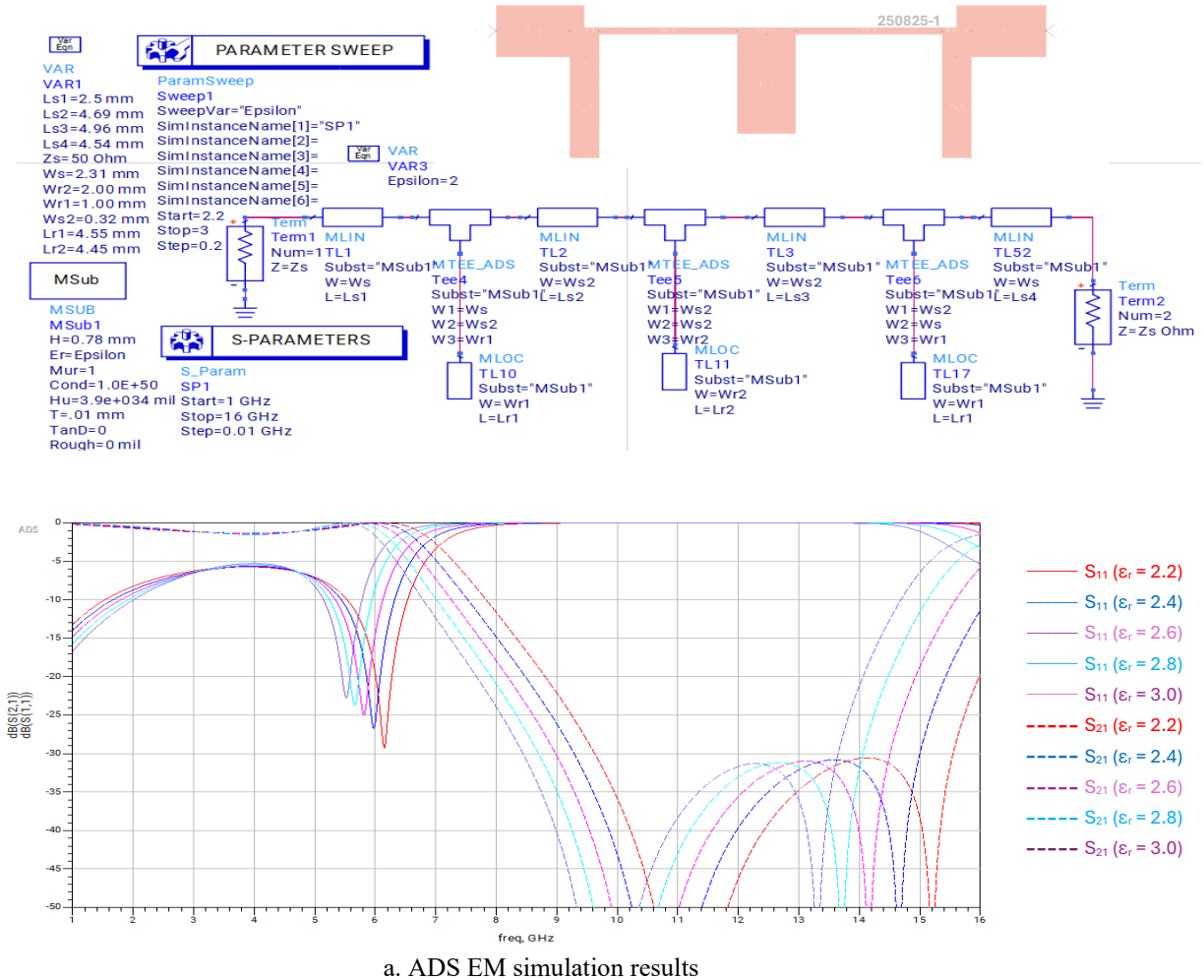

a. ADS EM simulation results

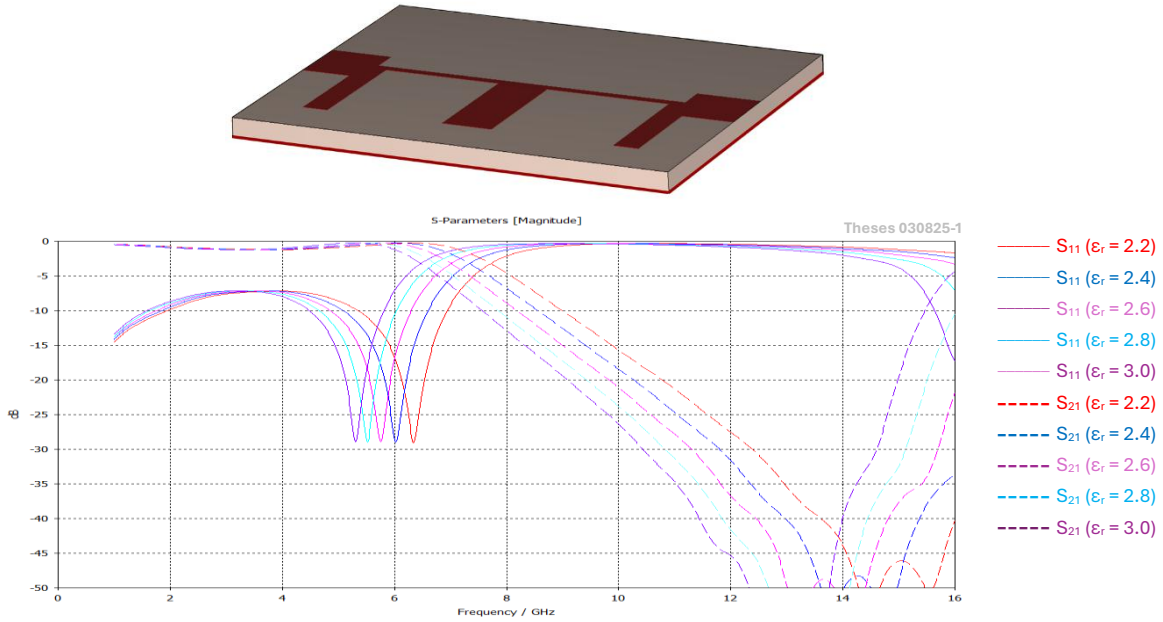

b. CST simulation results

Fig 6.1 ADS EM and CST simulations of a 3rd order stub filter

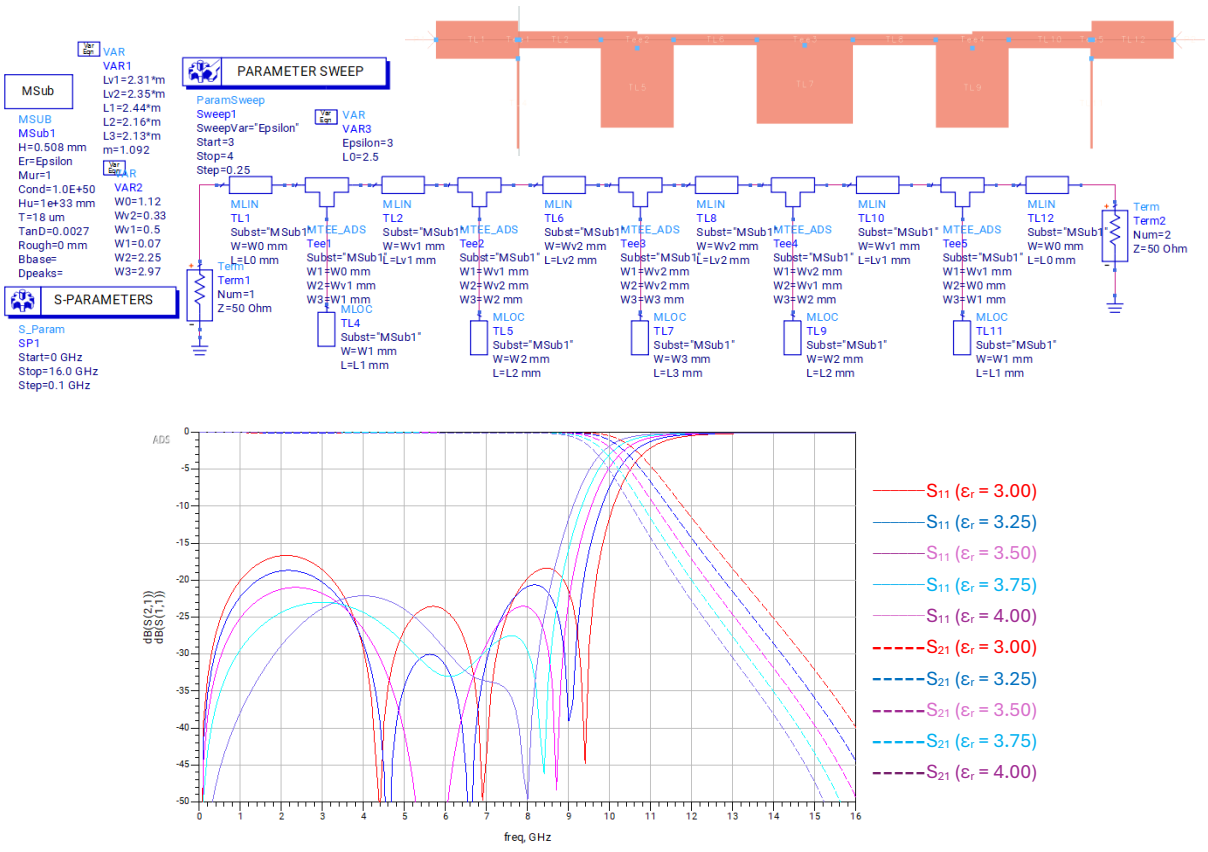

a. ADS EM simulation results

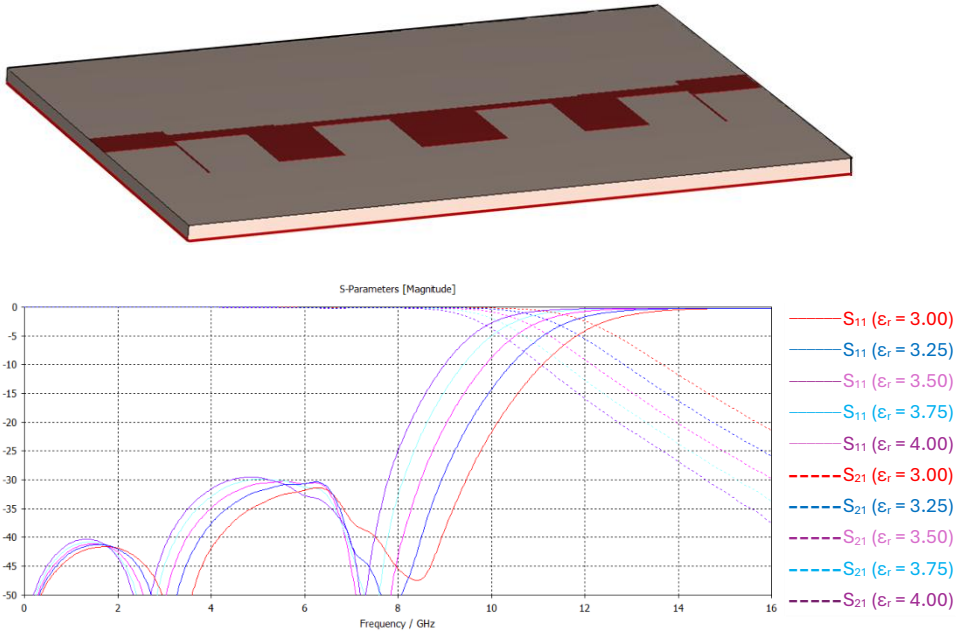

b. CST simulation results

Fig 6.2 ADS EM and CST simulations of a 5th order stub filter

6.2 Periodic-structure impedance and cell-count effects

Fig 6.3– Fig 6.5 show three families of ADS/Momentum simulations (with supporting plots of $|Z|$, $\Re\{Z\}$, $\Im\{Z\}$ overlaid on S-parameters) that quantify how unit-cell impedance and the number of repeated cells shape the band-pass response of periodic microstrip lattices realized on the BL037 liquid-crystal substrate ($\varepsilon_{r\perp}\approx2.2$, $\varepsilon_{r\parallel}\approx2.7$). Each family uses a different unit cell (non-symmetric single-sided stub; symmetric two-sided stub; symmetric single-sided stub with end matching), and each is swept in both dielectric state ($\varepsilon_{r\perp}$ vs. $\varepsilon_{r\parallel}$) and cell count. Common observations across all three sets (links to §5.6.2 and §5.6.4):

- Passband occurs when the input/Bloch impedance is close to 50 Ω: Wherever $|Z_{in}|\approx50$ Ω and the reactance is small ($\Im\{Z\}\rightarrow0$, with the sign set by the chosen topology), the structure exhibits a band-pass with $|S_{11}|\gtrsim10$–15 dB. This directly illustrates §5.6.2: the unit-cell impedance profile controls the dispersion and determines where the Bloch impedance becomes real and matches the feed, enabling propagation.
- Reactive signature depends on the unit cell (still consistent with §5.6.2): In the non-symmetric cell (Fig. 6.3), $\Im\{Z\}$ is negative in the passband (capacitive signature). In the symmetric two-sided cell (Fig. 6.4), $\Im\{Z\}$ is positive in the passband (inductive signature). In both cases, what matters for low reflection is that the reactance magnitude is small around the target band while $|Z_{in}| \approx 50$ Ω.
- Dielectric tuning shifts the same passband in the physically consistent direction. For a fixed band index, increasing ε_r (e.g., from $\varepsilon_{r\perp}\approx2.2$ to $\varepsilon_{r\parallel}\approx2.7$) moves the band downward in frequency ($f \propto 1/\varepsilon_{eff}^{1/2}$); decreasing ε_r shifts it upward. Apparent "opposite" movement happens only if different passbands are compared. This aligns with §5.6.2's phase-advance/shunt-susceptance view of the Bragg/passband condition.
- Increasing the number of cells widens the passband, but with diminishing returns, with a single stub the response is very narrow (notch-like). As the cell count increases (e.g., 4, 7, 10–15 cells), the useable passband widens and in-band $|S_{11}|$ improves (e.g., ~2

GHz with 4 cells and ≥10 dB return-loss; ~4 GHz with ~10–15 cells and ≈15 dB average return-loss in Fig. 6.4. This validates §5.6.4: more cells sharpen the transitions and deepen stopbands, but bandwidth growth saturates beyond a certain N because the dispersion curve is set by the unit cell. You gain selectivity and rejection, at the expense of length and group delay.

- End matching matters (interface to §5.6.1), In Fig 6.5, adding short tapered/quarter-wave matching sections at the ends reduces in-band ripple and improves |S11|, consistent with §5.6.1's guidance on feed-line impedance and transitions.

Fig 6.3– Non-symmetric, single-sided stub cell (1, 2, 3, 4 cells): Designed for ~60 GHz at $\varepsilon_{r\parallel}\approx 2.7$; at $\varepsilon_{r\perp}\approx 2.2$ the centre shifts upward (toward ~65 GHz). With 4 cells the passband reaches ~2 GHz with $|S_{11}|\approx 10$ dB. $\Im\{Z\}$ is negative in-band (capacitive signature). This set also shows that higher-anisotropy LC (e.g., GT3-23001) would increase separation between tuneable bands.

Fig 6.4– Symmetric, two-sided stub cell (1, 2, 3, 4, 7, 15 cells): Same design target; at $\varepsilon r\perp\approx 2.2$ the band shifts (here, downward to ~55 GHz). With ~15 cells the passband is ~4 GHz wide and average $|S_{11}|\approx 15$ dB. $\Im\{Z\}$ is positive in-band (inductive signature). This is a clean validation of §5.6.4's N-dependence with diminishing returns.

Fig 6.5– Symmetric, single-sided stub with input/output matching (1, 4, 7, 15 cells): Same tuning direction as above (lower εr → upward shift of the same passband). End matching improves in-band return loss and reduces ripple. $\Im\{Z\}$ is negative in-band (capacitive). Narrower feed lines help match the lattice, while slightly longer feeds also reduce parasitic coupling between adjacent stubs.

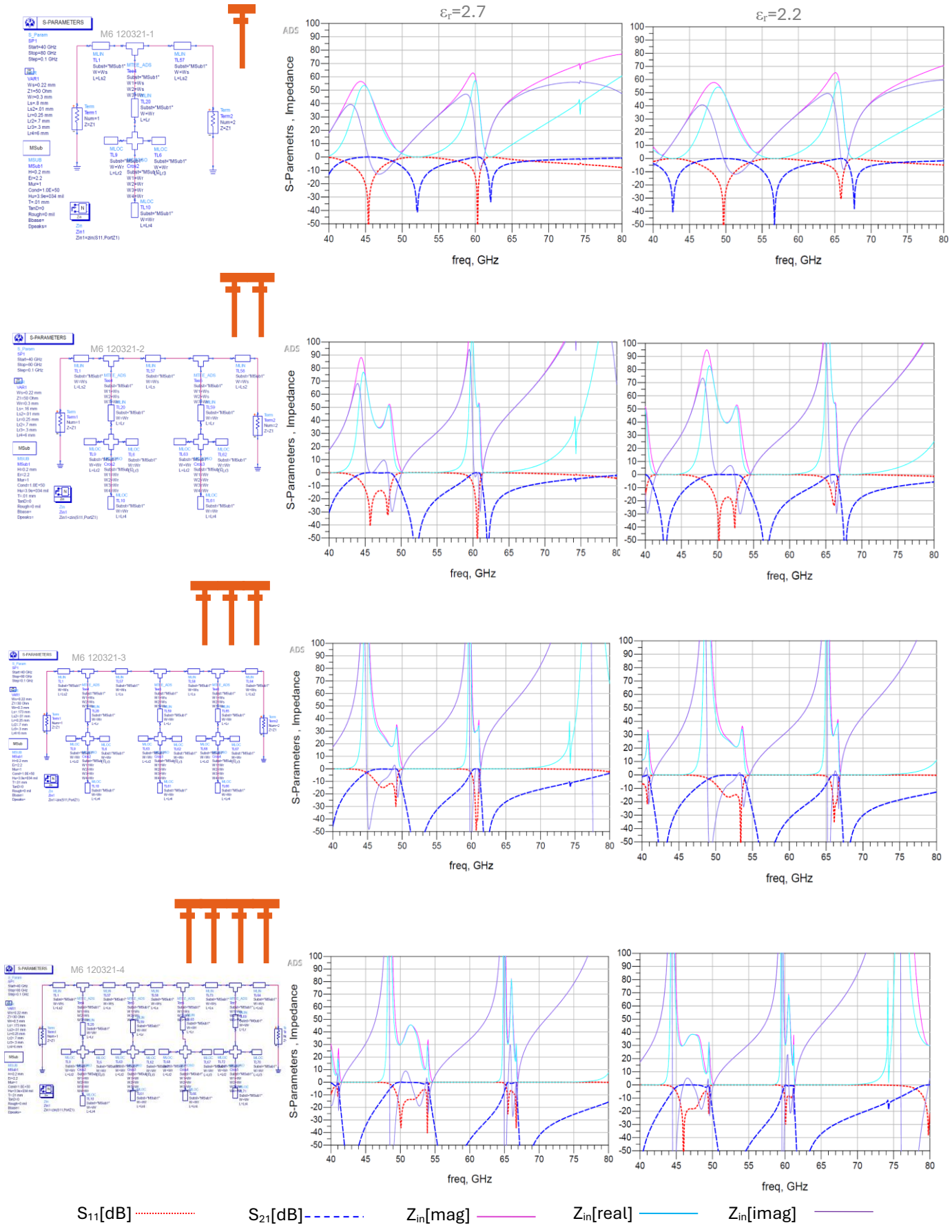

Fig 6.3 ADS simulations of non-symmetric single-sided stub filter (1, 2, 3, 4 cells)

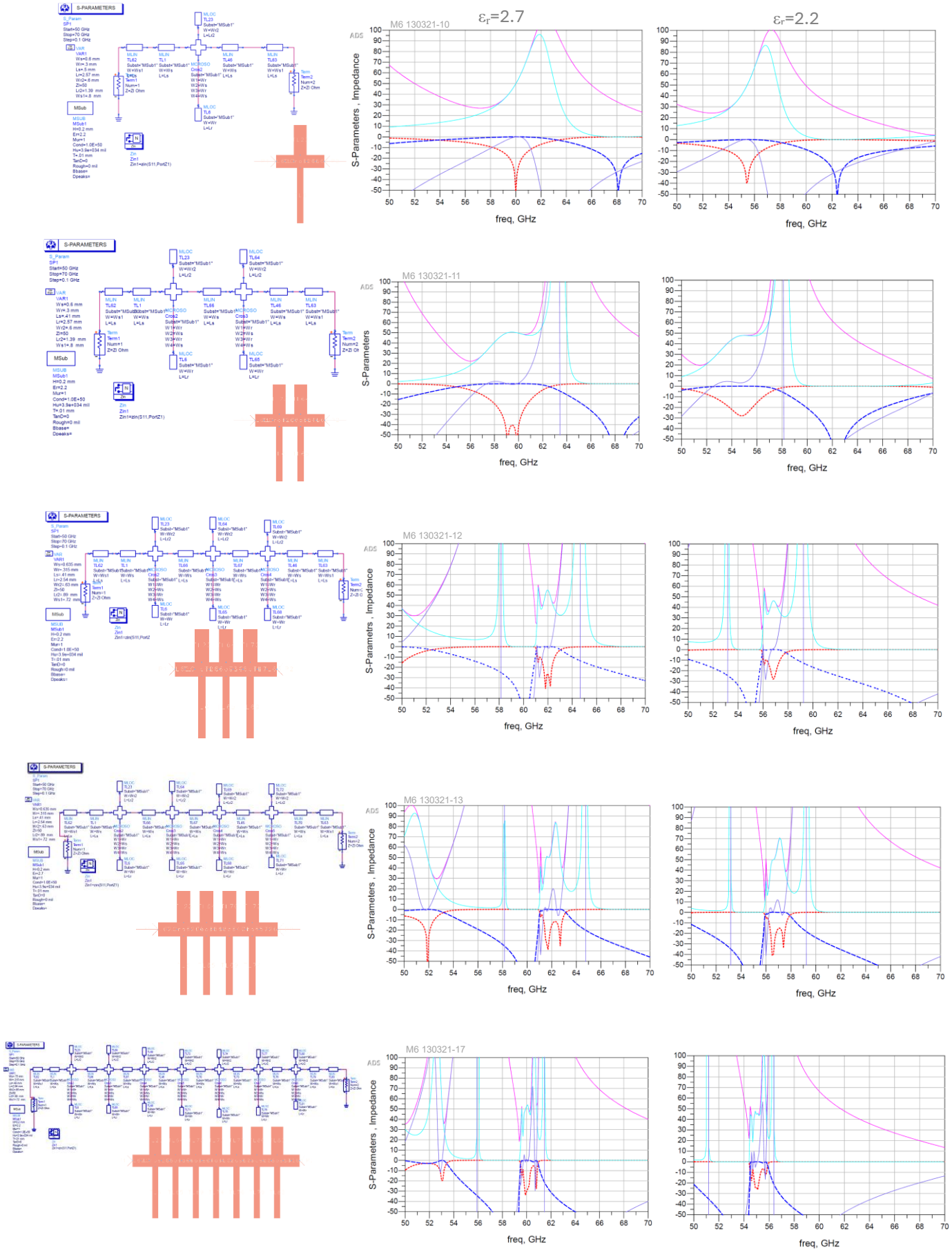

Fig 6.4 ADS simulations of symmetric, two-sided stub cell filter (1, 2, 3, 4, 7 cells)

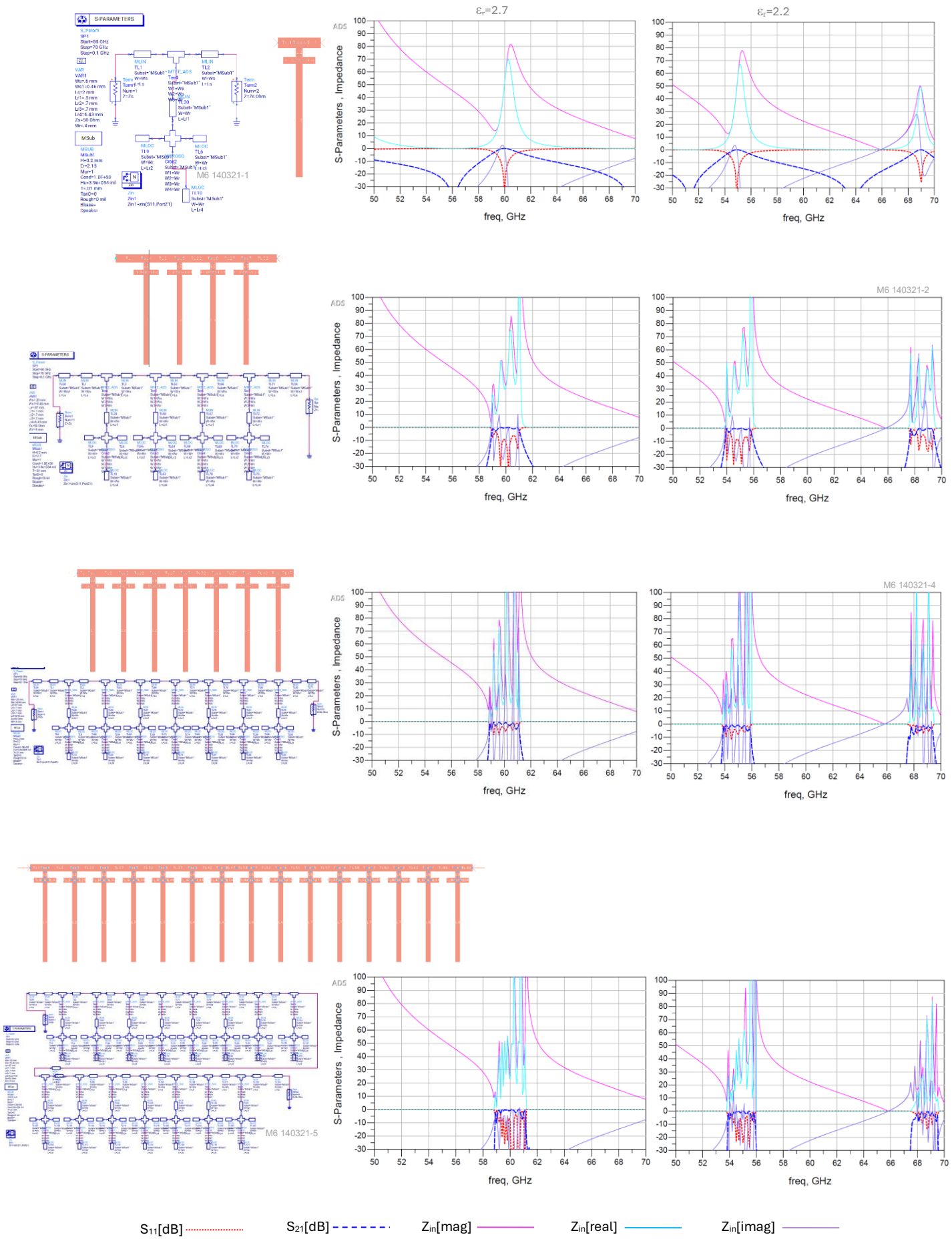

Fig 6.5 ADS simulations of symmetric one side filter (1, 4, 7, 15 cells)

6.3 Designed Periodic-structure Simulation Results

This section validates three periodic microstrip topologies (T1–T3) shown in Fig 6.6 by comparing ADS Momentum and CST Studio full-wave simulations with the MATLAB periodic-ABCD predictions developed in Chapter 5. The three unit-cell families used by the MATLAB calculators are shown in Fig 6.6 : (T1) single-sided open-stub periodic line; (T2) symmetric double-stub unit cell; (T3) a stepped/nested ladder variant. For the case studies we use N=5, 7, and 9 cascaded cells for T1–T3 respectively (see schematics in Fig 6.7a, Fig 6.8a, Fig 6.9a). All EM plots are renormalised to 50 Ω. Unless stated otherwise, the stack follows Substrate_LC60GHz (Cu 17 µm / polyimide 2.5 µm / LC 0.200 mm / polyimide 2.5 µm / Cu 17 µm) under a 0.5 mm lid, εr ≈ 2.2, with open/PML boundaries and full-face waveguide ports in CST (edge ports in Momentum). Two LC dielectric states are evaluated: $\varepsilon_r \approx 2.2$ (red) and $\varepsilon_r \approx 2.7$ (blue).

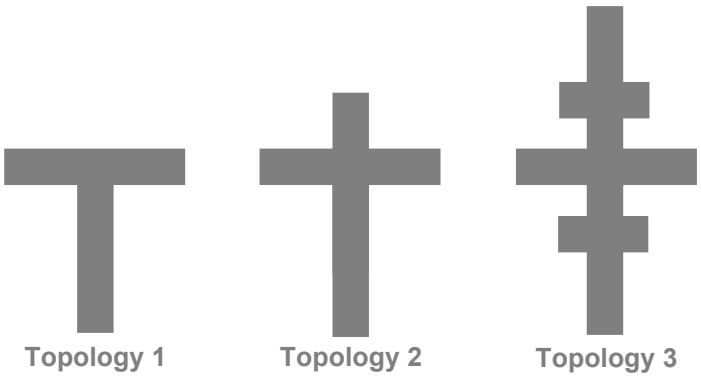

Fig 6.6 Unit Cell Topologies for Calculation Programmes

For a given N and geometry, the MATLAB periodic-ABCD (lossless unless loss is included) predicts the passband where the Bloch/input impedance approaches 50 Ω and Bragg edges near $\beta d \approx \pi \beta d \approx \pi$. In EM, the same passband appears as a peak in S_{21} with coincident minima in S_{11}; increasing εr lowers the centre frequency f_0 (longer electrical length) and typically tightens the bandwidth slightly, consistent with the dispersion picture in §5.5 and the Γ-based validation of §5.8.

Topology 1 - single-sided stub periodic line (N = 5) : Fig 6.7 overlays ADS (solid), CST dashed) and MATLAB (dotted) for both εr states. The S11 plot (Fig 6.7b) shows deep minima clustered around ~60 GHz for $\varepsilon_r \approx 2.2$ (red) and ~55–56 GHz for $\varepsilon_r \approx 2.7$ (blue), matching the MATLAB notches within a few percent. The corresponding S_{21} peaks (Fig 6.7c) align at the same f_0 values, with EM insertion loss slightly higher than MATLAB (expected: MATLAB curves are effectively loss-lite; EM includes copper roughness and tan δ). Small extra ripples/notches in EM near the upper Bragg edge are attributable to feed steps/tees and local junction capacitances that are not present in the idealised unit-cell ABCD.

Notes. Momentum ports need to span the line plus a modest lateral margin; excessively wide ports can couple into higher modes and soften the upper stopband. CST sensitivity to id/PML height shows up first as shallow oscillations on the blue S_{21} beyond ~64 GHz—tighten mesh and keep ≥5 mm clearance.

Topology 2 - symmetric two-sided stub unit cell (N = 7): Fig 6.8 demonstrates the expected flatter passband and more symmetric stopbands due to the cell symmetry. MATLAB correctly predicts the down-shift of $f0$ when εr increases (blue vs red) and the slightly narrower bandwidth. In S11 (Fig 6.8b) the EM minima for $\varepsilon_r \approx 2.2$ gather near ~60 GHz and for $\varepsilon_r \approx 2.7$ near ~55 GHz, consistent with the T1 trend. S_{21} (Fig 6.8c) shows good ADS↔CST agreement on passband frequency; CST's stopband sometimes appears marginally deeper because its full face ports and explicit lid model capture fringing better. Any small amplitude gap to MATLAB (0.2–0.5 dB) is explained by conductor and dielectric losses (Cu roughness ≈1 μm; LC tan $\delta \approx 0.001$; polyimide tan $\delta \approx 0.005$).

Topology 3 - stepped/nested ladder variant (N = 9): Fig 6.9 (TOP3_9cells) shows a sharper transition and deeper first stopband than T1/T2—an expected outcome of stronger dispersion from the stepped/nested loading. MATLAB predicts a crisp passband with steep skirts; ADS and CST follow the same trend, while revealing additional parasitic zeros near the upper stopband from the extra junctions in the stepped cell. The εr sweep again produces a monotonic

downward shift of f (red → blue), with bandwidth modestly reduced at εr ≈ 2.7. Agreement on f_0 is typically within ~2–3 %; the remaining differences are dominated by port referenceplane ignment and by the small series inductance/step capacitance of the feed transitions, which are intentionally abstracted in the lumped ABCD.

Consolidated observations (T1–T3) : Tuning behaviour is consistent across tools. Increasing εr from ~2.2 to ~2.7 lowers f_0 by roughly 6–7 % and slightly narrows BW, visible in S_{11} minima and S_{21} peaks in Fig 6.7- Fig 6.9 and reproduced by MATLAB.

Topology trends hold. As N increases (5→7→9) and the cell becomes more dispersive (T1→T2→T3), passband skirts steepen and stopbands deepen, with MATLAB giving the correct qualitative and near-quantitative behaviour.

Amplitude gaps are explainable. MATLAB curves sit ~0.2–0.5 dB higher in passband because EM includes conductor roughness and dielectric losses plus radiation/leakage captured by the open boundaries.

Reflection-coefficient validation. Across all three figures, $|S_{11}|$ minima coincide with the frequencies where the periodic Bloch/input impedance approaches 50 Ω, as derived in Chapter 5 (and used in the Γ recursion). Rapid S_{11} phase rotation at the Bragg edges (not shown here but present in the EM data) confirms the predicted sign change of the Bloch reactance.

Topology	LC εr	MATLAB f_0 (GHz)	ADS f_0 (GHz)	ADS error (%)	CST f_0 (GHz)	CST error (%)
T1 (N=5)	≈ 2.2	61.0	61.5	+0.8	61.0	0
	≈ 2.7	56.0	56.2	+0.4	55.6	-0.7
T2 (N=7)	≈ 2.2	60.5	60.8	+0.5	60.2	-0.5
	≈ 2.7	55.5	55.2	-0.5	55.0	-0.9
T3 (N=9)	≈ 2.2	63.0	63.2	+0.3	62.7	-0.5
	≈ 2.7	57.8	57.2	-1.0	56.9	-1.6

Table 6.1 Centre frequency comparison (EM vs MATLAB)

Table 6.1 consolidates the centre-frequency agreement between MATLAB and full-wave EM. Across the three topologies and two dielectric states, the mean absolute f_0 error is ≈0.6 % for ADS and ≈0.7 % for CST, confirming that the periodic-ABCD model predicts the passband location to within a few tenths of a gigahertz. The LC permittivity change from $\varepsilon_r \approx 2.2$ to $\varepsilon_r \approx$

2.7 produces a consistent down-shift of f_0 of ≈8.3 %, observed in both EM tools and reproduced by MATLAB. The small amplitude differences (EM slightly lower $|S_{21}|$) are attributable to conductor roughness and dielectric loss, which are intentionally simplified in the MATLAB model.

The 'MATLAB calculation' results shown in Fig 6.7, Fig 6.8 and Fig 6.9 are obtained from an analytical model based on the ABCD matrix representation of the periodic unit cell, as outlined in Fig 5.34. The unit-cell ABCD parameters are derived under quasi-TEM assumptions and cascaded to form an N-cell periodic structure, after which the overall network response is converted to S-parameters. These calculations are implemented in the integrated MATLAB scripts described in Appendix C. Unlike ADS Momentum and CST, which are full-wave electromagnetic solvers including discontinuities, radiation, and loss mechanisms, the MATLAB model represents an idealised analytical prediction. Consequently, the MATLAB responses appear smoother and broader; however, the centre-frequency locations, passband formation, and dielectric-tuning trends closely follow those predicted by the EM simulations. This agreement confirms the validity of the proposed OE–RC–ABCD analytical workflow while clarifying the different roles of analytical and full-wave models.

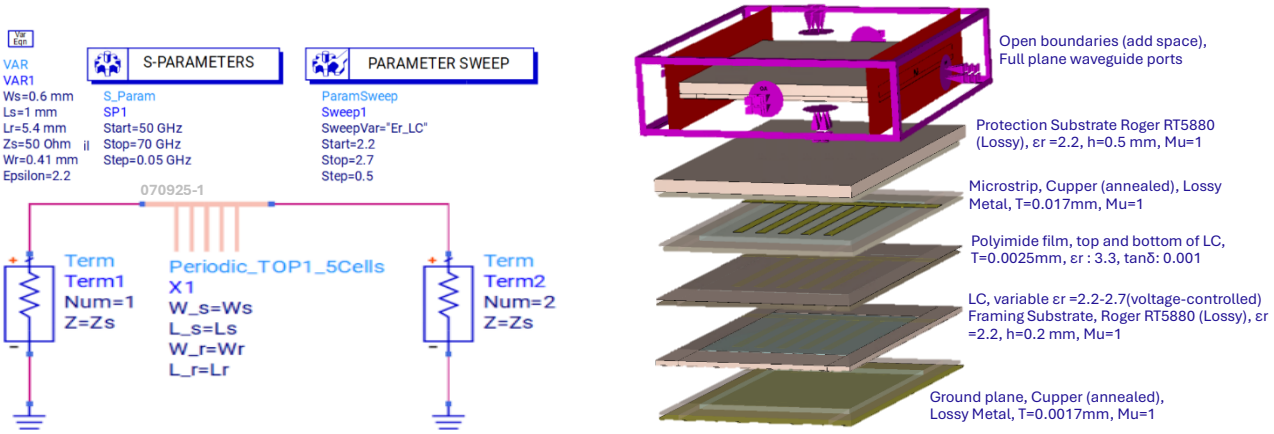

a. ADS EM and CST models of designed filter (topology 1)

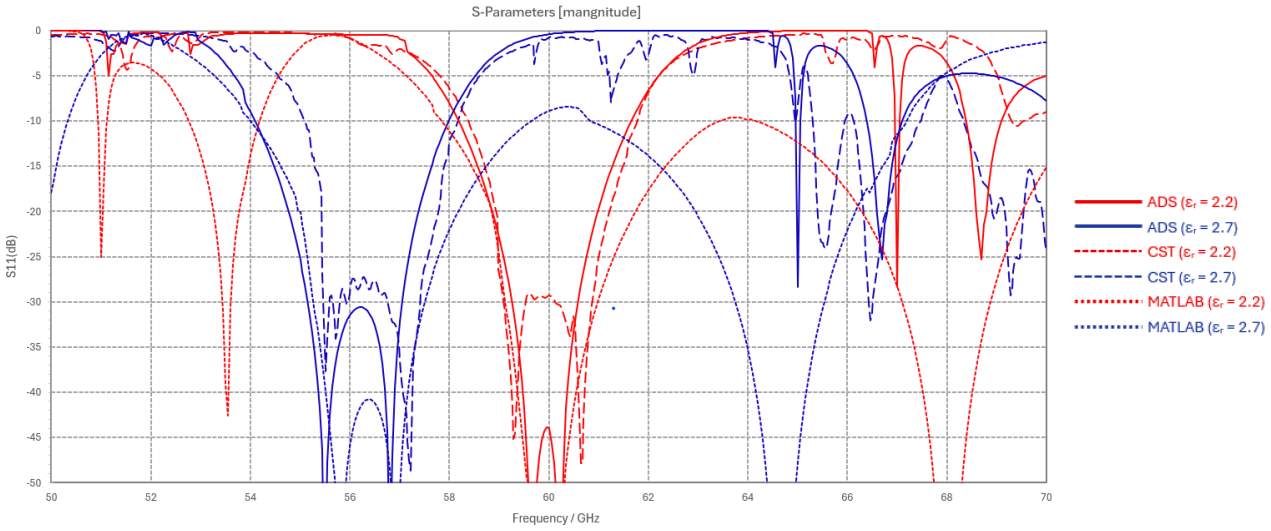

b. S_{11} results

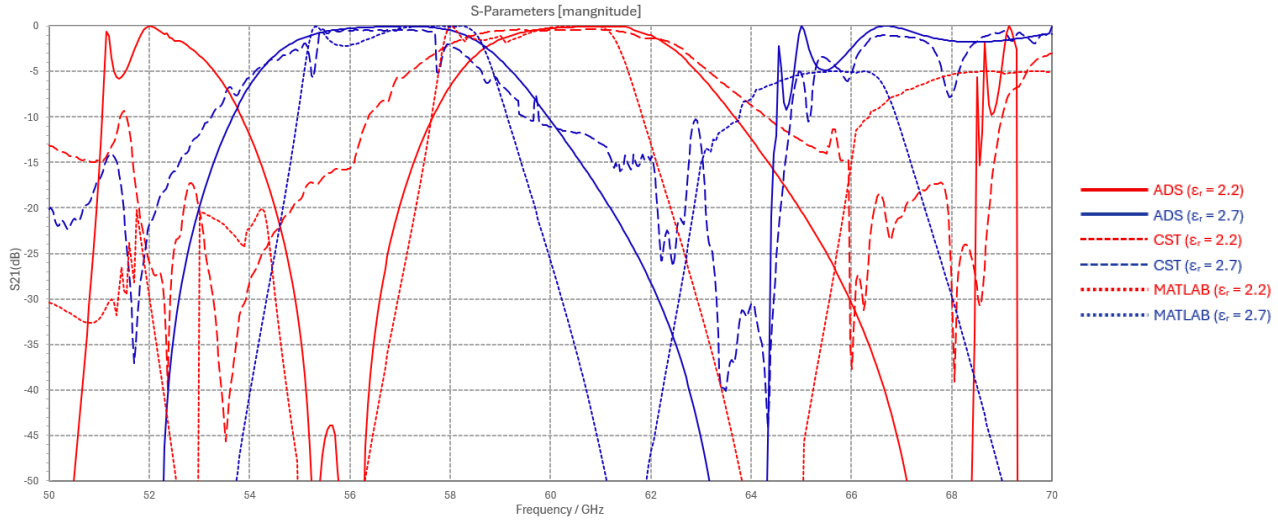

c. S_{21} results

Fig 6.7 Topology 1 (N=5), simulation results vs MATLAB calculations

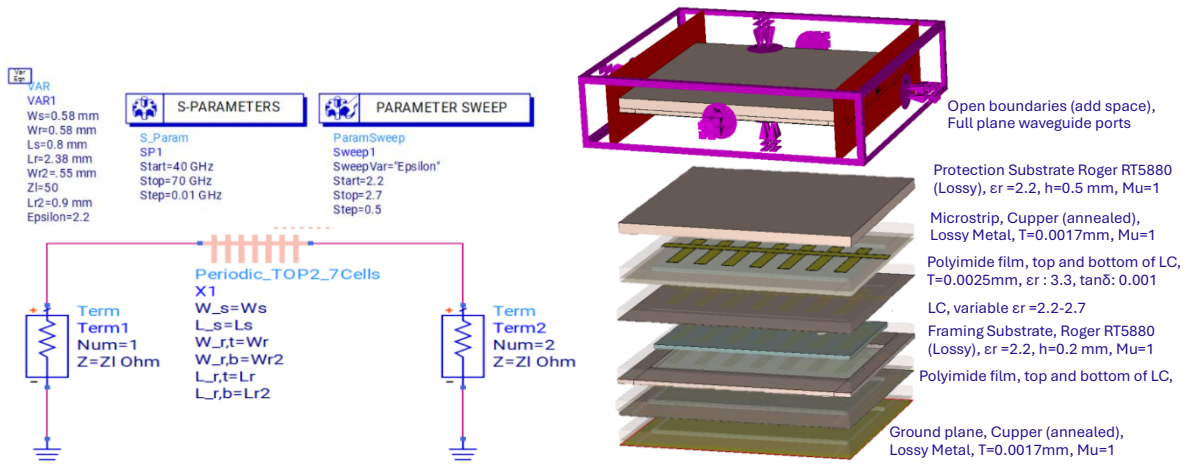

a. ADS EM and CST models of designed filter (topology 2)

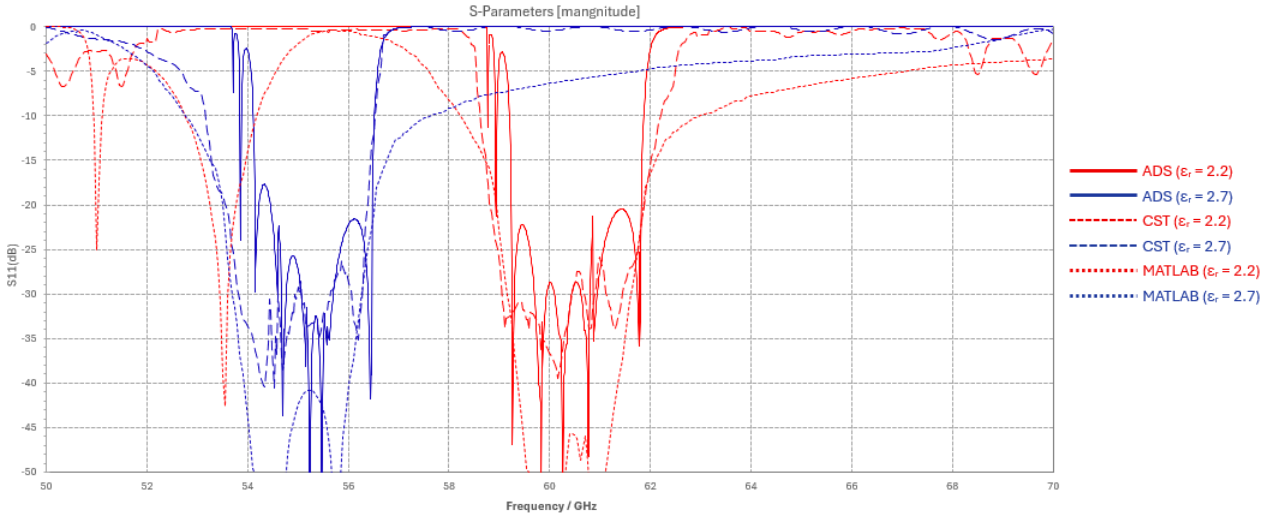

b. S_{11} results

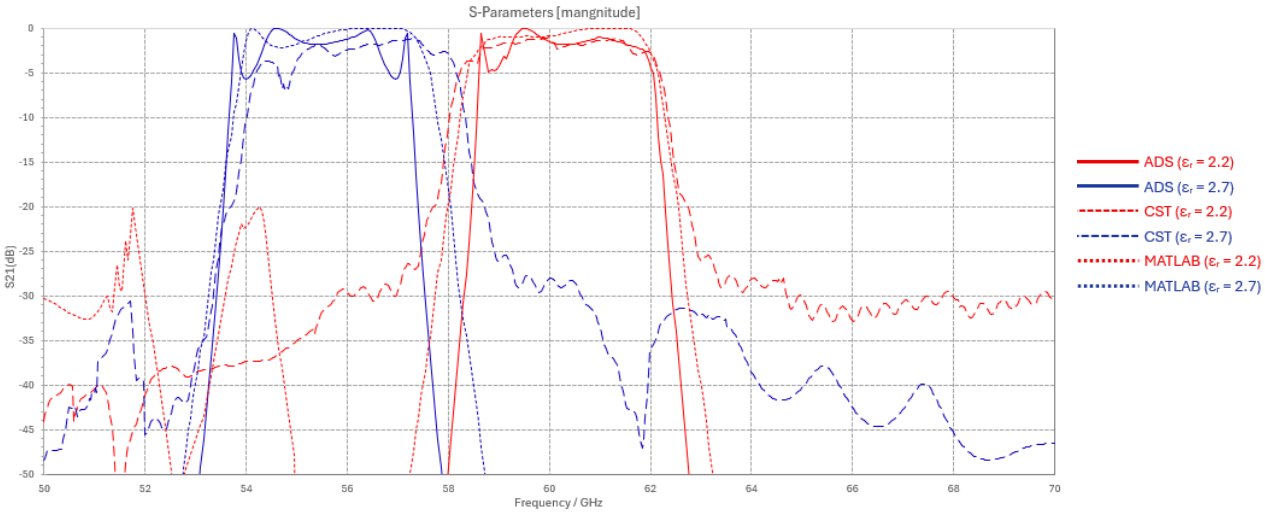

c. S_{21} results

Fig 6.8 Topology 2 (N=7), simulation results vs MATLAB calculations

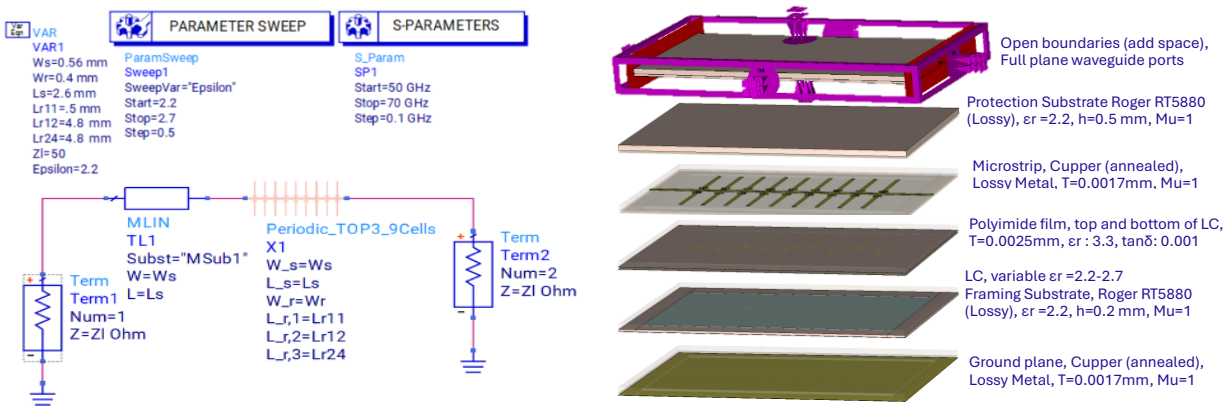

a. ADS EM and CST models of designed filter (topology 3)

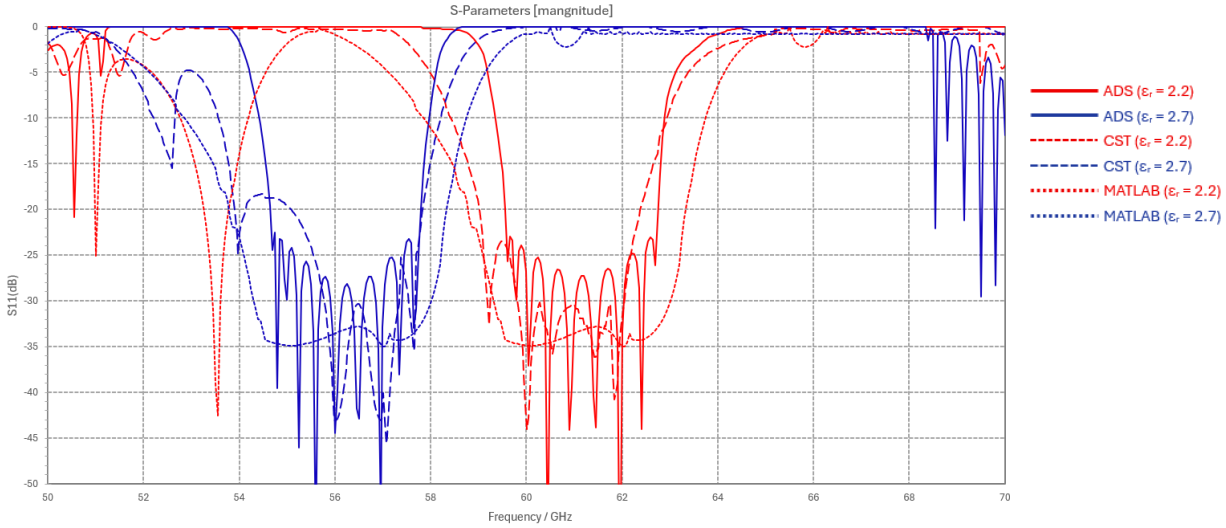

b. S_{11} results

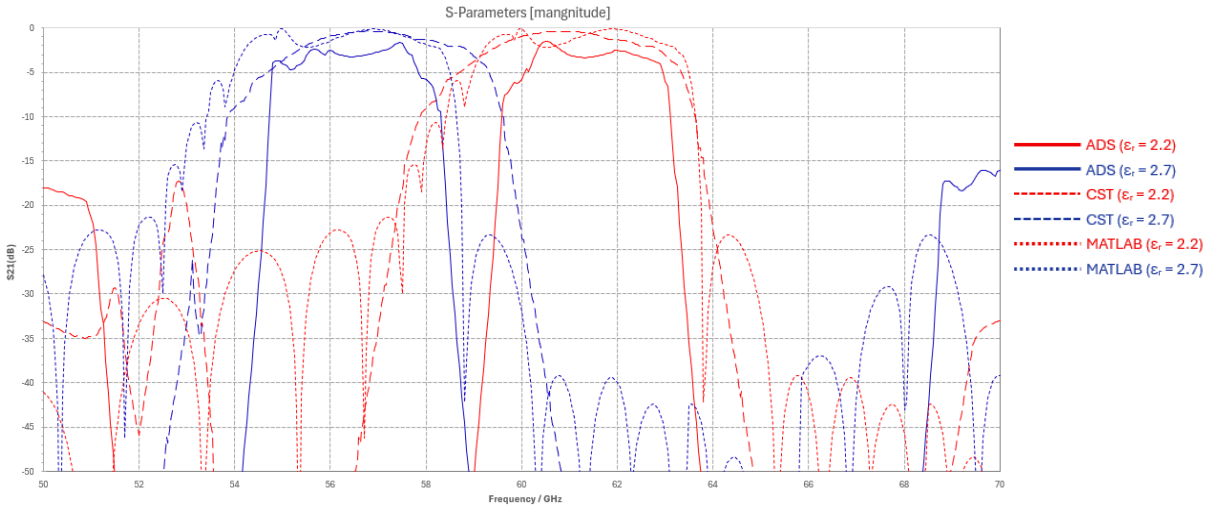

c. S_{21} results

Fig 6.9 Topology 3 (N=9), simulation results vs MATLAB calculations

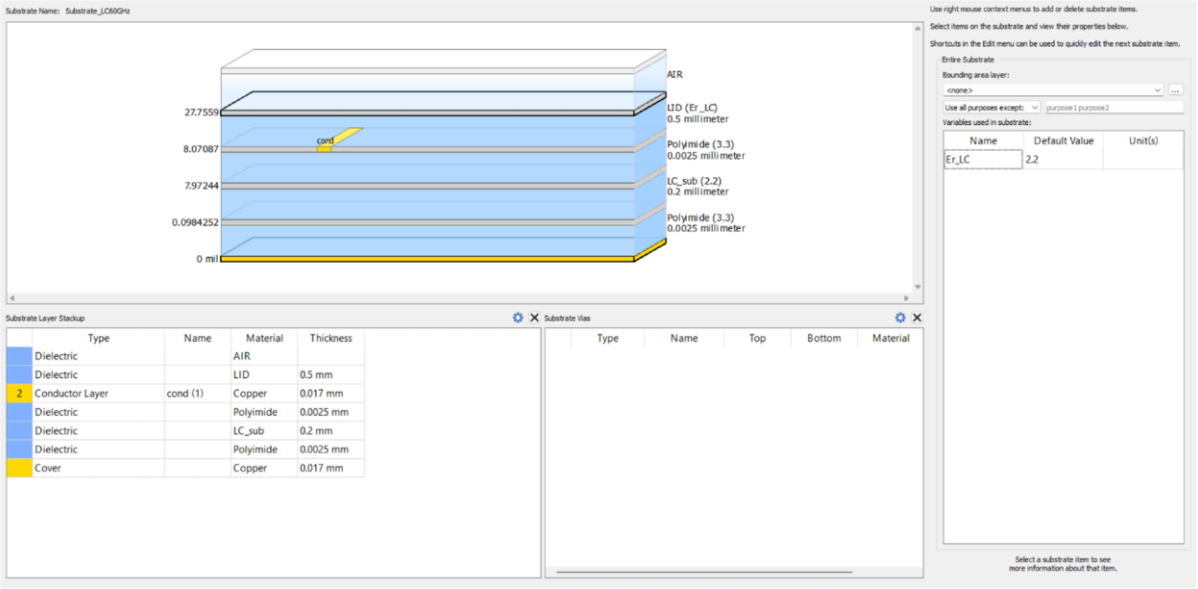

Fig 6.10 ADS stack and ε_r-sweep configuration (Momentum)

ADS stack and εr-sweep configuration (Momentum):

In ADS Momentum the substrate was defined as Substrate_LC60GHz (planar stack uniform over the layout): Cu 17 µm / PI 2.5 µm / LC 0.200 mm / PI 2.5 µm / Cu 17 µm, with a 0.5 mm lid ($\varepsilon_r \approx 2.2$) modelled as a superstrate layer. Conductor roughness ≈1 µm; losses: LC tanδ ≈ 0.001, PI tanδ ≈ 0.005. The LC layer's relative permittivity was exposed as an equationvariable Epsilon and bound to the LC dielectric (ε_r = Epsilon in the EM substrate editor). A PRAMETER SWEEP block evaluated Epsilon ∈ {2.2, 2.7} per EM run. Ports were edge ports, renormalised to 50 Ω with reference planes at the feed line ends; radiation boundaries were 'open' with ≥5 mm clearance; mesh was frequency-adaptive with local refinement at tees/steps/stub tips. Because Momentum uses a single uniform stack laterally, frame regions with fixed εr were omitted in ADS and are instead captured in the CST models; this explains small ADS ↔ CST stopband differences.

Packaging considerations:

The simulation results presented in Fig 6.7- Fig 6.9 and the substrate definition in Fig 6.10 focus on the intrinsic electromagnetic behaviour of the proposed LC-based periodic microstrip

filters. The ADS Momentum and CST models include the full multilayer substrate stack, metallisation thickness, LC cavity, and bias-dependent permittivity variation, but do not explicitly incorporate external packaging elements such as metallic enclosures, lids, wire-bond transitions, or hermetic sealing structures. Consequently, the reported responses represent the un-packaged filter performance under controlled and repeatable boundary conditions.

In practical implementations, packaging can introduce additional parasitic capacitances, cavity resonances, and radiation leakage, which may lead to small shifts in centre frequency, modified ripple levels, or Q-factor degradation, particularly at millimetre-wave frequencies. However, these effects are highly dependent on enclosure geometry, assembly tolerances, and bias-network routing, and are therefore implementation-specific rather than topology-specific. For this reason, packaging co-design is treated as a subsequent integration step, while the present study isolates and validates the proposed OE–Γ–ABCD synthesis workflow and its tunability trends. The comparative simulations in this chapter demonstrate that the observed frequency agility and sensitivity enhancement are governed primarily by periodic dispersion and LC permittivity variation, and are expected to remain valid when appropriate packaging is applied.

Chapter7 : Conclusions and Future Works

7.1 Conclusions

The rapid and comprehensive expansion of telecommunication systems operating in the 60 GHz spectrum, together with the requirement for frequency-tunable front-end components, provided the principal motivation for this research into millimetre-wave (MMW) tunable filters. Among the available architectures, microstrip periodic structures have been shown to provide robust, compact, and fabrication-friendly performance for band-pass filtering at these frequencies. In parallel, liquid-crystal (LC) substrates offer a practical and cost-effective means of achieving tunability through controlled permittivity, while remaining compatible with established microwave fabrication processes.

This thesis has presented a systematic framework for the design and analysis of LC-tunable periodic microstrip filters centred at 60 GHz. The theoretical basis drew upon the dispersion and impedance properties of periodically loaded transmission lines. The kd–βd diagram was employed to interpret the relationship between unit-cell reactance and the formation of passbands and stopbands, while the concept of Bloch impedance was applied to terminated periodic structures to identify conditions for passband transmission and to describe reflection behaviour. Complementary to S-parameter analysis, input-admittance and reflection-coefficient formulations were introduced as validation tools for predicting the behaviour of candidate unit cells. The research objectives were achieved by:

(1) Established a physics-based framework (kd–βd, Bloch impedance) and mapped LC permittivity changes to passband/stopband movement via ABCD/eigen analysis.

(2) Converted the theory into a compact design workflow that produces manufacturable geometries and predicted S-parameters before EM simulation.

(3) Verified the predictions by overlaying analytical S-parameters with ADS/CST results for several unit-cell cases and LC states, confirming accuracy and generality.

(4) Documented practical trade-offs (e.g., number of cells, symmetry/asymmetry, SIR vs. stub loading) to meet targets on bandwidth, insertion loss, and return loss.

On this theoretical and numerical foundation, a design methodology was proposed to translate dispersion and impedance requirements into practical unit-cell geometries. Several configurations were investigated, including simple open stubs, stepped-impedance resonators (SIRs), multi-SIR combinations, and both symmetric and asymmetric topologies. Circuit- and EM-level simulations in Keysight ADS and CST were employed to verify the analytical predictions, and optimisation routines were applied to refine geometrical parameters and improve return loss, insertion loss, and stopband rejection. The influence of the number of repeated cells was also examined, confirming the expected trade-offs between selectivity, insertion loss, and ripple behaviour.

In parallel, LC material properties were reviewed, with particular focus on molecular orientation and the associated anisotropy between vertical and horizontal permittivity states. Incorporating these models into the substrate demonstrated that modest variations in effective permittivity due to LC biasing can shift passband centre frequency and bandwidth significantly. This confirmed the suitability of periodic structures as a platform for tunable filters in the 60 GHz range.

Main contributions and findings:

- Unified, low-order design driver that links periodic-structure physics to geometry and predicted S-parameters—reducing trial-and-error EM sweeps.
- Predictive formulation for how LC permittivity shifts the passband centre and stopband edges, used to size and tune the unit cell.
- Cross-validation of the analysis with ADS/CST across multiple unit-cell cases, demonstrating robustness and generality.
- Compact MATLAB workflow that automates the steps and archives intermediates for traceability.

Taken together, these contributions form a coherent body of work, which are summarised in Fig 7.1. The figure illustrates how the research can be grouped into four domains. First, the adaptation of established periodic-structure concepts such as kd–βd diagrams and Bloch impedance to the context of LC-tunable filters. Second, the development of a design methodology combining odd–even mode analysis, reflection-coefficient-based validation, and ABCD/eigen-matrix techniques into a repeatable workflow. Third, the investigation of unit-cell designs, including stubs, SIRs, and multi-SIR structures, together with an assessment of symmetry versus asymmetry. Finally, demonstrations that LC substrates at 60 GHz can provide practical frequency tunability, validated through simulations. Each contribution represents a distinct element of the overall framework, which collectively establishes a systematic approach to the design of LC-tunable periodic microstrip filters.

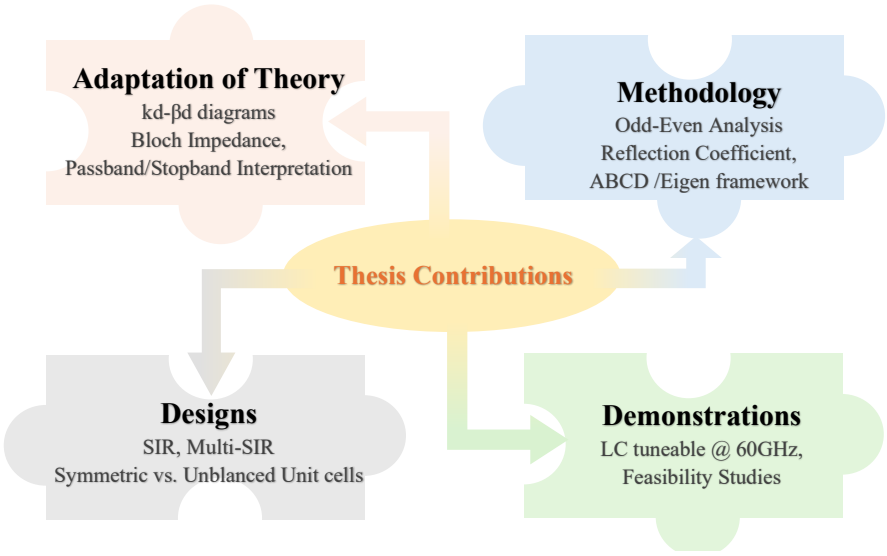

Fig 7.1 Summary of contributions

Positioning vs. state-of-the-art and technical value: Compared with alternative tunable-filter technologies (varactor/PIN/MEMS, SIW/waveguide), the proposed LC–periodic microstrip approach is fully planar, fabrication-friendly, and bias-reconfigurable at 60 GHz. Its novelty lies in the repeatable, analysis-driven workflow (rather than a single bespoke geometry), which shortens design cycles, clarifies trade-offs, and provides fast, quantitative predictions that agree with EM tools—thereby offering practical engineering value.

7.2 Future Works

The present study has demonstrated the feasibility of LC-tunable periodic filters through theoretical analysis, numerical computation, and circuit/EM simulation. Several areas remain open for future exploration. The most immediate step is fabrication and experimental validation, since only through prototyping can the accuracy of the proposed design methodology be confirmed under realistic manufacturing tolerances. At 60 GHz, where the free-space wavelength is approximately 5 mm, the required conductor widths and spacings are correspondingly small. When the microstrip width becomes comparable to or smaller than the substrate height, a significant fraction of the electromagnetic field propagates in the fringing region. This increases sensitivity to fabrication accuracy, environmental stability, and LC molecular alignment. The fabrication process is therefore expected to present challenges, particularly for complex multi-stub or asymmetric structures.

Experimental validation risks and mitigation strategies:

While this thesis has focused on analytical modelling and EM-based validation, experimental realisation at 60 GHz introduces several practical risks that must be carefully managed to ensure successful validation of the proposed theory:

First, fabrication tolerances become critical at millimetre-wave frequencies, where conductor widths, stub lengths, and inter-cell spacing are a small fraction of the guided wavelength. Deviations in lithography, etching, or substrate thickness can shift the passband centre frequency and alter stopband formation, potentially masking the intended dispersion-driven tuning effects. This risk can be mitigated by conservative geometry margins derived from sensitivity analysis and by validating unit-cell behaviour through incremental prototyping.

Second, liquid-crystal integration introduces challenges related to cavity uniformity, molecular alignment, and bias-field homogeneity. Non-uniform LC filling, air bubbles, or imperfect alignment layers may reduce effective tunability or introduce hysteresis not captured by the idealised models used in this thesis. Mitigation strategies include controlled spacer definition,

vacuum-assisted LC filling, and pre-tilt alignment techniques to stabilise molecular orientation prior to RF testing.

Third, packaging and interconnection effects represent a further source of discrepancy between theory and experiment. Bias-feed routing, enclosure parasitics, and probe or connector transitions may introduce additional resonances or losses that are not intrinsic to the periodic filter structure. These effects can be mitigated by co-designing the bias and RF structures, using well-characterised test fixtures, and performing calibration and de-embedding to isolate the filter response. Addressing these practical considerations will enable a rigorous experimental validation of the OE–Γ–ABCD synthesis workflow and establish confidence in its applicability to deployable 60 GHz tunable filter implementations.

A second area of future work concerns tolerance and yield analysis. Random variations in conductor dimensions, substrate thickness, or LC permittivity can have measurable effects on performance. Statistical techniques such as Monte Carlo analysis could be applied to quantify the resulting spread in filter characteristics and to assess design robustness. This would provide guidance for defining margins or guard bands in design rules. Related studies of conductor and dielectric loss, including surface roughness, alignment layers, and sealing processes, would provide further understanding of non-ideal effects at mm-wave frequencies.

Integration and packaging also represent important research directions. System-in-Package (SiP) and interposer platforms such as high-resistivity silicon, glass, or LTCC substrates offer promising routes for embedding LC-tunable filters with other front-end components. These approaches would require detailed study of biasing networks, electrode placement, and mechanical alignment to ensure stable tunability.

From a design perspective, the range of periodic unit cells could be extended to include multi-stub, pseudo-elliptic, or dual-band structures, enabling sharper transition slopes and wider tuning ranges. More detailed LC models, incorporating anisotropy and bias-dependent losses, could provide greater predictive accuracy once suitable material data are available. Finally, the

MATLAB toolchain developed in this work could be coupled with advanced optimisation methods, such as surrogate modelling or global–local search routines, to accelerate design iterations and enable co-design of filters with packaging and biasing structures.

These future research opportunities are conceptually mapped in Fig 7.2, which summarises the main directions for extending this work. The first domain, Fabrication, focuses on prototyping and measurement of LC-tunable periodic filters, together with tolerance analysis to assess the impact of dimensional and material variations. The second domain, System Integration, addresses packaging strategies and the exploration of advanced filter topologies for practical deployment. The third domain, Advanced Methods, points towards the use of enhanced optimisation techniques and co-simulation workflows to improve design efficiency and accuracy. Collectively, these directions define a pathway from the analytical and simulation-based results presented in this thesis towards practical, scalable, and deployable filter technologies for 60 GHz communications.

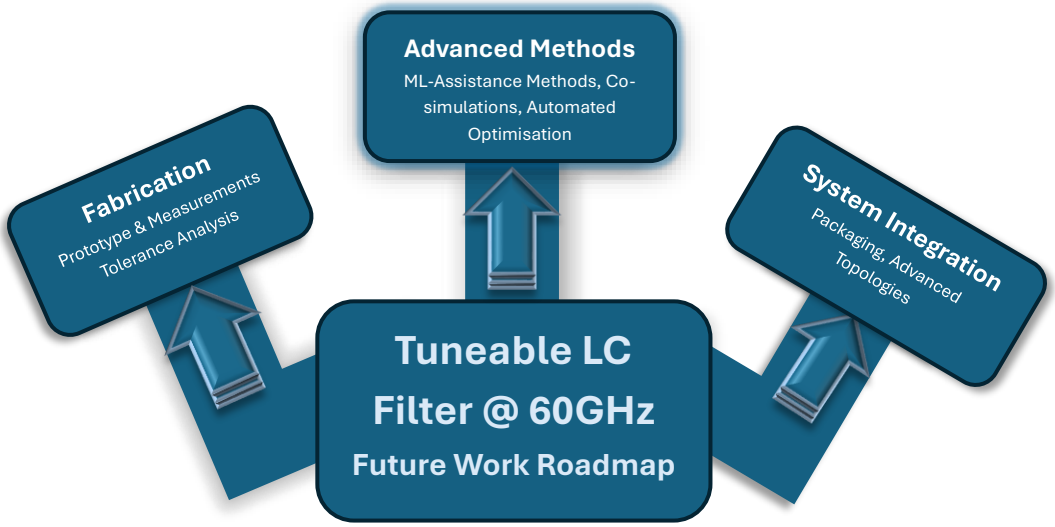

Fig 7.2 60GHz tuneable LC filter future work roadmap

References

[1] T. S. Rappaport, R. W. Heath Jr., R. C. Daniels and J. N. Murdock, Millimeter Wave Wireless Communications, New York: Prentice Hall, 2015.

[2] G. A. Siles, J. M. Riera and P. Garcia-del-Pino, "Atmospheric Attenuation in Wireless Communication Systems at Millimeter and THz Frequencies [Wireless Corner]," *IEEE Antennas and Propagation Magazine,* no. DOI: 10.1109/MAP.2015.2401796, February 2015.

[3] R.-0. E. Commission, "The development of 6G and possible implications for spectrum needs and guidance on the rollout of future wireless broadband networks," European Commission, Brussels, 14 June 2023.

[4] L. Chi, Z. Weng, Y. Qi and J. L. Drewniak, "A 60 GHz PCB Wideband antenna-in-Package for 5G/6G applications," *IEEE Antennas and Wireless Propagation Letters,* vol. 19, no. 11, November 2020.

[5] A. Babakhani, X. Guan, A. Komijani and A. Hajimiri, "A 77-GHz Phased- Array Transceiver With On-Chip Antennas in Silicon: Receiver and Antennas," *IEEE Journal of Solid-State Circuits,* vol. 41, no. 12, Dec 2006.

[6] R. &. Schwarz, "Wireless LAN at 60 GHz - IEEE 802.11 ad Explained, Application Note," Rohde & Schwarz, Application Note 1MA217.

[7] S. Missaoui and M. Kaddour, "Liquid-Crystal Based Reconfigurable Tuneable Filter with DBR Topology," *International Scholarly Research Network,* vol. 2011, no. Article ID 784615, 2011.

[8] R. Cahill, D. Linton and V. F. Fusco, "Sub-millimetre wave components for steerable antennas with supporting MMIC design," *ECIT the institute of Electronics, Communications and Information Technology.*

[9] J. Li and D. Chu, "Liquid Crystal-Based Enclosed Coplanar Waveguide Phase Shifter for 54–66 GHz Applications," *Crystals, MDPI,* 2019.

[10] T. Nose, R. Ito and M. Honma, "Potential of Liquid-Crystal Materials for Millimeter-Wave Application," *Applied Sciences,* 2018.

[11] J. Li, "Low-loss tunable dielectrics for millimeter-wave phase shifter: from material modelling to device prototyping," in *IOP Conference series, Materials Science and Engineering*, 2020.

[12] L. Cai, H. Xu and D. Chu, "Compact Liquid Crystal Based Tunable Band-Stop Filter with an Ultra-Wide Stopband by using Wave Interference Technology," *International Journal of Antennas and Propagation,* vol. 2017, no. ID 9670965, 2017.

[13] J. Torrecilla, V. Urruchi, J. M. Sanchez -Pena, N. Bennis, A. Carcia and D. Segovia, "Improving the Pass-Band Return Loss in Liquid Crystal Dual-Mode Bandpass Filters by Microstrip Patch Reshaping," *Materials,* Vols. 4524-4535, 2014.

[14] J. Torrecilla, E. Avila-Navarro, C. Marcos, V. Urruchi, J. M. Sanchez-Pena, J. Arias and M. M. Sanchez-Lopez, "Microwave Tuneable notch filter based on Liquid crystal using spiral spurline technology," *Microwave and optical technology letters,* Vols. 55 , No 10, no. Oct 2013, Oct 2013.

[15] C. Doan, S. Emami, A. M. Niknejad and R. W. Broderson, "Millimetre-wave CMOS design," *IEEE Solid-State Circuits,* vol. 40, pp. 144-155, Jan 2005.

[16] J. S. Hong and M. J. Lancaster, Microstrip Filters for RF/Microwave Application, John Wiley, 2001.

[17] A. A. Abidi, "RF CMOS comes of age," *IEEE Journal Solid-State Circuits,* vol. 39, no. No 4, pp. 549-561, Apr 2004.

[18] J. F. Berniguad, N. Martin and P. Laurent, “Liquid crystal tunable filter based on DBR topology,” in *36th European Microwave Conference (EuMC 06)*, Manchester, England, September 2006.

[19] K. Y. Chan, R. Ramer, R. R. Mansour and Y. J. Guo, “60 GHz to E-Band Switchable Bandpass Filter,” *IEEE Microwave and Wireless Components Letters,* vol. 24, no. No. 8, Aug 2014.

[20] S. Luo, C. C. Boon, L. Zhu and M. Anh Do, “A Compact Millimetre-Wave CMOS Bandpass Filter Using a Dual-mode Ring resonator,” in *2011 International Symposium on Integrated Circuits (ISIC)*, 2011.

[21] S. Xu, F. Meng, K. Ma and K. -S. Yeo, “State of the Art in Passive Bandpass Filter Solutions for 60 GHz Communications,” *ZTE Communications , Suppl. no S1,* vol. 14, pp. 14-19, Dec 2016.

[22] S. Srinath and B. Tech Alumnus, “Design of 3rd Order Coupled Line Bandpass Filter for Wireless Application using Agilent ADS,” School of Electronics Engineering, Vellore Institute of Technology, Tamil Nadu , india, July 2016.

[23] W. M. Laghari, M. Usman Baloch, M. A. Mengal and S. J. Shah, “Performance Analysis of Analog Butterworth Low Pass Filter as Compared to Chebyshev Type-I Filter, Chebyshev Type-II Filter and Elliptical Filter,” *Circuits and Systems,* no. SciRes, pp. 209-216, 2014 , 5, 20.

[24] E. G. Cristal and S. Frankel, “Hairpin line/half-wave parallel-coupled-line filters,” *IEEE Transaction Microwave Theory and Technique,* Vols. MTT-20, pp. 719-728, Nov 1972.

[25] L. Young, G. L. Matthaei and M. T. Jones, Microwave Filters, Impedance-Matching Networks, and Coupling Structures, Dedham, Mass: Artesh House, 1980.

[26] J. Gracia, J. Bonache and F. Martin, “Application of Electromagnetic Bandgaps to the Design of Ultra-Wide Bandpass Filters With Good Out-of-Band Performance,” *IEEE Transaction on Microwave and technologies,* vol. 54, no. No. 12, Dec 2006.

[27] D. M. Pozar, Periodic Structures Microwave Engineering, 4th ed, Sec.8.1, John Wiley & Sons, 4th Eddition, INC 8.1, 2012.

[28] R. E. Collin, Foundations for Microwave engineering , 2nd Ed, New York: John Wiley & Sons, Inc, 1992.

[29] Y.-W. Lin, J.-C. Lu and C.-Y. Chang, “Design of High-Order Wideband Planar Balun Filter in – Plane Bandpass Prototype,” *IEEE Transaction on Microwave Theory and Techniques,* Vols. 60 , No. 12, Jul 2012.

[30] M. Makimoto and S. Yamashita, “Bandpass filters using parallel coupled stripline stepped impedance resonators,” *IEEE Trans. Microwave Theory,* vol. 28, no. 12, pp. 1413-1417, 1980.

[31] A. K. Iyer and G. V. Eleftheriades, “Periodic structure for microwave engineering,” *IEEE Microwave Magazine,* vol. 13, no. 3, pp. 71-87, May 2012.

[32] W. Hu et al, “Liquid crystal tunable microstrip patch antenna,” *IEEE Transactions on Antennas and Propagation,* vol. 56, no. 1, pp. 13-22, 2008.

[33] C. G. Christodoulou et al, “Reconfigurable antenna for wireless and space applications,” *Proc. IEEE,* vol. 100, no. 7, pp. 2250-2261, 2012.

[34] M. Shahin et al, “60 GHz tunable microstrip filter using liquid crystal technology,” in *IEEE MTT-S International Microwave Symp.*, 2014.

[35] F. Gölden, “Tunable liquid crystal high-Q filter for milimeter -wave applications,” *IEEE Transactions on Microwave Theory and Techniques,* vol. 61, pp. 2515-2525, 2013.

[36] C. Caloz and T. Itoh, Electromagnetic Metamaterials: Transmission Line Theory and Microwave Applications, Wiley-IEEE Press, 2005.

[37] A. Fallahi and J. Perruisseau-Carrier, “Design of Tunable Biperiodic Graphene Metasurfaces,” *Physical Review B 86 (19), 195408,* 2012.

[38] A. A. Girich, A. A. Kharachenko, I. Tarapov, S. Mieszczak and J. Kols, “Microwave Surface states in periodic microstrips,” *Physics App,* 26 Feb 2019.

[39] S. Soni, D. D. Bishoni, S. Soni and Ramswroop, “Liquid Crystal and Application of Chlosteric Liquid Crystals in Laser,” *International Journal of Modern Physics Conference Series ,* vol. 22, pp. 736-740, 2013.

[40] G. A. DiLisi and J. Carroll, An Introduction to Liquid Crystals, Ohio, USA: University of Heights, Morgan & Claypool Publisher - ISBN 978-1-64327-681-6.

[41] P. Deo, D. Mirshekar Syahkal, L. Seddon, S. E. Day and F. A. Fernandez, “Microstrip Device for Broadband (15-65 GHz) Measurement of Dielectric Properties of Nematic Liquid Crystals,” *IEEE Transaction on Microwave Theory and Technologies.*

[42] P. Oswald, “Phase transitions and unwinding of cholesteric liquid crystals,” Laboratoire de Physique de l' École Normale Supérieure de Lyon, 46 allée d'Italie, Lyon Cedex , France.

[43] M. Armendariz, V. Sekar and K. Entesari, “Tunable SIW Bandpass Filters with PIN Diodes,” in *Proceeding of the 40th European Microwave Conference*, Electrical and Computer Engineering, Texas A&M University.

[44] A. Tackacs, D. Neculoiu, D. Vasilache , A. Muller, P. Pons, L. Bary and R. Plana, “Design of Tunable MEMS Filters for Millimeter Wave Systems,” in *IEEE MELECOM*, Benalmadena (Malaga), Spain , May 2006.

[45] A. k. Bain and P. Chand, Ferroelectrics: Principles and Applications, Wiley - VCH, Feb 2017.

[46] A. Aldrighi, M. Dragoman, S. Iordanescu, F. Nastase, S. Vulpe, A. Dinescu and D. Vasilache, “Low-voltage permittivity control of coplanar lines based on hafnium oxide ferroelectrics grown on silicon,” *IEEE Access,* Vols. 7 ;136686-136693. doi:10.1109/ACCESS.2019.2942430, 2019.

[47] C. H. Chen et al., “Liquid crystal technology for microwave applications,” *Progress In Electromagnetics Research,* vol. 141, pp. 197-217, 2013.

[48] P. S. Andreou, et al., “Dielectric properties of nematic liquid crystals at microwave frequencies,” *Liquid Crystals,* vol. 43, no. 13, p. 2175–2185, 2016.

[49] S. Mueller, M. Koeberle, F. Goelden, A. Penirschke, A. Lapanik, W. Haase and R. Jakoby, “W-Band Characterization of Anisotropic Liquid Crystals at Room Temperature,” in *Proceeding of the 38th European Microwave Conference*.

[50] P. Yaghmae, O. H. Karabey, B. Bates, C. Fumeax and R. Jakoby, “Electrically Tuned Microwave Devices Using Liquid Crystal Technology,” *International Journal of Antennas and Propagation,* 2014.

[51] J. Kim et al., “Polyimide-based alignment layers for liquid crystal devices,” *Molecular Crystals and Liquid Crystals,* vol. 576, no. 1, pp. 1-9, 2013.

[52] H. E. Hsu, “A study on the sealing process for liquid crystal devices,” *Journal of Electronic Packaging,* vol. 124, no. 3, pp. 233-238, 2002.

[53] D. Dolfi, M. Labeyrie, P. Joffre and J. P. Huignard, “Liquid crystal microwave phase shifter,” *Electronics Letters,* vol. 29(10), pp. 926-928, 1993.

[54] N. Martin, P. Laurent, G. Prigent, P. Gelin and F. Huret, “Technological Evolution and performances improvements of a tunable phase shifter using liquid crystal,” *Microwave and optical technology letters,* vol. 43(4), pp. 338-341.

[55] H. Zhou, L. Guo and A. Abbosh, “Liquid Crystal Tunable Stripline Phase Shifter,” in *5th Australian Microwave Symposium* , Melbourne , Australia, Feb 2003.

[56] A. Fritzsch, C. Bildik and R. Jakoby, “Tunable Ka-band phase shifter based on liquid crystals,” *IEEE MTT-S International, Microwave Symposium Digest (MTT),* pp. 1020-1023, May 2010.

[57] C. Fritzsch, F. Giacomozzi, O. Karabey, F. Goelden, F. Moessinger, A. Bildik, S. Colpo and R. Jakoby, “Tunable Ka-band phase shifter based on liquid crystals,” in *Microwave Integrated Circuits Conference (EuMIC), European IEEE (pp.522-525)*, October 2011.

[58] E. Polat et al, “Liquid Crystal Phase Shifter Based on Nonradiative Dielectric Waveguide Topology at W-Band,” *IEEE MTT-S International Microwave Symp.,* pp. 184-187, 2019 .

[59] R. Reese , M. Jost, H. Maune and R. Jakoby, “Design of a continuously tunable W-band phase shifter in dielectric waveguide topology,” *International Microwave Symposium,* 2017.

[60] M. Yazdanpanahi and D. Mirshekar-Syahkal, “Millimeter-wave liquid-crystal-based tunable bandpass filter,” *IEEE International Radio and Wireless Symposium (RWS),* pp. 139-142, January 2012.

[61] P. Yaghmaee, C. Fumeaux, B. Bates, A. Manabe, O. Karabey and R. Jakoby, “Frequency tunable S-band resonator using nematic liquid crystal,” *IEEE Electronics Letters,* vol. 48(13), pp. 798-800, 2012.

[62] R. Camley, Z. Celinski, Y. Garbovskiy and A. Glushchenko, “Liquid crystals for signal processing applications in the microwave and millimeter wave frequency ranges,” *Liquid Crystal Reviews,* vol. 6(1), pp. 17-52, 2018.

[63] F. Gaebler, A. Karabey, O. Goebel, A. Manabe and R. Jakoby, “Tunable band-pass filter based on liquid crystal. Goelden,” in *German Microwave Confernce*, 2010 - (pp. 139-142).

[64] J. Skulski and A. Szymanska, “Liquid crystal tunable microwave band stop filters,” in *In Electronic Technology Conference , International Society for optics and Photonics*, July 2013pp. 89022E-89022E.

[65] E. C. Economou et al, “Electrically tunable open stub bandpass filters based on nematic liquid crystals,” in *Phys. Rev. Appl. Vol. 8* , Dec. 2017 Art. no. 064012.

[66] Y. Liu, L. Zeng, S. Zhou, L. Li and S. McGrath, “A Wideband Millimeter-wave Tunable Filter based on Periodic Square Spiral Structure and Liquid Crystal Material,” in *31st Irish Signals System Conference Proceedings*, 2020 , pp1-4.

[67] E. Polat, F. Kamrath, S. Matic, H. Tesmer, A. Jimenez-Saez, D. Wang, H. Maune, R. Jakoby and M. Höft, “Novel Hybrid Electric/Magnetic Bias Concept for Tunable Liquid Crystal Based Filter,” *IEEE Journal of Microwaves,* vol. DOI 10.1109/JMV.2022.3180227, June 2022.

[68] T. Franke, A. Gaebler, A. E. Prasetiadi and R. Jakoby, “Tunable Ka-band waveguide resonators and a small band band-pass filter based on liquid crystals,” in *Proceeding of 44th European Microwave Conference* , 2014 , pp. 339-342.

[69] F. Kamrath, E. Polat, S. Matic, C. Schuster, D. Miek, H. Tesmer, P. Boe, D. Wang, H. Jakoby, H. Maune and M. Höft, “Bandwidth and Centre Frequency Reconfigurable Waveguide Filter Based on Liquid Crystal Technology,” *IEEE Journal of Microwaves,* vol. 2, no. No. 1, pp. 134-144, Jan 2022.

[70] D. Jiang, Y. Liu, G. Wang and Z. Zheng, “Tunable Substrate Integrated Waveguide Bandpass Filter Using Liquid Crystal Material,” *IEEE Access,* vol. 7, pp. 126265-126272, June 2019.

[71] M. Yazdanpanahi, P. Deo and D. Mirshekar-Syahkal, “Tunable Liquid-Crystal Millimeter-Wave Bandpass Filter Using Periodic Structure,” *School of Computer Sc. and Electronic Eng., University of Essex,* Vols. 978-1-4799-2181-2/14, no. University of Essex.

[72] S. Y. Huang and Y. H. Lee, "Fast and Accurate Calculation of Transmission Coefficients for an EBG Microstrip Structure," *Microwave and Optical Technology Letters,* vol. 52(4), pp. 793-797, April 2010.

[73] X. Guan and A. Hajimiri, "A 24 GHz CMOS front-end," *IEEE Journal of Solid-State Circuits,* Vols. Vol. 39 , No. 2, pp. 368-373, Feb 2004.

[74] S. Senouci and A. Zerguerras, "A Study of Periodic Microstrip Structures Using Finite Elementary Line (FEL) Approach," *American Journal of Physics and Applications,* vol. 5(4), pp. 52-59, 2017.

[75] P. J. Collings and M. Hird, Introduction to Liquid Crystals : Chemistry and Physics, London, UK: Taylor & France, 1977.

[76] P. G. Gennes and J. Prost, The Physics of Liquid crystals, 2nd ed, Oxford UK: Oxfor Univ. Press, 1993.

[77] C. Weickhmann, N. Nathrath, R. Gehring, A. Gaebler, M. Jost and R. Jakoby, "A Light-Weight Tunable Liquid Crystal Phase Shifter for an Efficient Phased-Array Antenna," in *European Microwave Conference*, 2013.

[78] M. Lei, Z. Nie, M. Yang, F. AnibalFernandez, C. Poole and S. E. Day, "A general design method for tunable microstrip devices at microwave frequency based on liquid crystal technology," Department of Electronic and Electrical Engineering, University College London,, London, United Kingdom, February 2013.

[79] V. Urruchi, C. Marcos, J. Tottcilla, J. M. Sanchez-Pena and K. Garbat, "Tuneable notch filter based on liquid crystal technology for microwave applications," *Materials (MDPI),* vol. 7, no. doi:10.3390/ma7064524, pp. 4524-4535, 2014.

[80] Z. C. Hao and J. S. Hong, "Microwave Theory Tech," IEEE Transaction 56(9) 2095 (2008), 2008.

[81] A. Ebrahimi, P. Yaghmaee, W. Withayachumnakul, C. Fumeaux, S. A. Sarawi and D. Abbott, "Interlayer Tuning of X-Band Frequency-Selective Surface Using Liquid Crystal," in *Asia-Pasific Microwave Conference Proceedings*, 2013.

[82] T. Kanda et al, "Fabrication of liquid-crystal-filled waveguide components," *IEEE Transactions on Microwave Theory and Techniques,* vol. 61, no. 1, pp. 403-410, 2013.

[83] H. H. Berger, "Contact resistance on metals," *Solid-State Electronics,* vol. 15, no. 2, pp. 145-158, 1972.

[84] N. Arnal et al, "Surface treatment and adhesion in copper–polyimide laminates," *Journal of Adhesion Science and Technology,* vol. 23, no. 1, pp. 37-52, 2009.

[85] T. Uchida and S. Kobayashi, "Liquid Crystals: Applications and Uses," *World Scientific,* 1992.

[86] A. Munoz-Cruzado, et al., "Liquid crystal infiltration and encapsulation for tunable microwave devices," *Microwave and Optical Technology Letters,* vol. 54, no. 1, pp. 212-216, 2012.

[87] J. Gao, L. Zhu, W. Menzel and F. Bogelsack, "Short-Circuited CPW Multiple-Mode Resonator for Ultra-Wideband (UWB) Bandpass Filter," *IEEE Microwave and Wireless Components Letters,* vol. 16 No. 1, March 2006.

[88] K. J. Lee and J. Lee, "Flip-chip interconnection techniques for RF and microwave devices," *IEEE Transactions on Components, Packaging and Manufacturing Technology,* vol. 9, p. 1603–1611, 2019.

[89] L. Yao, Q. Wu and H. Zhang, "Integration of liquid crystal-based tunable devices with microwave circuits," *Journal of Microwaves, Optoelectronics and Electromagnetic Applications,* vol. 20, no. 2, pp. 151-160, 2021.

[90] R. Tummala and M. Swaminathan, System-on-Package: Miniaturization of the Entire System, McGraw-Hill, 2020.

[91] M. Swaminathan and H. Shi, "Design and Fabrication of Silicon Interposers for RF Applications," *IEEE Transactions on Components, Packaging and Manufacturing Technology,* vol. 8, no. 3, pp. 472-482, 2018.

[92] M. Swaminathan, "Co-packaging of RFICs and tunable components for 5G and beyond," in *IEEE MTT-S International Microwave Symposium*, 2021.

[93] A. Vardi and D. Glikman, "System-in-package integration for RF front-ends.," *IEEE Communications Magazine,* vol. 55, no. 3, pp. 124-130, 2017.

[94] Y. Amano, A. Yamada, E. Suematsu and H. Sato, "A Low Cost Planar Filter for 60 GHz Applications," *Microwave Journal,* March 2001.

[95] N. Yang and Z. N. Chen, "Microstrip Line Periodic Structures with Capacitive and Resonant Element Loads," in *International Workshop on Antenna Technology (iWAT)*, 2005, .

[96] S. Lucyszyn, "Surface wave losses in monolithic millimetre-wave integrated circuits," *IEE Proceedings H (Microwaves, Antennas and Propagation),* vol. 139, no. 4, pp. 321-329, 1992.

[97] H. Kamada, "Reduction of Surface-Wave Loss in CMOS-Based Antenna-in-Package Modules Using High-Resistivity Silicon Substrate and Patterned Ground," *IEEE Transactions on Components, Packaging and Manufacturing Technology,* vol. 5, no. 9, p. 1246–1253, 2015.

[98] R. R. Tummala et al., "Glass as a substrate and interposer material for packaging of microelectronic and optoelectronic systems," *Journal of the American Ceramic Society,* vol. 96, no. 2, p. 491–506, 2013.

[99] C. P. Wong et al., "Low-loss glass substrates for millimeter-wave integrated passive devices," *IEEE Transactions on Components, Packaging and Manufacturing Technology,* vol. 3, no. 9, pp. 1508-1517, 2013.

[100] D. P. Sheen et al., "Low-temperature co-fired ceramic technology and applications: a review," *International Journal of Applied Ceramic Technology,* vol. 1, no. 3, pp. 230-239, 2004.

[101] J. H. Lee et al., "LTCC-based multilayer bandpass filters for wireless communication systems," *IEEE Transactions on Microwave Theory and Techniques,* vol. 49, no. 9, p. 1640–1646, 2001.

[102] M. Tentzeris, "Polymer and organic substrates for flexible and low-cost RF/microwave systems," *IEEE Transactions on Microwave Theory and Techniques,* vol. 60, no. 12, p. 3896–3906, 2012.

[103] J. C. Rautio, et al., "3-D printed microwave and millimeter-wave devices: The next fabrication frontier," *IEEE Microwave Magazine,* vol. 20, no. 4, pp. 65-75, 2019.

[104] L. Yang, et al., "3D-printed low-loss dielectric waveguides and resonators," *Additive Manufacturing,* vol. 36, p. 101575, 2020.

[105] H. T. Kim, et al, "Advanced organic interposer technologies for heterogeneous integration," *IEEE Transactions on Components, Packaging and Manufacturing Technology,* vol. 7, no. 6, p. 964–973, 2017.

[106] R. Tummala, "Heterogeneous integration on organic substrates for high-performance systems," *Proceedings of the IEEE,* vol. 103, no. 8, p. 1452–1467, 2015.

[107] J. Sor, Y. Qian and T. Itoh, "Miniature Low-Loss CPW Periodic Structures for Filter Applications," *IEEE Transactions on Microwave theory and Techniques,* vol. 49, no. No. 12, December 2001.

[108] D. Mirshekar , "EE316 RF Principles," 2009 P10-11.

[109] E. Hammerstad and Jensen, "Accurate Models for Microstrip Computer- Aided Design," *IEEE International Microwave Symposium,* no. M7-7-S, pp. 407-409, May 1980.

[110] W. Chang and C. Y. Chang, "Uniplanar microstrip periodic structure for microwave circuits," *Electronics Letters,* vol. 47, no. No 8, 2011.

[111] L. Brillouin, Wave Propagation in Periodic Structures , 2nd ed, Dover, 1953.

[112] W.-S. Chang and C.-Y. Chang, "Novel Microstrip Periodic Structure and Its Application to Microwave Filter Design," *IEEE Microwave and Wireless Components Letters,* vol. 21, no. No. 12 , March 2011.

[113] G. V. Eleftheriades and K. G. Balmain, Negative-Refraction Metamaterials: Fundamental Principles and Applications, Wiley-IEEE Press, 2005.

[114] A. A. Oliner, "Equivalent circuits for discontinuities in balanced strip transmission line," *IEEE Transaction Microwave Theory Tech.(Special Issue on Symp. on Microwave Structure Circuits,* Vols. MTT-3, pp. 134-143, 1995.

[115] V. e. al., "Periodically loaded transmission lines and their application in microwave filters," *IEEE Trans. Microwave Theory Tech.,* vol. 50, no. 6, p. 1489–1495, 2002.

[116] P. Silvester and P. Benedek, "Equivalent capacitances of microstrip open circuits," *IEEE Transactions Microwave Theory Technology,* Vols. MTT-20, pp. 511-516, Aug 1972.

[117] P. Benedek and P. Silvester, "Equivalent capacitances of microstrip gaps and steps," *IEEE Transaction Microwave theory tech,* Vols. MTT-21, no. 1972, pp. 729-733, 1972.

[118] P. Silvester and P. Benedek, "Microstrip discontinuity capacitances for right-angle bends, T-junctions and crossings," *IEEE Transaction Microwave theory Tech.,* Vols. MTT-21, pp. 341-346, 1973.

[119] P. Stuten, "Equivalent capacitances of T-junctions," *Electronics Letters,* vol. 9, pp. 552-553, Nov. 1973.

[120] A. Gouinath and P. Silvester, "Calculation of inductance of Infinite-length strips and its variation with frequency," *IEEE Transaction Microwave theory Tech,* Vols. MTT-21, p. 38W386, June 1973.

[121] A. Gopinath and B. Easter, "Moment method of calculating discontinuity inductance of microstrip right angled bends," *IEEE Transaction Microwave theory tech,* Vols. MTT-22, pp. 880-883, Oct. 1974.

[122] A. Tompsom and A. Gouinath, "Calculation of microstrip discontinuity inductance," *IEEE Transaction Microwave Theory tech,* Vols. MTT-23, pp. 648-655, Aug. 1975.

[123] I. Wolff, G. Kompa and R. Mehran , "Calculation method for microstrip discontinuities and T-junctions," *Electronics Letters,* vol. 8, p. 177, April 1972.

[124] G. Kompa and R. Mehran, "Planar waveguide model for calculating mmicrostrip components," *Electronics Letters,* vol. 11, pp. 459-460, Sept. 1975.

[125] W. Menzel and I. Wolff, "A Method for Calculating the Frequency Dependent Properties of Microstrip Discontinuities," *IEEE Transaction on Microwave Theory and Technique,* Vols. MTT-25, no. No. 2, pp. 2656-2664, February 1977.

[126] R. Mehran, "The frequency-dependent scattering matrix of microstrip right-angle bends, T-junctions and crossings," *Arch Elek. Ubertragung,* vol. 2, pp. 454-460, Nov. 1975.

[127] S. Y. Hyang and Y. H. Lee, "Tapered dual-plane compact electromagnetic band-gap microstrip filter structure," *IEEE Transactions on Microwave Theory and techniques,* Vols. MTT-25, no. No. 2, pp. 2565-2568, Sept 2005.

[128] D. M. Pozar, Impedance matching and tuning. Microwave Engineering, New Jersey, USA , ISBN: 8126510498: John Wiley and Sons Inc., 2012 , 4th Ed..

[129] M. Makimoto and S. Yamashita, Microwave Resonators and Filters for Wireless Communication, Springer, 2001.

[130] K. Chang, RF and Microwave Circuit and Component Design for Wireless Systems, Wiley-Interscience, 2002.

[131] X. Liu, W. Wu, W. Yuan, Y. Yuan and N. Yuan, "Design of stubs loaded SIR filters by reflection coefficient analysis," *International Journal of Electronics Communications (AEU),* vol. 88, pp. 120-125, 2018.

[132] J. Moa, X. Liub, H. Yangc and S. Liuc, "High-selectivity microstrip bandpass filters using stub-loaded resonators," *Optic,* vol. 126, pp. 2844-2847, 2015.

[133] J. A. G. Malherbe and T. Bopape, "Pseudo-Elliptic Bandpass Filter with Stepped Impedance Stubs," in *46th European Microwave Conference*, London - UK, Oct 2016.

[134] P. Velezl, I. Selgal, M. Sansl, I. Bonachel and F. Martini, "Design of Differential-Mode Wideband Bandpass Filters with Wide Stop band and Common-Mode Suppression by means of Multi section Mirrored Stepped Impedance Resonators (SIRs)," *IEEE Xplore,* Vols. 978-1-4799-8275-2/15, 2015.

[135] X. Gao, W. Feng and W. Che, "High-Selectivity Wideband Balanced Filters Using Coupled Lines With Open/Shorted Stubs," *IEEE Microwave and Wireless Components Letters ,* vol. 27, no. No. 3, March 2017.

[136] C.-L. Hsu, F.-C. Hsu and J.-T. Kuo, "Microstrip Bandpass Filters for Ultra-Wideband (UWB) Wireless Communications," *IEEE MTT-S International Microwave Symposium Digest ,* 2005.

[137] J. Xie, D. Tang, Y. Shu and X. Luo, "Compact UWB BPF With Broad Stopband Based on Loaded-Stub and C-Shape SIDGS Resonators," *IEEE Microwave and Wireless Components Letters ,* vol. 32, no. No. 5, May 2022.

[138] X. Shi, X. Xia, J. Liu and H. Yang, "Novel ultra-wideband (UWB) bandpass filter using multiple-mode resonator," *IEICE Electronics Express,* June 2016.

[139] X. Zheng and T. Jiang, "A Novel Triple Notch-Bands UWB Band-Pass Filter Using E-shaped Resonator and Open-Loaded Stubs," *IEICE Electronics Express,* June 2016.

[140] M.-H. Weng, H.-W. Wu and Y.-K. Su, "Compact and Low Loss Dual-Band Bandpass Filter Using Pseudo-Interdigital Stepped Impedance Resonators for WLANs," *IEEE Microwave and Wireless Components Letters,* vol. 17, no. No. 13, March 2007.

[141] Y. Wu, L. Cui, W. Zhang, L. Jiao, Z. Zhuang and Y. Liu, "High Performance Single-Ended Wideband and Balanced Bandpass Filters Loaded With Stepped-Impedance Stubs," *IEEE Access,* April 2017.

[142] H. Xu, X. Wang, Y. Wang, W. Cheng and X. Shi, "A Varactor-Tuned Dual-Passband Microstrip Filter Using Stepped Impedance Resonators," *International Conference on Microwave and Millimeter Wave Technology (ICMMT),* 2012.

[143] X. Dang, M. Li, Y. Li and K. D. Xu, "Dual-band bandpass filters using open-/short- circuited stub-loaded quarter-wavelength resonators," *IEEE MTT-S International microwave Workshop Series on Advanced Materials and Processes for RF and THz Applications (IMWS-AMP),* 2016.

[144] X. Lu, P. Ma, B. Wei, L. Zhao, A. Xu, B. Cao, X. Wang and X. Song, "The Asymmetrical Split Phenomenon of the Odd and Even Modes and Its Application to UWB HTS Filters," *IEEE Transaction on Applied Superconductivity ,* vol. 29, no. No. 4, June 2019.

[145] C. Quendo, E. Rius and C. Person, "An original topology of dual-band bandpass filter with attenuation poles," *IEEE MTT-S International Microwave Symp. Dig.,* p. 1153–1156, 2003.

[146] K. Ma, K. S. Yeo and M. Y. W. Chia, "A New Method to Design Bandpass Filters Using Even- and Odd-Mode Analysis," *IEEE Trans. Microw. Theory Techn.,* p. 3431–3438, 2008.

[147] J. Guera, A. Andujar and M. Huynh, "Advances in antenna technology for wireless handheld devices.," *International Journal on Antenna and Propagation,* vol. 1921, no. DOI: 10.1155/2013/838364, pp. 388-391, 2013.

[148] “A design method of multimode multiband bandpass filters”, IEEE Transactions on Microwave Theory & Techniques,” *IEEE Transaction on Microwave Theory & Techniques,* vol. 99, no. DOI: 10.1109/TMTT.2018.873584, pp. 2791-2799, 2018.

[149] C. Y. Chen and C. Y. HSU, “A simple and effective method for microstrip dual-band filters design,” *IEEE Microwave & Wireless Components Letters ,* vol. 16, no. DOI: 10.1109/LMWC.2006.873584, pp. 246-248, 2006.

[150] S. S. Olokede and B. A. Paul, “A novel microstrip feed based on the theory of small reflection,” *IEEE Radio and Antenna Days of the India Ocean St. Gilles-les-Bains (Reunion),* no. DOI: 10..1109/Radio 2016.7772018, 2016.

[151] N. Hendijani, A. Khalaj and V. K. Sharghi, “Design, simulation, and fabrication of tapered microstrip filters by applying the method of small reflections. In International Symposium on Telecommunications,” in *In International Symposium on Telecommunications*, Tehran, 2008, p 133-137 DOI:10.1109/ISTEL.2008.4651287.

[152] Y. Yuan, W. Wu and W. Yuan, “A method based on the theory of small reflections to design arbitrary passband microstrip filters,” *Radio Engineering,* vol. 27, no. No. 1 , DOI: 10.13164/re.2018.0214, pp. 214-220, 2018.

[153] K. Gupta and N. Sahayam, “A Review on Microstrip Filter for the Application in Communication System,” *International Research Journal of Engineering and Technology (IRJET),* vol. 05, no. 12, Dec 2018.

[154] S. Baskal and Y. S. Kim, “ABCD Matrices as Similarity Transformations of Wigner Matrices and Periodic Systems in Optics,” *Journal of the Optical Society of America,* October 2009.

[155] A. J. Prado and S. Kurokawa, “The eigenvalue analyses for non-symmetric three-phase transmission lines - the Clarke's matrix application,” in *Seventh Latin-Amerocan Congress in Electricity Generation and Transmission - GLAGTEE*, Vina del Mar , Chile, October 2007 .

[156] H. W. Dommel, Electromagnetic Transients Program, Oregon: Rule Book, 1984.

[157] “Transients Analysis Program Reference Manual,” Microtran Power System Analysis Corporation, Vancouver, Canada, 1992.

[158] A. Morched, B. Gustavsen and A. Tartibi, “A Universal Model for Accurate Calculation of Electromagnetic Transients on Overhead Lines and Underground Cables,” *IEEE Transaction on Power Delivery,* vol. 14, no. No. 3 , pp. 1032-1038, July 1999.

[159] R. Horn and C. Johnson, Matrix Analysis, 2nd ed, Cambridge: Cambridge University Press, 2013.

[160] A. Gelman, Bayesian Data Analysis , 3rd Ed, CRC Press, 2013.

[161] G. H. Golub and C. F. Van Loan, Matrix Computations , 4th ed.

[162] N. J. Higham, Accuracy and Stability of Numerical Alghorithms , 2nd ed, SIAM, 2002.

[163] R. E. Collin, Field theory of guided waves, New York: IEEE Press , 2nd Ed. Ch 9, 1992.

[164] J. Sor, Y. Qian and T. Itoh, “A Novel Low-Loss Slow-Wave CPW Periodic Structure for Filter Applications,” *IEEE MTT-S International Microwave Symposium digest,* vol. 1, no. MTT-S Feb 2001, pp. 307-310, Feb 2001.

[165] F. R. Yang, R. Coccioli, Y. Qian and T. Itoh, “Analysis and application of coupled microstrips on periodically patterned ground plane,” *International Microwave Symp.,* vol. 3, no. MTT-S 2000, pp. 1529-1532, June 2000.

[166] C. Hang, V. Radisic, Y. Qian and T. Itoh, “High efficiency power amplifier with novel PBG ground plane for harmonic tuning,” *IEEE MTT-S Int. Microwave Symp. Dig.,* vol. 2, pp. 807-810, June 1999.

[167] F. R. Yang, K. P. Ma, Y. Qian and T. Itoh, “A novel TEM waveguide using compact photonic-bandgap (UC-PBG) structure,” *IEEE Transction MTT-S Int. Microwave Theory Tech.,* vol. 47, no. No. 11, pp. 2092-2098, Nov 1999.

[168] K. P. Ma, J. Kim, F. R. Yang, Y. Qian and T. Itoh, “Leakage suppression in stripline circuits using a 2-D photonic bandgap lattice,” *IEEE MTT-S Internationl Microwave Symp. Diag. ,* vol. 1, pp. 73-76, June 1999.

[169] K. C. Gupta, R. Garg and I. J. Bahl, Computer Aided Design of Microwave Circuits, Dedham, Mass: Artech House, 1981.

Appendix A. Publications

- Abdolreza Divsalar, Shahin Salarian, Dariush Mirshekar-Syahkal, “MMW Tunable Periodic Filter Design”, The 8th International Conference on Antenna and Electromagnetic System (AES 2022, Marrakesh - Morocco, May 24-27, 2022)

- Abdolreza Divsalar, D. Mirshekar-Syahkal, “Modelling Technique for Finite Length Microstrip Periodic Structures for MMW Filter”, The 9th International Conference on Antenna and Electromagnetic Systems (AES-2023 Torremolinos - Spain, 5-8 June 2023)

- Abdolreza Divsalar, Dariush Mirshekar-Syahkal, “Design Method for MMW LC Tunable Microstrip Periodic Filters”, PhotonIcs & Electromagnetics Research Symposium (PIERS2023, Prague, Czech Republic, 3–6 July 2023), IEEE Xplore: 28 August 2023

Appendix B. Detail Formulas Derivation

B1. Resonate condition of SIR Stub using Odd-Even analysis

For Fig 5.16 even mode analysis, the equivalent circuit is open at the symmetrical line, and the input admittance is:

$$Y_{in,even} = Y_1 \frac{Y_a + \mathrm{j}\, \mathrm{Y}_1 \tan\theta_1}{\mathrm{Y}_1 + j\, Y_a \tan\theta_1}, \tag{B1.1}$$

$$\begin{cases} Y_a = Y_2 \dfrac{Y_b + \mathrm{j}\, \mathrm{Y}_2 \tan\theta_2}{\mathrm{Y}_2 + j\, Y_b \tan\theta_2} \\ Y_b = Y_3 \dfrac{Y_c + \mathrm{j}\, \mathrm{Y}_3 \tan\theta_3}{\mathrm{Y}_3 + j\, Y_c \tan\theta_3} \\ Y_c = jY_4 \tan\theta_4 \end{cases}. \tag{B1.2}$$

For the even mode, the SIR stub resonates when:

$$Y_{in,even} = 0, \tag{B1.3}$$

$$Y_a + \mathrm{j}\, \mathrm{Y}_1 \tan\theta_1 = Y_2 \frac{Y_b + \mathrm{j}\, \mathrm{Y}_2 \tan\theta_2}{\mathrm{Y}_2 + j\, Y_b \tan\theta_2} + \mathrm{j}\, Y_1 \tan\theta_1 = 0. \tag{B1.4}$$

Assuming:

$$K_1 = \frac{Y_1}{Y_2}, \quad K_2 = \frac{Y_2}{Y_3}, \quad K_3 = \frac{Y_3}{Y_4}, \tag{B1.5}$$

Then equation (4.49) can be expanded as follows:

$$Y_2(Y_b + \mathrm{j}\, \mathrm{Y}_2 \tan\theta_2) = -\mathrm{j}\, Y_1 \tan\theta_1 (\mathrm{Y}_2 + j\, Y_b \tan\theta_2), \tag{B1.6}$$

$$Y_2 Y_b + \mathrm{j}\, \mathrm{Y}_2\, Y_2 \tan\theta_2 = -\mathrm{j}\, Y_1\, \mathrm{Y}_2 \tan\theta_1 - Y_b\, \mathrm{Y}_1 \tan\theta_2 \tan\theta_1, \tag{B1.7}$$

$$\mathrm{j}\, \mathrm{Y}_1\, \mathrm{Y}_2 \tan\theta_1 + \mathrm{j}\, \mathrm{Y}_2\, Y_2 \tan\theta_2 = -Y_2 Y_b - Y_b\, \mathrm{Y}_1 \tan\theta_2 \tan\theta_1, \tag{B1.8}$$

$$\mathrm{j}\, \mathrm{Y}_2(\mathrm{Y}_1 \tan\theta_1 + Y_2 \tan\theta_2) = Y_b(-Y_2 - \mathrm{Y}_1 \tan\theta_2 \tan\theta_1), \tag{B1.9}$$

$$-\mathrm{j}\, \mathrm{Y}_2 \frac{\mathrm{Y}_1 \tan\theta_1 + Y_2 \tan\theta_2}{Y_2 + \mathrm{Y}_1 \tan\theta_2 \tan\theta_1} = Y_b = Y_3 \frac{Y_c + \mathrm{j}\, \mathrm{Y}_3 \tan\theta_3}{\mathrm{Y}_3 + j\, Y_c \tan\theta_3} = j\, Y_3 \frac{Y_4 \tan\theta_4 + \mathrm{Y}_3 \tan\theta_3}{\mathrm{Y}_3 - Y_4 \tan\theta_4 \tan\theta_3} =$$
$$= Y_3 \frac{Y_4 \tan\theta_4 + \mathrm{Y}_3 \tan\theta_3}{\mathrm{Y}_3 - Y_4 \tan\theta_4 \tan\theta_3}, \tag{B1.10}$$

$$-\mathrm{Y}_2\ (\mathrm{Y}_1\tan\theta_1 + Y_2\tan\theta_2)\,(\mathrm{Y}_3 - Y_4\tan\theta_4\tan\theta_3)$$
$$= Y_3(Y_4\tan\theta_4 + \mathrm{Y}_3\tan\theta_3)(Y_2 + \mathrm{Y}_1\tan\theta_2\tan\theta_1)\,, \tag{B1.11}$$

$$-\frac{\mathrm{Y}_2}{Y_3}\,\frac{\frac{\mathrm{Y}_1}{Y_2}\tan\theta_1 + \tan\theta_2}{1 + \frac{\mathrm{Y}_1}{Y_2}\tan\theta_1\tan\theta_2} = \frac{\tan\theta_4 + \frac{\mathrm{Y}_3}{Y_4}\tan\theta_3}{\frac{\mathrm{Y}_3}{Y_4} - \tan\theta_3\tan\theta_4}\,, \tag{B1.12}$$

$$-K_2\,\frac{\mathrm{K}_1\tan\theta_1 + \tan\theta_2}{1 + \mathrm{K}_1\tan\theta_2\tan\theta_1} = \frac{\tan\theta_4 + \mathrm{K}_3\tan\theta_3}{\mathrm{K}_3 - \tan\theta_4\tan\theta_3}\,, \tag{B1.13}$$

$$-K_2\,\frac{\mathrm{K}_3\mathrm{K}_1\tan\theta_1 + \mathrm{K}_3\tan\theta_2 - \mathrm{K}_1\tan\theta_1\,ta\,n\,\theta_3\,ta\,n\,\theta_4 - \tan\theta_2\tan\theta_3\tan\theta_4}{\tan\theta_4 + \mathrm{K}_3\tan\theta_3 + \mathrm{K}_1\tan\theta_1\tan\theta_2\ \tan\theta_4 + \mathrm{K}_1\mathrm{K}_3\tan\theta_1\tan\theta_2\ \tan\theta_3}$$
$$= 1\,, \tag{B1.14}$$

$$\mathrm{K}_1\mathrm{K}_2\,\mathrm{K}_3\tan\theta_1 - \mathrm{K}_2\mathrm{K}_3\tan\theta_2 + \mathrm{K}_3\tan\theta_3$$
$$+\tan\theta_4 + \mathrm{K}_1\mathrm{K}_3\tan\theta_1\tan\theta_2\ \tan\theta_3 + \mathrm{K}_1\tan\theta_1\tan\theta_2\ \tan\theta_4 - \mathrm{K}_1\tan\theta_1\,ta\,n\,\theta_3\,ta\,n\,\theta_4$$
$$-K_2\tan\theta_2\tan\theta_3\tan\theta_4 = 0\,. \tag{B1.15}$$

For Multi-SIR, single-Stub unit cell Fig 5.17, the even mode calculations will be as follows:

$$Y_{in,even} = Y_1\frac{Y_a + j\,Y_1\,tan\,\theta_1}{Y_1 + j\,Y_a\,tan\,\theta_1}\ , \tag{B1.16}$$

$$\begin{cases} Y_a = Y_2\dfrac{Y_b + \mathrm{j}\,\mathrm{Y}_2\tan\theta_2}{\mathrm{Y}_2 + j\,Y_b\tan\theta_2} & Y_b = Y_3\dfrac{Y_c + \mathrm{j}\,\mathrm{Y}_3\tan\theta_3}{\mathrm{Y}_3 + j\,Y_c\tan\theta_3} \\ Y_c = Y_2\dfrac{Y_c + \mathrm{j}\,\mathrm{Y}_2\tan\theta_2}{\mathrm{Y}_2 + j\,Y_c\tan\theta_2} & Y_d = Y_4\dfrac{Y_e + \mathrm{j}\,\mathrm{Y}_4\tan\theta_4}{\mathrm{Y}_4 + j\,Y_e\tan\theta_4} \\ Y_e = j\,Y_5\ \tan\theta_5 & \end{cases}\ , \tag{B1.17}$$

Calculations of the even mode analysis of Fig 5.19 is presented as follows:

$$Y_{in,even} = Y_1\frac{Y_a + \mathrm{j}\,\mathrm{Y}_1\tan\theta_1}{\mathrm{Y}_1 + j\,Y_a\tan\theta_1}\,, \tag{B1.18}$$

$$\begin{cases} Y_{a1} = Y_2 \dfrac{Y_{b1} + \mathrm{j}\, Y_2 \tan\theta_2}{Y_2 + j\, Y_{b1} \tan\theta_2} & Y_{a2} = Y_2 \dfrac{Y_{b2} + \mathrm{j}\, Y_2 \tan\theta_2}{Y_2 + j\, Y_{b2} \tan\theta_2} \\ Y_{b1} = Y_3 \dfrac{Y_{c1} + \mathrm{j}\, Y_3 \tan\theta_3}{Y_3 + j\, Y_{c1} \tan\theta_3} & Y_{b2} = Y_3 \dfrac{Y_{c2} + \mathrm{j}\, Y_3 \tan\theta_3}{Y_3 + j\, Y_{c2} \tan\theta_3} \\ Y_{c1} = j\, Y_4 \tan\theta_4 & Y_{c2} = j\, Y_4 \tan\theta_4 \end{cases}, \tag{B1.19}$$

Assuming that the structure is symmetrical with identical stepped impedances in both top and bottom sides of the main transmission line, we have:

$$Y_{a1} = Y_{a2} = Y_a \qquad Y_{b1} = Y_{b2} = Y_b \qquad Y_{c1} = Y_{c2} = Y_c\,, \tag{B1.20}$$

$$Y_a = 2Y_2 \frac{Y_b + \mathrm{j}\, Y_2 \tan\theta_2}{Y_2 + j\, Y_b \tan\theta_2}. \tag{B1.21}$$

With a similar analysis the even admittance of a unit cell with more stepped impedances of Fig 5.20 will be as follows:

$$Y_{in,even} = Y_1 \frac{Y_a + \mathrm{j}\, Y_1 \tan\theta_1}{Y_1 + j\, Y_a \tan\theta_1}\,, \tag{B1.22}$$

$$\begin{cases} Y_{a1} = Y_2 \dfrac{Y_{b1} + \mathrm{j}\, Y_2 \tan\theta_2}{Y_2 + j\, Y_{b1} \tan\theta_2} & Y_{a2} = Y_2 \dfrac{Y_{b2} + \mathrm{j}\, Y_2 \tan\theta_2}{Y_2 + j\, Y_{b2} \tan\theta_2} \\ Y_{b1} = Y_3 \dfrac{Y_{c1} + \mathrm{j}\, Y_3 \tan\theta_3}{Y_3 + j\, Y_{c1} \tan\theta_3} & Y_{b2} = Y_3 \dfrac{Y_{c2} + \mathrm{j}\, Y_3 \tan\theta_3}{Y_3 + j\, Y_{c2} \tan\theta_3} \\ Y_{c1} = Y_2 \dfrac{Y_{d1} + \mathrm{j}\, Y_2 \tan\theta_2}{Y_2 + j\, Y_{d1} \tan\theta_2} & Y_{c2} = Y_2 \dfrac{Y_{d2} + \mathrm{j}\, Y_2 \tan\theta_3}{Y_2 + j\, Y_{d2} \tan\theta_3} \\ Y_{d1} = Y_4 \dfrac{Y_{e1} + \mathrm{j}\, Y_4 \tan\theta_4}{Y_2 + j\, Y_{e1} \tan\theta_4} & Y_{d2} = Y_4 \dfrac{Y_{e2} + \mathrm{j}\, Y_4 \tan\theta_4}{Y_2 + j\, Y_{e2} \tan\theta_4} \\ Y_{e1} = j\, Y_5 \tan\theta_5 & Y_{e2} = j\, Y_5 \tan\theta_5 \end{cases}, \tag{B1.23}$$

For symmetrical and identical stepped impedances in the two sides of the transmission line, we have:

$$\begin{cases} Y_{a1} = Y_{a2} = Y_a\,;\; Y_{b1} = Y_{b2} = Y_b\,;\; Y_{c1} = Y_{c2} = Y_c \\ Y_{d1} = Y_{d2} = Y_d\,;\; Y_{e1} = Y_{e2} = Y_e \end{cases}; \tag{B1.24}$$

$$Y_a = 2Y_2 \frac{Y_b + \mathrm{j}\, Y_2 \tan\theta_2}{Y_2 + j\, Y_b \tan\theta_2}\,. \tag{B1.25}$$

B2. ABCD Matrix of periodic structure

Details of formula derivation of periodic structure ABCD matrix from the relevant unit cells matrix are as follows (refer to 5.9):

For reciprocal unit cell transmission matrix ABCD we have:

$$A_{UC}D_{UC} - B_{UC}C_{UC} = A_{UC}^2 - B_{UC}C_{UC} = 1\,, \tag{B2.1}$$

$$B_{UC}C_{UC} = A_{UC}^2 - 1. \tag{B2.2}$$

To determine the matrix Eigen values the following condition should be met below characteristic eigenvalue equation:

$$characteristic\ polynomial = \left|\begin{bmatrix} A_{UC} & B_{UC} \\ C_{UC} & D_{UC} \end{bmatrix} - \lambda I\right| = \left|\begin{bmatrix} A_{UC} & B_{UC} \\ C_{UC} & A_{UC} \end{bmatrix} - \lambda \begin{bmatrix} 1 & 0 \\ 0 & 1 \end{bmatrix}\right| = 0 \tag{B2.3}$$

$$(A_{UC} - \lambda)(A_{UC} - \lambda) - B_{UC}C_{UC} = A_{UC}^2 - 2A_{UC}\lambda + \lambda^2 - B_{UC}C_{UC} = 0\,. \tag{B2.4}$$

Therefore, the set of Eigen Value solutions or spectrum of the transmission matrix is:

$$\lambda_{1,2} = A_{UC} \pm \sqrt{A_{UC}^2 - 1}\ , \tag{B2.5}$$

$$\begin{bmatrix} A & B \\ C & D \end{bmatrix}^{EV} = \begin{bmatrix} \lambda_1 & 0 \\ 0 & \lambda_2 \end{bmatrix} = \begin{bmatrix} A_{UC} + \sqrt{A_{UC}^2 - 1} & 0 \\ 0 & A_{UC} - \sqrt{A_{UC}^2 - 1} \end{bmatrix}, \tag{B2.6}$$

$$\begin{bmatrix} A & B \\ C & D \end{bmatrix}^{UC,canonical} = \begin{bmatrix} -B_{UC} & -B_{UC} \\ -\sqrt{A_{UC}^2 - 1} & \sqrt{A_{UC}^2 - 1} \end{bmatrix}, \tag{B2.7}$$

$$\left(\begin{bmatrix} A & B \\ C & D \end{bmatrix}^{UC,canonical}\right)^{-1} = \frac{1}{2B_{UC}(\sqrt{A_{UC}^2 - 1})} \begin{bmatrix} \sqrt{A_{UC}^2 - 1} & B_{UC} \\ \sqrt{A_{UC}^2 - 1} & -B_{UC} \end{bmatrix}, \tag{B2.8}$$

$$\left(\begin{bmatrix} A & B \\ C & D \end{bmatrix}^{UC,canonical}\right)^{-1} = \begin{bmatrix} \frac{1}{2B_{UC}} & \frac{1}{2\sqrt{A_{UC}^2 - 1}} \\ \frac{1}{2B_{UC}} & \frac{-1}{2\sqrt{A_{UC}^2 - 1}} \end{bmatrix}. \tag{B2.9}$$

Based on eigen decomposition theorem, for N unit cells which are connected in cascade the overall transmission matrix ABCD will be as follows (PS=Periodic Structure):

$$\begin{bmatrix} A & B \\ C & D \end{bmatrix}^{PS} = \begin{bmatrix} A & B \\ C & D \end{bmatrix}^{UC} \begin{bmatrix} A & B \\ C & D \end{bmatrix}^{UC} \dots \begin{bmatrix} A & B \\ C & D \end{bmatrix}^{UC} \quad (N\ times) = \left\{ \begin{bmatrix} A_{UC} & B_{UC} \\ C_{UC} & D_{UC} \end{bmatrix} \right\}^{N} \quad \text{(B2.10)}$$

$$\begin{bmatrix} A & B \\ C & D \end{bmatrix}^{PS} = \begin{bmatrix} A_{PS} & B_{PS} \\ C_{PS} & D_{PS} \end{bmatrix}$$

$$= \begin{bmatrix} A & B \\ C & D \end{bmatrix}^{UC,canonical} \left(\begin{bmatrix} A & B \\ C & D \end{bmatrix}^{EV} \right)^{N} \left(\begin{bmatrix} A & B \\ C & D \end{bmatrix}^{UC,canonical} \right)^{-1} , \quad \text{(B2.11)}$$

Therefore,

$$\begin{bmatrix} A & B \\ C & D \end{bmatrix}^{PS} = \begin{bmatrix} -B_{UC} & -B_{UC} \\ -\sqrt{A_{UC}^2 - 1} & \sqrt{A_{UC}^2 - 1} \end{bmatrix} \left(\begin{bmatrix} A & B \\ C & D \end{bmatrix}^{EV} \right)^{N} \begin{bmatrix} \frac{1}{2B_{UC}} & \frac{1}{2\sqrt{A_{UC}^2 - 1}} \\ \frac{1}{2B_{UC}} & \frac{-1}{2\sqrt{A_{UC}^2 - 1}} \end{bmatrix}, \quad \text{(B2.12)}$$

$$\left(\begin{bmatrix} A & B \\ C & D \end{bmatrix}^{EV} \right)^{N} = \begin{bmatrix} (A_{UC} + \sqrt{A_{UC}^2 - 1})^N & 0 \\ 0 & (A_{UC} - \sqrt{A_{UC}^2 - 1})^N \end{bmatrix}, \quad \text{(B2.13)}$$

From (5.35) and (5.36) the periodic structure transmission matrix parameters will be:

$$A_{PS} = D_{PS} = \frac{\left[\left(A_{UC} + \sqrt{A_{UC}^2 - 1} \right)^N + \left(A_{UC} - \sqrt{A_{UC}^2 - 1} \right)^N \right]}{2}, \quad \text{(B2.14)}$$

$$B_{PS} = \frac{B_{UC} \left[\left(A_{UC} + \sqrt{A_{UC}^2 - 1} \right)^N - \left(A_{UC} - \sqrt{A_{UC}^2 - 1} \right)^N \right]}{\left(2\sqrt{A_{UC}^2 - 1} \right)}, \quad \text{(B2.15)}$$

$$C_{PS} = \frac{C_{UC} \left[\left(A_{UC} + \sqrt{A_{UC}^2 - 1} \right)^N - \left(A_{UC} - \sqrt{A_{UC}^2 - 1} \right)^N \right]}{\left(2\sqrt{A_{UC}^2 - 1} \right)}. \quad \text{(B2.16)}$$

B3. ABCD Matric of stepped impedance unit cell

Details of formula derivation of stepped impedance unit cell ABCD matrix are as follows (refer to 5.9.1).

$$\begin{bmatrix} A & B \\ C & D \end{bmatrix}^{S} = \begin{bmatrix} cos\,\theta_s/2 & j\,Z_s sin\,\theta_s/\,2 \\ j\,1/Z_s sin\,\theta_s/\,2 & cos\,\theta_s/2 \end{bmatrix}, \tag{B3.1}$$

$$\begin{bmatrix} A & B \\ C & D \end{bmatrix}^{R} = \begin{bmatrix} cos\,\theta_r & j\,Z_r sin\,\theta_r \\ j\,1/Z_r sin\,\theta_r & cos\,\theta_r \end{bmatrix}, \tag{B3.2}$$

$$\begin{bmatrix} A & B \\ C & D \end{bmatrix}^{UC} = \begin{bmatrix} cos\,\theta_s/2 & j\,Z_s sin\,\theta_s/\,2 \\ j\,1/Z_s sin\,\theta_s/\,2 & cos\,\theta_s/2 \end{bmatrix} \begin{bmatrix} 1 & 0 \\ jY & 1 \end{bmatrix} \begin{bmatrix} cos\,\theta_r & j\,Z_r sin\,\theta_r \\ j\,1/Z_r sin\,\theta_r & cos\,\theta_r \end{bmatrix}$$

$$\begin{bmatrix} 1 & 0 \\ jY & 1 \end{bmatrix} \begin{bmatrix} cos\,\theta_s/2 & j\,Z_s sin\,\theta_s/\,2 \\ j\,1/Z_s sin\,\theta_s/\,2 & cos\,\theta_s/2 \end{bmatrix}, \tag{B3.3}$$

$$\begin{aligned} A_{UC} = {} & cos(\theta_s)\,cos(\theta_r) - 1/2\,sin(\theta_s)\,sin\,(\theta_r)(Z_s/Z_r + Z_r/Z_s) \\ & + 0.5 Z_r Z_s Y^2 sin(\theta_s)\,sin(\theta_r) \\ & - Z_s Y\,sin(\theta_s)\,cos(\theta_r) - Z_r Y\,sin(\theta_r)\,cos(\theta_s)\,, \end{aligned} \tag{B3.4}$$

$$\begin{aligned} B_{UC} = {} & j\{Z_s\,sin(\theta_s)\,cos(\theta_r) - 1/2\,sin(\theta_r)/Z_r[Z_r^2 - Z_s^2 + cos\,(\theta_s)(Z_r^2 + Z_s^2)] \\ & - Z_s Z_r Y sin(\theta_s)\,sin(\theta_r) - Z_s^2 Y\,(1 \\ & - cos(\theta_s))\,cos(\theta_r) + 1/2\;\; Z_s^2 Z_r Y^2\,sin(\theta_r)\,(1 - cos(\theta_s)\}\,, \end{aligned} \tag{B3.5}$$

$$\begin{aligned} C_{UC} = {} & j\{1/Z_s\,sin(\theta_s)\,cos(\theta_r) + 1/2\,Z_r sin(\theta_r)[1/Z_r^2 - \frac{1^2}{Z_s} + cos\,(\theta_s)\left(\frac{1}{Z_r^2} + \frac{1^2}{Z_s}\right)] \\ & + Y cos(\theta_s)\,(1 + \cos\quad(\theta_s)) - Z_r/Z_s Y\,\sin\,\theta_s \sin\,\theta_r \\ & - 1/2\,Z_r Y^2 sin(\theta_s)(1 \\ & + cos(\theta_s)\}\,, \end{aligned} \tag{B3.6}$$

$$\begin{aligned} D_{UC} = {} & cos(\theta_s)\,cos(\theta_r) - 1/2\,sin(\theta_s)\,sin\,(\theta_r)(Z_s/Z_r + Z_r/Z_s) \\ & + 0.5 Z_r Z_s Y^2 sin(\theta_s)\,sin(\theta_r) \\ & - Z_s Y\,sin(\theta_s)\,cos(\theta_r) - Z_r Y\,sin(\theta_r)\,cos(\theta_s). \end{aligned} \tag{B3.7}$$

The value of induction of discontinuity of figure 5.13 will be:

$$L/h = 40.5[W_r/W_s - 1.0] - 75\,Ln(W_r/W_s) + 0.2[W_s/W_r - 1.0]^2[nH, m] \tag{B3.8}$$

Therefore, for a unit length microstrip inductance can be calculated from the following formulas:

$$L_{W_s} = \frac{Z_s(W_s)\sqrt{\varepsilon_{eff}(W_s)}}{c}, \tag{B3.9}$$

$$L_{W_r} = \frac{Z_r(W_r)\sqrt{\varepsilon_{eff}(W_r)}}{c}, \tag{B3.10}$$

Therefore:

$$L_s = \frac{L_{W_s}}{L_{W_s} + L_{W_r}} L, \tag{B3.11}$$

$$L_r = \frac{L_{W_r}}{L_{W_s} + L_{W_r}} L. \tag{B3.12}$$

Where W_s and W_r are the widths of the lines, $c = 3 \times 10^8\ m/s$

B4. ABCD Matrix of balance open stud unit cell

Details of formula derivation of open stud unit cell ABCD matrix are as follows (refer to 5.9.2 and Fig 5.31).

The ABCD matrix will be as follows:

$$\begin{bmatrix} A & B \\ C & D \end{bmatrix}^{Open\ Stub} = \begin{bmatrix} 1 & 0 \\ 2\ /\ Z_{in} & 1 \end{bmatrix}, \tag{B4.1}$$

Therefore, the transmission matrix of the unit cell will be:

$$\begin{bmatrix} A & B \\ C & D \end{bmatrix}^{UC} = \begin{bmatrix} A & B \\ C & D \end{bmatrix}^{S} \begin{bmatrix} A & B \\ C & D \end{bmatrix}^{Open\ Stub} \begin{bmatrix} A & B \\ C & D \end{bmatrix}^{S}, \tag{B4.2}$$

$$\begin{bmatrix} A & B \\ C & D \end{bmatrix}^{S} = \begin{bmatrix} cos\ \theta_s/2 & j\ Z_s sin\ \theta_s/\ 2 \\ j\ 1/Z_s sin\ \theta_s/\ 2 & cos\ \theta_s/2 \end{bmatrix}. \tag{B4.3}$$

Same as Figure 3.15, Z_s and θ_s represent characteristic impedance and electrical length of the source microstrip transmission line.

$$\begin{bmatrix} A & B \\ C & D \end{bmatrix}^{UC} = \begin{bmatrix} A_{UC} & B_{UC} \\ C_{UC} & D_{UC} \end{bmatrix}, \tag{B4.4}$$

$$A_{UC} = cos(\theta_s) + \frac{jZ_s}{Z_{in}} sin(\theta_s), \tag{B4.5}$$

$$B_{UC} = j[(Z_s\ sin(\theta_s)\ ) - Z_s^2/Z_{in}(1\text{-}\ cos(\theta_s)], \tag{B4.6}$$

$$C_{UC} = j[(1/Z_s\ sin(\theta_s)\ ) - 1/Z_s(1 + \cos(\theta_s)], \tag{B4.7}$$

$$D_{UC} = cos(\theta_s) + \frac{jZ_s}{Z_{in}} sin(\theta_s). \quad \text{(B4.8)}$$

B5. ABCD matrix of T-shape open stud unit cell

Details of formula derivation of T-shape open stud unit cell ABCD matrix are as follows (refer to 5.9.3 and Fig 5.32).

The ABCD matrix will be as follows:

$$\begin{bmatrix} A & B \\ C & D \end{bmatrix}^{Open\ Stud} = \begin{bmatrix} 1 & 0 \\ 1\ /\ Z_{in} & 1 \end{bmatrix}, \quad \text{(B5.1)}$$

Therefore, the transmission matrix of the unit cell will be:

$$\begin{bmatrix} A & B \\ C & D \end{bmatrix}^{UC} = \begin{bmatrix} A & B \\ C & D \end{bmatrix}^{S} \begin{bmatrix} A & B \\ C & D \end{bmatrix}^{Open\ Stud} \begin{bmatrix} A & B \\ C & D \end{bmatrix}^{S}, \quad \text{(B5.2)}$$

$$\begin{bmatrix} A & B \\ C & D \end{bmatrix}^{S} = \begin{bmatrix} cos\ \theta_s/2 & j\ Z_s sin\ \theta_s/\ 2 \\ j\ 1/Z_s sin\ \theta_s/\ 2 & cos\ \theta_s/2 \end{bmatrix}. \quad \text{(B5.3)}$$

Same as Fig 5.33, Z_s and θ_s represent characteristic impedance and electrical length of the source microstrip transmission line.

$$\begin{bmatrix} A & B \\ C & D \end{bmatrix}^{UC} = \begin{bmatrix} A_{UC} & B_{UC} \\ C_{UC} & D_{UC} \end{bmatrix}, \quad \text{(B5.4)}$$

$$A_{UC} = cos(\theta_s) + \frac{Z_s}{Z_{in}} sin(\theta_s), \quad \text{(B5.5)}$$

$$B_{UC} = j[(Z_s\ sin(\theta_s)\ ) - Z_s^2/Z_{in}(1\text{-}\ cos(\theta_s)], \quad \text{(B5.6)}$$

$$C_{UC} = j[(1/Z_s\ sin(\theta_s)\ ) - 1/Z_s(1 + \cos(\theta_s)], \quad \text{(B5.7)}$$

$$D_{UC} = cos(\theta_s) + \frac{Z_s}{Z_{in}} sin(\theta_s). \quad \text{(B5.8)}$$

B6. ABCD matrix of un-balance open stud unit cell

Details of formula derivation of un-balance open stud unit cell ABCD matrix are as follows (refer to 5.9.4 and Fig 5.33).

The ABCD matrix will be as follows:

$$\begin{bmatrix} A & B \\ C & D \end{bmatrix}^{UC} = \begin{bmatrix} A & B \\ C & D \end{bmatrix}^{S} \begin{bmatrix} A & B \\ C & D \end{bmatrix}^{J_1} \begin{bmatrix} A & B \\ C & D \end{bmatrix}^{R1} \begin{bmatrix} A & B \\ C & D \end{bmatrix}^{J_2} \begin{bmatrix} A & B \\ C & D \end{bmatrix}^{R2} \begin{bmatrix} A & B \\ C & D \end{bmatrix}^{J_3} \begin{bmatrix} A & B \\ C & D \end{bmatrix}^{R3} \begin{bmatrix} A & B \\ C & D \end{bmatrix}^{J_4} \begin{bmatrix} A & B \\ C & D \end{bmatrix}^{S}, \quad \text{(B6.1)}$$

As discussed before in 5.6 the transmission matrixes of J1 and J4 are equal. Also, the transmission matrix of J2 and J3 are equal. These can be expresses as:

Also, it is assumed that R1 and R3 are identical with equal transmission matrix. Therefore, the above equation for unit cell transmission matrix can be expressed as:

$$\begin{bmatrix} A & B \\ C & D \end{bmatrix}^{UC} = \begin{bmatrix} A & B \\ C & D \end{bmatrix}^{S} \begin{bmatrix} A & B \\ C & D \end{bmatrix}^{J_1} \begin{bmatrix} A & B \\ C & D \end{bmatrix}^{R1} \begin{bmatrix} A & B \\ C & D \end{bmatrix}^{J_2} \begin{bmatrix} A & B \\ C & D \end{bmatrix}^{R2} \begin{bmatrix} A & B \\ C & D \end{bmatrix}^{J_2} \begin{bmatrix} A & B \\ C & D \end{bmatrix}^{R1} \begin{bmatrix} A & B \\ C & D \end{bmatrix}^{J_1} \begin{bmatrix} A & B \\ C & D \end{bmatrix}^{S}, \quad \text{(B6.2)}$$

$$\begin{bmatrix} A & B \\ C & D \end{bmatrix}^{S} = \begin{bmatrix} cos\,\theta_s/2 & j\,Z_s sin\,\theta_s/2 \\ j\,1/Z_s sin\,\theta_s/2 & cos\,\theta_s/2 \end{bmatrix}, \quad \text{(B6.3)}$$

$$\begin{bmatrix} A & B \\ C & D \end{bmatrix}^{J_1} = \begin{bmatrix} A & B \\ C & D \end{bmatrix}^{J_4} = \begin{bmatrix} 1 & 0 \\ Y_1 & 1 \end{bmatrix} = \begin{bmatrix} 1 & 0 \\ 1/Z_1 & 1 \end{bmatrix}, \quad \text{(B6.4)}$$

$$\begin{bmatrix} A & B \\ C & D \end{bmatrix}^{R1} = \begin{bmatrix} A & B \\ C & D \end{bmatrix}^{R3} = \begin{bmatrix} cos\,\theta_{r1}/2 & j\,Z_{r1} sin\,\theta_{r1}/2 \\ j\,1/Z_{r1} sin\,\theta_{r1}/2 & cos\,\theta_{r1}/2 \end{bmatrix}, \quad \text{(B6.5)}$$

$$\begin{bmatrix} A & B \\ C & D \end{bmatrix}^{J_2} = \begin{bmatrix} A & B \\ C & D \end{bmatrix}^{J_3} = \begin{bmatrix} 1 & 0 \\ Y_2 & 1 \end{bmatrix} = \begin{bmatrix} 1 & 0 \\ 1/Z_2 & 1 \end{bmatrix}, \quad \text{(B6.6)}$$

$$\begin{bmatrix} A & B \\ C & D \end{bmatrix}^{R2} = \begin{bmatrix} cos\,\theta_{r2}/2 & j\,Z_{r2} sin\,\theta_{r2}/2 \\ j\,1/Z_{r2} sin\,\theta_{r2}/2 & cos\,\theta_{r2}/2 \end{bmatrix}. \quad \text{(B6.7)}$$

Therefore, the ABCD transmission matrix of the unit cell will be:

$$\begin{bmatrix} A & B \\ C & D \end{bmatrix}^{UC} = \begin{bmatrix} cos\,\theta_s/2 & j\,Z_s sin\,\theta_s/2 \\ j\,1/Z_s sin\,\theta_s/2 & cos\,\theta_s/2 \end{bmatrix} \begin{bmatrix} 1 & 0 \\ 1/Z_1 & 1 \end{bmatrix} \begin{bmatrix} cos\,\theta_{r1}/2 & j\,Z_{r1} sin\,\theta_{r1}/2 \\ j\,1/Z_{r1} sin\,\theta_{r1}/2 & cos\,\theta_{r1}/2 \end{bmatrix} \begin{bmatrix} 1 & 0 \\ 1/Z_2 & 1 \end{bmatrix} \begin{bmatrix} cos\,\theta_{r2}/2 & j\,Z_{r2} sin\,\theta_{r2}/2 \\ j\,1/Z_{r2} sin\,\theta_{r2}/2 & cos\,\theta_{r2}/2 \end{bmatrix} \begin{bmatrix} 1 & 0 \\ 1/Z_2 & 1 \end{bmatrix} \begin{bmatrix} cos\,\theta_{r1}/2 & j\,Z_{r1} sin\,\theta_{r1}/2 \\ j\,1/Z_{r1} sin\,\theta_{r1}/2 & cos\,\theta_{r1}/2 \end{bmatrix} \begin{bmatrix} 1 & 0 \\ 1/Z_1 & 1 \end{bmatrix} \begin{bmatrix} cos\,\theta_s/2 & j\,Z_s sin\,\theta_s/2 \\ j\,1/Z_s sin\,\theta_s/2 & cos\,\theta_s/2 \end{bmatrix}. \quad \text{(B6.8)}$$

Appendix C. Calculation Programmes

This appendix documents the computational framework used to synthesise, tune, and evaluate periodic microstrip filters built from four unit-cell topologies (T1–T4). The programs implement the analytical developments of Chapter 5 and generate the numerical results reported in Chapter 6. The four unit-cell geometries are shown in Fig. 6.6.

All calculations are consolidated in the MATLAB® script Periodic_Filter_ T1T4.m, structured into six sections:

1. **Inputs** - acquisition of frequency targets, bandwidth, material constants for the stacked line (LC, polyimide, lid), layer thicknesses, number of cells, frequency sweep, and a topology selector (T1–T4).
2. **Stack & widths** - effective-stack substitutions (Eqs. 5.13–5.16) with standard microstrip relations (Eqs. 5.6–5.12) to compute the 50-Ω line width, effective permittivity ε_{eff}, and guided wavelength at f_0 for the LC low/nominal/high cases.
3. **Initialisation (topology-specific)**, odd/even-mode seeding of unit-cell electrical lengths. For T1/T2, open-stub seeds are used; for T3, the Odd–Even SIR relations (Appendix B, B1.1–B1.15); for T4, the dual-ladder even-mode condition (Eqs. 71.22–71.23). Geometries correspond to those in Fig 6.6.
4. **Optimisation**, reflection-coefficient recursion of the periodic chain (Eqs. 5.58–5.64) with an in-band objective on |Γ| and an out-of-band floor. Topology-specific shunt admittances are evaluated exactly from the seeded electrical lengths.
5. **Periodic ABCD → S-parameters**, unit-cell ABCD (TL–shunt–TL), N-cell cascade, and conversion to S_{11}, S_{21} across the sweep. Corner analyses at LC_{min} and LC_{max}.
6. **Report**, extraction of centre frequency, 3-dB bandwidth, insertion loss, return-loss range, and passband ripple for each LC corner, exports as Excel and MAT files.

Usage and outputs: The script executes interactively and writes intermediate .mat files per section. The file section5_abcd_sparams.xlsx contains frequency-swept S-parameters for LC_{min} and LC_{max}. Units are: frequency in GHz; thicknesses in mm; copper thickness in μm; Z_0=50 Ω

Assumptions and limits:

Lines and stubs are modelled as lossless for synthesis and comparison; conductor and dielectric losses are addressed in full-wave validation (Chapter 6). Effective-stack modelling follows the substitutions of Sec. 5.2 and is appropriate for the geometry of Fig 5.4. Optimisation targets are chosen to satisfy the specified bandwidth while preserving out-of-band rejection for practical N.

Cross-references: Derivations: Sec. 5.2 (stack/microstrip relations), Sec. 5.7.4 (initialisation), Appendix B (T3 Odd–Even), Eqs. 71.22–71.23 (T4 even-mode), Sec. 5.8 (recursion), Sec. 5.9 (periodic ABCD). Geometrical definitions and simulation benchmarking: Fig 6.6 and Chapter 6.

```
function Periodic_Filter_T1T4()
%% ========================================================================
%  Periodic_Filter_T1T4.m
%  Section mapping (thesis refs):
%    1) Inputs (f0, BW, stack εr/thicknesses, Ncells, sweep, Topology)
%    2) Stack substitutions + 50 Ω widths + λg  (Sec. 5.2; Eqs. 5.6–5.16)
%    3) Even/Odd initialisation of unit cell (Sec. 5.7.4; Eqs. 5.42, 5.48–5.49)
%    4) Γ-recursion optimisation (Sec. 5.8; Eqs. 5.58–5.64)
%    5) Periodic ABCD of N cells (Sec. 5.9; Eqs. 5.71–5.73) → S11/S21
%    6) Final report + Excel summaries
%
%  Topology selector:
%    1 = T1: single open stub
%    2 = T2: symmetric dual open stubs
%    3 = T3: SIR ladder (single branch)       ← Fig. 5.17 & B1.1–B1.15
%    4 = T4: dual SIR branches (symmetric)    ← Eqs. (71.22)–(71.23)
%%  Notes:
%    • Units: frequency in GHz; all thicknesses in mm; copper thickness in µm.
% ========================================================================
%% -------------------------- Section 1: Inputs --------------------------
P = section1_inputs();      % (interactive, robust) → struct P
save('section1_inputs.mat','P');
%% ------------- Section 2: Stack + 50Ω width + λg at f0 ----------------
S2 = section2_stack(P);     % solves Wphys, Zc, εeff, λg for LCmin/nom/max
save('section2_stack_widths.mat','S2');
%% ---- Section 3: Even/Odd initialisation for selected Topology ----------
S3 = section3_init(P, S2);  % topology-specific initial geometry
save('section3_initial_dims.mat','S3');
%% -------- Section 4: Γ-recursion optimisation (|Γ|, BW) ----------------
S4 = section4_optimize(P, S2, S3);  % optimised geometry per topology
save('section4_optim.mat','S4');
%% ---- Section 5: Periodic ABCD → S11/S21 (LCmin & LCmax corners) -------
S5 = section5_abcd(P, S2, S4);      % S-params + ABCD, writes Excel
save('section5_abcd_sparams.mat','S5');
%% -------------------- Section 6: Final report/summary -------------------
section6_report(P, S2, S4, S5); end     % prints & writes summary Excel
%% ========================================================================
% Section 1 — Inputs
%
% This section collects (with thesis cross-refs):
%   • f0, BW: centre frequency & required −3 dB passband width
%       – Used by Γ-recursion optimisation (Sec. 5.8, Eqs. (5.58)–(5.64)) and periodic ABCD
evaluation (Sec. 5.9, Eqs. (5.71)–(5.73)).
%   • εr_LC (min,max), εr_PI, εr_LID:
%       – Enter the dielectric constants for the stacked microstrip (Fig. 5.4). They feed
%         the effective-stack substitutions in Sec. 5.2 around Eqs. (5.13)–(5.16) and the
%         classic microstrip relations (Eqs. (5.6)–(5.12)).
%   • h_LC, h_PI, h_LID, t_Cu:
%       – Geometrical thicknesses for Fig. 5.4; h_eq and εr,stack are formed per Eqs.
%        (5.13)–(5.16); t_Cu is kept for the optional finite-thickness correction in
%         Sec. 5.2.
%   • Ncells:
%       – Number of repeated unit cells in the periodic structure (Sec. 5.6 / Fig. 5.6)
%         used in Γ-recursion and T^N (Sec. 5.9).
%   • Frequency sweep [f_start : f_step : f_stop]:
%       – Used throughout for S- and Γ-plots and 3 dB bandwidth reporting.
%========================================================================

function P = section1_inputs()
disp('=== Section 1 — Inputs (Topologies 1–4) ===');
disp('Units: f in GHz, thickness in mm, t_Cu in µm. ENTER = default.');
DEF.f0_GHz     = 60;  % target centre (within 57–66 GHz V/60 GHz bands)
DEF.BW_req_GHz = 3.0;  % required passband width
DEF.erLC_min = 2.20; DEF.erLC_max = 2.70; % LC low and high states(Chapter 4 material data)
DEF.erPI = 3.30; DEF.erLID    = 2.20; % Polyimide & Lid/superstrate (Sec. 5.2 & Fig. 5.4)
DEF.hLC_mm     = 0.200; DEF.hPI_mm  = 0.0025; DEF.hLID_mm = 0.500; DEF.tCu_um = 18;
```

```
% LC , polyimide, lid/superstrate and copper layers thickness (mm)
DEF.Ncells     = 7; % number of unit cells (Sec. 5.6 / Fig. 5.6)
DEF.fStart_GHz = 50; DEF.fStop_GHz = 70; DEF.fStep_GHz = 0.1; % Frequency sweep used by
% later sections
DEF.Topology   = 2;   % Topologies 1,2,3,4 (see header)
P.f0_GHz      = askNum('Centre frequency f0 [GHz]', DEF.f0_GHz, 30, 120);
P.BW_req_GHz  = askNum('Required -3 dB BW [GHz]',   DEF.BW_req_GHz, 0.1, 30);
P.erLC_min    = askNum('LC εr,min', DEF.erLC_min, 1.5, 10);
P.erLC_max    = askNum('LC εr,max', DEF.erLC_max, 1.5, 10);
if P.erLC_max < P.erLC_min, [P.erLC_min, P.erLC_max] = deal(P.erLC_max, P.erLC_min);
end
P.erPI        = askNum('Polyimide εr,PI', DEF.erPI, 2, 5);
P.erLID       = askNum('Lid εr,LID', DEF.erLID, 1.5, 5);
P.hLC_mm      = askNum('LC thickness h_LC [mm]', DEF.hLC_mm, 0.01, 2);
P.hPI_mm      = askNum('Polyimide thickness h_PI (each) [mm]', DEF.hPI_mm, 1e-4, 0.1);
P.hLID_mm     = askNum('Lid thickness h_LID [mm]', DEF.hLID_mm, 0.01, 5);
P.tCu_um      = askNum('Copper thickness t_Cu [µm]', DEF.tCu_um, 1, 100);
P.Ncells      = askInt('Number of unit cells N', DEF.Ncells, 1, 200);
P.fStart_GHz  = askNum('Sweep start [GHz]', DEF.fStart_GHz, 0.1, 1e3);
P.fStop_GHz   = askNum('Sweep stop  [GHz]', DEF.fStop_GHz,  0.2, 2e3);
P.fStep_GHz   = askNum('Sweep step  [GHz]', DEF.fStep_GHz,  0.001, 100);
P.Topology    = askInt('Topology (1=T1, 2=T2, 3=T3, 4=T4)', DEF.Topology, 1, 4);
P.f_vec_GHz   = (P.fStart_GHz:P.fStep_GHz:P.fStop_GHz).';
P.Z0_target   = 50;                       % ADS/CST reference
P.heq_mm      = P.hLC_mm + 2*P.hPI_mm;    % Eq. (5.13)
P.tCu_mm      = P.tCu_um*1e-3;
fprintf('Chosen Topology: T%d\n\n', P.Topology);
end

%% ========================================================================
% Section 2 — Permittivity of stack structure + 50Ω widths + λg (LCmin/nom/max)
%
% This section calculates(with thesis cross-refs):
%    • Geometry: Fig. 5.4 (polyimide–LC–polyimide under strip + lid/superstrate).
%    • Stack substitutions (Chapter 5) to adapt Eqs. (5.6)–(5.12) to Fig. 5.4:
%       h_eq  = h_LC + 2 h_PI        ← Eq. (5.13)
%       ε_b   = h_eq / (2 h_PI/ε_PI + h_LC/ε_LC)        ← Eq. (5.15)
%       ε_r,stack ≈ 1 + K_sub(ε_b–1) + (1–K_sub) F_LID (ε_LID–1)  ← Eq. (5.14)
%       with  K_sub = ½(1 + 1/√(1+12 h_eq/W)), F_LID = 1 – exp(–π h_LID/W) ← (5.14),(5.16)
%    • Microstrip relations (Z0, ε_eff) Sec. 5.2 with Eqs. (5.6)–(5.12).
%========================================================================
function S2 = section2_stack(P)
fprintf('=== Section 2 — Stack & Widths (Eqs. 5.6–5.16) ===\n');
cases = struct('name',{'LCmin','LCnom','LCmax'}, ...
               'erLC',[P.erLC_min, mean([P.erLC_min P.erLC_max]), P.erLC_max]);
for k=1:3
    erLC   = cases(k).erLC;
    er_b   = P.heq_mm / ( (2*P.hPI_mm)/P.erPI + (P.hLC_mm)/erLC ); % Eq. (5.15)
    [W_phys, W_eff, Zc, eeff, er_stack, Ksub, Flid] = ...
        solve_width_for_Z0(P.heq_mm, er_b, P.erLID, P.hLID_mm, P.Z0_target, P.tCu_mm);
    lamg0_mm = (3e11/P.f0_GHz)/sqrt(eeff);  % λ0/√εeff at f0, in mm (c0≈3e11 mm·GHz)
    cases(k).er_b     = er_b;
    cases(k).W_phys   = W_phys;
    cases(k).W_eff    = W_eff;
    cases(k).Zc       = Zc;
    cases(k).eeff     = eeff;
    cases(k).er_stack = er_stack;
    cases(k).Ksub     = Ksub;
    cases(k).Flid     = Flid;
    cases(k).lamg0_mm = lamg0_mm;
    fprintf(' %s: W=%.4f mm, Zc=%.2f Ω, εeff=%.4f, λg=%.4f mm\n', ...
            cases(k).name, W_phys, Zc, eeff, lamg0_mm);
end
S2.P     = P;
S2.Cases = cases;  end % (1=min, 2=nom, 3=max)
% ---- Section 2 helper: width solve using Hammerstad + stack model ----
```

```
function [W_phys, W_eff, Zc, eeff, er_stack, K_sub, F_lid] = ...
    solve_width_for_Z0(heq_mm, er_b, erLID, hLID_mm, Z0_target, tCu_mm)
    % Scalar error for fzero: Z0(W_eff) - target
    Zerr = @(W) ( Z0_only(W, heq_mm, er_b, erLID, hLID_mm) - Z0_target );
    % Bracket W in [a,b]
    a = max(0.02, 0.02*heq_mm);
    b = 10*heq_mm;
    Za = Zerr(a); Zb = Zerr(b);
    if sign(Za) == sign(Zb)
        Ws = logspace(log10(max(1e-3,0.02)), log10(10*heq_mm), 200);
        Zs = arrayfun(Zerr, Ws);
        idx = find(diff(sign(Zs))~=0, 1);
        if isempty(idx), error('Could not bracket root for Z0 width solve.');
end
        a = Ws(idx); b = Ws(idx+1); end
    % Solve for effective width
    W_eff = fzero(Zerr, [a b]);
    % Thickness correction
    [~, eeff_tmp] = Z0_eeff(W_eff, heq_mm, er_b, erLID, hLID_mm);
    dW   = tCu_mm/pi * (1 + 1/eeff_tmp);
    W_phys = max(W_eff - dW, 0.01);
    % Polish
    for it = 1:3
        W_eff2 = W_phys + dW;
        [~, eeff_tmp] = Z0_eeff(W_eff2, heq_mm, er_b, erLID, hLID_mm);
        dW = tCu_mm/pi * (1 + 1/eeff_tmp);
        W_phys = max(W_eff - dW, 0.01); end
    % Final eval
    W_eff = W_phys + dW;
    [Zc, eeff, er_stack, K_sub, F_lid] = Z0_eeff(W_eff, heq_mm, er_b, erLID, hLID_mm);
end
function Z0 = Z0_only(W_eff, heq_mm, er_b, erLID, hLID_mm)
    [Z0, ~] = Z0_eeff(W_eff, heq_mm, er_b, erLID, hLID_mm);
end
function [Z0, eeff, er_stack, K_sub, F_lid] = Z0_eeff(W_eff, heq_mm, er_b, erLID, hLID_mm)
    K_sub    = 0.5*(1 + 1./sqrt(1 + 12*(heq_mm./W_eff)));    % Eq. (5.14) term
    F_lid    = 1 - exp(-pi*(hLID_mm./W_eff));                  % Eq. (5.16)
    er_stack = 1 + K_sub.*(er_b - 1) + (1 - K_sub).*F_lid.*(erLID - 1);  % Eq. (5.14)
    [Z0, eeff] = hammerstad_Z0(W_eff, heq_mm, er_stack);  end
function [Z0, eeff] = hammerstad_Z0(W, h, er)
    u = W./h;
    eeff = (er+1)/2 + (er-1)/2 ./ sqrt(1 + 12./u);
    if u <= 1
        Z0 = (60./sqrt(eeff)).*log(8./u + 0.25.*u);
else
        Z0 = (120*pi./sqrt(eeff)) ./ (u + 1.393 + 0.667.*log(u + 1.444));     end
    Z0 = Z0(1); eeff = eeff(1);
end

function S3 = section3_init(P, S2)
%% ========================================================================
%  Section 3 — Initial estimation (topology-specific)
%
%  This section calculates:
%    - Odd-mode input admittance into the spine (half-cell)
%    - Even-mode with two symmetric open stubs (each width Wr, length L2)
%  References:
%    • Sec. 5.7.4 (Fig. 5.25): even/odd guidance for T1/T2.
%    • Appendix B (B1.1–B1.15): SIR ladder resonance for T3.
%    • Eqs. (71.22)–(71.23): double SIR ladders (even-mode) for T4.
%    • Uses ε_eff and Zc from Section 2 (Hammerstad; Eqs. 5.6–5.12).
%  Output:
%    • section3_initial_dims.mat : struct S3 with Ws, Wr, L1, L2, Ls, etc.
% ========================================================================
TopoID = P.Topology;                % 1..4
Nom    = S2.Cases(2);               % nominal LC
```

```
c0       = 299792458;
f0       = P.f0_GHz*1e9;
beta0    = (2*pi*f0/c0)*sqrt(Nom.eeff);     % rad/m
beta0_mm = beta0/1e3;                       % rad/mm
lamg0_mm = (c0/f0)/sqrt(Nom.eeff)*1e3;
Ws = Nom.W_phys;   Wr = Nom.W_phys;
switch TopoID
case 1   % T1: single open stub
    th1 = pi/4; th2 = 3*pi/4;
    L1 = th1/beta0_mm;  L2 = th2/beta0_mm;
    Ls = 0.25*lamg0_mm;  extra = struct();
case 2   % T2: symmetric dual open stubs
    th1 = pi/4; th2 = 3*pi/4;
    L1 = th1/beta0_mm;  L2 = th2/beta0_mm;
    Ls = 0.25*lamg0_mm;  extra = struct('Nstub',2);
case 3   % T3: SIR ladder (Appendix B: B1.1–B1.15)
    K = [1,1,1];
    th1 = pi/4; th3 = pi/4; th4 = pi/4;
    th2 = solve_t3_theta2(th1, th3, th4, K);
    L1 = th1/beta0_mm; L2 = th2/beta0_mm;
    L3 = th3/beta0_mm; L4 = th4/beta0_mm;
    Ls = 0.25*lamg0_mm; extra = struct('L3_mm',L3,'L4_mm',L4,'K',K);
case 4   % T4: dual SIR ladders (Eqs. 71.22–71.23)
    K = [1,1,1,1];
    th1=pi/4; th2=pi/3; th3=pi/4; th4=pi/4; th5=pi/4;
    th2 = solve_t4_theta2([th1 th2 th3 th4 th5], K);
    L1=th1/beta0_mm; L2=th2/beta0_mm; L3=th3/beta0_mm; L4=th4/beta0_mm; L5=th5/beta0_mm;
    Ls=0.25*lamg0_mm; extra = struct('L3_mm',L3,'L4_mm',L4,'L5_mm',L5,'K',K);
otherwise
    error('Unknown Topology (1–4).');
end
S3 = struct('Ws_mm',Ws,'Wr_mm',Wr,'L1_mm',L1,'L2_mm',L2,'Ls_mm',Ls, ...
            'lamg0_mm',lamg0_mm,'beta0mm',beta0_mm,'extra',extra);
fprintf('=== Section 3 — Initial dimensions (Topology %d) ===\n', TopoID);
fprintf('Ws=Wr=%.4f mm, L1=%.4f mm, L2=%.4f mm, Ls=%.4f mm\n', S3.Ws_mm, S3.Wr_mm,
S3.L1_mm, S3.L2_mm, S3.Ls_mm);
if isfield(S3.extra,'L3_mm'), fprintf('L3=%.4f mm\n', S3.extra.L3_mm);  end
if isfield(S3.extra,'L4_mm'), fprintf('L4=%.4f mm\n', S3.extra.L4_mm);  end
if isfield(S3.extra,'L5_mm'), fprintf('L5=%.4f mm\n', S3.extra.L5_mm);  end
end
% ---- helpers used by Section 3 ----
function th2 = solve_t3_theta2(th1, th3, th4, K)
    K1=K(1); K2=K(2); K3=K(3);
    f = @(t2) ...
      K1*K2*K3*tan(th1) - K2*K3*tan(t2) + K3*tan(th3) + tan(th4) + ...
      ( K1*K3*tan(th1)*tan(t2)*tan(th3) + K1*tan(th1)*tan(t2)*tan(th4) ...
      - K1*tan(th1)*tan(th3)*tan(th4) - K2*tan(t2)*tan(th3)*tan(th4) );
    th2 = fzero(f, 3*pi/4);
end
function th2 = solve_t4_theta2(th, K)
    th1=th(1); th2=th(2); th3=th(3); th4=th(4); th5=th(5); %#ok<ASGLU>
    f = @(x) Yin_even_T4([th1 x th3 th4 th5], K);
    th2 = fzero(@(x) real(f(x)), pi/3);
end
function Yin = Yin_even_T4(th, K)
    th1=th(1); th2=th(2); th3=th(3); th4=th(4); th5=th(5);
    Y1=1;  Y2=Y1/K(1); Y3=Y2/K(2); Y4=Y3/K(3); Y5=Y4/K(4);
    Ye = 1j*Y5*tan(th5);
    Yd = Y4*(Ye + 1j*Y4*tan(th4)) / (Y4 + 1j*Ye*tan(th4));
    Yc = Y2*(Yd + 1j*Y2*tan(th2)) / (Y2 + 1j*Yd*tan(th2));
    Yb = Y3*(Yc + 1j*Y3*tan(th3)) / (Y3 + 1j*Yc*tan(th3));
    Ya1= Y2*(Yb + 1j*Y2*tan(th2)) / (Y2 + 1j*Yb*tan(th2));
    Ya = 2*Ya1;
    Yin= Y1 * ( Ya + 1j*Y1*tan(th1) ) / ( Y1 + 1j*Ya*tan(th1) );
end
```

```
function S4 = section4_optimize(P, S2, S3)
%% ========================================================================
%  Section 4 — Γ-recursion optimisation (topology-specific)
%  This section calculates:
%    - reflection coefficient of unit cell
%    - change geometry of unit cell and optimise based on lowest reflection coefficient
%  References:
%    • Sec. 5.8; Eqs. (5.58)–(5.64): recursion form.
%    • Exact local reflection for a shunt admittance: Γ_sh = -y/(2+y), y=Ysh/Y1.
%  Output:
%    • section4_optim.mat : struct S4 with L2/Ls (and S11_dB vs f), cost J, etc.
% ========================================================================
TopoID = P.Topology;
Nom    = S2.Cases(2);
% Frequency vector (Hz)
fvec = P.f_vec_GHz(:)*1e9;
[Lopt, rep] = sec4_opt_core(TopoID, P, Nom, S3, fvec);
fprintf('=== Section 4 — Optimisation complete (Topology %d) ===\n', TopoID);
fprintf('L2=%.4f mm, Ls=%.4f mm (L1=%.4f mm retained for phase)\n', Lopt.L2_mm, Lopt.Ls_mm,
Lopt.L1_mm);
[~,i0] = min(abs(P.f_vec_GHz - P.f0_GHz));
fprintf('S11(f0=%.2f GHz) = %.2f dB\n', P.f0_GHz, rep.S11_dB(i0));
S4 = struct('P',P,'G3',S3,'Lopt',Lopt,'S11_dB',rep.S11_dB,'f_Hz',rep.fvec,'J',rep.J);
end
% ---- core optimiser & helpers ----
function [Lopt, report] = sec4_opt_core(TopoID, P, Nom, G3, fvec)
    c0=299792458; eeff=Nom.eeff; Zc=Nom.Zc; Y1=1/Zc;
    beta=(2*pi*fvec/c0).*sqrt(eeff); bmm=beta/1e3;
    f0=P.f0_GHz*1e9; BW=P.BW_req_GHz*1e9; f_lo=f0-BW/2; f_hi=f0+BW/2;
    inBand=(fvec>=f_lo)&(fvec<=f_hi); outBand=~inBand;
    Gt_center=0.10; Gt_in=0.15; Gmin_out=0.55;
    w_center=5; w_in=2; w_out=1;
    x0 = initial_vector_from_G3(TopoID, G3);
    opts = optimset('Display','iter','TolX',1e-5,'TolFun',1e-
8,'MaxFunEvals',3000,'MaxIter',1500);
    costfun=@(x) cost_generic(x, TopoID, bmm, Y1, inBand, outBand, ...
                              Gt_center,Gt_in,Gmin_out, w_center,w_in,w_out, G3, P);
    [X,J]=fminsearch(costfun, x0, opts);
    Lopt = pack_lengths(TopoID, X, G3);
    % Final Γ sweep
    Ysh = Yshunt_dispatch(TopoID, bmm, Nom, Lopt, G3);
    G   = gamma_total(bmm, P.Ncells, @() Ysh, Lopt.Ls_mm, Y1);
    report = struct('X',X,'J',J,'S11_dB',20*log10(abs(G)+eps),'fvec',fvec);
end
function G = gamma_total(bmm, N, Yfun, Ls_mm, Y1)
    y  = Yfun()./Y1;
    Gs = - y ./ (2 + y);
    th = bmm .* Ls_mm;  e = exp(-2j*th);
    G  = zeros(size(bmm));
    for n=N:-1:1
        G = (Gs + G.*e) ./ (1 + Gs.*G.*e);  end
end
function Y = Yshunt_dispatch(TopoID, bmm, Case, L, G3)
    switch TopoID
    case 1, Y = Ysh_T1(bmm, Case, L.L2_mm);
    case 2, Y = 2*Ysh_T1(bmm, Case, L.L2_mm);
    case 3, Y = Ysh_T3(bmm, Case, [L.L2_mm, G3.extra.L3_mm, G3.extra.L4_mm], G3.extra.K);
    case 4, Y = Ysh_T4(bmm, Case, [L.L2_mm, G3.extra.L3_mm, G3.extra.L4_mm,
G3.extra.L5_mm], G3.extra.K);
    otherwise, error('Unknown Topology.');  end
end
function Y = Ysh_T1(bmm, Case, L2)
    Y2=1/Case.Zc; th2=bmm.*L2; Y=1j*Y2.*tan(th2);  end
function Y = Ysh_T3(bmm, Case, L, K)
    L2=L(1); L3=L(2); L4=L(3);
    Y1=1/Case.Zc; Y2=Y1/K(1); Y3=Y2/K(2); Y4=Y3/K(3);
```

```
    th2=bmm.*L2; th3=bmm.*L3; th4=bmm.*L4;
    Yc=1j*Y4.*tan(th4);
    Yb=Y3.*(Yc+1j*Y3.*tan(th3))./(Y3+1j*Yc.*tan(th3));
    Ya=Y2.*(Yb+1j*Y2.*tan(th2))./(Y2+1j*Yb.*tan(th2));
    Y = Ya;
end
function Y = Ysh_T4(bmm, Case, L, K)
    L2=L(1); L3=L(2); L4=L(3); L5=L(4);
    Y1=1/Case.Zc; Y2=Y1/K(1); Y3=Y2/K(2); Y4=Y3/K(3); Y5=Y4/K(4);
    th2=bmm.*L2; th3=bmm.*L3; th4=bmm.*L4; th5=bmm.*L5;
    Ye=1j*Y5.*tan(th5);
    Yd=Y4.*(Ye+1j*Y4.*tan(th4))./(Y4+1j*Ye.*tan(th4));
    Yc=Y2.*(Yd+1j*Y2.*tan(th2))./(Y2+1j*Yd.*tan(th2));
    Yb=Y3.*(Yc+1j*Y3.*tan(th3))./(Y3+1j*Yc.*tan(th3));
    Ya1=Y2.*(Yb+1j*Y2.*tan(th2))./(Y2+1j*Yb.*tan(th2));
    Y = 2*Ya1; end
function x0 = initial_vector_from_G3(TopoID, G3)
    switch TopoID
    case {1,2}, x0 = [G3.L2_mm, G3.Ls_mm];
    case 3,     x0 = [G3.L2_mm, G3.Ls_mm];
    case 4,     x0 = [G3.L2_mm, G3.Ls_mm];  end
end
function L = pack_lengths(TopoID, X, G3)
    L = struct('L1_mm',G3.L1_mm,'L2_mm',X(1),'Ls_mm',X(2));
    if TopoID==3
        L.L3_mm=G3.extra.L3_mm; L.L4_mm=G3.extra.L4_mm;
    elseif TopoID==4
        L.L3_mm=G3.extra.L3_mm; L.L4_mm=G3.extra.L4_mm; L.L5_mm=G3.extra.L5_mm;  end
end
function J = cost_generic(x, TopoID, bmm, Y1, inBand, outBand, ...
                          GtC,GtIn,GminOut, wC,wI,wO, G3, P)
    L = pack_lengths(TopoID, x, G3);
    Y = Yshunt_dispatch(TopoID, bmm, struct('Zc',1/Y1), L, G3);
    G = gamma_total(bmm, P.Ncells, @() Y, L.Ls_mm, Y1);
    a = abs(G);
    [~,i0] = min(abs(P.f_vec_GHz - P.f0_GHz));
    eC = max(a(i0)-GtC,0).^2;
    eI = mean(max(a(inBand)-GtIn,0).^2);
    eO = mean(max(GminOut - a(outBand),0).^2);
    J  = wC*eC + wI*eI + wO*eO;
End

function S5 = section5_abcd(P, S2, S4)
%% ========================================================================
%  Section 5 — Periodic ABCD (N cells) → S11/S21 (topology-specific)
%
%  This section calculates
%  - Periodic structure ABCD matrix for N cells over sweep frequency range
%  - S11, S21 over sweep frequency range
%  References:
%    • Unit cell: TL(½Ls) – Shunt(Ysh) – TL(½Ls).
%    • Periodic cascade via eigendecomposition: T_total = (T_uc)^N (Sec. 5.9).
%    • ABCD → S at Z0=50 Ω.
%  Output:
%    • section5_abcd_sparams.xlsx : Sheets LCmin, LCmax
%    • section5_abcd_sparams.mat  : All, Z0, Lopt, Ncells
% ========================================================================
TopoID = P.Topology;
Cases  = S2.Cases;
Z0     = 50;
Ncells = P.Ncells;
% Frequency axis (Hz)
if isfield(S4,'f_Hz') && ~isempty(S4.f_Hz)
    f = S4.f_Hz(:); else
    f = P.f_vec_GHz(:) * 1e9;
end
```

```
fGHz = f/1e9;
% Corners
Corner(1).name='LCmin'; Corner(1).eeff=Cases(1).eeff; Corner(1).Zc=Cases(1).Zc;
Corner(2).name='LCmax'; Corner(2).eeff=Cases(3).eeff; Corner(2).Zc=Cases(3).Zc;
All = struct([]);
for ic=1:2
    eeff = Corner(ic).eeff; Zc_ln=Corner(ic).Zc; Y1=1/Zc_ln;
    beta=(2*pi*f/299792458).*sqrt(eeff); bmm=beta/1e3;
    % Topology-specific shunt at the tap:
    Ysh = Yshunt_dispatch_local(TopoID, bmm, Corner(ic), S4.Lopt, S4.G3);
    % Unit cell ABCD
    Tseg = abcd_tline(Zc_ln, (bmm.*S4.Lopt.Ls_mm)/2);
    Tsh  = abcd_shuntB(imag(Ysh));
    Tuc  = mult2x2(mult2x2(Tseg, Tsh), Tseg);
    % Periodic cascade
    Ttot = matpow2x2(Tuc, Ncells);
    % ABCD → S-parameters
    [S11, S21] = abcd2s_2port(Ttot, Z0);
    All(ic).name   = Corner(ic).name;
    All(ic).fGHz   = fGHz;
    All(ic).S11    = S11;
    All(ic).S21    = S21;
    All(ic).S11_dB = 20*log10(abs(S11)+eps);
    All(ic).S21_dB = 20*log10(abs(S21)+eps);
    All(ic).A      = squeeze(Ttot(1,1,:));
    All(ic).B      = squeeze(Ttot(1,2,:));
    All(ic).C      = squeeze(Ttot(2,1,:));
    All(ic).D      = squeeze(Ttot(2,2,:));  end
% Excel + MAT
fnameX = 'section5_abcd_sparams.xlsx';
if exist(fnameX,'file'), delete(fnameX);  end
for ic=1:2
    T = table(All(ic).fGHz, abs(All(ic).S11), abs(All(ic).S21), ...
              All(ic).S11_dB, All(ic).S21_dB, ...
              real(All(ic).A), imag(All(ic).A), ...
              real(All(ic).B), imag(All(ic).B), ...
              real(All(ic).C), imag(All(ic).C), ...
              real(All(ic).D), imag(All(ic).D), ...
              'VariableNames', {'f_GHz','S11_mag','S21_mag','S11_dB','S21_dB', ...
                                'A_re','A_im','B_re','B_im','C_re','C_im','D_re','D_im'});
    writetable(T, fnameX, 'Sheet', All(ic).name); end
S5 = struct('Results',All,'Z0',Z0,'Ncells',Ncells,'TopoID',TopoID,'Lopt',S4.Lopt);
save('section5_abcd_sparams.mat','S5');
fprintf('=== Section 5 complete (Topology %d) ===\n', TopoID);
fprintf('Excel written: %s (Sheets: LCmin, LCmax)\n', fnameX);
end
% ---- Section 5 local helpers ----
function Y = Yshunt_dispatch_local(TopoID, bmm, Case, Lopt, G3)
    switch TopoID
    case 1, Y = Ysh_T1(bmm, Case, Lopt.L2_mm);
    case 2, Y = 2*Ysh_T1(bmm, Case, Lopt.L2_mm);
    case 3, Y = Ysh_T3(bmm, Case,[Lopt.L2_mm, G3.extra.L3_mm, G3.extra.L4_mm], G3.extra.K);
    case 4, Y = Ysh_T4(bmm, Case, [Lopt.L2_mm, G3.extra.L3_mm, G3.extra.L4_mm,
G3.extra.L5_mm], G3.extra.K);
    otherwise, error('Unknown Topology (1–4).');  end
end
% ---- ABCD utilities (unchanged) ----
function T = abcd_tline(Zc, theta)
    cth = cos(theta);  sth = sin(theta);
    T = zeros(2,2,numel(theta));
    T(1,1,:) = cth;
    T(1,2,:) = 1j*Zc.*sth;
    T(2,1,:) = 1j*(sth./Zc);
    T(2,2,:) = cth;end
function T = abcd_shuntB(B)
    T = zeros(2,2,numel(B));
```

```
    T(1,1,:) = 1;     T(1,2,:) = 0;
    T(2,1,:) = 1j*B;  T(2,2,:) = 1;
end
function Tout = mult2x2(T1, T2)
    n = size(T1,3);  Tout = zeros(2,2,n);
    for k = 1:n, Tout(:,:,k) = T1(:,:,k) * T2(:,:,k); end
end
function Tpwr = matpow2x2(T, N)
    n = size(T,3);  Tpwr = zeros(2,2,n);
    for k = 1:n
        Tk = T(:,:,k); [V,D] = eig(Tk);
        if rcond(V) > 1e-12
            Dn = diag(diag(D).^N);
            Tpwr(:,:,k) = V * Dn / V;
        else
            Tpwr(:,:,k) = eye(2);p = Tk; e = N;
            while e > 0
                if bitand(e,1), Tpwr(:,:,k) = Tpwr(:,:,k) * p; end
                p = p*p; e = bitshift(e,-1); end
        end
    end
end
function [S11, S21] = abcd2s_2port(T, Z0)
    A = squeeze(T(1,1,:)); B = squeeze(T(1,2,:));
    C = squeeze(T(2,1,:)); D = squeeze(T(2,2,:));
    den = (A + B./Z0 + C.*Z0 + D);
    S11 = (A + B./Z0 - C.*Z0 - D) ./ den;
    S21 = 2 ./ den; end
function section6_report(P, S2, S4, S5)
%% ========================================================================
% Section 6 — Final report (metrics, tuning, summary Excel)
%  This section reports:
%   - Key filter parameters for LCmin & LCmax
%  References:
%  Fig. 5.4; Eqs. (5.6)–(5.16), (5.42), (5.48)–(5.49), (5.58)–(5.64), (5.71)–(5.73))
% ========================================================================
fprintf('=== Section 6 — Final Report ===\n');
R = S5.Results; fGHz = R(1).fGHz;
for i = 1:2
    S11_dB = R(i).S11_dB;
    S21_dB = R(i).S21_dB;
    [pk,idx] = max(abs(R(i).S21));     % use |S21|
    f0 = fGHz(idx);
    IL = -20*log10(abs(pk)+eps);
    thr = 20*log10(abs(pk)+eps) - 3;   % 3 dB down
    [flo,fhi,bw] = band_3dB(fGHz, S21_dB, thr, idx);
    inB = (fGHz>=flo) & (fGHz<=fhi);
    RLmin = min(S11_dB(inB));
    RLmax = max(S11_dB(inB));
    ripple = max(S21_dB(inB)) - min(S21_dB(inB));
    fprintf('-- %s -- f0=%.3f GHz, BW=%.3f GHz [%.3f, %.3f], IL=%.2f dB, RL=[%.1f, %.1f]
dB, Ripple=%.2f dB\n',...
       R(i).name, f0, bw, flo, fhi, IL, RLmin, RLmax, ripple); end
end
% ---- helper used above ----
function [f_lo, f_hi, bw] = band_3dB(f, S21_dB, thr_dB, idx_pk)
    n  = numel(f);  th = thr_dB;
    iL = idx_pk; while iL > 1   && S21_dB(iL-1) >= th, iL = iL-1;
end
    iH = idx_pk; while iH < n   && S21_dB(iH+1) >= th, iH = iH+1;
end
    f_lo = f(iL); f_hi = f(iH);
    if iL > 1
        f1=f(iL-1); f2=f(iL); y1=S21_dB(iL-1); y2=S21_dB(iL);
        if y2~=y1, f_lo = f1 + (th - y1)*(f2 - f1)/(y2 - y1); end
    end
```

```
    if iH < n
        f1=f(iH); f2=f(iH+1); y1=S21_dB(iH); y2=S21_dB(iH+1);
        if y2~=y1, f_hi = f1 + (th - y1)*(f2 - f1)/(y2 - y1); end
    end
    bw = max(f_hi - f_lo, 0);
end
function val = askNum(prompt, defaultVal, minVal, maxVal)
% Ask for a scalar numeric value with default & range checking.
    if nargin < 2, defaultVal = []; 
end
    if nargin < 3, minVal = -inf; end
    if nargin < 4, maxVal = +inf; end
    while true
        if isempty(defaultVal)
            s = input(sprintf('%s : ', prompt), 's'); else
            s = input(sprintf('%s  [%g] : ', prompt, defaultVal), 's'); end
        if isempty(s) && ~isempty(defaultVal)
            val = defaultVal; break;
        end
        v = str2double(s);
        if ~isnan(v) && isscalar(v) && v >= minVal && v <= maxVal
            val = v; break;
        else
            fprintf('  -> Please enter a number in [%.4g, %.4g].\n', minVal, maxVal);
        end
    end
end

function val = askInt(prompt, defaultVal, minVal, maxVal)
% Ask for an integer with default & bounds.
    v = askNum(prompt, defaultVal, minVal, maxVal);
    val = round(v);
end
```